Application of a Micropolar Model to the Localization Phenomena in Granular Materials: General Model, Sensitivity Analysis and Parameter Optimization

Von der Fakultät Bau- und Umweltingenieurwissenschaften
der Universität Stuttgart zur Erlangung der Würde
eines Doktor-Ingenieurs (Dr.-Ing.)
genehmigte Abhandlung

Vorgelegt von

Dipl.-Ing. Bernd Scholz

aus

Stuttgart

Hauptberichter: Prof. Dr.-Ing. Wolfgang Ehlers
Mitberichter: Prof. Dr.-Ing. Paul Steinmann

Tag der mündlichen Prüfung: 15. August 2007

Institut für Mechanik (Bauwesen) der Universität Stuttgart
Lehrstuhl II, Prof. Dr.-Ing. W. Ehlers
2007

Editor:

Prof. Dr.-Ing. W. Ehlers

Acknowledgments

Deutsche Zusammenfassung

Die mechanische Beschreibung granularer Medien ist in vielen Gebieten des Ingenieurwesens von Bedeutung. Insbesondere kommen granulare Materialien, im speziellen Sand, oft im Baugrund vor und somit ist die Kenntnis der mechanischen Eigenschaften dieser Materialien wichtig zur Berechnung der Lastabtragung von Bauwerken. Desweiteren ist das Verständnis des Verhaltens granularer Materialen von Bedeutung zur Vorhersage von geologischen Katastrophen wie Böschungs- oder Grundbrüchen. Der Grund für das Auftreten dieser Phänomene liegt im mechanisch instabilen Verhalten granularer Medien. So kann bei Böschungs- oder Grundbrüchen beobachtet werden, dass die gesamte Deformation in dünnen Bändern oder Flächen, den sogenannten Scherbändern bzw. Scherflächen konzentriert ist. Die Erforschung dieser Lokalisierungsphänomene, welche unmittelbar mit dem instabilen Verhalten dieser Materialien zusammenhängen, ist Bestandteil der aktuellen Materialforschung, sowie das Thema der vorliegenden Arbeit.

Ausgangspunkt

Die ersten Ansätze zur mathematischen Beschreibung des mechanischen Verhaltens geomechanischer Materialien stammen von *Coulomb* aus dem 18. Jahrhundert. Darin wurden diese Materialen als Reibungsmaterialen beschrieben. Das bedeutet, dass diese Materialen nur dann als Festkörper bezeichnet werden können, wenn sie unter einer Druckspannung stehen. Fehlt diese Druckspannung, fallen diese Reibungsmaterialen auseinander und das mechanische Verhalten gleicht dem einer Flüssigkeit.

Bei der genaueren Betrachtung granularer Materialien wird weiterhin deutlich, dass es sich um Mehrphasenmaterialien handelt, d. h. sie bestehen neben dem granularen Festkörperskelett (z. B. Sandkörner) zusätzlich noch aus einem Porenfluid, im allgemeinen Luft oder Wasser. Dieses Porenfluid kann einen erheblichen Einfluss auf die mechanischen Eigenschaften des Materials haben, z. B. wird die Setzung von Bauwerken bei tonigen Böden wesentlich von dem langsamen Ausfließen des Wassers beeinflusst. Zur Erfassung der Wirkung des Porenfluids sowie der Interaktion zwischen Fluid und Festkörper wurde die *Theorie der porösen Medien* entwickelt, welche im wesentlichen auf die Arbeiten von *Truesdell & Toupin* [132], *de Boer* [12] sowie *de Boer & Ehlers* [14] zurückgeht. Da in der vorliegenden Arbeit ein trockener Sand beschrieben wird, kann der Einfluss des Porenfluids vernachlässigt werden. Somit beschränkt sich die Anwendung der *Theorie der porösen Medien* auf die Beschreibung eines Einphasenmaterials unter Berücksichtigung des Einflusses des veränderlichen Porenvolumens auf die Steifigkeit.

Eine weitere wesentliche Eigenschaft granularer Materialien ist die Instabilität dieser Materialen, d. h. das plötzliche Versagen während der Lastabtragung. Dieses Phänomen kann bei Erdrutschen oder Grundbrüchen in der Natur beobachtet werden und kann mittels Biaxial- oder Triaxialversuchen im Labor reproduziert werden. Dabei ist zu beobachten, dass sich beim plötzlichen Versagen des Materials sogenannte Scherbänder bilden, worin die gesamte Deformation konzentriert ist (Lokalisierungsproblem). Der Grund für diese Instabilität ist das entfestigende Verhalten granularer Materialien. Während normaler-

weise mit zunehmender Verzerrung auch die Spannung zunimmt, kommt es beim entfestigenden Verhalten zur Abnahme der Spannung mit zunehmender Verformung, was zum Versagen der Probe führt. Die Ursache für die plötzlich auftretende Entfestigung bei granularen Materialien liegt im dilatanten Verformungsverhalten dieser Materialien, welches z. B. beim Triaxialversuch anhand der Volumenzunahme der Probe beobachtet wird. Infolge der hohen Steifigkeit des Festköpermaterials gegenüber der Steifigkeit der Probe kann das Festkörpervolumen als konstant angesehen werden. Die Volumenzunahme ist somit direkt mit der Zunahme des Porenvolumens verbunden und kann somit als Ursache für die Entfestigung des Materials angesehen werden.

Bei Verwendung der standard (*Boltzmann*) Kontinuumstheorie zur Simulation solcher Lokalisierungsprobleme führt das entfestigende Verhalten auf ein mathematisch schlecht gestelltes Problem, was sich darin zeigt, dass die berechnete Dicke des sich bildenden Scherbandes mit zunehmender Netzverfeinerung stetig abnimmt, bis im Grenzfall die Scherbanddicke gegen null geht. Aus Versuchen ist jedoch bekannt, dass die Scherbanddicke im Bereich von 10 bis 30 mittleren Partikeldurchmessern liegt. Dies zeigt zum einen, dass die Verwendung der standard Kontinuumstheorie zu unphysikalischen Ergebnissen führt, und zum anderen ist diese Beobachtung ein Hinweis auf die Existenz einer intrisischen Längenskalierung im Material. Demzufolge muss zur physikalisch korrekten Modellierung des Lokalisierungsverhaltens granularer Materialien, das Verhalten des Materials auf der Mikroskala berücksichtigt werden.

Eine Möglichkeit dazu ist die detaillierte Simulation der einzelnen Partikel des Materials mit Hilfe von Partikelmodellen. Da zur Modellierung makroskopischer Randwertprobleme eine immense Anzahl von Partikeln berücksicht werden müsste, ist jedoch klar, dass eine solch detaillierte Modellierung der Mikrostruktur nicht zur Simulation realer Randwertprobleme geeignet ist. Aus diesem Grund werden die Einflüsse der Effekte auf der Mikroskala innerhalb einer erweiterten Kontinuumstheorie berücksichtigt. In der vorliegenden Arbeit wird dazu die *Cosserat*-Theorie, welche auch oft als mikropolare Theorie bezeichnet wird, verwendet. Dabei wird der Einfluss der gemittelten Partikelrotationen auf der Mikroskala mit Hilfe zusätzlicher Rotationsfreiheitsgrade auf das makroskopische Verhalten übertragen.

Obwohl Partikelmodelle aufgrund des großen numerischen Aufwands zur Simulation realer Randwertprobleme im allgemeinen ungeeignet sind, können vereinfachte Partikelmodelle zur Verifikation der *Cosserat*-Theorie herangezogen werden. Ein Vorteil der Verwendung von Partikelmodellen zur Verifikation gegenüber Experimenten mit granularen Materialien liegt darin, dass neben der Breite des Scherbandes auch die Rotationen der Partikel, sowie die zwischen den einzelnen Partikeln wirkenden Kräfte zur Verifikation betrachtet werden können.

Zur Berechnung realistischer Probleme ist neben der physikalisch korrekten Modellierung des Materials auch die Kenntnis der Werte aller Materialparameter notwendig. Aufgrund der Komplexität des Materialmodells ist eine direkte Messung der Materialparameter nicht möglich. Statt dessen müssen die Methoden der Parameteridentifikation zur Ermittlung der Materialparameter herangezogen werden, d. h. ein inverses Problem muss formuliert werden, welches mit Hilfe der Methoden der nichtlinearen Optimierung gelöst werden kann. Dabei sind die Materialparameter die Unbekannten, während das Ergebnis

des Randwertproblems (Kräfte und Verformungen) durch die Messergebnisse bekannt ist. Die Lösung des Problems besteht in dem Satz der Materialparameter, welche den Fehler zwischen Messung und Simulation minimieren. Da in der vorliegenden Arbeit sowohl das elastische Verhalten, die plastische Ver- und Entfestigung des Materials sowie die zur Regularisierung des Lokalisierungsproblems notwendige erweiterte Theorie verwendet wird, ist zur Identifikation aller Materialparameter ein schrittweises Vorgehen notwendig. Dazu werden zunächst homogene Versuche zur Identifikation der Parameter des standard Kontinuums verwendet und anschließend die zusätzlichen Parameter infolge der *Cosserat*-Theorie anhand inhomogener Versuche unter Berücksichtigung der Scherbandbildung ermittelt.

Ziele und Ergebnisse

Das Ziel der Arbeit ist die umfassende Beschreibung des mechanischen Verhaltens granularer Reibungsmaterialen. Dies schließt sowohl das homogene Verhalten als auch die Beschreibung der Lokalisierungsphänomene ein.

Demzufolge wurde zunächst ein Modell zur Beschreibung des homogenen Materialverhaltens entwickelt. Dazu wurde in dieser Arbeit ein nichtlineares Elastizitätsgesetz in Anlehnung an die Arbeiten von *Eipper* [58], *Müllerschön* [105] und *Schanz* [116] formuliert. Zur Beschreibung des plastischen Materialverhaltens wurde desweiteren das Einflächenfließkriterium nach *Ehlers* [39, 40] verwendet, gekoppelt mit einer verzerrungsgesteuerten, plastischen Verfestigung in Anlehnung an die Arbeiten von *Kim & Lade* [82, 86, 87] und *Bolzon* et al. [15]. Zur zusätzlichen Berücksichtigung des entfestigenden Verhaltens wurde ein neuer Ansatz entwickelt, bei welchem die plastische Volumendehnung in der Entwicklung der Fließfläche berücksichtigt wird. Dies führt bei dilatantem, plastischem Fließen, d.h. Zunahme des Volumens, zu einer Entfestigung des Materials.

Als Folge dieser Entfestigung bilden sich Scherbänder und die Elliptizität der zugrundeliegenden Differentialgleichungen geht verloren (schlecht gestelltes Problem), was zur Netzabhängigkeit der Lösung führt. Durch die Berücksichtigung der gemittelten Mikrorotationen mittels der *Cosserat*-Theorie kann das Problem regularisiert weden, siehe z. B. *Mühlhaus* [102], *Mühlhaus & Vardoulakis* [104], *de Borst* [16] und *Steinmann* [127]. Ein Problem bei der Verwendung der *Cosserat*-Theorie ist, neben der numerischen Implementierung, die Identifikation der zusätzlichen Materialparameter. Dazu ist die Betrachtung inhomogener Biaxialversuche mit Scherbandbildung erforderlich. Der regularisierende Effekt der *Cosserat*-Theorie zeigt sich bei diesen Versuchen zum einen im allmählichen Abfall der Last-Verschiebungskurve und zum anderen in der Breite des einspringenden Scherbandes. Beide Effekte werden in der vorliegenden Arbeit zur Identifikation der Materialparameter des polaren Verhaltens, welches mittels der erweiterten Theorie beschrieben wird, herangezogen. Zur Erfassung der Scherbandbreite wurde dazu innerhalb der Arbeit ein neues Verfahren entwickelt.

Zusätzlich zur Identifikation der Materialparameter der *Cosserat*-Theorie müssen auch die Parameter des homogenen Materialverhaltens bestimmt werden, anhand von Versuchsdaten des homogenen Bereichs von Triaxial- und Biaxialversuchen. Dies umfasst

die Parameter des elastischen Verhaltens sowie die der plastischen Ver- und Entfestigung. Die Identifikation aller Materialparameter wurde in zwei Schritten durchgeführt, wobei im ersten Schritt die Parameter des nicht polaren Teils des Materialverhaltens anhand homogener Versuche identifiziert wurden, und basierend auf diesen Ergebnissen im zweiten Schritt die Parameter des polaren Verhaltens.

Generell stellt die Identifikation der Materialpararmeter ein inverses Problem dar. In Anbetracht des hohen numerischen Aufwandes zur Lösung des inhomogenen Randwertproblems mit Scherbandbildung wurde in der vorliegenden Arbeit das gradientenbasierte SQP-Verfahren (*Sequential Quadratic Programing*) zur Lösung des inversen Problems herangezogen, wobei die darin benötigten Gradienten mittels der semi-analytischen Sensitivitätsanalyse ermittelt wurden. Damit kann ein Minimum innerhalb weniger Iterationsschritte gefunden werden, wobei zusätzlich z. B. mittels Variation der Startwerte sichergestellt werden muss, dass es sich bei dem gefundenen Minimum auch um das globale Minimum, im physikalisch sinnvollen Wertebereich der Materialparameter, handelt. Solche Verfahren sind in der Literatur ausführlich beschrieben, siehe z. B. *Schittkowski* [118] oder *Spellucci* [125]. Beispiele für die Anwendung dieser Verfahren zur Parameteridentifikation finden sich in *Mahnken* [95], *Mahnken & Stein* [96] und *Müllerschön* [105].

Eine weitere Methode zur Simulation granularer Materialien sind die sogenannten Partikelmodelle, bei denen die einzelnen Körner des Materials direkt simuliert werden. Diese Methoden gehen auf die *Molekular Dynamik* zurück und wurden in der Arbeit von *Cundall & Strack* [23] erstmals auf granulare Materialien angewandt. In der vorliegenden Arbeit wurden diese Methoden zur Verifikation der Ergebnisse der *Cosserat*-Theorie herangezogen. Dazu wurden mittels einer Homogenisierungsmethode, basierend auf der Arbeit von *Ehlers* et al. [50], aus den Partikelbewegungen (Verschiebungen und Rotationen) die Verzerrungen und Krümmungen im Sinne der *Cosserat*-Theorie ermittelt. Des weiteren wurden aus den Kräften zwischen den Partikeln, die Spannungen und Momentenspannungen berechnet. Es konnte damit gezeigt werden, dass der qualitative Verlauf der homogenisierten Ergebnisse des Partikelmodells entlang des Scherbandes mit den Ergebnissen der erweiterten Kontinuumstheorie übereinstimmt. Darüber hinaus konnte gezeigt werden, dass der im Rahmen der *Cosserat*-Theorie konstitutiv angenommene Zusammenhang zwischen den für die Regularisierung maßgeblichen Krümmungen und den Momentenspannungen auch in den Partikelmodellen als Ergebnis der Simulation auftrat. Durch diese Ergebnisse wird deutlich, dass die Berücksichtigung der Rotationen im Rahmen eines *Cosserat*-Kontinuums ein physikalisch korrekter Ansatz zur Modellierung von Lokalisierunsphänomenen innerhalb granularer Materialen ist.

Gliederung der Arbeit

Nach einer kurzen Einführung in **Kapitel 1** wird in **Kapitel 2** das verwendete Modell im Rahmen der erweiterten Kontinuumstheorie vorgestellt. Dies beeinhaltet die kinematischen Beziehungen, die Bilanzgleichungen sowie die konstitutiven Annahmen.

In **Kapitel 3** werden die im vorherigen Kapitel eingeführten Gleichungen unter Verwendung der *Methode der Finiten Elemente* in Raum und Zeit diskretisiert.

Die Methoden zur Identifikation der in den diskretisierten Gleichungen auftretenden Materialparametern werden in **Kapitel 4** vorgestellt. Dabei werden zunächst die verwendeten Methoden der nichtlinearen Optimierung vorgestellt und anschließend das schrittweise Vorgehen der Identifikation erläutert.

Zum effektiven Einsatz der verwendeten gradientenbasierten Optimierungsmethoden ist die semi-analytische Ermittlung der Sensitivitäten notwendig. Diese wird in **Kapitel 5** in Bezug auf die diskretisierten Gleichungen ausgeführt.

Im folgenden wird in **Kapitel 6** der gesamte Identifikationsprozess am Beispiel von *Hostun* Sand demonstriert. Wobei Versuchsdaten der Universitäten Stuttgart und Grenoble zugrundegelegt werden.

Abschließend wird in **Kapitel 7** mit dem Partikel Modell ein weiterer Ansatz zur Simulation granularer Materialien vorgestellt, und es wird anhand der Simulation des Biaxialversuches gezeigt, dass die damit erhaltenen Ergebnisse qualitativ mit denen der *Cosserat*-Theorie übereinstimmen.

Contents

Chapter 1: Introduction and Overview

1.1   Motivation

The mechanical description of granular media is required in several branches of engineering such as powder technologies or sintering processes. Moreover, sand as a granular material, often appears in the underground. Thus, the understanding of such materials is a wide field in the context of practical geotechnical engineering. Since, whenever a building is planned, one has to answer the question whether the material in the ground will be able to carry the load. Further on, the understanding of the behavior of granular materials is also important to protect people and buildings from geological fatalities like base failures or landscapes, cf. Figure 1.1. The reason for such phenomena can be found in the instability of the material, which is characterized by a sudden failure of the material. Typically, during these phenomena, one can observe that the whole deformation is concentrated in a very thin zone, the so-called localization zone, also denoted as shear band. The understanding of the fundamental mechanism of these localization phenomena, which is associated with the material instability, is a wide field in the current research and also the topic of the presented work.

Figure 1.1: Landslide, McClure Pass, Colorado 1994,
`http://landslides.usgs.gov/learningeducation/images/slides/slide11.jpg`.

1.2   Introduction

The mathematical investigation of geotechnical problems began with the works of *Coulomb* in the 18th century, where geomaterials such as sand are characterized as frictional materials. Those frictional materials can only be handled as solids, if they are pre-loaded by a confining pressure. Without such an confining pressure, the manner of these materials swaps into a fluid-like behavior, which is well-known, e. g., from the outflow of silos or from the flow in sand glasses.

Taking a closer look on granular materials, it is obvious that these materials contain voids filled with a pore fluid (usually air or water). Thus, for a complete description of the material behavior in addition to the solid material, the pore fluid as well as the interaction forces between the solid skeleton and the pore fluid, must be considered. This can be done in the context of *Theory of Porous Media* (TPM). Due to the fact that in the presented work a dry sand is taken into account, the influence of pore fluid (air) on the overall material behavior is negligible. Consequently, the approach of the TPM can be reduced to a single-phase material under consideration of the influence of the variable pore volume on the overall material stiffness.

Furthermore, granular materials show instability effects, i. e., during a continuous increase of the load, the material will suddenly fail. This can be observed in nature in base or slope failures, like it is exemplarily shown in Figure 1.1. Moreover, such instability effects can be also observed in material tests, like triaxial or biaxial tests. During such tests, one can notice that the failure of the material is associated with the formation of one or more shear bands, wherein the whole deformation is concentrated. The reason for this material instability can be generally found in a softening behavior, i. e., whereas normally the stress increases with the increasing of the deformation, softening means that the stress decreases during growing deformations. In the framework of granular media, material softening is caused by the increase of the pore volume during the deformation process. This so-called dilatant behavior can be observed in material tests by the measurement of the volumetric strain. Thus, e. g., in triaxial experiments, one can notice that the volume of the specimen increases during vertical loading. Therewith, the volume of the pores in the material grows, which goes along with the reduction of the material stiffness. Within the standard continuum mechanical description, this effect leads to a so-called ill-posed problem. As a result, the computed thickness of the shear bands tends to zero, whereas material tests show a finite thickness of the shear band in the range about 10 to 30 average particle diameters. This disagreement shows, on the one hand, that the results using the standard (*Boltzmann*) continuum theory are unphysical and, on the other hand, this observation gives a hint to the existence of an intrinsic length scale in the material. Following this, for a physical correct modeling of such localization effects, the material behavior on the microscale must be taken into account. One possibility, therefore, is a detailed modeling of the microstructure based on particle models, which denotes a more or less exact simulation of the single material grains. Due to the fact that for computations of realistic problems billions of grains would have to be modeled, it is clear that for the computation of such problems a detailed modeling of the single grains is inapplicable. Hence, the effects on the microscale have to be considered in a continuum model. In the

present work, this is carried out by the application of the *Cosserat* or micropolar theory, where the mean values of the grain rotations, the so-called microrotations, are included by additional rotational degrees of freedom. Although the particle models are not suitable for the simulation of real problems, they can be applied for the verification of the micropolar continuum model. With the particle models, in contrast to experimental set ups, one is able to observe the rotations of single particles as well as the forces between the particles. Thus, based on a homogenization strategy over an appropriate *Representative Elementary Volume* (*REV*), the appearance of the additional micropolar degrees of freedom as well as of the couple stress as their energetic conjugated forces can be shown, cf. Figure 1.2.

| material grains | REV | forces and moments on the REV | stress and couple stress |
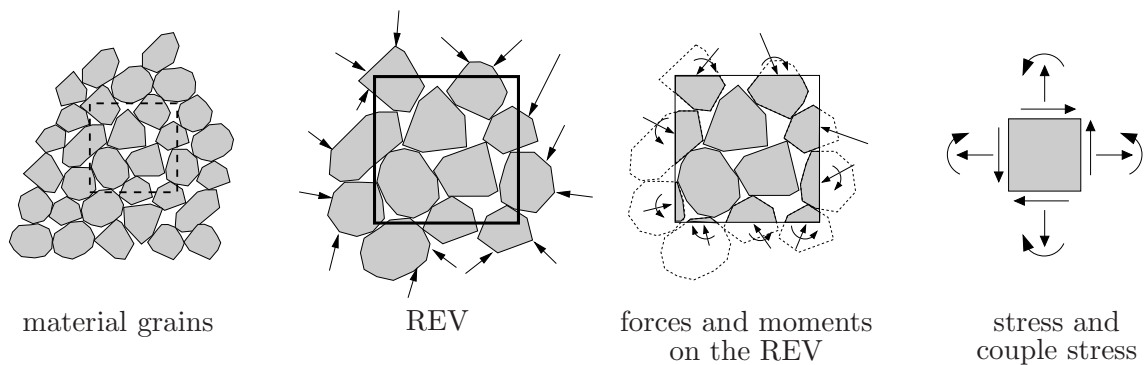
Figure 1.2: From granular material to the micropolar approach.

For the computation of realistic problems, additionally to a physical correct modeling of the material behavior, all parameters of the applied material model for a specific material must be known. As a consequence of the complexity of the applied material model, a direct experimental determination of the material parameters is not possible. Instead of that, the parameters have to be identified based on a so-called inverse problem. Thereby, the material parameters are the unknowns and the results of the boundary-value problem, e. g., the stress-strain relationship, are given via the data of material tests. With these test data, the material parameters are detected by minimizing the error between the measured quantities and the numerically computed values. This approach leads to the wide field of the non-linear optimization, which is a well-founded area in mathematics. Hence, a lot of different methods exist for the solution of this minimization problem. Furthermore, in consideration of the high number of different material parameters in the model, the identification process is performed stepwise. This stepwise identification can also be founded by the fact that the effects of the micropolarity only appear in case of inhomogeneous material test, e. g., in case of shear banding or at boundary-layer effects. Following this, the overall identification process is separated into two major steps. Firstly, the identification of the parameters governing the behavior observed on homogeneous material tests and, secondly, the identification of the parameters of micropolarity, wherefore inhomogeneous material tests are required.

1.3   Aims and state of the art

The aim of this contribution is the description of the mechanical behavior of granular materials. This includes the localization phenomena as well as the material behavior during homogeneous loading. Thus, firstly, the non-polar behavior of these materials has to be considered, because the hardening and softening behavior observed thereby is the basic effect for the occurrence of localization zones. The modeling of this non-polar standard part is carried out by use of an elasto-plasticity approach in combination with a strain-driven evolution of the yield condition considering hardening as well as softening effects. The development of such elasto-plasticity models in the context of geomaterials is a wide field in the geomechanical science and a lot of papers have been published concerning this topic beginning with papers from *Gudehus* [67], *Desai* [25] or *Vermeer* [133] in the 1970's up to later publications by, e. g., *Kim & Lade* [82,86,87], *Gajo & Wood* [63], *Bolzon* et al. [15] or *McDowell* et al. [100]. All these publications contain isotropic or kinematic hardening laws based on experimental observations. Additionally, softening effects are described in papers by *Liu* et al. [91] or *Dubujet & Doanh* [36].

As a consequence of the material softening, the whole plastic strain is concentrated into small localization zones, i. e., the homogeneous deformation state, which can be observed at the beginning of the loading, swaps into an inhomogeneous state indicated by the occurrence of shear bands. This behavior was proved by material tests, cf., e. g., *Mokni* and *Desrues* [101], *Wang & Lade* [136] or *Desrues & Viggiani* [80]. Due to the fact that the computation of this localization phenomena using the standard continuum theory leads to an ill-posed problem, regularization methods are required. For this reason, in the framework of the numerical mechanics, a lot of methods have been developed, generally, basing on higher order terms in the kinematical description. One of these methods is the so-called gradient plasticity, where higher order gradients of the plastic strain are considered in the material model, cf., e. g., *Mühlhaus & Aifantis* [103] or *de Borst & Mühlhaus* [17]. Another possibility for the regularization is the averaging of strain measures over a finite region, which yields so-called integral or non-local continua, cf., e. g., *Pijaudier-Cabot & Bažant* [111] and *Jirásek* [81]. In contrast to these mainly numerical motivated regularization techniques, a regularization of the ill-posed localization problem can also be obtained by a detailed consideration of the material properties. Hence, if the material allows a viscoplastic approach, e. g., by use of the overstress principle from *Perzyna* [110], this also yields a regularization of the problem. Examples therefore are given in *Ellsiepen* [59], *Schrefler* [119] or *Wieners* et al. [140]. In the case of granular material, the micropolar properties of the underlying microstructure can be taken into account with the application of the *Cosserat* or micropolar theory. This approach goes back to the *Cosserat* brothers [22] in 1909 and was rediscovered in 1958 by *Günther* [69] and later on from *Schaefer* [115], *Lippmann* [90] and *Besdo* [9]. Further investigation of the understanding of this approach was promoted by the work of *Eringen* and *Kafadar* [60] in 1976, wherein the micropolar theory is formulated as a special case in contexts of a general micromorphic continuum. A first application of the *Cosserat* theory to the regularization of ill-posed localization problems is demonstrated in papers by *Mühlhaus* [102], *Mühlhaus & Vardoulakis* [104] and *de Borst* [16]. Further developments and applications

are described, e. g., by *de Borst* [16], *Grammenoudis* [66], *Steinmann* [127], *Steinmann & Stein* [129] and moreover in combination with porous geomaterials in *Diebels* [26, 27], *Ehlers* [41], *Ehlers & Volk* [55], *Volk* [135], and *Ammann* [2].

Due to the fact that granular material generally falls into the group of porous materials, for a correct modeling of these materials the well-founded *Theory of Porous Media* (TPM) has to be taken into account. This theory traces back to the work by *Truesdell & Toupin* [132], whereas the theory in the current understanding is based on publications by *de Boer* [12], *de Boer & Ehlers* [14] and *Ehlers* [37, 41]. In the present contribution, the pore fluid of the porous medium has a negligible influence on the overall material behavior. Anyhow, the TPM is considered due to the fact that a compression point exists, as the densest possible package of the material grains, cf. *Eipper* [58] or *Mahnkopf* [98].

For the computation of realistic boundary-value problems, all parameters, which are used in the material model must be known. For this reason, the methods of the parameter identification based on non-linear optimization methods are required. Generally, all these methods can be classified, on the one hand, in the stochastic methods like the group of genetic algorithms, cf. *Schwefel* [123] or the neural networks and, on the other hand, in the deterministic methods. Representatives of this group are the gradient-free simplex methods, cf. *Nelder & Mead* [107] or *Powell* [112] as well as the gradient-based *Newton* like methods, cf. *Schittkowski* [118] or *Spellucci* [125]. The advantage of the deterministic methods in comparison to the stochastic methods are the lower computation costs. Whereas with the statistical methods 1000 or even much more steps are required for the finding of the minimum, the deterministic method requires only a few steps. But, otherwise, the deterministic methods always step into the next local minimum, whereas with the stochastic methods one is able to find the global minimum, independent of the initial set of start parameters. The application of such optimization methods to the parameter identification of standard, non-polar materials is a unique technique. Applications in the framework of an elasto-plastic or elasto-viscoplastic approach are given, e. g., in *Mahnken* [95], *Mahnken & Stein* [96], *Müllerschön* [105] or *Thielecke* [131]. However, the identification of the additional material parameters of the *Cosserat* theory is a new challenge. Thus, the main focus of this work is on the development of a new method for the identification of these additional parameters. This will be carried out basing on data from inhomogeneous biaxial tests, whereby in addition to the stress-strain relation the geometry of the shear band is considered.

In consequence of the high numerical effort for the numerical simulation of the biaxial test during the identification procedure, stochastic methods are excluded due to the required high number of numerical computations. Following this, a deterministic, gradient-based method is applied, whereby the computational costs can be furthermore reduced by the application of the semi-analytical sensitivity analysis. This denotes the exact computation of the derivatives of the numerically calculated results with respect to the material parameters. Such methods, in context to the *Finite Element Method*, have at first been presented by *Adelmann & Haftka* [1] and later on by *Barthold* [3], *Kleiber* [83] and *Vidal & Haber* [134].

Finally in this work, with the particle model, another method to consider the micropolar properties of the material, is discussed. Thereby, in contrast to the continuum model,

the microstructure, namely, the single material grains is directly modeled. Due to the high numerical effort of this method, the computation of real boundary-value problems is only possible in a restricted way. But anyhow, simplified particle models can be used for the demonstration that granular materials can be physically correctly modeled by the *Cosserat* theory. Such particle models were first introduced by *Cundall & Strack* [23], basing on the methods of *Molecular Dynamics*. Further developments are given in the works by *Chang & Ma* [21], *D'Addetta* [24] or *Luding* [92]. Applying these particle models to the simulation of the biaxial test following *Ehlers & Wenz* [57] and *Ehlers* et. al [53] in combination with a homogenization strategy for granular media developed by *Ehlers* et al. [50], the appearance of couple stress along the localization zone can be demonstrated within the presented work, which denotes that the *Cosserat* theory is the physically correct approach for the simulation of localization phenomena of granular media.

1.4   Outline of the thesis

The thesis is divided into six main chapters with the following content.

In **Chapter 2**, the micropolar continuum model is presented. This includes the kinematics, the balances equations, the linearization of the kinematics for the geometrically linear approach and, finally, the constitutive assumptions.

Following this, in **Chapter 3** the set of equations resulting from the introduced model are discretized in space and time. Therefore, firstly, the required balance equations are transformed from the strong to the weak formulations and, afterwards, the single steps for the solution of the resulting non-linear system of equations based on the *Finite Element Method* are illustrated.

Thus, one is able to compute exemplary boundary-value problems and, moreover, one is able to simulate material tests, which are required for the identification of the material parameters. The identification methods are illustrated in **Chapter 4**. Therein the applied methods for the solution of the associated non-linear optimization problem are presented and the single steps of the overall identification process are discussed.

For the effective usage of the identification methods, the semi-analytical computation of the sensitivities of the measured quantities with respect to the material parameters is necessary. For this reason, in **Chapter 5** the procedure of the semi-analytical sensitivity analysis in context of the used material model is introduced.

Following this, in **Chapter 6** the whole identification process of the material parameters is exemplarily shown by use of *Hostun* sand data. This task contains the determination of the material parameters governing the non-polar elasticity and plasticity as well as the identification of the additional parameters in consequence of the *Cosserat* theory.

Finally, this thesis is concluded by the application of a particle model to the simulation of granular media. In **Chapter 7**, the principal set up of the discrete particle model is explained, and the application to the model for the simulation of the biaxial tests is demonstrated. Based on homogenization methods, it is shown that the results of the particle model are qualitatively equivalent with the results of the *Cosserat* continuum.

Chapter 2: Foundations of the Micropolar Theory

In this Chapter, the basic equations of the *Cosserat* or micropolar theory are introduced, which traces back to the *Cosserat* brothers [22] in 1909. In the 1960's this theory was rediscovered by *Günther* [69] and *Schaefer* [115] in context with dislocation problems. Further developments are shown by the work of *Eringen & Kafadar* [60] as well as by works of, e. g., *Nowacki* [109] or *Diepolder* [32]. Whereas, applications especially in context of granular geomaterials are given in *Mühlhaus & Vardoulakis* [104] and by *de Borst* [16], or generally in context of localization phenomena by *Dietsche* et al. [33] or *Steinmann & Willam* [130]. The notations used in this work in the framework of the micropolar elasto-plasticity are mainly taken from papers by *Diebels* [27], *Ehlers* [41], *Ehlers* et al. [45] *Ehlers & Volk* [54–56], *Steinmann* [127, 128], as well as by *Volk* [135].

Firstly, in this chapter, the kinematic relations are introduced in Section 2.1 , followed by the balance equations in Section 2.2. Since the constitutive settings are formulated for the geometrically linear case, the linearization of the kinematic relations is illustrated in Section 2.3 and, finally, the constitutive settings are discussed in Section 2.4

2.1 Kinematics of micropolar materials

In the framework of the micropolar theory, a material point $\mathcal{P}$ is assumed as a small rigid microbody, also denoted as microparticle, with a very small but not zero extension. Consequently, in addition to a defined position in space, this microbody has a defined orientation. Thus, for the complete kinematic description of micropolar deformations, additionally to the displacement field, an independent rotation field has to be taken into account.

2.1.1 Motion and micromotion

The motion and micromotion of a material point $\mathcal{P}$, embedded in a micropolar body $\mathcal{B}$, is governed by two kinematical mechanisms. The first is the motion function

$$\mathbf{x} = \boldsymbol{\chi}\left(\mathbf{X},\, t\right), \tag{2.1}$$

whereby each spatial point in the reference configuration at the location $\mathbf{X}$ is mapped to the location $\mathbf{x}$ of the actual configuration at the time t. Thus, the displacement vector

$$\mathbf{u} = \mathbf{x} - \mathbf{X} \tag{2.2}$$

can be introduced, describing the motion of $\mathcal{P}$. The second kinematical mechanism is the micromotion

$$\boldsymbol{\xi} = \bar{\mathbf{R}}\left(\mathbf{X},\, t\right)\boldsymbol{\Xi}, \tag{2.3}$$
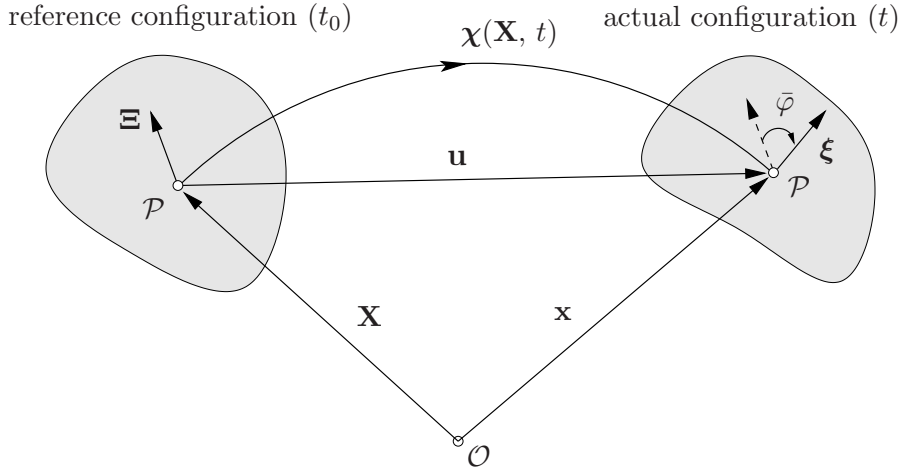
Figure 2.1: Motion and micromotion of a micropolar body $\mathcal{B}$.

where $\boldsymbol{\xi}$ and $\boldsymbol{\Xi}$ can be understood as rigid directors, fixed to the material points in order to represent the local orientation of $\mathcal{P}$, cf. Figure 2.1. Following this, the micromotion, which is governed by the proper orthogonal tensor function $\bar{\mathbf{R}}(\mathbf{X}, t)$, describes the image of the change of the particle orientation in the different configurations, i. e., the rotation of the director $\boldsymbol{\Xi}$ around the rotation vector $\bar{\boldsymbol{\varphi}}$ with the angle $\bar{\varphi}$.

By use of (2.1), the material deformation gradient is defined as

$$\mathbf{F} := \operatorname{Grad} \boldsymbol{\chi}(\mathbf{X}, t) = \operatorname{Grad} \mathbf{x} = \mathbf{I} + \operatorname{Grad} \mathbf{u}, \tag{2.4}$$

where $\mathbf{I}$ is the second-order identity tensor. Further on, the operator $\operatorname{Grad}(\cdot)$ denotes the partial derivative of $(\cdot)$ with respect to the reference configuration $\mathbf{X}$.

With the material deformation gradient $\mathbf{F}$, differential line elements $\mathrm{d}\mathbf{X}$ of the reference configuration can be mapped to the actual configuration:

$$\mathrm{d}\mathbf{x} = \mathbf{F}\,\mathrm{d}\mathbf{X}. \tag{2.5}$$

Furthermore, additional transport mechanisms for area elements $\mathrm{d}\mathbf{A}$ and volume elements $\mathrm{d}V$ of the reference configuration to the respective quantities $\mathrm{d}\mathbf{a}$ and $\mathrm{d}v$ of the actual configuration can be constructed, cf. *de Boer* [11]:

$$\begin{aligned} \mathrm{d}\mathbf{a} &= (\det \mathbf{F})\,\mathbf{F}^{T-1}\,\mathrm{d}\mathbf{A}\,, \\ \mathrm{d}v &= (\det \mathbf{F})\,\mathrm{d}V\,. \end{aligned} \tag{2.6}$$

2.1.2   Strain measure for non-polar materials

Concerning the development of deformation measures, $\mathbf{F}$ can be decomposed in the following manner:

$$\mathbf{F} = \mathbf{R}\,\mathbf{U} = \mathbf{V}\,\mathbf{R}\,, \tag{2.7}$$

wherein $\mathbf{U}$ and $\mathbf{V}$ are the symmetric right and left stretch tensors, whereas $\mathbf{R}$ is a proper orthogonal rotation tensor, i.e.,

$$\mathbf{R}^T\,\mathbf{R} = \mathbf{I} \quad \text{and} \quad \det \mathbf{R} = 1\,. \tag{2.8}$$

Considering non-polar materials, strain measures can be constructed by using the length variation of line elements during the motion. Hence, on the one hand, the square length of the line element $\mathrm{d}\mathbf{x}$ in the actual configuration can be expressed by the corresponding line element $\mathrm{d}\mathbf{X}$ of the reference configuration, viz.:

$$\|\mathrm{d}\mathbf{x}\|^2 = \mathrm{d}\mathbf{x} \cdot \mathrm{d}\mathbf{x} = \mathrm{d}\mathbf{X} \cdot \mathbf{F}^T\,\mathbf{F}\,\mathrm{d}\mathbf{X} := \mathrm{d}\mathbf{X} \cdot \mathbf{C}\,\mathrm{d}\mathbf{X}\,. \tag{2.9}$$

On the other hand, the square of the length of a line element $\mathrm{d}\mathbf{X}$ of the reference configuration expressed by a corresponding line element $\mathrm{d}\mathbf{x}$ of the actual configuration yields

$$\|\mathrm{d}\mathbf{X}\|^2 = \mathrm{d}\mathbf{X} \cdot \mathrm{d}\mathbf{X} = \mathrm{d}\mathbf{x} \cdot \mathbf{F}^{T\,-1}\,\mathbf{F}^{-1}\,\mathrm{d}\mathbf{x} := \mathrm{d}\mathbf{x} \cdot \mathbf{B}^{-1}\,\mathrm{d}\mathbf{x}\,. \tag{2.10}$$

The obtained tensors,

$$\mathbf{C} = \mathbf{F}^T\,\mathbf{F} = \mathbf{U}\,\mathbf{U} \quad \text{and} \quad \mathbf{B} = \mathbf{F}\,\mathbf{F}^T = \mathbf{V}\,\mathbf{V}\,, \tag{2.11}$$

are the so-called right and left *Cauchy-Green* deformation tensors $\mathbf{C}$ and $\mathbf{B}$.

Additional strain measures are obtained by regarding the difference of squares of line elements of the referential and actual configuration. Following this, one obtains:

$$\begin{aligned} \|\mathrm{d}\mathbf{x}\|^2 - \|\mathrm{d}\mathbf{X}\|^2 &= \mathrm{d}\mathbf{X} \cdot \mathbf{C}\,\mathrm{d}\mathbf{X} - \mathrm{d}\mathbf{X} \cdot \mathrm{d}\mathbf{X} = \mathrm{d}\mathbf{X} \cdot (\mathbf{C} - \mathbf{I})\,\mathrm{d}\mathbf{X} \quad \text{and} \\ \|\mathrm{d}\mathbf{x}\|^2 - \|\mathrm{d}\mathbf{X}\|^2 &= \mathrm{d}\mathbf{x} \cdot \mathrm{d}\mathbf{x} - \mathrm{d}\mathbf{x} \cdot \mathbf{B}^{-1}\,\mathrm{d}\mathbf{x} = \mathrm{d}\mathbf{x} \cdot (\mathbf{I} - \mathbf{B}^{-1})\,\mathrm{d}\mathbf{x}\,, \end{aligned} \tag{2.12}$$

which results in the definition of the *Green-Lagrange*an and the *Almansi*an strain tensors:

$$\mathbf{E} := \tfrac{1}{2}\,(\mathbf{C} - \mathbf{I}) \quad \text{and} \quad \mathbf{A} := \tfrac{1}{2}\,(\mathbf{I} - \mathbf{B}^{-1})\,. \tag{2.13}$$

2.1.3 Strain measure for micropolar materials

The principal difference between a micropolar and a non-polar continuum is the existence of an independent rotation field $\bar{\boldsymbol{\varphi}}$ in addition to the displacement field $\mathbf{u}$ at the micropolar continuum. Hence, the whole rotation $\bar{\mathbf{R}}$ of the director $\boldsymbol{\Xi}$ can be split into two parts. The first one is the continuum rotation $\mathbf{R}$, which results from the polar decomposition of $\mathbf{F}$, cf. (2.7), and the second one is the so-called free or independent rotation $\overset{*}{\mathbf{R}}$, cf. Figure 2.2. Therewith, one obtains:

$$\bar{\mathbf{R}} = \overset{*}{\mathbf{R}}\,\mathbf{R}\,. \tag{2.14}$$

Proceeding from an *Euler-Rodrigues* representation of the spatial rotation, the rotation tensors $\bar{\mathbf{R}}$, $\mathbf{R}$ and $\overset{*}{\mathbf{R}}$ can be expressed via:

$$\bar{\mathbf{R}} = \bar{\mathbf{e}} \otimes \bar{\mathbf{e}} + (\mathbf{I} - \bar{\mathbf{e}} \otimes \bar{\mathbf{e}}) \cos \bar{\varphi} + (\bar{\mathbf{e}} \times \mathbf{I}) \sin \bar{\varphi} \, ,$$

$$\mathbf{R} = \mathbf{e} \otimes \mathbf{e} + (\mathbf{I} - \mathbf{e} \otimes \mathbf{e}) \cos \varphi + (\mathbf{e} \times \mathbf{I}) \sin \varphi \, , \qquad (2.15)$$

$$\overset{*}{\mathbf{R}} = \overset{*}{\mathbf{e}} \otimes \overset{*}{\mathbf{e}} + (\mathbf{I} - \overset{*}{\mathbf{e}} \otimes \overset{*}{\mathbf{e}}) \cos \overset{*}{\varphi} + (\overset{*}{\mathbf{e}} \times \mathbf{I}) \sin \overset{*}{\varphi} \, .$$

Therein, $\bar{\varphi}$, φ and $\overset{*}{\varphi}$ are the values of the rotation vectors $\bar{\boldsymbol{\varphi}}$, $\boldsymbol{\varphi}$ and $\overset{*}{\boldsymbol{\varphi}}$, whereas $\bar{\mathbf{e}}$, $\mathbf{e}$ and $\overset{*}{\mathbf{e}}$ are the axes of the related rotations, i.e.,

$$\bar{\boldsymbol{\varphi}} = \bar{\varphi} \, \bar{\mathbf{e}} \, , \quad \boldsymbol{\varphi} = \varphi \, \mathbf{e} \quad \text{and} \quad \overset{*}{\boldsymbol{\varphi}} = \overset{*}{\varphi} \, \overset{*}{\mathbf{e}} \, . \qquad (2.16)$$

Due to the fact that the vector addition theorems for the rotation vectors are not valid these rotation vectors cannot be denoted as true vectors.

Whereas the strain measure of the non-polar continuum is performed by squares of line elements, in case of a micropolar continuum, scalar products between line elements and directors have to be taken into account. Thus, one obtains the first micropolar deformation tensor by expressing the scalar product between the line element $d\mathbf{x}$ and the director $\boldsymbol{\xi}$ of the actual configuration by $d\mathbf{X}$ and $\boldsymbol{\Xi}$ of the reference configuration:

$$\boldsymbol{\xi} \cdot d\mathbf{x} = \boldsymbol{\Xi} \cdot \bar{\mathbf{R}}^T \mathbf{F} \, d\mathbf{X} =: \boldsymbol{\Xi} \cdot \bar{\mathbf{U}} \, d\mathbf{X} \, . \qquad (2.17)$$

In the same manner, the scalar product between line elements and directors in the reference configuration can be expressed by the corresponding quantities of the actual configurations:

$$\boldsymbol{\Xi} \cdot d\mathbf{X} = \boldsymbol{\xi} \cdot \bar{\mathbf{R}} \, \mathbf{F}^{-1} d\mathbf{x} =: \boldsymbol{\xi} \cdot \bar{\mathbf{V}}^{-1} d\mathbf{x} \, . \qquad (2.18)$$
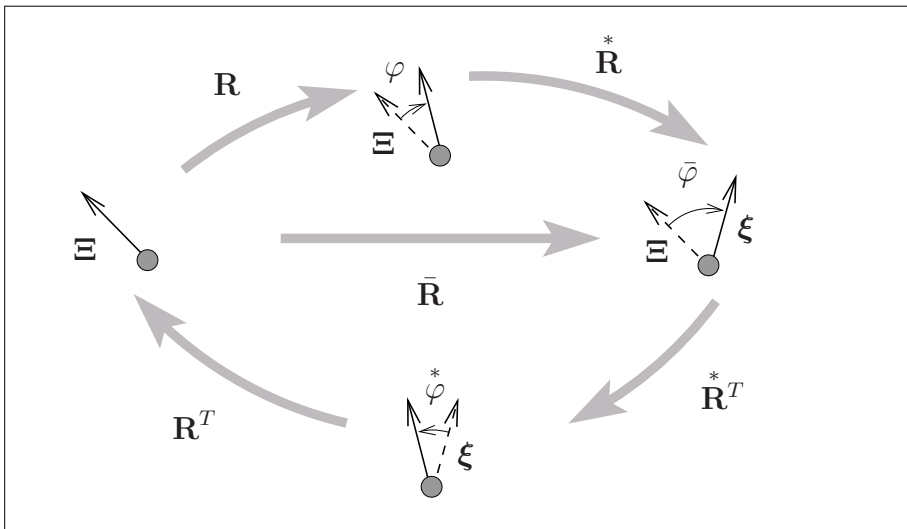
Figure 2.2: Rotation tensors and angles.

The resulting deformation tensors

$$\bar{\mathbf{U}} = \bar{\mathbf{R}}^T \mathbf{F} \quad \text{and} \quad \bar{\mathbf{V}} = \mathbf{F} \bar{\mathbf{R}}^T \tag{2.19}$$

can be also obtained by the micropolar decomposition of $\mathbf{F}$:

$$\mathbf{F} = \bar{\mathbf{R}} \bar{\mathbf{U}} = \bar{\mathbf{V}} \bar{\mathbf{R}} . \tag{2.20}$$

In analogy to the non-polar continuum, further strain tensors are obtained on the basis of the difference between scalar products of line elements and directors of the reference and the actual configuration:

$$\boldsymbol{\xi} \cdot \mathrm{d}\mathbf{x} - \boldsymbol{\Xi} \cdot \mathrm{d}\mathbf{X} = \boldsymbol{\Xi} \cdot (\bar{\mathbf{U}} - \mathbf{I}) \, \mathrm{d}\mathbf{X} = \boldsymbol{\xi} \cdot (\mathbf{I} - \bar{\mathbf{V}}^{-1}) \, \mathrm{d}\mathbf{x} . \tag{2.21}$$

This approach leads to the micropolar *Green-Lagrange*an type as well as the *Euler-Almansi*an type strain tensors:

$$\bar{\mathbf{E}} := \bar{\mathbf{U}} - \mathbf{I} \quad \text{and} \quad \bar{\mathbf{A}} := \mathbf{I} - \bar{\mathbf{V}}^{-1} . \tag{2.22}$$

For the complete description of the micropolar deformations, additionally to the strain measures, curvature measures are required. Thus, to obtain a third-order curvature tensor of the reference configuration, the gradient $\operatorname{Grad} \bar{\mathbf{R}}$ of the rotation tensor with respect to the reference configuration is back rotated to the reference configuration, cf. *Ehlers* [41] or *Steinmann* [127]:

$$^R\overset{3}{\mathbf{C}} := (\bar{\mathbf{R}}^T \operatorname{Grad} \bar{\mathbf{R}})^{\underline{3}} . \tag{2.23}$$

Therein, the symbol $(\cdot)^{\underline{i}}$ defines a contraction of the arguments in parentheses towards a tensor of i-th order. Accordingly, a third-order curvature tensor of the actual configuration can be constructed by the forward rotation of the gradient of $\bar{\mathbf{R}}$ with respect to the actual configuration:

$$\overset{3}{\mathbf{C}} := [\, ((\operatorname{grad} \bar{\mathbf{R}})^{\overset{23}{T}} \bar{\mathbf{R}}^T)^{\underline{3}}]^{\overset{23}{T}} = -(\bar{\mathbf{R}} \operatorname{grad} \bar{\mathbf{R}}^T)^{\underline{3}} , \tag{2.24}$$

where $(\cdot)^{\overset{ik}{T}}$ is a transposition of $(\cdot)$ with respect to the i-th and k-th basis systems and $\operatorname{grad}(\cdot) = \operatorname{Grad}(\cdot) \mathbf{F}^{-1}$ stands for the gradient with respect to the actual configuration $\mathbf{x}$. From (2.23) and (2.24) in combination with

$$\operatorname{Grad}(\bar{\mathbf{R}}^T \bar{\mathbf{R}}) = \overset{3}{\mathbf{0}} \quad \text{and} \quad \operatorname{grad}(\bar{\mathbf{R}}^T \bar{\mathbf{R}}) = \overset{3}{\mathbf{0}} , \tag{2.25}$$

which results from $(2.8)_1$, it is concluded that the curvature tensors are skew-symmetric with respect to the first two basis systems:

$$^R\overset{3}{\mathbf{C}} = -^R\overset{3}{\mathbf{C}}{}^{\overset{12}{T}} \quad \text{and} \quad \overset{3}{\mathbf{C}} = -\overset{3}{\mathbf{C}}{}^{\overset{12}{T}} , \tag{2.26}$$

Hence, second-order curvature tensors can be defined as their axial tensors:

$$\begin{aligned}
^R\bar{\mathbf{C}} &:= \operatorname{axl}(^R\overset{3}{\mathbf{C}}) = -\tfrac{1}{2} \, (\overset{3}{\mathbf{E}} \, ^R\overset{3}{\mathbf{C}})^{\underline{2}} \quad \text{and} \\
\bar{\mathbf{C}} &:= \operatorname{axl}(\overset{3}{\mathbf{C}}) = -\tfrac{1}{2} \, (\overset{3}{\mathbf{E}} \, \overset{3}{\mathbf{C}})^{\underline{2}} ,
\end{aligned} \tag{2.27}$$

where $\overset{3}{\mathbf{E}}$ is the *Ricci* permutation tensor, cf. Appendix B.1.3.

2.2   Balance relations

In general, balance relations are axiomatic statements resulting from physical observations. In the framework of continuum mechanics, balance relations exist for the conservation of mass, momentum, moment of momentum, energy and entropy. Thereby, the energy balance, as an axiomatic statement, is only required if temperature effects are taken into account. Due to the fact that in the context of the present work only isothermal effects are considered, the relevant balances for the description of boundary-value problems are the balances of mass, momentum and moment of momentum, which are illustrated in the following. For a detailed discussion of the balance relations of energy and entropy the interested reader is referred to *Ehlers* [41], *Ghadiani* [64] or *Steinmann* [127].

The structure of the above mentioned balance equations can be generalized in the following manner by supposing Ψ or $\boldsymbol{\Psi}$ as the densities of the volume-specific scalar- or vector-valued quantities in the body $\mathcal{B}$ (cf. *Haupt* [75] or *Ehlers* [37, 41]):

$$
\begin{aligned}
\frac{\mathrm{d}}{\mathrm{d}t} \int_{\mathcal{B}} \Psi \, \mathrm{d}v &= \int_{\partial\mathcal{B}} \boldsymbol{\phi} \cdot \mathbf{n} \, \mathrm{d}a + \int_{\mathcal{B}} \psi \, \mathrm{d}v + \int_{\mathcal{B}} \hat{\Psi} \, \mathrm{d}v \quad \text{or} \\
\frac{\mathrm{d}}{\mathrm{d}t} \int_{\mathcal{B}} \boldsymbol{\Psi} \, \mathrm{d}v &= \int_{\partial\mathcal{B}} \boldsymbol{\Phi} \, \mathbf{n} \, \mathrm{d}a + \int_{\mathcal{B}} \boldsymbol{\psi} \, \mathrm{d}v + \int_{\mathcal{B}} \hat{\boldsymbol{\Psi}} \, \mathrm{d}v \, .
\end{aligned}
\tag{2.28}
$$

Therein, $\boldsymbol{\phi} \cdot \mathbf{n}$ or $\boldsymbol{\Phi}\,\mathbf{n}$ are the scalar- or vector-valued density of the effluxes of the quantity through the surface $\partial\mathcal{B}$ of the body $\mathcal{B}$, where $\mathbf{n}$ is the outside-oriented unit normal vector. Moreover, ψ or $\boldsymbol{\psi}$ are the supply terms of the mechanical quantities and $\hat{\Psi}$ or $\hat{\boldsymbol{\Psi}}$ are the production terms of the mechanical quantity.

Assuming that the fields Ψ and $\boldsymbol{\Psi}$ are continuous and continuously differentiable, one obtains by differentiation of the left hand side of (2.28) under consideration of $\mathrm{d}\dot{v} = \operatorname{div}\dot{\mathbf{x}} \, \mathrm{d}v$:

$$
\begin{aligned}
\frac{\mathrm{d}}{\mathrm{d}t} \int_{\mathcal{B}} \Psi \, \mathrm{d}v &= \int_{\mathcal{B}} (\dot{\Psi} + \Psi \operatorname{div}\dot{\mathbf{x}}) \, \mathrm{d}v \quad \text{or} \\
\frac{\mathrm{d}}{\mathrm{d}t} \int_{\mathcal{B}} \boldsymbol{\Psi} \, \mathrm{d}v &= \int_{\mathcal{B}} (\dot{\boldsymbol{\Psi}} + \boldsymbol{\Psi} \operatorname{div}\dot{\mathbf{x}}) \, \mathrm{d}v \, ,
\end{aligned}
\tag{2.29}
$$

where, $\operatorname{div}(\cdot)$ is the divergence operator corresponding to the spatial gradient $\operatorname{grad}(\cdot)$. Using the *Gauß*ian divergence theorem in order to transform the surface integrals of (2.28) into volume integrals, the local forms of the balance relations are given by:

$$
\begin{aligned}
\dot{\Psi} + \Psi \operatorname{div}\dot{\mathbf{x}} &= \operatorname{div}\boldsymbol{\phi} + \psi + \hat{\Psi} \\
\dot{\boldsymbol{\Psi}} + \boldsymbol{\Psi} \operatorname{div}\dot{\mathbf{x}} &= \operatorname{div}\boldsymbol{\Phi} + \boldsymbol{\psi} + \hat{\boldsymbol{\Psi}} \, .
\end{aligned}
\tag{2.30}
$$

2.2.1 Balance of mass

The mass balance results from the postulation that the mass of a body $\mathcal{B}$ is conserved,

$$\int_{\mathcal{B}} \rho \, dv = \text{const.} \quad \Longrightarrow \quad \frac{d}{dt} \int_{\mathcal{B}} \rho \, dv = 0 \,, \tag{2.31}$$

where ρ represents the local mass density. Comparing the above equation with the general structure of a scalar-valued balance relation $(2.28)_1$, the following quantities can be identified:

$$\Psi = \rho \,, \quad \boldsymbol{\phi} = 0 \,, \quad \psi = 0 \quad \text{and} \quad \hat{\Psi} = 0 \,.$$

Using the general relation $(2.30)_1$, this results directly in the local form of the mass balance:

$$\dot{\rho} + \rho \, \text{div} \, \dot{\mathbf{x}} = 0 \,. \tag{2.32}$$

2.2.2 Balance of momentum

The momentum $\mathbf{p}$ of the body $\mathcal{B}$ is defined via

$$\mathbf{p} := \int_{\mathcal{B}} \rho \, \dot{\mathbf{x}} \, dv \,. \tag{2.33}$$

Balancing this quantity, one axiomatically introduces that the temporal change of the momentum corresponds to the sum of surface and body forces acting on the body $\mathcal{B}$, viz.:

$$\frac{d}{dt} \int_{\mathcal{B}} \rho \, \dot{\mathbf{x}} \, dv = \int_{\partial \mathcal{B}} \mathbf{t} \, da + \int_{\mathcal{B}} \rho \, \mathbf{b} \, dv \,. \tag{2.34}$$

Therein, $\mathbf{t}$ is the stress vector on the surface $\partial \mathcal{B}$ of the body $\mathcal{B}$, which is associated with the *Cauchy* stress tensor $\mathbf{T}$ by the *Cauchy* theorem:

$$\mathbf{t} = \mathbf{T} \, \mathbf{n} \,. \tag{2.35}$$

Furthermore, $\rho \, \mathbf{b}$ is the supply term, whereby $\mathbf{b}$ is normally interpreted as the overall gravitation $\mathbf{g}$. The comparison with (2.28) results in the following relations:

$$\boldsymbol{\Psi} = \rho \, \dot{\mathbf{x}} \,, \quad \boldsymbol{\Phi} = \mathbf{T} \,, \quad \boldsymbol{\psi} = \rho \, \mathbf{b} \quad \text{and} \quad \hat{\boldsymbol{\Psi}} = \mathbf{0} \,.$$

Thus, under consideration of the local mass balance (2.32), one obtains with $(2.30)_2$ the local form of the balance of momentum:

$$\rho \, \ddot{\mathbf{x}} = \text{div} \, \mathbf{T} + \rho \, \mathbf{b} \,. \tag{2.36}$$

2.2.3   Balance of moment of momentum

With the balance of moment of momentum, one postulates axiomatically that the temporal change of the moment of momentum is equal to the sum of the moments acting on the body $\mathcal{B}$. In the case of micropolar materials, the supply terms consist, one the one hand, in the moments caused by the stress vector $\mathbf{x} \times \mathbf{t}$ and, on the other hand, in the couple stress vectors $\mathbf{m}$. Furthermore, the angular micro velocity $\bar{\boldsymbol{\omega}} = \dot{\bar{\boldsymbol{\varphi}}}$ representing the rotational velocity of the microparticles has to be taken into account. Thus, one obtains:

$$\frac{\mathrm{d}}{\mathrm{d}t} \int_{\mathcal{B}} (\mathbf{x} \times \rho\,\dot{\mathbf{x}} + \rho\,\bar{\boldsymbol{\Theta}}\,\bar{\boldsymbol{\omega}})\,\mathrm{d}v = \int_{\mathcal{B}} (\mathbf{x} \times \rho\,\mathbf{b} + \rho\,\mathbf{c})\,\mathrm{d}v + \int_{\partial\mathcal{B}} (\mathbf{x} \times \mathbf{t} + \mathbf{m})\,\mathrm{d}a\,, \qquad (2.37)$$

where, $\bar{\boldsymbol{\Theta}}$ is the tensor of microinertia, i. e., the rotational inertia of a material point of the micropolar continuum (microparticle). For further details, the interested reader is referred to the works by *Ehlers* [41], *Eringen & Kafadar* [60] or by *Volk* [135]. Furthermore, $\mathbf{c}$ is the body couple force per unit mass and $\mathbf{m}$ is the couple stress vector on the surface $\partial\mathcal{B}$ of the body $\mathcal{B}$. In analogy to (2.35), $\mathbf{m}$ is associated with the couple stress tensor $\mathbf{M}$ by:

$$\mathbf{m} = \mathbf{M}\,\mathbf{n}\,. \qquad (2.38)$$

Similar to the previously illustrated balances, the local form of the balance of moment of momentum is obtained by the comparison with the general structure $(2.28)_2$:

$$\boldsymbol{\Psi} = \mathbf{x} \times \rho\,\dot{\mathbf{x}} + \rho\,\bar{\boldsymbol{\Theta}}\,\bar{\boldsymbol{\omega}}\,, \quad \boldsymbol{\Phi} = \mathbf{x} \times \mathbf{T} + \mathbf{M}\,, \quad \boldsymbol{\psi} = \mathbf{x} \times \rho\,\mathbf{b} + \rho\,\mathbf{c} \quad \text{and} \quad \hat{\boldsymbol{\Psi}} = \mathbf{0}\,.$$

Following this, the general structure $(2.30)_2$ in combination with the balance of mass (2.32) and momentum (2.36) yields the local form of the balance of moment of momentum:

$$\rho\,(\bar{\boldsymbol{\Theta}}\,\bar{\boldsymbol{\omega}})^{\boldsymbol{\cdot}} = \mathbf{I} \times \mathbf{T} + \mathrm{div}\,\mathbf{M} + \rho\,\mathbf{c}\,. \qquad (2.39)$$

2.3   Linearization

With the assumption of small deformations, i. e., small displacement gradients $\mathrm{Grad}\,\mathbf{u}$ in combination with small rotations $\bar{\boldsymbol{\varphi}}$, the general non-linear theory can be reduced to the geometrically linear theory using the standard methods of the linearization, cf., e. g., *Haupt* [75], *Ehlers* [41] or *Volk* [135]. For demonstration purposes, an arbitrary tensor function $\mathbf{Y}$ is considered, generally depending on the material deformation gradient $\mathbf{F}$ and the rotation field $\bar{\boldsymbol{\varphi}} = \bar{\varphi}\,\bar{\mathbf{e}}$, i. e., $\mathbf{Y}(\mathbf{F}, \bar{\varphi})$. Thus, the formal linearization of $\mathbf{Y}$ is given via a *Taylor* series around the undeformed state ($\mathbf{F} = \mathbf{I}$ and $\bar{\varphi} = 0$), which is truncated after the linear term (cf. *Ehlers* [41]):

$$\mathbf{Y}_{\mathrm{lin.}} = \mathbf{Y}\Big|_{\substack{\mathbf{F}=\mathbf{I}\\ \bar{\varphi}=0}} + \frac{\partial\mathbf{Y}}{\partial\mathbf{F}}\Big|_{\substack{\mathbf{F}=\mathbf{I}\\ \bar{\varphi}=0}} (\mathbf{F}-\mathbf{I}) + \frac{\partial\mathbf{Y}}{\partial\bar{\varphi}}\Big|_{\substack{\mathbf{F}=\mathbf{I}\\ \bar{\varphi}=0}} \bar{\varphi}\,. \qquad (2.40)$$

The truncation after the linear term yields that $\mathrm{Grad}\,(\cdot)$ and $\mathrm{grad}\,(\cdot)$ are congruent cf. *Haupt* [75] and thus, in the following, generally denoted as $\mathrm{Grad}\,(\cdot)$. Furthermore, the

non-polar strain tensors $\mathbf{E}$ and $\mathbf{A}$ of the referential and the actual configurations coincide with the geometrical linear strain tensor $\boldsymbol{\varepsilon}$. In the case of the micropolar theory, the geometrical linearization also implies the coinciding of the micropolar strain and curvature tensors of the referential and actual configurations,

$$\bar{\mathbf{E}} \approx \bar{\mathbf{A}} \quad \text{and} \quad {}^{R}\overset{3}{\mathbf{C}} \approx \overset{3}{\mathbf{C}}, \tag{2.41}$$

Moreover, in the geometrically linear theory, the rotation vector $\bar{\boldsymbol{\varphi}}$ gets the status of a true vector, i. e., the vector addition theorems are valid.

2.3.1 Linearization of the rotation tensor

Considering the *Euler-Rodrigues* notation $(2.15)_1$, the rotation tensor $\bar{\mathbf{R}} = \bar{\mathbf{R}}(\bar{\boldsymbol{\varphi}})$ only depends on the total rotations $\bar{\boldsymbol{\varphi}} = \bar{\varphi}\,\bar{\mathbf{e}}$. Thus, its linearization is given by

$$\bar{\mathbf{R}}_{\text{lin.}} = \bar{\mathbf{R}}\Big|_{\bar{\varphi}=0} + \frac{\partial \bar{\mathbf{R}}}{\partial \bar{\varphi}}\Big|_{\bar{\varphi}=0} \bar{\varphi} = \mathbf{I} + (\bar{\mathbf{e}} \times \mathbf{I})\,\bar{\varphi}\,, \tag{2.42}$$

Using the relation, $(\bar{\mathbf{e}} \times \mathbf{I})\,\bar{\varphi} = \bar{\boldsymbol{\varphi}} \times \mathbf{I} = -\overset{3}{\mathbf{E}}\,\bar{\boldsymbol{\varphi}}$, the above equation results in the linearized form of the rotation tensor and its transposed:

$$\bar{\mathbf{R}}_{\text{lin.}} = \mathbf{I} - \overset{3}{\mathbf{E}}\,\bar{\boldsymbol{\varphi}} \quad \text{and} \quad \bar{\mathbf{R}}^{T}_{\text{lin.}} = \mathbf{I} + \overset{3}{\mathbf{E}}\,\bar{\boldsymbol{\varphi}}\,. \tag{2.43}$$

In the same way, the linearization of the free rotation $\overset{*}{\mathbf{R}}$ as well as of the continuum rotation $\mathbf{R}$ is obtained as:

$$\overset{*}{\mathbf{R}}_{\text{lin.}} = \mathbf{I} - \overset{3}{\mathbf{E}}\,\overset{*}{\boldsymbol{\varphi}} \quad \text{and} \quad \mathbf{R}_{\text{lin.}} = \mathbf{I} - \overset{3}{\mathbf{E}}\,\boldsymbol{\varphi}\,. \tag{2.44}$$

Therewith, the additional decomposition of the geometrically linear rotation vectors can be shown. From (2.14), one can conclude that

$$\bar{\mathbf{R}}_{\text{lin.}} = \overset{*}{\mathbf{R}}_{\text{lin.}}\,\mathbf{R}_{\text{lin.}}\,, \tag{2.45}$$

in combination with (2.43), one obtains the following relation,

$$\mathbf{I} - \overset{3}{\mathbf{E}}\,\bar{\boldsymbol{\varphi}} = (\mathbf{I} - \overset{3}{\mathbf{E}}\,\overset{*}{\boldsymbol{\varphi}})\,(\mathbf{I} - \overset{3}{\mathbf{E}}\,\boldsymbol{\varphi})\,. \tag{2.46}$$

By neglecting the second-order terms, this yields the additional decomposition of $\bar{\boldsymbol{\varphi}}$:

$$\bar{\boldsymbol{\varphi}} = \boldsymbol{\varphi} + \overset{*}{\boldsymbol{\varphi}}\,. \tag{2.47}$$

2.3.2   Linearization of the micropolar strain tensor

The linearization of the strain tensor is exemplarily demonstrated for the *Green-Lagrangean* type strain tensor $\bar{\mathbf{E}}$, cf. (2.22), depending on $\mathbf{F}$ and $\bar{\varphi}$, cf. *Ehlers* [41] or *Volk* [135]:

$$\bar{\mathbf{E}}_{\text{lin.}} = \bar{\mathbf{E}}\Big|_{\substack{\mathbf{F}=\mathbf{I}\\\bar{\varphi}=0}} + \frac{\partial \bar{\mathbf{E}}}{\partial \mathbf{F}}\Big|_{\substack{\mathbf{F}=\mathbf{I}\\\bar{\varphi}=0}} (\mathbf{F}-\mathbf{I}) + \frac{\partial \bar{\mathbf{E}}}{\partial \bar{\varphi}}\Big|_{\substack{\mathbf{F}=\mathbf{I}\\\bar{\varphi}=0}} \bar{\varphi}$$

$$= \quad \mathbf{0} \quad + (\mathbf{I}\otimes\mathbf{I})^{\overset{23}{T}}(\mathbf{F}-\mathbf{I}) - (\bar{\mathbf{e}}\times\mathbf{I})\,\bar{\varphi}\,. \tag{2.48}$$

Therein, $(\mathbf{I}\otimes\mathbf{I})^{\overset{23}{T}}$ corresponds to the fourth-order identity tensor $\overset{4}{\mathbf{I}}$ and $\bar{\mathbf{e}}\times\mathbf{I}$ can be expressed by the *Ricci* permutation tensor $\overset{3}{\mathbf{E}}$, cf. *Ehlers* [42]. Hence, the geometrically linear *Cosserat* strain tensor is given by:

$$\bar{\varepsilon} := \bar{\mathbf{E}}_{\text{lin.}} = \operatorname{Grad}\mathbf{u} + \overset{3}{\mathbf{E}}\,\bar{\varphi}\,. \tag{2.49}$$

This generally non-symmetric tensor can be split into a symmetric and a skew-symmetric part:

$$\bar{\varepsilon}_{\text{sym}} = \tfrac{1}{2}\left(\operatorname{Grad}\mathbf{u} + \operatorname{Grad}^T\mathbf{u}\right) =: \varepsilon \quad \text{and}$$

$$\bar{\varepsilon}_{\text{skw}} = \tfrac{1}{2}\left(\operatorname{Grad}\mathbf{u} - \operatorname{Grad}^T\mathbf{u}\right) + \overset{3}{\mathbf{E}}\,\bar{\varphi} = \overset{3}{\mathbf{E}}\,\overset{*}{\varphi}\,. \tag{2.50}$$

Therewith, on the one hand, it is shown that the symmetric part $\bar{\varepsilon}_{\text{sym}}$ is equal to the linearized strain tensor ε of non-polar materials. On the other hand, the above equation demonstrates that the skew-symmetric part is directly associated with the additional free rotations $\overset{*}{\varphi}$ of the *Cosserat* theory.

2.3.3   Linearization of the micropolar curvature tensor

Finally, the linearization of the micropolar curvature is exemplarily demonstrated by use of the curvature tensor $\overset{3}{^{R}\mathbf{C}}$ of the referential configuration, cf. 2.23, which only depends on the rotations $\bar{\varphi}$. Thus, its linearization can be written as, cf. *Ehlers* [41] or *Volk* [135]:

$$\overset{3}{^{R}\mathbf{C}}_{\text{lin.}} = \quad \overset{3}{^{R}\mathbf{C}}\Big|_{\bar{\varphi}=0} \quad + \left(\bar{\mathbf{R}}^T \frac{\partial \operatorname{Grad}\bar{\mathbf{R}}}{\partial \bar{\varphi}}\right)^{\underline{3}}\Big|_{\bar{\varphi}=0}\bar{\varphi} + \left(\frac{\partial \bar{\mathbf{R}}^T}{\partial \bar{\varphi}}\operatorname{Grad}\bar{\mathbf{R}}\right)^{\underline{3}}\Big|_{\bar{\varphi}=0}\bar{\varphi}$$

$$= \quad \overset{3}{\mathbf{0}} \quad - \quad \operatorname{Grad}(\overset{3}{\mathbf{E}}\,\bar{\varphi}) \quad + \quad \overset{3}{\mathbf{0}} \tag{2.51}$$

$$= -(\overset{3}{\mathbf{E}}\operatorname{Grad}\bar{\varphi})^{\underline{3}}\,.$$

The resulting linear, third-order curvature tensor can be reduced in the same manner as (2.27) to its axial second-order tensor

$$\bar{\kappa} := {}^{R}\bar{\mathbf{C}}_{\text{lin.}} = \tfrac{1}{2}\,(\overset{3}{\mathbf{E}}\overset{3}{\mathbf{E}})^{\underline{2}}\operatorname{Grad}\bar{\varphi} = \tfrac{1}{2}\,2\,\mathbf{I}\operatorname{Grad}\bar{\varphi} = \operatorname{Grad}\bar{\varphi}\,, \tag{2.52}$$

cf. *Ehlers* [42], which is defined as the geometrically linear curvature tensor of the *Cosserat* theory.

2.4   Constitutive settings

For the coupling of the kinematic relations, namely the strain and curvature measures, with the stress and couple stress tensors occurring in the balance equations, constitutive equations are required. With the introduction of these constitutive equations, the type of the material is defined, in contrast the in the previous sections discussed kinematic and balance equations, which are applicable to every type of micropolar material. Besides, the granular materials considered in the framework of this work, such micropolar materials can also be metallic or polymer foams or composite materials.

In this section, firstly, the observation results of material tests of dry sand are described. Basing on these observations, the general settings of the model are defined, followed by the detailed description of the elastic and plastic material properties as well as the formulation of the required hardening and softening laws.

2.4.1   Observations during material tests

Generally, the characterization of a material is based on observations from different material tests, whereby, in the case of granular materials, the triaxial test is the most usual experiment. For this test, a cylindrical specimen is stabilized, in an initial step, by a confining pressure. Then, a load platen is slowly, displacement-driven pressed down. During the loading process the vertical stress σ_{11}, the vertical strain ε_{11} as well as the volumetric strain ε^V are measured. A detailed description of this test is given in Appendix A.1. An exemplary stress-strain relationship including unloading-loading cycles is shown in Figure 2.3. Taking a closer look at the unloading-loading cycles, it is obvious that a part of the strain remains after a complete unloading, i.e., the reduction of the vertical load up
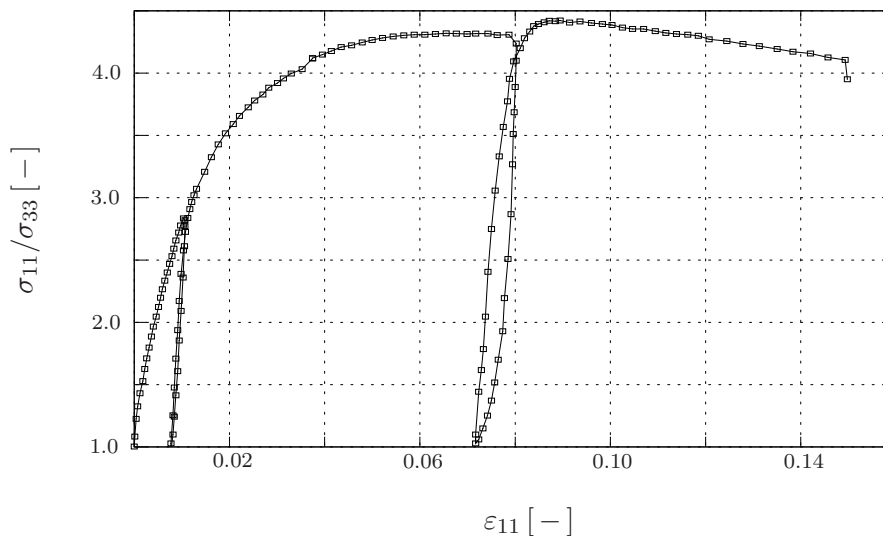
Figure 2.3: Exemplary stress-strain relationship with unloading-loading cycles from a triaxial test.

to the initial isotropic stress state. This observation indicates the occurrence of plastic strain. Following this, for a correct modeling of this material, an elastic-plastic approach is required. Moreover, in Figure 2.3, it can be recognized that the elastic stiffness of the material, given by the slope of the unloading-loading cycles, is higher than the tangent of the stress-strain curve at the starting of the vertical loading. Following this, one can conclude that plasticity is already present at the beginning of the loading. In the framework of elasto-plasticity, this denotes that the increase of the stress is the result of the extension of the yield surface in consequence of plastic yielding, i. e., plastic hardening occurs. During the further loading process, the yield stress reaches its maximum, which is in the stress-strain relation shown in Figure 2.3 at a strain of circa 0.08. After this maximum stress a decrease of the stress can be observed which can be interpreted as a contraction of the yield surface, i. e., plastic softening behavior. Both effects have to be considered in the modeling of the material using appropriate hardening as well as softening formulations for the evolution of the plastic yield condition.

Additional to the observations on triaxial compression tests, hydrostatic triaxial tests show that the material does not seem to be unbounded compressible, cf. Figure 2.4. Therein, the increase of the elastic stiffness of the material with the compression up to an imaginary compression point, i. e. an infinite slope of the stress-strain relation, can be observed by considering the unloading-loading cycles. This denotes that a linear approach will not be sufficient for the description of the elastic part of the material behavior.
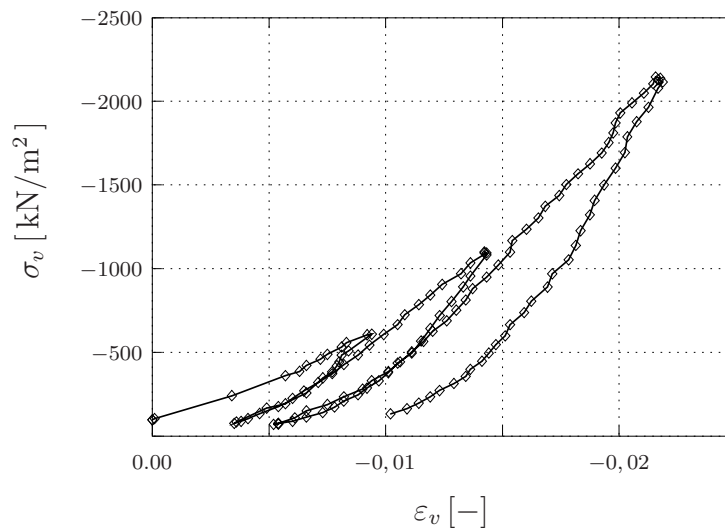
Figure 2.4: Hydrostatic loading of a sand specimen.

For the study of the micropolar effects by means of localization phenomena, further material tests are required, which allow the observation of the development of a shear band. A suitable test for this purpose is given via the biaxial test, cf. Appendix A, whereby, additionally to the measurements of the vertical stress and strain as well as the volumetric strain, the formation of a shear band can be observed by application of the stereophotogrammetry method, cf. *Mokni & Desrues* [101]. These measurements show a finite

thickness of the shear band, cf. Figure 2.5, whereas, computations using the *Finite Element Method* on the basis of the standard, non-polar theory yield a singularity of the shear band thickness, as far as the mesh refinement is possible. This denotes that a regularization of the numerical problem is naturally given by the microstructure of the material, which is taken into account by application of the micropolar theory. Up to now, no detailed measurements about the grain rotations in the shear band exist, which would be an indicator of the occurrence of micropolar effects on the grain scale of the material. However, on the basis of computations with particle models, it can be shown that the occurrence of shear bands is associated with particle rotations. Furthermore, by the application of appropriate homogenization methods it can be demonstrated that these rotations are connected with couple stresses, cf. Chapter 7. The results presented in Chapter 7 clearly suggest the characterization of these granular materials as micropolar materials.

(a) (b)
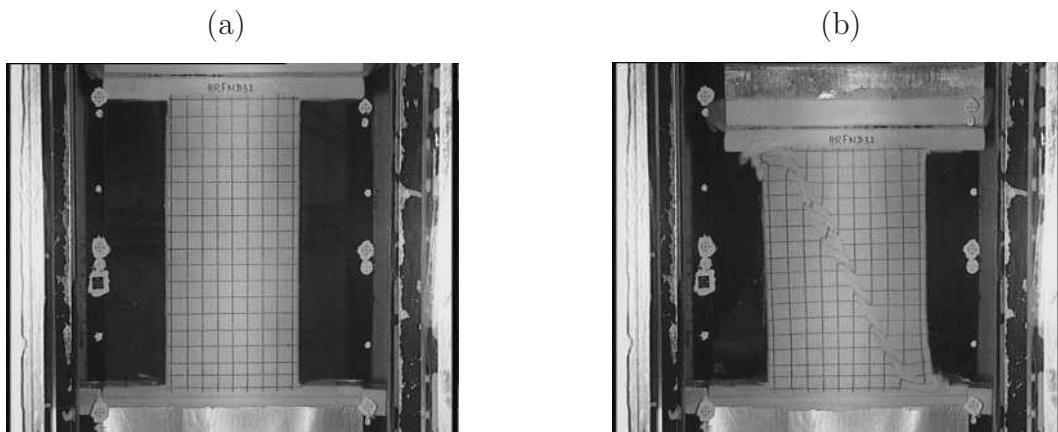
Figure 2.5: Biaxial test: (a) at the begining and (b) at the final state with a shear band (*Laboratoire 3S, Grenoble*).

2.4.2 General model settings

Based on the above described observations obtained from material tests, the resulting general model settings will be specified in the following. Therefore, the general balance equations have been reduced for the geometrically linear and static case due to the fact that no rate-dependent effects are studied in the framework of this thesis. Afterwards, the elasto-plastic decomposition is discussed and, finally, the porosity of the granular material is taken into account.

Geometrically linear balance equations

In the geometrically linear case, the referential and actual configuration are infinitesimally adjacent. Therewith, the stress tensor of the actual and the stress tensor of the reference configuration are approximately the same. Hence, instead of the stress tensor $\mathbf{T}$ of the

actual configuration, $\boldsymbol{\sigma}$ is introduced as the stress tensor of the geometrically linear theory. In analogy, the couple stress tensor $\mathbf{M}$ for the geometrically linear case is indicated as $\boldsymbol{\mu}$. In combination with the assumption of the static case, which denotes that the acceleration $\ddot{\mathbf{x}}$, the velocity $\dot{\mathbf{x}}$ as well as the rotational acceleration $\dot{\bar{\boldsymbol{\omega}}}$ and the rotational velocity $\bar{\boldsymbol{\omega}}$ vanish, the balance equations of mass (2.32), momentum (2.36) and moment of momentum (2.39) can be reduced in the following manner:

$$
\begin{aligned}
\text{mass:} \qquad & \rho = \rho_0 \, (\det \mathbf{F})^{-1} \,, \\[1mm]
\text{momentum:} \qquad & \mathbf{0} = \operatorname{Div} \boldsymbol{\sigma} + \rho_0 \, \mathbf{g} \,, \\[1mm]
\text{m.\,o.\,m.:} \qquad & \mathbf{0} = \mathbf{I} \times \boldsymbol{\sigma} + \operatorname{Div} \boldsymbol{\mu} \,,
\end{aligned}
\tag{2.53}
$$

where ρ_0 is the initial material density. Furthermore, the body couple stress per unit mass $\mathbf{c}$ in the balance of moment of momentum, cf. (2.39), is set to zero, since such a quantity is not known in nature.

Elasto-plastic decomposition

The elasto-plastic model requires the split of the strain and curvature tensors into an elastic and a plastic part. In the framework of the general geometrically non-linear approach, this is usually carried out by a multiplicative split of the deformation gradient $\mathbf{F}$ in an elastic and a plastic part, $\mathbf{F}_e$ and $\mathbf{F}_p$, cf., e.g., *Haupt* [74, 75] or *Ehlers* [38]:

$$
\mathbf{F} = \mathbf{F}_e \, \mathbf{F}_p \,.
\tag{2.54}
$$

Connected with the image of a stress free, plastic intermediate configuration, cf., e.g., *Haupt* [75], this approach yields an additive split of the non-polar strain tensor

$$
\mathbf{E} = \mathbf{E}_e + \mathbf{E}_p
\tag{2.55}
$$

in an elastic part $\mathbf{E}_e$ and plastic a part $\mathbf{E}_p$. In the case of micropolar materials, a similar approach in combination with the assumption of a further multiplicative split of the overall rotation tensor,

$$
\bar{\mathbf{R}} = \bar{\mathbf{R}}_e \, \bar{\mathbf{R}}_p \,,
\tag{2.56}
$$

results in an additive split of the *Cosserat* strain tensor $\bar{\mathbf{E}}$ as well as of the third-order curvature tensor $\overset{3}{{}^{R}\bar{\mathbf{C}}}$, cf. *Steinmann* [127]:

$$
\bar{\mathbf{E}} = \bar{\mathbf{E}}_e + \bar{\mathbf{E}}_p \quad \text{and} \quad \overset{3}{{}^{R}\bar{\mathbf{C}}} = \overset{3}{{}^{R}\bar{\mathbf{C}}_e} + \overset{3}{{}^{R}\bar{\mathbf{C}}_p} \,.
\tag{2.57}
$$

For the geometrically linear case, this results in an additive split of the geometrically linear strain tensor $\bar{\boldsymbol{\varepsilon}}$ and the curvature tensor $\bar{\boldsymbol{\kappa}}$:

$$
\bar{\boldsymbol{\varepsilon}} = \bar{\boldsymbol{\varepsilon}}_e + \bar{\boldsymbol{\varepsilon}}_p \quad \text{and} \quad \bar{\boldsymbol{\kappa}} = \bar{\boldsymbol{\kappa}}_e + \bar{\boldsymbol{\kappa}}_p \,.
\tag{2.58}
$$

Consideration of the porosity of the material

Regarding sand on the microscale, one can identify the single grains of the material as well as the empty space, normally filled with air or water, cf. Figure 2.6. Therewith, sand can be classified as a porous material. Such material can be well described by use of the *Theory of Porous Media* (TPM). This theory goes back to the works of *Truesdell & Toupin* [132] and *Bowen* [18, 19], whereby the formulations in the current understanding are based on the works of *de Boer & Ehlers* [14] as well as *Ehlers* [37, 38, 41]. Moreover a good overview is given in the book of *de Boer* [13] as well as in *Ehlers* [39] or *Markert* [99] and examples for the application on granular material are demonstrated in *Blome* [10], *Ehlers & Blome* [44], *Ehlers* et al. [48] or *Wieners* et al. [138]. Within this theory, usually, a multi-phase material is described consisting of a solid and one or more pore fluids, whereby the quantities of the mixture result from the quantities of the single phases and their interactions. Due to the fact that in the case of dry sand the influence of the pore fluid, namely air, can be neglected, the application of the TPM can be reduced to an empty solid skeleton, cf. *Müllerschön* [105]. Hence, the effects of the TPM are reduced to the coupling of the material stiffness and the porosity by the introduction of an non-linear elastic law regarding the existence of an compression point. Such a behavior is observed in hydrostatic triaxial tests, cf. Figure 2.4, wherein the increase of the stiffness with the compression of the material can be recognized.
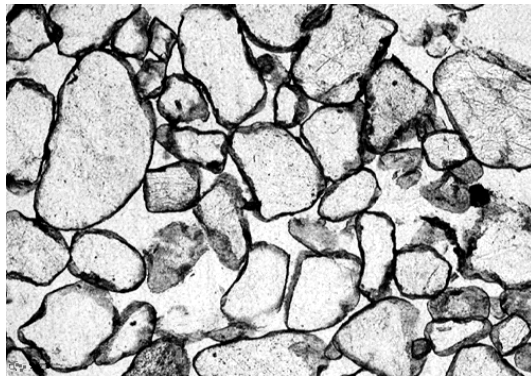
Figure 2.6: Porous structure of sand.

Generally, in the framework of the TPM, the volume V of the multiphasic aggregate $\mathcal{B}$ results from the sum of the partial volumes of the single constituents φ^α, with $\alpha = 1, \dots, k$:

$$V = \int_{\mathcal{B}} \mathrm{d}v = \sum_{\alpha=1}^{k} V^\alpha \quad \text{with} \quad V^\alpha = \int_{\mathcal{B}} \mathrm{d}v^\alpha =: \int_{\mathcal{B}} n^\alpha \, \mathrm{d}v \,. \tag{2.59}$$

Therewith, the volume fraction n^α is defined as the local ratio of the volume element dv^α with respect to the volume element $\mathrm{d}v$ of the overall media:

$$n^\alpha = \frac{\mathrm{d}v^\alpha}{\mathrm{d}v} \,. \tag{2.60}$$

Considering a two phase material consisting of a solid phase φ^S and a fluid phase φ^F in combination with the assumption that no vacant space remains in the overall medium, (2.59) directly leads to the saturation condition:

$$n^S + n^F = 1 \,. \tag{2.61}$$

In this case, $\mathrm{d}v^F = n^F \, \mathrm{d}v$ is the local volume fraction of the pore fluid, which is similar to the pore volume and $\mathrm{d}v^S = n^S \, \mathrm{d}v$ represents the local solid volume fraction, which is in the case of granular material similar to the volume of the grains. Further on, the effective or realistic density of the solid grain material is defined by

$$\rho^{SR} := \frac{\mathrm{d}m^S}{\mathrm{d}v^S} \,, \tag{2.62}$$

in contrast to the bulk or global density

$$\rho = \rho^S := \frac{\mathrm{d}m^S}{\mathrm{d}v} \,, \tag{2.63}$$

which is considered in the mass balance $(2.53)_1$.

The observation that the stiffness of the grain material is much higher than the stiffness of the material as a package of grains yields to the simplification of rigid grains. This assumption denotes that the whole deformation is caused by motion and rotation of the grains. As a consequence, the effective density remains at the initial value, i. e., $\rho^{SR} = \rho_0^{SR}$, which denotes that the solid phase is materially incompressible. Thus, the mass balance $(2.53)_1$ can be reduced to a volume balance relation of the solid skeleton:

$$n^S = n_0^S \, (\det \mathbf{F})^{-1} \,, \tag{2.64}$$

where n_0^S is the initial solid volume fraction. In combination with the elasto-plastic decomposition of $\mathbf{F}$, cf. (2.54), the above equation can be written as:

$$n^S = n_0^S \, (\det \mathbf{F}_e)^{-1} \, (\det \mathbf{F}_p)^{-1} \,. \tag{2.65}$$

Within the geometrical linear theory, $(\det \mathbf{F}_e)^{-1}$ and $(\det \mathbf{F}_p)^{-1}$ in equation (2.65) can be expressed by the volumetric strain $\varepsilon_e^V = \bar{\boldsymbol{\varepsilon}}_e \cdot \mathbf{I}$ and $\varepsilon_p^V = \bar{\boldsymbol{\varepsilon}}_p \cdot \mathbf{I}$:

$$n^S = n_0^S \, (1 - \varepsilon_e^V) \, (1 - \varepsilon_p^V) \,. \tag{2.66}$$

Moreover, one can define the plastic volume fraction

$$n_p^S := n_0^S \, (1 - \varepsilon_p^V) \,, \tag{2.67}$$

which can be understood as the solid volume fraction of the merely plastic deformed material. Thus, (2.66) can be written as:

$$n^S = n_p^S \, (1 - \varepsilon_e^V) \,. \tag{2.68}$$

2.4.3 Elastic material properties

In consequence of the assumption of rigid and uncrushable grains, an arrangement without pore spaces is impossible and, thus, the solid material cannot fill out the whole volume. This fact leads to the maximal reachable solid volume fraction:

$$n_{\max}^S < 1 . \tag{2.69}$$

Therein, $n_{\max}^S$ represents a material parameter depending on the size and geometry of the grains, which restricts the possible elastic volumetric strain to its maximum value:

$$\varepsilon_{e\,\mathrm{crit}}^V = 1 - \frac{n_{\max}^S}{n_p^S} . \tag{2.70}$$

Hence, an elasticity law has to guarantee that the appearing volumetric elastic strain ε_e^V is smaller than $\varepsilon_{e\,\mathrm{crit}}^V$, whereby, $n^S < n_{\max}^S$ is ensured. This leads to the following requirements:

1. The volumetric stiffness of the material,

$$k_v = \frac{\partial \sigma^V}{\partial \varepsilon_e^V} \quad \text{with} \quad \sigma^V = \tfrac{1}{3}\,\boldsymbol{\sigma}\cdot\mathbf{I}\,, \tag{2.71}$$

   must be coupled with the volumetric strain ε^V.

2. For $\varepsilon^V = 0$, the *Hooke*an elastic law should be obtained.

3. For $\varepsilon_e^V \to \varepsilon_{e\,\mathrm{crit}}^V$, the volumetric stiffness as well as the hydrostatic stress, represented by the first invariant $\mathrm{I}_\sigma = \boldsymbol{\sigma}\cdot\mathbf{I}$ of the stress tensor, must go to infinity, i.e., $\mathrm{I}_\sigma \to \infty$ and $k_v \to \infty$.

Under consideration of these requirements, an elasticity law based on the works of *Eipper* [58], *Müllerschön* [105] and *Schanz* [116] is formulated. Proceeding from an additive split of the free *Helmholtz* energy $\rho_0\,\psi$ into a stored elastic part $\rho_0\,\psi^e$ and a plastic part $\rho_0\,\psi^p$, the purely elastic part of the solid skeleton per reference volume is assumed to be given as

$$\rho_0\,\psi^e = \mu\,\bar{\boldsymbol{\varepsilon}}_{e\,\mathrm{sym}}\cdot\bar{\boldsymbol{\varepsilon}}_{e\,\mathrm{sym}} + \lambda\,\varepsilon_{e\,\mathrm{crit}}^V\,\left\{\varepsilon_e^V + \varepsilon_{e\,\mathrm{crit}}^V\,\left[\ln(\varepsilon_{e\,\mathrm{crit}}^V - \varepsilon_e^V) - \ln\varepsilon_{e\,\mathrm{crit}}^V\right]\right\} +$$
$$+ \mu_c\,\bar{\boldsymbol{\varepsilon}}_{e\,\mathrm{skw}}\cdot\bar{\boldsymbol{\varepsilon}}_{e\,\mathrm{skw}} + \mu_c\,(l_c)^2\,\bar{\boldsymbol{\kappa}}_e\cdot\bar{\boldsymbol{\kappa}}_e . \tag{2.72}$$

Therein, μ and λ are the *Lamé* constants whereas μ_c and l_c are the additional parameters of the *Cosserat* theory. Hence, μ_c governs the influence of the skew symmetric part of the elastic *Cosserat* strain $\bar{\boldsymbol{\varepsilon}}_{e\,\mathrm{skw}}$ and l_c can be interpreted as an intrinsic length scale. With the introduction of the free *Helmholtz* energy (2.72), the elastic material behavior is completely described. On the basis of the theory of conjugated variables, cf., e.g., *Eringen & Kafadar* [60] or *Nowacki* [109], the stress tensor $\boldsymbol{\sigma}$ is given by the derivative of $\rho_0\,\psi^e$ with respect to the strain tensor $\bar{\boldsymbol{\varepsilon}}_e$,

$$\boldsymbol{\sigma} := \rho_0\,\frac{\partial\psi^e}{\partial\bar{\boldsymbol{\varepsilon}}_e} = 2\,\mu\,\bar{\boldsymbol{\varepsilon}}_{e\,\mathrm{sym}} + \lambda\,\frac{\varepsilon_{e\,\mathrm{crit}}^V}{\varepsilon_{e\,\mathrm{crit}}^V - \varepsilon_e^V}\,\varepsilon_e^V\,\mathbf{I} + 2\,\mu_c\,\bar{\boldsymbol{\varepsilon}}_{e\,\mathrm{skw}} , \tag{2.73}$$

where the couple stress tensor $\boldsymbol{\mu}$ is given by the derivative of $\rho_0 \, \psi^e$ with respect to the curvature $\bar{\boldsymbol{\kappa}}_e$,

$$\boldsymbol{\mu} := \rho_0 \frac{\partial \psi^e}{\partial \bar{\boldsymbol{\kappa}}_e} = 2 \, \mu_c \, (l_c)^2 \, \bar{\boldsymbol{\kappa}}_e \,. \tag{2.74}$$

Remark: In (2.73) and (2.74), the standard suggestion that μ and μ_c are independent constants has been used (cf. *Ehlers Volk* [55] *Nowacki* [109]). However, it will be shown later that the elastic constants of the *Cosserat* theory, μ_c and l_c, are strongly correlated, cf. Section 6.2. As a result, only one of them can be identified by material tests successfully. Thus, it will be suggested to set $\mu_c = \mu$, which yields the following simplification of (2.73) and (2.74):

$$\boldsymbol{\sigma} = 2 \, \mu \, \bar{\boldsymbol{\varepsilon}}_e + \lambda \, \frac{\varepsilon^V_{e \, \mathrm{crit}}}{\varepsilon^V_{e \, \mathrm{crit}} - \varepsilon^V_e} \, \varepsilon^V_e \, \mathbf{I} \quad \text{and}$$

$$\boldsymbol{\mu} = 2 \, \mu \, (l_c)^2 \, \bar{\boldsymbol{\kappa}}_e \,. \tag{2.75}$$

2.4.4   Plastic material properties

Generally, granular materials are counted among in the group of frictional materials, which are characterized by the dependency of the yield stress on the confining pressure, expressed by the first invariant I_σ of the stress tensor $\boldsymbol{\sigma}$. Furthermore, these materials exhibit a volumetric plastic yielding in addition to a plastic shear deformation in contrast to the most non-porous materials, e. g., metals. The coupling of the yield stress and the confining pressure, by use of a frictional angle, was firstly described by the yield condition by *Drucker & Prager* [35]. In further developments, the influence of the *Lode* angle is considered as well as it is taken into account that the friction angle is not constant but dependent on the confining pressure, i. e., on I_σ. Therewith, the decrease of the friction angle at high pressures, which can be observed in material tests, can be considered, cf., e. g., *Gudehus* [67] or *Lade & Duncan* [85]. Moreover, using the *Drucker & Prager* yield condition, during purely hydrostatic loading no plasticity occurs. This is in contrast to the observed yielding from hydrostatic triaxial tests, cf. Section 2.4.1. For this reason, during further investigations, the yield surface was firstly closed by a cap, cf. *Vermeer* [133] and, finally, single-surface yield conditions were developed with the advantage that they are completely differentiable. In the context of this work, the single-surface yield condition following *Ehlers* [39, 40] is applied, which fulfills the above described requirements.

Since this yield condition has basically been defined for non-polar material with symmetric stresses $\boldsymbol{\sigma} = \boldsymbol{\sigma}_{\mathrm{sym}}$, in the framework of micropolar materials, additionally, the influence of the skew symmetric part $\boldsymbol{\sigma}_{skw}$ of the stress and the couple stress $\boldsymbol{\mu}$ have to be also considered, cf. *Ehlers & Volk* [55] and *Steinmann* [127]. Thus, the yield condition of

Ehlers is extended in the following manner, cf. *Ehlers & Scholz* [51, 52]:

$$F := \left(\Gamma\, \mathrm{II}^D_{\sigma\,\text{sym}} + k_\sigma\, \mathrm{II}_{\sigma\,\text{skw}} + k_\mu\, \boldsymbol{\mu}\cdot\boldsymbol{\mu} + \tfrac{1}{2}\,\alpha\, \mathrm{I}^2_\sigma + \frac{1}{\delta^2}\mathrm{I}^4_\sigma \right)^{1/2} + \beta\, \mathrm{I}_\sigma + \frac{1}{\epsilon}\,\mathrm{I}^2_\sigma - \kappa\,,$$

$$\text{with} \quad \Gamma = \left(1 + \gamma\, \frac{\mathrm{III}^D_{\sigma\,\text{sym}}}{(\mathrm{II}^D_{\sigma\,\text{sym}})^{3/2}} \right)^m\,.$$

(2.76)

Therein, I_σ is the first invariant of the stress tensor $\boldsymbol{\sigma}$, $\mathrm{II}^D_{\sigma\,\text{sym}}$ and $\mathrm{III}^D_{\sigma\,\text{sym}}$ are the negative second invariant and the third invariant of the symmetric part of the deviator of $\boldsymbol{\sigma}$, whereas $\mathrm{II}_{\sigma\,\text{skw}}$ denotes the second negative invariant of the skew-symmetric part of $\boldsymbol{\sigma}$. Moreover, the original version of *Ehlers* [39] has been modified by replacing the parameters δ and ϵ with their reciprocal values in order to obtain a unique formulation for the evolution of the parameters in the hardening and softening equations, cf. Section 2.4.5. In the case of symmetric stresses of non-polar materials, the yield surface F can be exhibited in the principal stress space, cf. Figure 2.7.
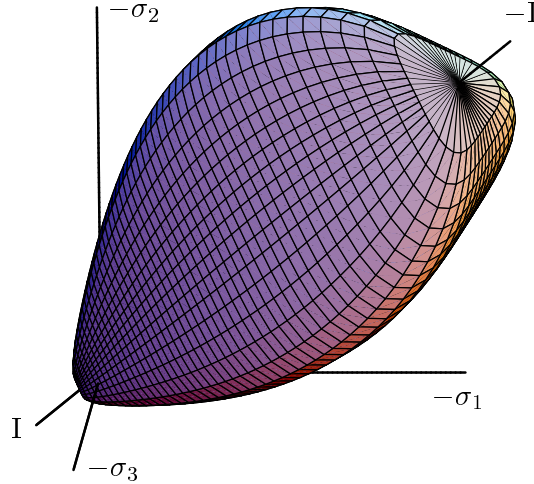
Figure 2.7: Single-surface yield criterion from *Ehlers* [39] in the principal stress space.

The above form of the yield condition contains nine parameters α, β, δ, ϵ, κ, γ, m, k_σ and k_μ. By neglecting the very small cohesion of dry sand, the parameters κ and α can be assumed to be zero. Furthermore, the parameters γ and m can be merged by use of the convexity condition of the yield criterion, cf. Ehlers [39]:

$$m = \frac{2}{9} + \frac{\sqrt{3}}{3\,\gamma}\,.$$

(2.77)

Thus, the six parameters β, δ, ϵ, γ, k_σ and k_μ remain in the yield condition.

Due to the fact that frictional materials generally show a non-associated yielding, the introduction of a plastic potential

$$G := \left(\psi_1\, \mathrm{II}^D_{\sigma\,\text{sym}} + k_\sigma\, \mathrm{II}_{\sigma\,\text{skw}} + k_\mu\, \boldsymbol{\mu}\cdot\boldsymbol{\mu} + \tfrac{1}{2}\,\alpha\, \mathrm{I}^2_\sigma + \frac{1}{\delta^2}\mathrm{I}^4_\sigma \right)^{1/2} + \psi_2\, \beta\, \mathrm{I}_\sigma + \frac{1}{\epsilon}\mathrm{I}^2_\sigma$$

(2.78)

Hydrostatic plane   Deviatoric plane
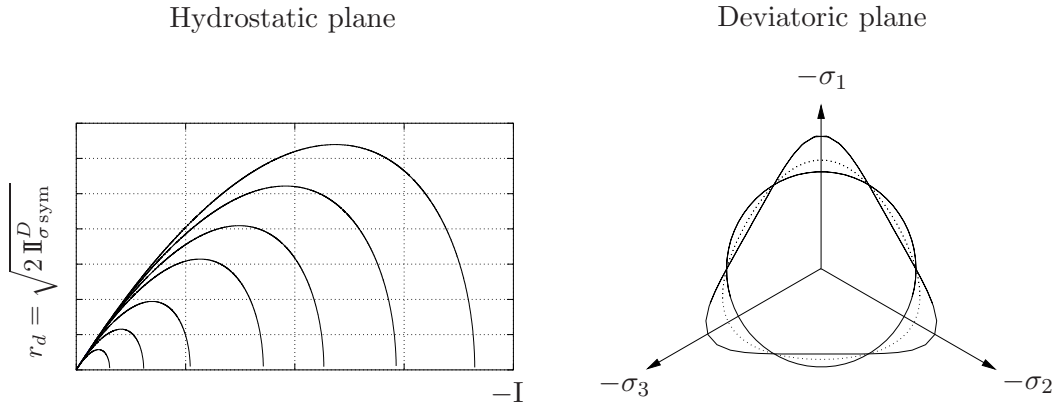
Figure 2.8: Evolution of the yield criterion in the hydrostatic and deviatoric plane of the principal stress space.

with the additional parameters ψ_1 and ψ_2 is necessary. Thus, the evolution of the plastic strain and curvature follows from

$$\dot{\boldsymbol{\varepsilon}}_p = \Lambda \, \frac{\partial G(\boldsymbol{\sigma}, \, \boldsymbol{\mu})}{\partial \boldsymbol{\sigma}} \quad \text{and} \quad \dot{\boldsymbol{\kappa}}_p = \Lambda \, \frac{\partial G(\boldsymbol{\sigma}, \, \boldsymbol{\mu})}{\partial \boldsymbol{\mu}} \, , \tag{2.79}$$

where Λ is the plastic multiplier. In the case of standard elasto-plasticity, Λ can be determined using the *Kuhn-Tucker* conditions,

$$F \leq 0 \, , \quad \Lambda \geq 0 \, , \quad \Lambda \, F = 0 \, . \tag{2.80}$$

However, using a viscoplastic model including the overstress concept of *Perzyna* type [110], Λ is directly given by

$$\Lambda = \frac{1}{\eta} \, \left\langle \frac{F}{\sigma_0} \right\rangle^r \, , \tag{2.81}$$

where η is the viscoplastic relaxation time, σ_0 is the reference stress and r is the viscoplastic exponent. Furthermore, $\langle \cdot \rangle$ are the *Macaulay* brackets, which are defined by $\langle \cdot \rangle := \frac{1}{2} \left[(\cdot) + |(\cdot)| \right]$.

Remark: In case of vanishing relaxation times, i.e., $\eta \to 0$, the viscoplastic evolution yields the condition $F = 0$, cf. *Haupt* [75]. Hence, using small values for η in combination with $\sigma_0 > 0$ and $r = 1$, one obtains nearly the elasto-plasticity model, which is numerically better conditioned than the direct use of the *Kuhn-Tucker* conditions (2.80).

2.4.5   Hardening and softening behavior

On granular materials, plastic deformations can be observed with the onset of the loading. Consequently, the yield surface is nearly a singular point at the beginning of the loading and increases with the plastic deformation. For the modeling of such a behavior, the introduction of a plastic hardening law is necessary, cf., e.g., *Gajo & Wood* [63], *Kim*

& *Lade* [82, 86, 87] or *Vermeer* [133]. Further on, in triaxial compression tests on dense sand a decrease of the vertical load after exceeding the maximum load can be observed, cf. Figure 2.3. This effect, which is caused by a decrease of the yield stress, can be interpreted as a result of the increasing pore volume due to dilatancy. Both effects, the increase and the decrease of the yield condition have to be taken into account in the formulation of the evolution of the yield condition. Therefore, a new evolution law for the yield condition is introduced, whereby the evolution $\dot{p}_i$ of the parameters p_i summarized in the parameter vector $\mathbf{p}$ is split into a volumetric $\dot{p}_i^V$ and a deviatoric $\dot{p}_i^D$ part:

$$\dot{p}_i = \dot{p}_i^V + \dot{p}_i^D = (\overset{\star}{p}_i - p_i)\,(C_{pi}^V\,\dot{\varepsilon}_p^V + C_{pi}^D\,\|\dot{\varepsilon}_p^D\|)$$

$$\text{with} \quad p_i(t=0) = p_{i\,0} \quad \text{and} \quad \mathbf{p} = (\beta,\,\delta,\,\epsilon,\,\gamma)^T. \tag{2.82}$$

Therein, $\overset{\star}{p}_i$ is the maximum value of p_i, C_{pi}^V and C_{pi}^D represent the volumetric and deviatoric evolution constants whereas $p_{i\,0}$ is the initial value of the parameter p_i. The parameters k_σ and k_μ, which are associated with the *Cosserat* theory, are excluded from the evolution, since they are only active during shear banding. In Figure 2.8, an exemplary evolution of the yield function in the hydrostatic as well as in the deviatoric plane is shown, where σ_1, σ_2 and σ_3 are the principal stresses. Therein, the isotropic hardening in the hydrostatic plane due to the parameters β, δ and ϵ can be seen. In the deviatoric plane, the change from a circle to a triangle shape by the evolution of the parameter γ is illustrated, which is in conformity with the experimental results of *Yamada & Ishihara* [142].

Remark: As a result of the deviator norm $\|\dot{\varepsilon}_p^D\|$, the deviatoric part of (2.82) always yields plastic hardening. In contrast, the volumetric part $\dot{\varepsilon}_p^V$ can be positive or negative. Thus, in the case of contractant deformations, the volumetric part causes plastic hardening, whereas, in case of dilatant deformations, plastic softening occurs. This material softening yields the instability of the material, which can be observed in material tests by the incoming of shear bands, cf. Chapter 6. Following this the volumetric part of evolution of the yield condition is essential for the simulation of localization effect.

Chapter 3: Discretization in Space and Time

For the solution of initial boundary-value problems based on the model presented in Chapter 2, numerical methods are indispensable due to the fact that analytical solutions are only available for some special cases. For this purpose, the weak formulations of the balance of momentum and the balance of moment of momentum are required. Furthermore, following, e.g., *Ehlers & Volk* [55], *Steinmann* [127] and *Volk* [135], the displacement vector $\mathbf{u}$ and the total rotations $\bar{\boldsymbol{\varphi}}$ are used as primary variables. The space and time dependent equations given by the weak formulations, have to be discretized in both, the spatial and temporal domains. In the spatial domain, the discretization is carried out on the basis of the *Finite Element Method* (FEM), whereas for the time discretization the *Finite Difference Scheme* is applied. The resulting non-linear system of *Differential-Algebraic Equations* (DAE) is solved by use of the *Newton-Raphson* method, which requires the linearization of the time and space discrete equations.

The discretization methods are introduced very briefly in this chapter. The reader interested in more fundamental details is referred to textbooks of *Bathe* [5], *Braess* [20], *Hughes* [79], *Schwarz* [121] or *Zienkiewicz & Taylor* [143]. Furthermore, a general overview on the numerical time integration of DAE systems can be found in the works of *Hairer* et al. [70, 71] or *Wood* [141]. Moreover a detailed description of the formulations used in this thesis is presented by *Diebels* et al. [31], *Ehlers* et al. [43, 47, 48] and in the work by *Ellsiepen* [59].

In this chapter, firstly, the weak formulations of the governing balance equations are introduced cf. Section 3.1. On the basis of these formulations, the spatial discretization using the FEM is carried out in Section 3.2 and, afterwards, the time integration is introduced in Section 3.3. For the evaluation of the weak forms of the balance equation, the stress and the couple stress tensors are required. Thus, the computation of these tensors using the discrete primary variables is demonstrated in Section 3.4. Finally, in Section 3.4, the solution procedure of the global system of equations by use of the *Newton-Raphson* method is illustrated.

3.1   Weak formulations

The weak formulations of the governing balance relations are obtained from the corresponding strong formulations for the geometrically linear and static case (2.53) by the following steps, which are exemplary demonstrated for the balance of momentum:

1. Scalar multiplication with the test function $\delta\mathbf{u}$,

$$\operatorname{div}\boldsymbol{\sigma}\cdot\delta\mathbf{u} + \rho\,\mathbf{g}\cdot\delta\mathbf{u} = 0\,, \tag{3.1}$$

2. integration over the domain Ω of the body $\mathcal{B}$,

$$\int_\Omega \operatorname{div} \boldsymbol{\sigma} \cdot \delta\mathbf{u}\,\mathrm{d}v + \int_\Omega \rho\,\mathbf{g} \cdot \delta\mathbf{u}\,\mathrm{d}v = 0 \quad \text{and} \tag{3.2}$$

3. applying the chain rule of the divergence theorem and the *Gauß*ian integral theorem to obtain a divergence-free volumetric part as well as a surface part representing the *Neumann* boundary conditions,

$$\begin{aligned}
\int_\Omega \operatorname{div} \boldsymbol{\sigma} \cdot \delta\mathbf{u}\,\mathrm{d}v &= \int_\Omega [\operatorname{div}(\boldsymbol{\sigma}\,\delta\mathbf{u}) - \boldsymbol{\sigma} \cdot \operatorname{Grad} \delta\mathbf{u}]\,\mathrm{d}v = \\
&= \int_{\partial\Omega} (\boldsymbol{\sigma}\,\delta\mathbf{u}) \cdot \mathbf{n}\,\mathrm{d}a - \int_\Omega \boldsymbol{\sigma} \cdot \operatorname{Grad} \delta\mathbf{u}\,\mathrm{d}v = \\
&= \int_{\partial\Omega} \boldsymbol{\sigma}\,\mathbf{n} \cdot \delta\mathbf{u}\,\mathrm{d}a - \int_\Omega \boldsymbol{\sigma} \cdot \operatorname{Grad} \delta\mathbf{u}\,\mathrm{d}v\,,
\end{aligned} \tag{3.3}$$

where $\partial\Omega$ represents the boundary surface of the domain Ω, and $\mathbf{n}$ is the outside oriented normal vector on $\partial\Omega$.

This procedure is well-known within the framework of the FEM. Particularly in the case of the micropolar theory, a detailed description can be found in *Diebels & Ehlers* [28, 29]. Furthermore, for the complete definition of initial boundary-value problems, additionally to the weak forms of the balance of momentum $(2.53)_2$ and the balance of moment of momentum $(2.53)_3$ boundary conditions on the surface $\partial\Omega$ have to be defined. For this reason, the whole boundary $\Gamma = \partial\Omega$ of Ω is split into a part, on which the generalized stress or *Neumann* conditions Γ_σ or Γ_μ defining the stress or couple stress boundary conditions are significant and another *Dirichlet* part Γ_u or Γ_ϕ, on which the primary variables $\mathbf{u}$ and $\bar{\boldsymbol{\varphi}}$ have to be specified.

Thus, using the above described steps (3.1)-(3.3) and furthermore by testing the balance of moment of momentum with the total rotation $\bar{\boldsymbol{\varphi}}$, the following results are obtained:

- Balance of momentum

$$\mathcal{G}_M = \int_\Omega \boldsymbol{\sigma} \cdot \operatorname{Grad}(\delta\mathbf{u})\,\mathrm{d}v - \int_\Omega \rho\,\mathbf{g} \cdot \delta\mathbf{u}\,\mathrm{d}v - \int_{\Gamma_\sigma} \boldsymbol{\sigma}\,\mathbf{n} \cdot \delta\mathbf{u}\,\mathrm{d}a = 0, \tag{3.4}$$

- Balance of moment of momentum

$$\mathcal{G}_{MoM} = -\int_\Omega (\mathbf{I} \times \boldsymbol{\sigma}) \cdot \delta\bar{\boldsymbol{\varphi}}\,\mathrm{d}v + \int_\Omega \boldsymbol{\mu} \cdot \operatorname{Grad}(\delta\bar{\boldsymbol{\varphi}})\,\mathrm{d}v - \int_{\Gamma_\mu} \boldsymbol{\mu}\,\mathbf{n} \cdot \delta\bar{\boldsymbol{\varphi}}\,\mathrm{d}a = 0. \tag{3.5}$$

+ integration point

• rotations $\bar{\boldsymbol{\varphi}}$ and displacement $\mathbf{u}$

⊙ rotations $\bar{\boldsymbol{\varphi}}$
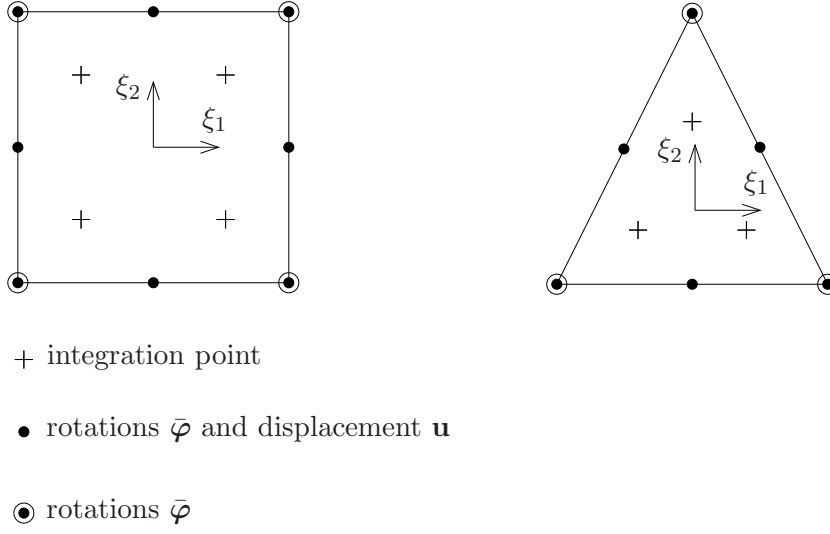
Figure 3.1: Two-dimensional *Taylor-Hood* elements.

3.2   Discretization in the spatial domain

The spatial discretization of the primary variables $\mathbf{u}$ and $\bar{\boldsymbol{\varphi}}$ is carried out on the basis of a mixed finite element formulation using so-called *Taylor-Hood* elements, cf. Figure 3.1. This kind of elements are well-known in literature in the context of coupled solid-fluid problems within the TPM, cf., e.g., *Ehlers & Ellsiepen* [46] and *Wieners* et al. [138–140]. Applications in the framework of the *Cosserat* theory can be found in *Ammann* [2], *Ehlers & Volk* [55] or *Volk* [135]. Thereby, quadratic shape functions $\boldsymbol{\phi}$ are used for the approximation of the displacement field $\mathbf{u}$, whereas linear shape functions $\boldsymbol{\psi}$ are used for the approximation of the total rotations $\bar{\boldsymbol{\varphi}}$. Following this, one obtains:

$$\mathbf{u} \approx \mathbf{u}^h = \tilde{\mathbf{u}}^h + \sum_{i=1}^{N} \boldsymbol{\phi}^i \, \mathbf{u}_i, \qquad \bar{\boldsymbol{\varphi}} \approx \bar{\boldsymbol{\varphi}}^h = \tilde{\bar{\boldsymbol{\varphi}}}^h + \sum_{i=1}^{M} \boldsymbol{\psi}^i \, \bar{\boldsymbol{\varphi}}_i \,, \tag{3.6}$$

where $\mathbf{u}^h$ and $\bar{\boldsymbol{\varphi}}^h$ represent the approximated displacement and rotation fields and with $\tilde{\mathbf{u}}^h$ and $\tilde{\bar{\boldsymbol{\varphi}}}^h$ the *Dirichlet* boundary conditions are considered. Moreover, N and M are the number of translational and rotational nodes of one element, whereas $\mathbf{u}_i$ and $\bar{\boldsymbol{\varphi}}_i$ are the discrete, nodal values of the fields of primary variables. Applying the *Bubnov-Galerkin* method for the approximation of the test functions $\delta\mathbf{u}$ and $\delta\bar{\boldsymbol{\varphi}}$, the same shape functions as for the approximation of the primary variables are used:

$$\delta\mathbf{u}^h = \sum_{i=1}^{N} \boldsymbol{\phi}^i \, \delta\mathbf{u}_i, \qquad \delta\bar{\boldsymbol{\varphi}}^h = \sum_{i=1}^{M} \boldsymbol{\psi}^i \, \delta\bar{\boldsymbol{\varphi}}_i \,. \tag{3.7}$$

Furthermore, the stress tensor $\boldsymbol{\sigma}$, the couple stress tensor $\boldsymbol{\mu}$ as well as the hardening variables

$$\mathbf{p} = (\beta, \, \delta, \, \epsilon, \, \gamma)^T \tag{3.8}$$

cf. (2.82), the internal variables

$$\mathbf{q} = (\varepsilon_p^{11},\ \ldots,\ \varepsilon_p^{33},\ \kappa_p^{11},\ \ldots,\ \kappa_p^{33})^T \tag{3.9}$$

cf. (2.79), and plastic multiplier Λ are computed at the integration points of the numerical quadrature cf. Figure 3.1.

Based on the discrete nodal displacements $\mathbf{u}_i$ and rotations $\bar{\boldsymbol{\varphi}}_i$ cf. (3.6), and the discretized test functions $\delta\mathbf{u}_i$ and $\delta\bar{\boldsymbol{\varphi}}_i$ cf. (3.7), the weak formulations (3.4) and (3.5) can be element-wise expressed as

$$\mathcal{G}_M^E \quad = \int\limits_{\Omega_E} \sum_{i=1}^N \boldsymbol{\sigma}\cdot\mathrm{Grad}\,\boldsymbol{\phi}^i\,\delta\mathbf{u}_i\,\mathrm{d}v - \int\limits_{\Omega_E} \sum_{i=1}^N \rho\,\mathbf{g}\cdot\boldsymbol{\phi}^i\,\delta\mathbf{u}_i\,\mathrm{d}v - \int\limits_{\Gamma_\sigma} \sum_{i=1}^N \boldsymbol{\sigma}\,\mathbf{n}\cdot\boldsymbol{\phi}^i\,\delta\mathbf{u}_i\,\mathrm{d}a\,,$$

$$\mathcal{G}_{MoM}^E = -\int\limits_{\Omega_E} \sum_{i=1}^M (\mathbf{I}\times\boldsymbol{\sigma})\cdot\boldsymbol{\psi}^i\,\delta\bar{\boldsymbol{\varphi}}_i\,\mathrm{d}v + \int\limits_{\Omega_E} \sum_{i=1}^M \boldsymbol{\mu}\cdot\mathrm{Grad}\,\boldsymbol{\psi}^i\,\delta\bar{\boldsymbol{\varphi}}\,\mathrm{d}v - \int\limits_{\Gamma_\mu} \sum_{i=1}^M \boldsymbol{\mu}\,\mathbf{n}\cdot\boldsymbol{\psi}^i\,\delta\bar{\boldsymbol{\varphi}}_i\,\mathrm{d}a\,,$$

$$\tag{3.10}$$

wherein Ω_E is the volume of the regarded finite element.

Generally, in the framework of the FEM, the shape and the test functions are expressed with respect to a so-called reference element, which is defined in the local coordinates $\boldsymbol{\xi}$, cf. Figure 3.1. The relation to the physical or global coordinates $\mathbf{x}$ is given by the geometry transformation:

$$\mathbf{x}(\boldsymbol{\xi}) = \sum_{i=1}^{N_{\mathrm{geo}}} \phi_{\mathrm{geo}}^i(\boldsymbol{\xi})\,\mathbf{x}_i\,. \tag{3.11}$$

Therein, $\mathbf{x}(\boldsymbol{\xi})$ describes an arbitrary position in the element depending on the local coordinates $\boldsymbol{\xi}$, N_{geo} is the number of nodes in the element, $\phi_{\mathrm{geo}}^i(\boldsymbol{\xi})$ includes the shape functions for the geometry transformation, and $\mathbf{x}_i$ represents the global coordinates of the i-th node in the element. Applying the isoparametric concept, the shape functions for the geometry transformation ϕ_{geo}^i are equal to the quadratic shape functions ϕ^i and, consequently, N_{geo} is equal to N in equation $(3.6)_1$. Using the geometry transformation (3.11) volumetric integrals with respect to local coordinates $\boldsymbol{\xi}$ can be transformed to global coordinates $\mathbf{x}$ basing on the substitute rule of the integral calculus:

$$\int\limits_{\Omega_E} f(\mathbf{x})\,\mathrm{d}v = \int\limits_{\Omega_{E\,r}} f(\mathbf{x}(\boldsymbol{\xi}))\,J_E(\boldsymbol{\xi})\,\mathrm{d}v_r\,. \tag{3.12}$$

Therein, $\Omega_{E\,r}$ is the volume of the reference element, $\mathrm{d}v_r$ is the incremental volume element in local coordinates and

$$J_E(\boldsymbol{\xi}) = \det\left(\frac{\mathrm{d}\mathbf{x}(\boldsymbol{\xi})}{\mathrm{d}\boldsymbol{\xi}}\right) \tag{3.13}$$

is the so-called *Jacobi*an determinant. Furthermore, the geometry transformation (3.11) is relevant for the computation of the gradient $\mathrm{Grad}\,\phi(\boldsymbol{\xi})$ of the shape functions $\phi(\boldsymbol{\xi})$ with respect to the global degree of freedom $\mathbf{x}$, i.e.,

$$\mathrm{Grad}\,\phi(\boldsymbol{\xi}) = \frac{\mathrm{d}\phi(\boldsymbol{\xi})}{\mathrm{d}\mathbf{x}} = \frac{\mathrm{d}\phi(\boldsymbol{\xi})}{\mathrm{d}\boldsymbol{\xi}}\left(\frac{\mathrm{d}\mathbf{x}(\boldsymbol{\xi})}{\mathrm{d}\boldsymbol{\xi}}\right)^{-1}\,. \tag{3.14}$$

To obtain the discrete element residuals proceeding from (3.10), the integral over the element volume Ω_E is carried out by the *Gauß* integration. This denotes that the integral is replaced by the sum over the integration points q using the weighting factors w_q. Furthermore, the element-wise discretized weak formulations $\mathcal{G}_M^E$ and $\mathcal{G}_{MoM}^E$ are tested separately in every degree of freedom of the element by a convenient choice of the test functions. Hence, one obtains the following relations for the i-th global degree of freedom of the element residuals:

$$
R_{M\,i}^E \quad = \sum_{q=1}^{N_q} \sum_{p=1}^{N} \left\{ \sigma_{(i)j}^q \, \phi_{(i),j}^{p\,q} - \rho \, g_{(i)} \, \phi_{(i)}^{p\,q} - f_{(i)} \, \phi_{(i)}^{p\,q} \right\} \, w_q \, J_E^q ,
$$

$$
R_{MoM\,i}^E = \sum_{q=1}^{N_q} \sum_{p=1}^{M} \left\{ -(e_{(i)mn} \, \sigma_{nm}) \, \psi_{(i)}^{p\,q} + \mu_{(i)j}^q \, \psi_{(i),j}^{p\,q} - m_{(i)} \, \phi_{(i)}^{p\,q} \right\} \, w_q \, J_E^q .
$$

(3.15)

Therein, the tensors and vectors are written in index notation, whereby the *Einstein* summation is used, i.e. summation over repeating indices, excepting bracketed indices. Furthermore, e_{imn} stands for the *Ricci* permutation symbol, N_q is the number of integration points, whereas N and M are the number of translational and rotational nodes in the element. Moreover, q is the index of the integration point, p is the index of the node number and i and j are the indices of the global coordinates. Following this, $\phi_i^{p\,q}$ and $\psi_i^{p\,q}$ are the values of the p-th shape function at the integration point q in direction of the global degree of freedom i, whereas $\phi_{i,j}^{p\,q}$ and $\psi_{i,j}^{p\,q}$ denote the derivatives of $\psi_i^{p\,q}$ and $\phi_i^{p\,q}$ with respect to the global degree of freedom x_j. Finally, the *Neumann* boundary conditions are taken into account by the discrete nodal forces and moments f_i and m_i on the node i. Due to the fact that the shape and test functions are used in the local coordinates, the transformation to the global coordinates is carried out by use of the *Jacobi*an determinant J_E (3.13), whereby J_E^q indicates the value of J_E at the integration point q.

The components $R_{M\,i}^E$ and $R_{MoM\,i}^E$ of element-wise residua of the balance of momentum and of the balance of moment of momentum are summarized for all degrees of freedom of the element in the vectors $\mathbf{R}_M^E$ and $\mathbf{R}_{MoM}^E$, which are combined to the entire element-wise residual vector:

$$
\mathbf{R}^E = \begin{pmatrix} \mathbf{R}_M^E \\ \mathbf{R}_{MoM}^E \end{pmatrix} .
$$

(3.16)

Finally, the global system of equations is obtained by the sum over all element residua by applying the assembling operator $\mathbf{A}_i^n$, which replaces the element-wise defined degree of freedom i by the global degree of freedom n. Thus, the n-th component of the global residuum vector $\mathbf{R}$ is given via

$$
R_n = \sum_{E=1}^{N_E} \sum_{i=1}^{N_y} \mathbf{A}_i^n R_i^E \overset{!}{=} 0 ,
$$

(3.17)

where N_E represents the number of elements in the Finite Element mesh and N_y is the number of degrees of freedom per element.

For the numerical solution of the resulting, generally non-linear system of equations

$$\mathbf{R} \overset{!}{=} \mathbf{0} \, , \tag{3.18}$$

using the *Newton-Raphson* method, the calculation of the tangent matrix of (3.17) is necessary. For this reason, in the first instance, the derivatives of the element-wise, discrete weak formulation (3.10) with respect to the discrete primary variables $\mathbf{u}_j$ and $\bar{\varphi}_i$ are required, which are given by:

$$\frac{\mathrm{d}\mathcal{G}_M^E}{\mathrm{d}\mathbf{u}_j} = \int\limits_{\Omega_E} \sum_{i=1}^{N} \frac{\mathrm{d}\boldsymbol{\sigma}}{\mathrm{d}\bar{\boldsymbol{\varepsilon}}} \frac{\mathrm{d}\bar{\boldsymbol{\varepsilon}}}{\mathrm{d}\mathbf{u}_j} \operatorname{Grad} \boldsymbol{\phi}^i \, \delta\mathbf{u}_i \, \mathrm{d}v \, ,$$

$$\frac{\mathrm{d}\mathcal{G}_M^E}{\mathrm{d}\bar{\varphi}_j} = \int\limits_{\Omega_E} \sum_{i=1}^{N} \left(\frac{\mathrm{d}\boldsymbol{\sigma}}{\mathrm{d}\bar{\boldsymbol{\varepsilon}}} \frac{\mathrm{d}\bar{\boldsymbol{\varepsilon}}}{\mathrm{d}\bar{\varphi}_j} + \frac{\mathrm{d}\boldsymbol{\sigma}}{\mathrm{d}\bar{\boldsymbol{\kappa}}} \frac{\mathrm{d}\bar{\boldsymbol{\kappa}}}{\mathrm{d}\bar{\varphi}_j} \right) \operatorname{Grad} \boldsymbol{\phi}^i \, \delta\mathbf{u}_i \, \mathrm{d}v \, ,$$

$$\frac{\mathrm{d}\mathcal{G}_{MoM}^E}{\mathrm{d}\mathbf{u}_j} = -\int\limits_{\Omega_E} \sum_{i=1}^{M} \left[\mathbf{I} \times (\frac{\mathrm{d}\boldsymbol{\sigma}}{\mathrm{d}\bar{\boldsymbol{\varepsilon}}} \frac{\mathrm{d}\bar{\boldsymbol{\varepsilon}}}{\mathrm{d}\mathbf{u}_j}) \right] \boldsymbol{\psi}^i \, \delta\bar{\varphi}_i \, \mathrm{d}v \, + \tag{3.19}$$

$$+ \int\limits_{\Omega_E} \sum_{i=1}^{M} \frac{\mathrm{d}\boldsymbol{\mu}}{\mathrm{d}\bar{\boldsymbol{\varepsilon}}} \frac{\mathrm{d}\bar{\boldsymbol{\varepsilon}}}{\mathrm{d}\mathbf{u}_j} \operatorname{Grad} \boldsymbol{\psi}^i \, \delta\bar{\varphi}_i \, \mathrm{d}v \, ,$$

$$\frac{\mathrm{d}\mathcal{G}_{MoM}^E}{\mathrm{d}\bar{\varphi}_j} = -\int\limits_{\Omega_E} \sum_{i=1}^{M} \left[\mathbf{I} \times (\frac{\mathrm{d}\boldsymbol{\sigma}}{\mathrm{d}\bar{\boldsymbol{\varepsilon}}} \frac{\mathrm{d}\bar{\boldsymbol{\varepsilon}}}{\mathrm{d}\bar{\varphi}_j} + \frac{\mathrm{d}\boldsymbol{\sigma}}{\mathrm{d}\bar{\boldsymbol{\kappa}}} \frac{\mathrm{d}\bar{\boldsymbol{\kappa}}}{\mathrm{d}\bar{\varphi}_j}) \right] \boldsymbol{\psi}^i \, \delta\bar{\varphi}_i \, +$$

$$+ \int\limits_{\Omega_E} \sum_{i=1}^{M} \left(\frac{\mathrm{d}\boldsymbol{\mu}}{\mathrm{d}\bar{\boldsymbol{\varepsilon}}} \frac{\mathrm{d}\bar{\boldsymbol{\varepsilon}}}{\mathrm{d}\bar{\varphi}_j} + \frac{\mathrm{d}\boldsymbol{\mu}}{\mathrm{d}\bar{\boldsymbol{\kappa}}} \frac{\mathrm{d}\bar{\boldsymbol{\kappa}}}{\mathrm{d}\bar{\varphi}_j} \right) \operatorname{Grad} \boldsymbol{\psi}^i \, \delta\bar{\varphi}_i \, \mathrm{d}v \, .$$

Basing on the above derivatives of the weak formulations, the discrete derivatives of the element residua are obtained in the same manner as above for calculation of the discrete element residua, $\mathbf{R}_M^E$ and $\mathbf{R}_{MoM}^E$, cf. (3.15), by the following steps:

1. testing separately in every degree of freedom by an appropriate choice of the test functions $\delta\mathbf{u}_i$ and $\delta\bar{\varphi}_i$, and

2. replacing the integral with the summation over the integration points, by use of the *Gauß* integration.

Thus, one obtains the following formulations written in index notation:

$$\frac{\mathrm{d}R_{M\,i}^{E}}{\mathrm{d}u_r^E} = \sum_{q=1}^{N_q}\sum_{p=1}^{M}\left\{\frac{\mathrm{d}\sigma_{(i)j}}{\mathrm{d}\bar{\varepsilon}_{(r)m}}\,\phi_{(r),m}^{pq}\,\phi_{(i),j}^{pq}\right\}\,w_q\,J_E^q\,,$$

$$\frac{\mathrm{d}R_{M\,i}^{E}}{\mathrm{d}\bar{\varphi}_r^E} = \sum_{q=1}^{N_q}\sum_{p=1}^{M}\left\{\frac{\mathrm{d}\sigma_{(i)j}}{\mathrm{d}\bar{\varepsilon}_{mn}}\,e_{mn(r)}\,\psi_{(r)}^{pq}\,\phi_{(i),j}^{pq}\right\}\,w_q\,J_E^q\,,$$

$$\frac{\mathrm{d}R_{MoM\,i}^{E}}{\mathrm{d}u_r^E} = \sum_{q=1}^{N_q}\sum_{p=1}^{M}\left\{e_{(i)mn}\,\frac{\mathrm{d}\sigma_{mn}}{\mathrm{d}\bar{\varepsilon}_{(r)k}}\,\phi_{(i),j}^{pq}\,\psi_{(i)}^{pq} + \frac{\mathrm{d}\mu_{(i)j}}{\mathrm{d}\bar{\varepsilon}_{(r)m}}\,\phi_{(r),m}^{pq}\,\psi_{(i),j}^{pq}\right\}\,w_q\,J_E^q\,, \tag{3.20}$$

$$\frac{\mathrm{d}R_{MoM\,i}^{E}}{\mathrm{d}\bar{\varphi}_r^E} = \sum_{q=1}^{N_q}\sum_{p=1}^{M}\left\{e_{(i)mn}\left(\frac{\mathrm{d}\sigma_{mn}}{\mathrm{d}\bar{\varepsilon}_{lk}}\,e_{lk(r)} + \frac{\mathrm{d}\sigma_{mn}}{\mathrm{d}\bar{\kappa}_{(r)k}}\,\psi_{(r),k}^{pq}\right)\,\psi_{(i)}^{pq} + \right.$$

$$\left. + \left(\frac{\mathrm{d}\mu_{(i),j}}{\mathrm{d}\bar{\varepsilon}_{lk}}\,e_{lk(r)} + \frac{\mathrm{d}\mu_{(i),j}}{\mathrm{d}\bar{\kappa}_{(r)k}}\,\psi_{(r),k}^{pq}\right)\,\psi_{(i),j}^{pq}\right\}\,w_q\,J_E^q\,.$$

Wherein, r indexes the components of the element-wise defined displacement $\mathbf{u}^E$ and rotation $\bar{\boldsymbol{\varphi}}^E$ vectors, respectively, whereas the other indices have the same meaning as in (3.15).

The four terms in (3.20) can be combined to the following element tangent matrix

$$\frac{\mathrm{d}\mathbf{R}^E}{\mathrm{d}\mathbf{y}^E} = \begin{bmatrix} \dfrac{\mathrm{d}\mathbf{R}_M^E}{\mathrm{d}\mathbf{u}^E} & \dfrac{\mathrm{d}\mathbf{R}_M^E}{\mathrm{d}\bar{\boldsymbol{\varphi}}^E} \\[2ex] \dfrac{\mathrm{d}\mathbf{R}_{MoM}^E}{\mathrm{d}\mathbf{u}^E} & \dfrac{\mathrm{d}\mathbf{R}_{MoM}^E}{\mathrm{d}\bar{\boldsymbol{\varphi}}^E} \end{bmatrix}\,, \tag{3.21}$$

where $\mathbf{y}^E = ((\mathbf{u}^E)^T, (\bar{\boldsymbol{\varphi}}^E)^T)^T$. Finally, the global tangent of the system of equations (3.18) is obtained by assembling the single element tangent matrices (3.21). Thus, the components of the global tangent matrix are given by:

$$\frac{\mathrm{d}R_n}{\mathrm{d}y_m} = \sum_{E=1}^{N_E}\sum_{n=1}^{N_y}\mathbf{A}_i^n\mathbf{A}_j^m\frac{\mathrm{d}R_i^E}{\mathrm{d}y_r^E}\,, \tag{3.22}$$

whereby the degrees of freedom of the element i and r are replaced by the global degrees of freedom m and n. Moreover, therein,

$$\mathbf{y} = ((\mathbf{u}_1^E)^T, (\bar{\boldsymbol{\varphi}}_1^E)^T, \ldots, (\mathbf{u}_{N_E}^E)^T, (\bar{\boldsymbol{\varphi}}_{N_E}^E)^T)^T \tag{3.23}$$

contains the whole set of degrees of freedom of the Finite Element mesh.

3.3   Discretization in the temporal domain

The global residual $\mathbf{R}$ (3.17) depends directly on the time t as well as on the primary variables, which are summarized in $\mathbf{y}$. Due to the viscoplasticity, it depends further on the history variables $\mathbf{q}$ (3.9), the hardening variables $\mathbf{p}$ (3.8) as well as their time derivatives, i.e.:

$$\mathbf{R} = \mathbf{R}(t, \mathbf{y}, \mathbf{q}, \dot{\mathbf{q}}, \mathbf{p}, \dot{\mathbf{p}}) = \mathbf{0}. \tag{3.24}$$

The system of equations, given therewith, with the dimension $N_E \cdot N_y$ is only sufficient for the computation of the primary variables $\mathbf{y}$. For the additional computation of the internal and hardening variables, $\mathbf{q}$ and $\mathbf{p}$, the viscoplastic evolution equations (2.79) and (2.81) as well as the hardening equations, cf. (2.82), which can be expressed by a vector-valued function $\mathbf{h}(\dot{\varepsilon}_p^V, \|\dot{\varepsilon}_p^D\|)$, are also required. The resulting evolution equations are solved independently at every integration point of the Finite Element mesh. Hence, in addition to the global coupled equations (3.24), one obtains $N_E \cdot N_q \cdot Q$ (Q: number of internal and hardening variables) local equations, cf. *Ehlers & Ellsiepen* [46] or *Ellsiepen* [59], which can be written as:

$$\mathbf{l}(t, \mathbf{y}, \mathbf{q}, \dot{\mathbf{q}}, \mathbf{p}, \dot{\mathbf{p}}) = \mathbf{A} \begin{pmatrix} \dot{\mathbf{q}} \\ \dot{\mathbf{p}} \end{pmatrix} - \mathbf{r}(\mathbf{y}, \mathbf{q}, \mathbf{p}) = \begin{pmatrix} \dot{\boldsymbol{\varepsilon}}_p \\ \dot{\boldsymbol{\kappa}}_p \\ 0 \\ \dot{\mathbf{p}} \end{pmatrix} - \begin{pmatrix} \Lambda \dfrac{\partial G}{\partial \boldsymbol{\sigma}} \\ \Lambda \dfrac{\partial G}{\partial \boldsymbol{\mu}} \\ \Lambda - \dfrac{1}{\eta} \left\langle \dfrac{F}{\sigma_0} \right\rangle^r \\ \mathbf{h}(\dot{\varepsilon}_p^V, \|\dot{\varepsilon}_p^D\|) \end{pmatrix} = \mathbf{0}. \tag{3.25}$$

Therein, it is obvious that $\mathbf{A}$ is the singular matrix

$$\mathbf{A} = \begin{pmatrix} \mathbf{I}_{3\times3} & \mathbf{0} & 0 & \mathbf{0} \\ \mathbf{0} & \mathbf{I}_{3\times3} & 0 & \mathbf{0} \\ \mathbf{0} & \mathbf{0} & 0 & \mathbf{0} \\ \mathbf{0} & \mathbf{0} & 0 & \mathbf{I}_{4\times4} \end{pmatrix}, \tag{3.26}$$

where $\mathbf{I}_{i\times i}$ is the $i \times i$ unit matrix. Furthermore, equations (3.24) and (3.25) can be combined to a system of *Differential-Algebraic Equations* (DAE)

$$\mathbf{F}(t, \mathbf{y}, \mathbf{q}, \dot{\mathbf{q}}, \mathbf{p}, \dot{\mathbf{p}}) = \begin{bmatrix} \mathbf{R}(t, \mathbf{y}, \mathbf{q}, \dot{\mathbf{q}}, \mathbf{p}, \dot{\mathbf{p}}) \\ \mathbf{l}(t, \mathbf{y}, \mathbf{q}, \dot{\mathbf{q}}, \mathbf{p}, \dot{\mathbf{p}}) \end{bmatrix} = \mathbf{0}. \tag{3.27}$$

The solution procedure of such DAE systems is well-known in literature, cf., e.g., *Diebels* et al. [31], wherein error controlled *Runge-Kutta* methods are recommended for the solution of DAE's. Due to the fact that in the context of this work the time dependency only has the character of a load-scaling factor, the simpler implicit *Euler* method is applied

for the time discretization. For this method, the internal and hardening variables $\mathbf{q}$ and $\mathbf{p}$ at the time t_n are expressed by a first order backward *Taylor* series:

$$\mathbf{q}(t_{n-1}) = \mathbf{q}(t_n) - \dot{\mathbf{q}}(t_n)\,\Delta t + \mathcal{O}(\Delta t^2) \quad \text{and}$$

$$\mathbf{p}(t_{n-1}) = \mathbf{p}(t_n) - \dot{\mathbf{p}}(t_n)\,\Delta t + \mathcal{O}(\Delta t^2) \quad \text{where} \quad \Delta t = t_n - t_{n-1}\,. \tag{3.28}$$

Hence, the temporal derivatives of $\mathbf{q}$ and $\mathbf{p}$, by neglecting second and higher order terms, yield:

$$\dot{\mathbf{q}}(t_n) = \frac{\mathbf{q}(t_n) - \mathbf{q}(t_{n-1})}{\Delta t} \quad \text{and} \quad \dot{\mathbf{p}}(t_n) = \frac{\mathbf{p}(t_n) - \mathbf{p}(t_{n-1})}{\Delta t}\,. \tag{3.29}$$

Remark: The reason for the above abstract formulation of the problem (3.25) is that this formulation allows a clear specification of the type of the underlying differential equations. Thus, the system (3.27) can be identified as a system of *Differential-Algebraic Equations* (DAE), because $\mathbf{A}$ is a singular matrix. Otherwise, if $\mathbf{A}$ were regular, the system would be called as system of *Ordinary Differential Equations* (ODE).

3.4 Computation of the stress and couple stress

The computation of the stress $\boldsymbol{\sigma}$ and the couple stress $\boldsymbol{\mu}$ is carried out at every integration point of the Finite Element mesh. Therefore, the total strain and curvature tensors are expressed by the discrete translations $\mathbf{u}_i$ and rotations $\bar{\boldsymbol{\varphi}}_i$ using the shape functions (3.6),

$$\bar{\boldsymbol{\varepsilon}}(\mathbf{x}) = \sum_{i=1}^{N} \operatorname{Grad} \phi^i(\mathbf{x})\,\mathbf{u}_i + \overset{3}{\mathbf{E}} \sum_{i=1}^{M} \psi^i(\mathbf{x})\,\bar{\boldsymbol{\varphi}}_i\,,$$

$$\bar{\boldsymbol{\kappa}}(\mathbf{x}) = \sum_{i=1}^{M} \operatorname{Grad} \psi^i(\mathbf{x})\,\bar{\boldsymbol{\varphi}}_i\,. \tag{3.30}$$

Basing on the constitutive equations given in Section 2.4 in combination with the above expression for the strain and curvature, the required stress tensor $\boldsymbol{\sigma}$ and couple stress tensor $\boldsymbol{\mu}$ as well as the hardening variables $\mathbf{p}$, the plastic multiplier Λ and the internal variables $\mathbf{q}$ can be computed. For this purpose, the system of equations

$$\mathbf{G}_n = (\mathbf{G}_n^1,\ \mathbf{G}_n^2,\ \mathrm{g}_n^3,\ \mathrm{g}_n^4,\ \mathrm{g}_n^5,\ \mathrm{g}_n^6,\ \mathrm{g}_n^7)^T = \mathbf{0}\,, \tag{3.31}$$

which is given in detail in Table 3.1, is solved at the integration points. Therein, $\mathbf{G}_n^1$ and $\mathbf{G}_n^2$ are tensorial equations representing the elasticity law (2.73) and (2.74) at the time step n. The equations g_n^3 until g_n^7 are scalar functions, where the viscoplasticity concept (2.81) is expressed by g_n^3 and the equations g_n^4 to g_n^7 govern the evolution of the parameters of the yield condition following the hardening law (2.82). Consequently, the system of equations

(3.31) contains altogether a set of 25^1 material parameters summarized in the vector s, whereby 16 parameters, summarized in s_p, are associated with the plastic hardening:

$$\mathsf{s} = (\mu, \lambda, \mu_c, l_c, n_0^S, \psi_1, \psi_2, , k_\mu, k_\sigma, \mathsf{s}_p^T)^T$$

$$\text{with} \quad \mathsf{s}_p = (\epsilon_0, C_\epsilon^V, C_\epsilon^D, \overset{\star}{\epsilon}, \delta_0, C_\delta^V, C_\delta^D, \overset{\star}{\delta}, \gamma_0, C_\gamma^V, C_\gamma^D, \overset{\star}{\gamma}, \beta_0, C_\beta^V, C_\beta^D, \overset{\star}{\beta})^T .$$

(3.32)

Furthermore, as for the solution of the global system of equations (3.18) the consistent tangent matrix, cf. (3.22), is required. Regarding (3.19) or (3.20), respectively, it is obvious that the computation of this tangent matrix bases on the derivatives of the stress $\boldsymbol{\sigma}$ and couple stress $\boldsymbol{\mu}$ with respect to the discrete strain $\bar{\boldsymbol{\varepsilon}}$ and curvature $\bar{\boldsymbol{\kappa}}$. These derivatives are obtained by the implicit derivative of the system of equations (3.31) with respect to the strain and curvature. With the definition of the generalized strain and stress vectors,

$$\boldsymbol{\mathcal{E}} := (\bar{\varepsilon}_{11}, \ldots, \bar{\varepsilon}_{33}, \bar{\kappa}_{11}, \ldots \bar{\kappa}_{33})^T \quad \text{and}$$

$$\boldsymbol{\Sigma} := (\sigma_{11}, \ldots \sigma_{33}, \mu_{11}, \ldots, \mu_{33})^T$$

(3.33)

and, moreover, by summarizing the unknowns of (3.31) in the vector

$$\boldsymbol{\mathcal{S}}_n := (\boldsymbol{\Sigma}^T, \Lambda_n, \epsilon_n, \delta_n, \gamma_n, \beta_n)^T ,$$

(3.34)

the system (3.31) can be written as:

$$\mathbf{G}_n(\boldsymbol{\mathcal{E}}_n, \boldsymbol{\mathcal{S}}_n(\boldsymbol{\mathcal{E}}_n)) \equiv \mathbf{0} .$$

(3.35)

Following this, the implicit derivative of $\mathbf{G}_n$ is obtained via

$$\frac{\mathrm{d}\mathbf{G}_n}{\mathrm{d}\boldsymbol{\mathcal{E}}_n} = \frac{\partial \mathbf{G}_n}{\partial \boldsymbol{\mathcal{E}}_n} + \frac{\partial \mathbf{G}_n}{\partial \boldsymbol{\mathcal{S}}_n} \frac{\mathrm{d}\boldsymbol{\mathcal{S}}_n}{\mathrm{d}\boldsymbol{\mathcal{E}}_n} \overset{!}{=} \mathbf{0} .$$

(3.36)

Hence, the above equation represents a linear system of equations, which can be solved for $\mathrm{d}\boldsymbol{\mathcal{S}}_n/\mathrm{d}\boldsymbol{\mathcal{E}}_n$. Regarding (3.34), it is clear that $\mathrm{d}\boldsymbol{\mathcal{S}}_n/\mathrm{d}\boldsymbol{\mathcal{E}}_n$ contains the global tangent $\mathrm{d}\boldsymbol{\Sigma}_n/\mathrm{d}\boldsymbol{\mathcal{E}}_n$, i.e., the derivatives $\mathrm{d}\boldsymbol{\sigma}_n/\mathrm{d}\bar{\boldsymbol{\varepsilon}}_n$ and $\mathrm{d}\boldsymbol{\mu}_n/\mathrm{d}\bar{\boldsymbol{\kappa}}_n$ as well as $\mathrm{d}\boldsymbol{\sigma}_n/\mathrm{d}\bar{\boldsymbol{\kappa}}_n$ and $\mathrm{d}\boldsymbol{\mu}_n/\mathrm{d}\bar{\boldsymbol{\varepsilon}}_n$, which are summarized in the so called consistent tangent $\boldsymbol{\mathcal{C}}_n$, viz.,

$$\boldsymbol{\mathcal{C}}_n := \frac{\mathrm{d}\boldsymbol{\Sigma}_n}{\mathrm{d}\boldsymbol{\mathcal{E}}_n} = \begin{bmatrix} \dfrac{\mathrm{d}\boldsymbol{\sigma}_n}{\mathrm{d}\bar{\boldsymbol{\varepsilon}}_n} & \dfrac{\mathrm{d}\boldsymbol{\sigma}_n}{\mathrm{d}\bar{\boldsymbol{\kappa}}_n} \\ \dfrac{\mathrm{d}\boldsymbol{\mu}_n}{\mathrm{d}\bar{\boldsymbol{\varepsilon}}_n} & \dfrac{\mathrm{d}\boldsymbol{\mu}_n}{\mathrm{d}\bar{\boldsymbol{\kappa}}_n} \end{bmatrix} .$$

(3.37)

Note that in the case of purely elastic material behaviour the derivatives $\mathrm{d}\boldsymbol{\sigma}_n/\mathrm{d}\bar{\boldsymbol{\varepsilon}}_n$ and $\mathrm{d}\boldsymbol{\mu}_n/\mathrm{d}\bar{\boldsymbol{\kappa}}_n$ direcly result from the elastic law, and $\mathrm{d}\boldsymbol{\sigma}_n/\mathrm{d}\bar{\boldsymbol{\kappa}}_n$ as well as $\mathrm{d}\boldsymbol{\mu}_n/\mathrm{d}\bar{\boldsymbol{\varepsilon}}_n$ vanish. Whereas in the case of elasto-plasticity the above described implicit method for the computation of the tangent is necessary and the derivatives $\mathrm{d}\boldsymbol{\sigma}_n/\mathrm{d}\bar{\boldsymbol{\kappa}}_n$ and $\mathrm{d}\boldsymbol{\mu}_n/\mathrm{d}\bar{\boldsymbol{\varepsilon}}_n$ come into play.

---

[1]The parameters of the viscoplasticity η, σ_0 and r are not listed in (3.32), because these parameters are only used due to numerical advantages of the viscoplastic approach for the numerical realization of the standard elasto-plasticity.

elasticity law $\mathbf{G}_n^1 = \boldsymbol{\sigma}_n - \left(2\,\mu\,\bar{\boldsymbol{\varepsilon}}_{e\,\mathrm{sym}\,n} + \lambda\,\dfrac{\varepsilon_{e\,\mathrm{crit}}^V}{\varepsilon_{e\,\mathrm{crit}}^V - \varepsilon_{e\,n}^V}\,\varepsilon_{e\,n}^V + 2\,\mu_c\,\bar{\boldsymbol{\varepsilon}}_{e\,\mathrm{skw}\,n}\right) = \mathbf{0}$

$\mathbf{G}_n^2 = \boldsymbol{\mu}_n - 2\,\mu_c\,(l_c)^2\,\bar{\boldsymbol{\kappa}}_{e\,n} \hspace{4.5cm} = \mathbf{0}$

with $\bar{\boldsymbol{\varepsilon}}_{e\,n} = \bar{\boldsymbol{\varepsilon}}_n - \bar{\boldsymbol{\varepsilon}}_{p\,n-1} - \dfrac{\dot{\bar{\boldsymbol{\varepsilon}}}_{p\,n}}{t_n - t_{n-1}}$

$\bar{\boldsymbol{\kappa}}_{e\,n} = \bar{\boldsymbol{\kappa}}_n - \bar{\boldsymbol{\kappa}}_{p\,n-1} - \dfrac{\dot{\bar{\boldsymbol{\kappa}}}_{p\,n}}{t_n - t_{n-1}}$

plastic yielding $\dot{\bar{\boldsymbol{\varepsilon}}}_{p\,n} = \Lambda_n\,\dfrac{\partial G(\boldsymbol{\sigma}_n,\,\boldsymbol{\mu}_n)}{\partial \boldsymbol{\sigma}_n}$

$\dot{\bar{\boldsymbol{\kappa}}}_{p\,n} = \Lambda_n\,\dfrac{\partial G(\boldsymbol{\sigma}_n,\,\boldsymbol{\mu}_n)}{\partial \boldsymbol{\mu}_n}$

with the plastic potential $G(\boldsymbol{\sigma}_n,\,\boldsymbol{\mu}_n)$ from (2.78)

viscoplasticity $\mathrm{g}_n^3 = \Lambda_n - \dfrac{1}{\eta}\left\langle \dfrac{F(\boldsymbol{\sigma}_n,\,\boldsymbol{\mu}_n)}{\sigma_0}\right\rangle^r = 0$

with the yield condition $F(\boldsymbol{\sigma}_n,\,\boldsymbol{\mu}_n)$ from (2.76)

plastic hardening $\mathrm{g}_n^4 = \dfrac{\beta_n - \beta_{n-1}}{t_n - t_{n-1}} - (\overset{\star}{\beta} - \beta_n)\,(C_\beta^V\,\dot{\varepsilon}_{p\,n}^V + C_\beta^D\,\|\dot{\bar{\boldsymbol{\varepsilon}}}_{p\,n}^D\|) = 0$

$\mathrm{g}_n^5 = \dfrac{\delta_n - \delta_{n-1}}{t_n - t_{n-1}} - (\delta_n - \overset{\star}{\delta})\,(C_\delta^V\,\dot{\varepsilon}_{p\,n}^V + C_\delta^D\,\|\dot{\bar{\boldsymbol{\varepsilon}}}_{p\,n}^D\|) = 0$

$\mathrm{g}_n^6 = \dfrac{\epsilon_n - \epsilon_{n-1}}{t_n - t_{n-1}} - (\epsilon_n - \overset{\star}{\epsilon})\,(C_\epsilon^V\,\dot{\varepsilon}_{p\,n}^V + C_\epsilon^D\,\|\dot{\bar{\boldsymbol{\varepsilon}}}_{p\,n}^D\|) = 0$

$\mathrm{g}_n^7 = \dfrac{\gamma_n - \gamma_{n-1}}{t_n - t_{n-1}} - (\overset{\star}{\gamma} - \gamma_n)\,(C_\gamma^V\,\dot{\varepsilon}_{p\,n}^V + C_\gamma^D\,\|\dot{\bar{\boldsymbol{\varepsilon}}}_{p\,n}^D\|) = 0$

Table 3.1: Time discrete system of equations to be solved at every integration point at the time step n.

For the sake of completeness, the whole resulting system of equations, which has to be solved in the integration points in order to obtain the consistent tangent, is given in detail

below:

$$
\begin{bmatrix}
\dfrac{\mathrm{d}\mathbf{G}_n^1}{\mathrm{d}\bar{\boldsymbol{\varepsilon}}_n} & \dfrac{\mathrm{d}\mathbf{G}_n^1}{\mathrm{d}\bar{\boldsymbol{\kappa}}_n} \\[2mm]
\dfrac{\mathrm{d}\mathbf{G}_n^2}{\mathrm{d}\bar{\boldsymbol{\varepsilon}}_n} & \dfrac{\mathrm{d}\mathbf{G}_n^2}{\mathrm{d}\bar{\boldsymbol{\kappa}}_n} \\[2mm]
\dfrac{\mathrm{d}g_n^3}{\mathrm{d}\bar{\boldsymbol{\varepsilon}}_n} & \dfrac{\mathrm{d}g_n^3}{\mathrm{d}\bar{\boldsymbol{\kappa}}_n} \\[2mm]
\dfrac{\mathrm{d}g_n^4}{\mathrm{d}\bar{\boldsymbol{\varepsilon}}_n} & \dfrac{\mathrm{d}g_n^4}{\mathrm{d}\bar{\boldsymbol{\kappa}}_n} \\[2mm]
\dfrac{\mathrm{d}g_n^5}{\mathrm{d}\bar{\boldsymbol{\varepsilon}}_n} & \dfrac{\mathrm{d}g_n^5}{\mathrm{d}\bar{\boldsymbol{\kappa}}_n} \\[2mm]
\dfrac{\mathrm{d}g_n^6}{\mathrm{d}\bar{\boldsymbol{\varepsilon}}_n} & \dfrac{\mathrm{d}g_n^6}{\mathrm{d}\bar{\boldsymbol{\kappa}}_n} \\[2mm]
\dfrac{\mathrm{d}g_n^7}{\mathrm{d}\bar{\boldsymbol{\varepsilon}}_n} & \dfrac{\mathrm{d}g_n^7}{\mathrm{d}\bar{\boldsymbol{\kappa}}_n}
\end{bmatrix}
=
\begin{bmatrix}
\dfrac{\partial\mathbf{G}_n^1}{\partial\bar{\boldsymbol{\varepsilon}}_n} & \dfrac{\partial\mathbf{G}_n^1}{\partial\bar{\boldsymbol{\kappa}}_n} \\[2mm]
\dfrac{\partial\mathbf{G}_n^2}{\partial\bar{\boldsymbol{\varepsilon}}_n} & \dfrac{\partial\mathbf{G}_n^2}{\partial\bar{\boldsymbol{\kappa}}_n} \\[2mm]
\dfrac{\partial g_n^3}{\partial\bar{\boldsymbol{\varepsilon}}_n} & \dfrac{\partial g_n^3}{\partial\bar{\boldsymbol{\kappa}}_n} \\[2mm]
\dfrac{\partial g_n^4}{\partial\bar{\boldsymbol{\varepsilon}}_n} & \dfrac{\partial g_n^4}{\partial\bar{\boldsymbol{\kappa}}_n} \\[2mm]
\dfrac{\partial g_n^5}{\partial\bar{\boldsymbol{\varepsilon}}_n} & \dfrac{\partial g_n^5}{\partial\bar{\boldsymbol{\kappa}}_n} \\[2mm]
\dfrac{\partial g_n^6}{\partial\bar{\boldsymbol{\varepsilon}}_n} & \dfrac{\partial g_n^6}{\partial\bar{\boldsymbol{\kappa}}_n} \\[2mm]
\dfrac{\partial g_n^7}{\partial\bar{\boldsymbol{\varepsilon}}_n} & \dfrac{\partial g_n^7}{\partial\bar{\boldsymbol{\kappa}}_n}
\end{bmatrix}
+
\begin{bmatrix}
\dfrac{\partial\mathbf{G}_n^1}{\partial\boldsymbol{\sigma}_n} & \dfrac{\partial\mathbf{G}_n^1}{\partial\boldsymbol{\mu}_n} & \dfrac{\partial\mathbf{G}_n^1}{\partial\Lambda_n} & \dfrac{\partial\mathbf{G}_n^1}{\partial\epsilon_n} & \dfrac{\partial\mathbf{G}_n^1}{\partial\delta_n} & \dfrac{\partial\mathbf{G}_n^1}{\partial\gamma_n} & \dfrac{\partial\mathbf{G}_n^1}{\partial\beta_n} \\[2mm]
\dfrac{\partial\mathbf{G}_n^2}{\partial\boldsymbol{\sigma}_n} & \dfrac{\partial\mathbf{G}_n^2}{\partial\boldsymbol{\mu}_n} & \dfrac{\partial\mathbf{G}_n^2}{\partial\Lambda_n} & \dfrac{\partial\mathbf{G}_n^2}{\partial\epsilon_n} & \dfrac{\partial\mathbf{G}_n^2}{\partial\delta_n} & \dfrac{\partial\mathbf{G}_n^2}{\partial\gamma_n} & \dfrac{\partial\mathbf{G}_n^2}{\partial\beta_n} \\[2mm]
\dfrac{\partial g_n^3}{\partial\boldsymbol{\sigma}_n} & \dfrac{\partial g_n^3}{\partial\boldsymbol{\mu}_n} & \dfrac{\partial g_n^3}{\partial\Lambda_n} & \dfrac{\partial g_n^3}{\partial\epsilon_n} & \dfrac{\partial g_n^3}{\partial\delta_n} & \dfrac{\partial g_n^3}{\partial\gamma_n} & \dfrac{\partial g_n^3}{\partial\beta_n} \\[2mm]
\dfrac{\partial g_n^4}{\partial\boldsymbol{\sigma}_n} & \dfrac{\partial g_n^4}{\partial\boldsymbol{\mu}_n} & \dfrac{\partial g_n^4}{\partial\Lambda_n} & \dfrac{\partial g_n^4}{\partial\epsilon_n} & \dfrac{\partial g_n^4}{\partial\delta_n} & \dfrac{\partial g_n^4}{\partial\gamma_n} & \dfrac{\partial g_n^4}{\partial\beta_n} \\[2mm]
\dfrac{\partial g_n^5}{\partial\boldsymbol{\sigma}_n} & \dfrac{\partial g_n^5}{\partial\boldsymbol{\mu}_n} & \dfrac{\partial g_n^5}{\partial\Lambda_n} & \dfrac{\partial g_n^5}{\partial\epsilon_n} & \dfrac{\partial g_n^5}{\partial\delta_n} & \dfrac{\partial g_n^5}{\partial\gamma_n} & \dfrac{\partial g_n^5}{\partial\beta_n} \\[2mm]
\dfrac{\partial g_n^6}{\partial\boldsymbol{\sigma}_n} & \dfrac{\partial g_n^6}{\partial\boldsymbol{\mu}_n} & \dfrac{\partial g_n^6}{\partial\Lambda_n} & \dfrac{\partial g_n^6}{\partial\epsilon_n} & \dfrac{\partial g_n^6}{\partial\delta_n} & \dfrac{\partial g_n^6}{\partial\gamma_n} & \dfrac{\partial g_n^6}{\partial\beta_n} \\[2mm]
\dfrac{\partial g_n^7}{\partial\boldsymbol{\sigma}_n} & \dfrac{\partial g_n^7}{\partial\boldsymbol{\mu}_n} & \dfrac{\partial g_n^7}{\partial\Lambda_n} & \dfrac{\partial g_n^7}{\partial\epsilon_n} & \dfrac{\partial g_n^7}{\partial\delta_n} & \dfrac{\partial g_n^7}{\partial\gamma_n} & \dfrac{\partial g_n^7}{\partial\beta_n}
\end{bmatrix}
\begin{bmatrix}
\dfrac{\mathrm{d}\boldsymbol{\sigma}_n}{\mathrm{d}\bar{\boldsymbol{\varepsilon}}_n} & \dfrac{\mathrm{d}\boldsymbol{\sigma}_n}{\mathrm{d}\bar{\boldsymbol{\kappa}}_n} \\[2mm]
\dfrac{\mathrm{d}\boldsymbol{\mu}_n}{\mathrm{d}\bar{\boldsymbol{\varepsilon}}_n} & \dfrac{\mathrm{d}\boldsymbol{\mu}_n}{\mathrm{d}\bar{\boldsymbol{\kappa}}_n} \\[2mm]
\dfrac{\mathrm{d}\Lambda_n}{\mathrm{d}\bar{\boldsymbol{\varepsilon}}_n} & \dfrac{\mathrm{d}\Lambda_n}{\mathrm{d}\bar{\boldsymbol{\kappa}}_n} \\[2mm]
\dfrac{\mathrm{d}\epsilon_n}{\mathrm{d}\bar{\boldsymbol{\varepsilon}}_n} & \dfrac{\mathrm{d}\epsilon_n}{\mathrm{d}\bar{\boldsymbol{\kappa}}_n} \\[2mm]
\dfrac{\mathrm{d}\delta_n}{\mathrm{d}\bar{\boldsymbol{\varepsilon}}_n} & \dfrac{\mathrm{d}\delta_n}{\mathrm{d}\bar{\boldsymbol{\kappa}}_n} \\[2mm]
\dfrac{\mathrm{d}\gamma_n}{\mathrm{d}\bar{\boldsymbol{\varepsilon}}_n} & \dfrac{\mathrm{d}\gamma_n}{\mathrm{d}\bar{\boldsymbol{\kappa}}_n} \\[2mm]
\dfrac{\mathrm{d}\beta_n}{\mathrm{d}\bar{\boldsymbol{\varepsilon}}_n} & \dfrac{\mathrm{d}\beta_n}{\mathrm{d}\bar{\boldsymbol{\kappa}}_n}
\end{bmatrix}
=
\begin{bmatrix}
\mathbf{0} & \mathbf{0} \\[2mm]
\mathbf{0} & \mathbf{0} \\[2mm]
0 & 0 \\[2mm]
0 & 0 \\[2mm]
0 & 0 \\[2mm]
0 & 0 \\[2mm]
0 & 0
\end{bmatrix}.
$$

$$(3.38)$$

3.5 Solution of the global system of equations

After the weak formulations have been discretized in the spatial and temporal domain, the resulting global non-linear system of equations:

$$\mathbf{R}_n(\mathbf{y}_n) = \mathbf{0}.\,,\tag{3.39}$$

has to solved by an iterative procedure for the primary variables $\mathbf{y}_n$ at the time t_n. This is carried out by use of the *Newton-Raphson* iteration procedure. Hence, one obtains for the i-th iteration step the following linear system of equations:

$$\frac{\mathrm{d}\mathbf{R}_{ni}}{\mathrm{d}\mathbf{y}_{ni}}\,\Delta\mathbf{y}_{ni} - \mathbf{R}_{ni} = \mathbf{0}\,,\tag{3.40}$$

where $\mathrm{d}\mathbf{R}_{ni}/\mathrm{d}\mathbf{y}_{ni}$ is the consistent tangent, cf. (3.22). The above linear system can be solved directly for the increment $\Delta\mathbf{y}_{ni}$. Thus, the solution vector of the current iteration step is updated via

$$\mathbf{y}_{ni+1} = \mathbf{y}_{ni} + \alpha_i\,\Delta\mathbf{y}_{ni},\tag{3.41}$$

whereby with $\alpha_i \leq 1$ a damping parameter can be considered. Based on the updated, new global solution vector $\mathbf{y}_{ni+1}$, the new residual $\mathbf{R}_{ni+1}$ is evaluated again. In this manner, the procedure is repeated until the $L2$-norm of the residual fulfills a user-defined tolerance, i. e.,

$$\|\mathbf{R}_{ni+1}\| < \mathrm{tol}\,.\tag{3.42}$$

The overall procedure of the solution of the system can be summarily concluded in the following steps, cf. Figure 3.2:

global procedure   **element-wise procedure**

$$\mathbf{R}_n(\mathbf{y}_{ni})$$

$$\boldsymbol{\mathcal{E}}_{ni},\ \boldsymbol{\mathcal{S}}_{ni},\ \mathbf{q}_{ni}$$

$$\frac{\mathrm{d}\mathbf{R}_n}{\mathrm{d}\mathbf{y}_{ni}}$$

$$\frac{\mathrm{d}\boldsymbol{\Sigma}_{ni}}{\mathrm{d}\boldsymbol{\mathcal{E}}_{ni}}$$

$$\Delta\mathbf{y}_{ni} = \left(\frac{\mathrm{d}\mathbf{R}_n}{\mathrm{d}\mathbf{y}_{ni}}\right)^{-1}\mathbf{R}_n$$

$$\mathbf{y}_{n\,i+1} = \mathbf{y}_{ni} + \alpha_i\Delta\mathbf{y}_{ni}$$

$$n=n+1$$

$$i=i+1$$

$$\mathbf{R}_n(\mathbf{y}_{n\,i+1})$$

$$\boldsymbol{\mathcal{E}}_{n\,i+1},\ \boldsymbol{\mathcal{S}}_{n\,i+1},\ \mathbf{q}_{n\,i+1}$$

no $\|\mathbf{R}_{n\,i+1}\| < \mathrm{tol}$

yes

$$\mathbf{y}_n = \mathbf{y}_{n\,i+1}$$
$$\mathbf{q}_n = \mathbf{q}_{n\,i+1}$$
$$\boldsymbol{\mathcal{S}}_n = \boldsymbol{\mathcal{S}}_{n\,i+1}$$
$$t_{n+1} = t_n + \Delta t_n$$
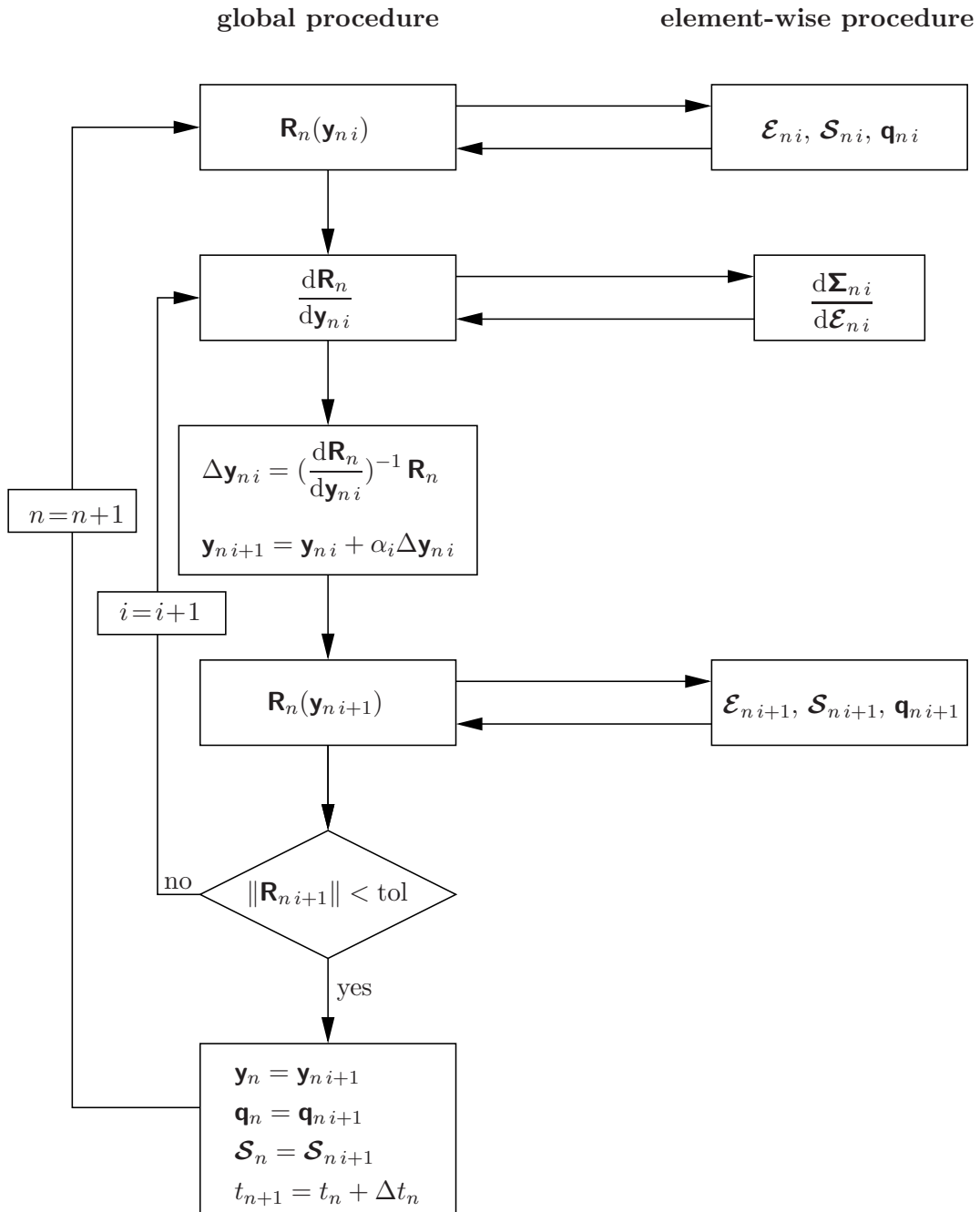
Figure 3.2: Iteration procedure for the solution of the global system of equations.

1. Computation of the residual $\mathbf{R}_{ni}$, at the time step n and the iteration step i, basing on the current vector of primary variables $\mathbf{y}_{ni}$. This step includes, on the element level, the solution of the local system of equations, cf. Table 3.1, at every integration point of the Finite Element mesh.

2. Computation of the consistent tangent, cf. (3.22), basing on the element-wise com-

puted local algorithmic tangents, cf. (3.37).

3. Solution of the global linear system of equations (3.40) of the current iteration step i for $\Delta\mathbf{y}_{n\,i}$ and, therewith, updating of the primary variables.

4. Computation of the new residual $\mathbf{R}_{n\,i+1}$ basing on the updated primary variables $\mathbf{y}_{n\,i+1}$.

5. Verification of a user-defined tolerance. If the tolerance is not fulfilled, i is set to $i+1$ and steps 2 until 5 are repeated.

6. Otherwise, if the tolerance is fulfilled, all required variables will be saved and the next time step will be computed, i. e., the time-step index n is set to $n+1$.

In this manner, the solution of the system is carried out until the final time t_{end} is reached.

Chapter 4: Parameter Identification

In Chapter 2, a model for the simulation of the behavior of granular materials has been introduced and in Chapter 3, the numerical implementation based on the *Finite Element Method* (FEM) has been demonstrated. Thus, one is able to compute some exemplary boundary-value problems. However, for the simulation of the real behavior of a specific material, the values of the material parameters in the constitutive equations must be known. Whereas the determination of these values is very simple in the case of an elementary material model such as the *Hooke*an elasticity law, it becomes a very complex task, if a more detailed material model is used containing a lot of coupled material parameters. In this case, the task of the parameter identification leads to an inverse problem, which can be solved by using the methods of the nonlinear optimization. Such methods are well-known in mathematics, cf., e.g., *Spellucci* [76], *Luenberger* [94] or *Beck & Arnold* [7]. Examples of the application of these methods to the parameter identification of elasto-plastic and elasto-viscoplastic materials, respectively, are given in *Benedix* [8], *Ehlers* et al. [49], *Mahnken & Stein* [96], *Mahnken & Steinmann* [97], *Müllerschön* [105] or *Scheday* [117].

For the determination of the material parameters, first of all, material tests must be found, on which the effects of the single parameters on the material behavior can be observed. If this is possible, the material parameters can be determined by using an optimization algorithm, which will be described in detail within this chapter. Subsequently, the reliability of the identified values has to be checked by use of the so-called error analysis, which is as important as the identification of the values itself. For instance, an eventual result of the error analysis could be that the influence of one parameter on the quantities observed in material tests (e.g., measured stress or strain data) is nearly zero. Or another result of the error analysis could be that the effect of two or more parameters is nearly identical. In both cases, these parameters cannot be identified with the chosen set of material tests and, thus, one has to check whether the inclusion of additional material tests is possible. If this is not the case, the constitutive laws will have to be reduced by neglecting one or more parameters, because indeterminable material parameters make no sense in a constitutive law. Following this, already during the generation of constitutive laws, one has to take into account that realizable material tests must exist, which allow the successful identification of the introduced material parameters. Thus, the identification process can be seen as an important part in the complete modeling procedure of the material behavior.

In this chapter, firstly, an overview about the various methods for the determination of material parameters is given in Section 4.1, followed by a detailed description of the *Sequential Quadratic Programing* (SQP) method, which is applied in this work for the solution of the inverse problem, cf. Section 4.2. In consideration of the high number of different material parameters in the constitutive laws, the complete identification process is split into single steps illustrated in Section 4.3. Due to the fact that the identification of the *Cosserat* parameters requires the consideration of the thickness of the shear band,

a new method for the inclusion of the corresponding data in the identification process has been developed, cf. Section 4.4. Finally, within this chapter, the reliability of the determined material parameters will be discussed using the error analysis, cf. Section 4.5.

4.1   Overview

Generally speaking, experimental data which characterize the material behavior, are required for the identification of the material parameters. In the case of granular media, e. g. sand, triaxial tests are one of the most popular experimental set-ups to characterize the non-polar behavior. Additionally, biaxial tests, wherein the incoming of a shear band can be observed and the corresponding strain can be measured by using the stereophotogrammetry, are taken into account for the investigation of the micropolar behavior. Based on these test data, the task of the parameter identification is the determination of the set of material parameters $\mathbf{s}$, which yields the best correlation between experimental and numerical results. This is carried out by the minimization of the difference between numerically computed and measured data. Hence, the parameter identification represents a minimization problem. In the engineering context, this task is called an inverse problem, because the solution of the boundary-value problem is given with the test data, whereas the material parameters are the unknowns. In contrast to that, within the direct problem, the material parameters are known and the solution of the boundary-value problem itself is required.

The associated minimization problem is formulated by use of an objective function $f(\mathbf{s})$, usually based on the least squares method. Following this, the sum of the squares of the differences between the measured data $\tilde{\phi}$ and the corresponding results of the simulation $\phi(\mathbf{s})$ depending on the material parameters $\mathbf{s}$, has to be minimized:

$$f(\mathbf{s}) := \sum_{n=1}^{N} w_n [\, \phi_n(\mathbf{s}) - \tilde{\phi}_n \,]^2 \quad \rightarrow \quad \min . \tag{4.1}$$

Therein, w_n is a weighting factor and N is the number of discrete data points. Additionally, the possible values of the material parameters are restricted to their physically reasonable ranges by use of N_{iq} inequality constraints $g_j(\mathbf{s})$. Furthermore, in some cases the formulation of N_{eq} equality constraints $h_i(\mathbf{s})$ is convenient:

$$\begin{aligned} \text{inequality constraints:} \quad & g_j(\mathbf{s}) \geq 0 \quad \text{with} \quad j = 1, \ldots, N_{iq} , \\ \text{equality constraints:} \quad & h_i(\mathbf{s}) = 0 \quad \text{with} \quad i = 1, \ldots, N_{eq} . \end{aligned} \tag{4.2}$$

Thus, with the objective function (4.1) in combination with the constraints (4.2), the inverse problem is completely defined. The computation of the solution $\hat{\mathbf{s}}$ of this problem is in general a problem in the framework of the non-linear optimization, whereby, in many cases the existence of a unique minimum is not even known. Hence, a lot of various methods for the solution of this problem were developed in the past. All those methods can be classified into two categories, namely, the deterministic and stochastic

strategies. From a mathematical point of view, this classification corresponds to the differentiation between the local and global optimization methods. The fundamental advantage of the stochastic methods like the *Monte Carlo* strategy or *Evolution* strategies, cf., e.g., *Schwefel* [123] is the possibility to find the global minimum of the objective function in a defined region, in contrast to the deterministic methods. But, otherwise, within these methods a high number of evaluations of the objective function is required, which are always coupled with a numerical simulation of the related material tests. For this reason, stochastic methods are only appropriate, if the evaluation of the objective function is numerically very cheap. Thus, if a FE simulation with more than a few elements is necessary for the simulation of the material test, the application of these strategies will generally be impossible. In this case, the deterministic methods have to be applied. These methods need only a few calculations of the objective function, but their usage is only feasible in the environment of the global minimum. Due to the fact that within this work a fully computation of an inhomogeneous strain field, connected with high numerical costs, is required, cf. Section 4.3, a deterministic method is used. Thereby, one has to verify, as far as possible, if the obtained solution is the global minimum, e.g., by repeating the optimization procedure with different initial values. The existing various deterministic methods can be furthermore classified into two categories. Firstly, in the gradient-based or *Newton*-like methods, generally denoted as *SQP* (*Sequential Quadratic Programming*), whereby, the most popular ones are the *Gauss-Newton* method, the *Levenberg-Marquardt* method and the *BFGS* (*Broyden-Fletcher-Goldfarb-Shanno*) method, cf., e.g., *Heinz & Spellucci* [76], *Luenberger* [94] or *Schittkowski* [118]. Secondly, in the gradient-free methods, whereby the most usual ones given by the large group of the simplex-based methods, cf., e.g., *Nelder & Mead* [107], *Spendley* [126] or *Powell* [112], as well as the *Response Surface Method* method, cf., e.g., *Myers & Montgomery* [106]. Due to the fact that for the gradient-free methods no modification of the FEM code in terms of the computation of the gradient with respect to the material parameters **s** is required, these methods can be easily implemented, which is their main advantage. In all cases, where an effective computation of the gradient is available, the gradient-based methods are favorable. Another reason for the computation of the gradient is the performance of the error analysis, wherefore, at least, the gradient for the final set of material parameters **ŝ** must be known.

Note in passing that one method to avoid the coding of the gradient in combination with gradient-based methods is the numerical computation of the gradient. Therewith, the implementation of the gradient-based methods is as simple as the implementation of the gradient-free methods, but the effectivity is generally less than the direct use of a gradient-free method.

4.2   Identification procedure (SQP-method)

In consideration of the high numerical costs for the simulations of the material tests, especially, for the required simulation of the biaxial tests with shear banding, the gradient-based *SQP*-method with the semi-analytical determination of the gradient has been chosen

for the solution of the inverse problem. In the following, the single steps of this method are illustrated.

4.2.1   Associated *Lagrange*an function

In the first step, the equality and inequality conditions, cf. (4.2), are combined with the objective function (4.1) by use of the *Lagrange* multipliers μ_j and λ_j to the so-called associated *Lagrange*an function:

$$\mathcal{L}(\mathbf{s}, \boldsymbol{\mu}, \boldsymbol{\lambda}) = f(\mathbf{s}) - \boldsymbol{\mu}^T \mathbf{h}(\mathbf{s}) - \boldsymbol{\lambda}^T \mathbf{g}(\mathbf{s}) \quad \rightarrow \quad \text{stat.}$$

$$\text{with} \quad \boldsymbol{\mu} = (\mu_1, \ldots, \mu_n)^T, \quad \mathbf{h}(\mathbf{s}) = (h_1(\mathbf{s}), \ldots, h_n(\mathbf{s}))^T, \quad n = N_{eq}, \tag{4.3}$$

$$\boldsymbol{\lambda} = (\lambda_1, \ldots, \lambda_m)^T, \quad \mathbf{g}(\mathbf{s}) = (g_1(\mathbf{s}), \ldots, g_m(\mathbf{s}))^T, \quad m = N_{iq}.$$

This associated *Lagrange*an function represents a dual problem to the minimizing problem (4.1) under consideration of the equality and inequality conditions (4.2). It can be shown that the solution of (4.3) is identical with the solution of the original problem under some continuous requirements, cf. *Spellucci* [124] or *Heinz & Spellucci* [76]. Moreover, with the application of the associated *Lagrange*an function, the type of the problem changes from a constrained minimizing problem to a saddle-point problem.

Necessary conditions for the existence of a solution of (4.3) are the so-called *Karush-Kuhn-Tucker* conditions:

$$\mathbf{F}(\mathbf{s}, \boldsymbol{\mu}, \boldsymbol{\lambda}) := \begin{cases} \dfrac{\mathrm{d}\mathcal{L}}{\mathrm{d}\mathbf{s}} = \dfrac{\mathrm{d}f(\mathbf{s})}{\mathrm{d}\mathbf{s}} - \boldsymbol{\mu}^T \dfrac{\mathrm{d}\mathbf{h}(\mathbf{s})}{\mathrm{d}\mathbf{s}} - \boldsymbol{\lambda}^T \dfrac{\mathrm{d}\mathbf{g}(\mathbf{s})}{\mathrm{d}\mathbf{s}} = \mathbf{0}, \\[2mm] \dfrac{\partial\mathcal{L}}{\partial\boldsymbol{\mu}} = -\mathbf{h}(\mathbf{s}) = \mathbf{0}, \\[2mm] \boldsymbol{\lambda}\, \mathbf{I}_{\mathrm{n\times n}} \left(\dfrac{\partial\mathcal{L}}{\partial\boldsymbol{\lambda}}\right)^T = -\boldsymbol{\lambda}\, \mathbf{I}_{\mathrm{n\times n}}\, \mathbf{g}^T(\mathbf{s}) = \mathbf{0}, \\[2mm] \lambda_i \geq 0, \\[2mm] g_i(\mathbf{s}) \geq 0, \end{cases} \tag{4.4}$$

$$i = 1, \ldots, n \quad \text{and} \quad n = N_{iq},$$

where $\mathbf{I}_{\mathrm{n\times n}}$ is the n × n unit matrix. Furthermore, a sufficient condition for a local minimum $f(\hat{\mathbf{s}})$ of the objective function $f(\mathbf{s})$ (4.1) is the positive definiteness of the *Hesse*an matrix at the solution $\hat{\mathbf{s}}$ of the optimizing problem, i. e.,

$$\mathbf{v}^T \frac{\mathrm{d}^2 f(\hat{\mathbf{s}})}{\mathrm{d}\mathbf{s}\,\mathrm{d}\mathbf{s}^T} \mathbf{v} > 0, \tag{4.5}$$

where $\mathbf{v}$ is an arbitrary vector of the same dimension as $\mathbf{s}$.

4.2.2   *Active Set* strategy

For the consideration of the inequality conditions $g_i(\mathbf{s})$ during the solution procedure of the minimizing problem, the so-called *Active Set* strategy is applied. Using this strategy,

the whole set $\mathcal{I} = \{g_1, \ldots, g_{Niq}\}$ of the given inequality conditions is split into a set of active constraints $g_i \in \mathcal{I}_{\text{act}}$, which are currently significant, i. e., $g_i(\mathbf{s}) = 0$ and a set of inactive constraints $g_j \notin \mathcal{I}_{\text{act}}$, where $g_j(\mathbf{s}) > 0$. Based on this split, the solution of the optimization problem is carried out by use of the following procedure:

1. A local minimum of $f(\mathbf{s})$ is computed with the initial active set $\mathcal{I}_{\text{act}}^0$.

2. The *Karush-Kuhn-Tucker* conditions (4.4) are verified with respect to the obtained solution. If they are fulfilled, the assumed *Active Set* will correspond to the solution and the minimum under consideration of the inequality condition will be found.

3 In the other case, i. e., if the *Karush-Kuhn-Tucker* conditions (4.4) are violated, in the third step, a new *Active Set* $\mathcal{I}_{\text{act}}^1$ will be generated and, therewith, the minimum of the objective function will again be computed.

This procedure is continued as long as the *Karush-Kuhn-Tucker* conditions are fulfilled with the actual *Active Set* $\mathcal{I}_{\text{act}}^n$ at the iteration step n. Thus, only equality conditions have to be considered during the solution of one iteration step.

4.2.3 Iteration procedure

Due to the fact that by the application of the *Active Set* strategy, the inequality constraints of the current active set $g_i \in \mathcal{I}_{\text{act}}^n$ become equality constraints, only equality constraints have to be considered during the iteration. Thus, the current active inequality constraints can be summarized in the vector $\bar{\mathbf{g}}(\mathbf{s})$ and combined with the equality constraints $\mathbf{h}(\mathbf{s})$ to the generalized equality constraints

$$\bar{\mathbf{h}}(\mathbf{s}) := (\, \mathbf{h}^T(\mathbf{s}),\, \bar{\mathbf{g}}^T(\mathbf{s})\,)^T = \mathbf{0}\,. \tag{4.6}$$

Thus, in the associated *Lagrange* function, no inequality constraints occur and, therewith, the optimization problem (4.3) can be reduced to

$$\mathcal{L}(\mathbf{s},\, \boldsymbol{\mu}) = f(\mathbf{s}) - \bar{\boldsymbol{\mu}}^T\, \bar{\mathbf{h}}(\mathbf{s}) \quad \rightarrow \quad \text{stat.}. \tag{4.7}$$

Therein, $\bar{\boldsymbol{\mu}}$ represent the *Lagrange*an multipliers, which are associated with generalized equality constraints $\bar{\mathbf{h}}$. In consequence, the necessary conditions for the existence of a minimum are given via

$$\mathbf{F}(\mathbf{s},\, \bar{\boldsymbol{\mu}}) := \begin{cases} \dfrac{\mathrm{d}\mathcal{L}}{\mathrm{d}\mathbf{s}} = \dfrac{\mathrm{d}f(\mathbf{s})}{\mathrm{d}\mathbf{s}} - \boldsymbol{\mu}^T\, \dfrac{\mathrm{d}\bar{\mathbf{h}}(\mathbf{s})}{\mathrm{d}\mathbf{s}} = \mathbf{0}\,, \\[3mm] \dfrac{\partial\mathcal{L}}{\partial\bar{\boldsymbol{\mu}}} = \qquad - \bar{\mathbf{h}}(\mathbf{s}) \qquad = \mathbf{0}\,. \end{cases} \tag{4.8}$$

These conditions represent, in contrast to (4.4), a non-linear system of equations, i. e.,

$$\mathbf{F}(\mathbf{x}) = \mathbf{0} \quad \text{with} \quad \mathbf{x} = (\mathbf{s}^T, \bar{\boldsymbol{\mu}}^T)^T\,, \tag{4.9}$$

which can be solved by use of the *Newton*-like iteration procedure:

$$\mathbf{x}_{i+1} = \mathbf{x}_i + \alpha_i \, [\,\frac{\mathrm{d}\mathbf{F}(\mathbf{x})}{\mathrm{d}\mathbf{x}}\Big|_{\mathbf{x}_i}]^{-1} \, \mathbf{F}(\mathbf{x}_i) \, . \tag{4.10}$$

Therein, α_i is the line-search parameter and $\mathrm{d}\mathbf{F}(\mathbf{x}_i)/\mathrm{d}\mathbf{x}$ is given via

$$\frac{\mathrm{d}\mathbf{F}(\mathbf{x}_i)}{\mathrm{d}\mathbf{x}} = \begin{bmatrix} \dfrac{\mathrm{d}^2 f(\mathbf{s})}{\mathrm{d}\mathbf{s}\,\mathrm{d}\mathbf{s}^T} - \boldsymbol{\mu}^T \dfrac{\mathrm{d}^2 \bar{\mathbf{h}}(\mathbf{s})}{\mathrm{d}\mathbf{s}\,\mathrm{d}\mathbf{s}^T} & -\dfrac{\mathrm{d}\bar{\mathbf{h}}(\mathbf{s})}{\mathrm{d}\mathbf{s}} \\[4mm] -\dfrac{\mathrm{d}\bar{\mathbf{h}}(\mathbf{s})}{\mathrm{d}\mathbf{s}} & \mathbf{0} \end{bmatrix} . \tag{4.11}$$

Regarding the above expression, it is obvious that for the calculation of $\mathrm{d}\mathbf{F}(\mathbf{x})/\mathrm{d}\mathbf{x}$ the first and second gradients $\mathrm{d}\bar{\mathbf{h}}(\mathbf{s})/\mathrm{d}\mathbf{s}$ and $\mathrm{d}^2\bar{\mathbf{h}}(\mathbf{s})/(\mathrm{d}\mathbf{s}\,\mathrm{d}\mathbf{s}^T)$ of the generalized equality conditions $\bar{\mathbf{h}}(\mathbf{s})$ are required. This gradients can be easily calculated, because the equality and inequality conditions in $\bar{\mathbf{h}}(\mathbf{s})$ are mostly given as linear relations. Moreover, for the calculation of $\mathrm{d}\mathbf{F}(\mathbf{x})/\mathrm{d}\mathbf{x}$, the second gradient $\mathrm{d}^2 f(\mathbf{s})/(\mathrm{d}\mathbf{s}\,\mathrm{d}\mathbf{s}^T)$ of the objective function is needed, which is denoted as the *Hessean* Matrix of $f(\mathbf{s})$. The computation of this *Hessean* Matrix will be discussed as follows.

4.2.4   Approximation of the *Hesse*an matrix

The differences between the various gradient-based methods can be found in the various methods for the approximation of the *Hessean* matrix $\mathbf{H}$. This *Hessean* matrix is given by the second gradient of the objective function (4.1):

$$\mathbf{H} := \frac{\mathrm{d}^2 f}{\mathrm{d}\mathbf{s}\,\mathrm{d}\mathbf{s}^T} = 2 \sum_{n=1}^{N} w_n \left[\frac{\mathrm{d}\phi_n(\mathbf{s})}{\mathrm{d}\mathbf{s}} \left(\frac{\mathrm{d}\phi_n(\mathbf{s})}{\mathrm{d}\mathbf{s}}\right)^T + (\phi_n(\mathbf{s}) - \tilde{\phi}_n)^T \frac{\mathrm{d}^2\phi_n(\mathbf{s})}{\mathrm{d}\mathbf{s}\,\mathrm{d}\mathbf{s}^T} \right] . \tag{4.12}$$

The problem in the computation of $\mathbf{H}$ is the appearance of the second derivative of $\phi(\mathbf{s})$ with respect to the material parameters $\mathbf{s}$. The exact computation of this second gradient is very complex and connected with high numerical costs. For this reason, the approximation $\bar{\mathbf{H}}$ of the *Hessean* matrix $\mathbf{H}$ using only the first gradient is a usual method within the gradient-based identification methods. Another advantage of using an approximated *Hessean* matrix is that the approximation can be carried out in such a way that the positive definiteness of the *Hessean* matrix is definitely given, which is not necessarily the case, if the exact *Hessean* matrix is used.

The simplest approximation of the *Hessean* matrix is the usage of the identity for the approximated *Hessean* matrix, i. e., $\bar{\mathbf{H}} = \mathbf{I}$. With a view to the iteration procedure (4.10) it can be seen that, therewith, the search direction is directly assumed in direction of the steepest decrease. A better approximation of the *Hessean* can be obtained by a closer look on (4.12). Thus, it is obvious that the second derivative of $\phi(\mathbf{s})$ is weighted with the error between the measured values $\tilde{\phi}$, which represent the exact solution of the inverse problem, and the approximated values $\phi(s)$. Following this, the influence of this second gradient decreases the more than $\mathbf{s}$ approximates the real solution. Therewith, a proper

approximation $\bar{\mathbf{H}}$ of the exact *Hessean* matrix $\mathbf{H}$ around the solution is given by the so-called *Gauß-Newton* matrix

$$\mathbf{H}_{GN} = 2 \sum_{n=1}^{N} w_n \frac{\mathrm{d}\phi_n(\mathbf{s})}{\mathrm{d}\mathbf{s}} \left(\frac{\mathrm{d}\phi_n(\mathbf{s})}{\mathrm{d}\mathbf{s}}\right)^T . \tag{4.13}$$

Although, therewith a suitable approximation of the *Hessean* matrix is given, the disadvantage of using this approximation is the possible appearance of nearly zero values of the diagonal elements. This problem can be avoided by the addition of small values μ on the diagonal elements, which yields the *Levenberg-Marquardt* method.

Another very popular way, and probably the most effective method for the approximation of $\mathbf{H}$ is the *BFGS* method, which is applied in the frame of this work. Within this method, the *Hessean* matrix is approximated on the basis of the following iterative procedure:

$$\mathbf{H}_{BFGS} = \bar{\mathbf{H}}_i = \bar{\mathbf{H}}_{i-1} - \frac{\bar{\mathbf{H}}_{i-1} \Delta\mathbf{s} \Delta\mathbf{s}^T \bar{\mathbf{H}}_{i-1}}{\Delta\mathbf{s}^T \bar{\mathbf{H}}_{i-1} \Delta\mathbf{s}} + \frac{\Delta\mathbf{q} \Delta\mathbf{q}^T}{\Delta\mathbf{q}^T \Delta\mathbf{s}}$$

$$\text{with} \quad \Delta\mathbf{s} = \mathbf{s}_i - \mathbf{s}_{i-1} \quad \text{and} \quad \Delta\mathbf{q} = \frac{\mathrm{d}f(\mathbf{s}_i)}{\mathrm{d}\mathbf{s}} - \frac{\mathrm{d}f(\mathbf{s}_{i-1})}{\mathrm{d}\mathbf{s}} . \tag{4.14}$$

Therein, i indexes the current iteration step of the *Newton*-like procedure, cf. (4.10). Moreover, for the first step, a positive definite start matrix is needed, wherefore, e. g., the *Levenberg-Marquardt* matrix can be used.

An overview about the above mentioned methods for the approximation of the *Hessean* matrix is given in Table 4.1. Therein, it can be seen that the *Levenberg-Marquardt* method can also be interpreted as the result of a combination of the Gradient method (steepest decrease) and the *Gauß-Newton* method.

method	approximation of $\mathbf{H}$
Gradient method	$\bar{\mathbf{H}} = \mathbf{I}$
Gauß-Newton	$\bar{\mathbf{H}} = \mathbf{H}_{GN}$
Levenberg-Marquardt	$\bar{\mathbf{H}} = \mathbf{H}_{GN} + \mu \mathbf{I}$
BFGS	$\bar{\mathbf{H}} = \mathbf{H}_{BFGS}$

Table 4.1: Overview about the most popular gradient-based optimization methods.

4.2.5 Multi-criterion objective function

In many cases of the parameter identification for complex materials, one single type of material test is not sufficient for the identification of all material parameters. In these cases, different tests or different measured quantities of one test have to be considered during the identification procedure, e. g., measurements of the stress and volumetric strain from an triaxial compression test. This inclusion of multiple quantities results in a multi-criterion

minimization problem, cf., e.g., *Rao* [113], which is characterized by k independent objective functions

$$f_k(\mathbf{s}) = \sum_{i=1}^{N_k} w_i^k \, (\phi_i^k(\mathbf{s}) - \tilde{\phi}_i^k)^2 \quad \rightarrow \quad \min, \quad \text{with} \quad k = 1, \ldots, K, \qquad (4.15)$$

where K is the number of the different quantities, which are considered in N_k data points. It is obvious that in this case, generally, no solution vector $\hat{\mathbf{s}}$ exists, which minimizes all objective functions simultaneously. Instead of this, the improvement of one objective function is connected with the degradation of the others. Thus, to obtain a solution, one has to combine the different objective functions to a single one:

$$f(\mathbf{s}) = \sum_{k=1}^{K} W_k \, f_k(\mathbf{s}) \,. \qquad (4.16)$$

Therein, W_k are weighting factors, which are necessary for the normalization of the different quantities of the single objective functions $f_k(\mathbf{s})$. Furthermore, with these weighting factors, the relevance of the single criterions can be balanced. Thus, the weighting factors can be written in the form

$$W_k = \frac{1}{(\phi_0^k)^2 \, N_k} \,, \qquad (4.17)$$

where ϕ_0^k are the reference values for the single quantities, whereas with N_k the possibility is taken into account that the different quantities can be considered on various numbers of data points.

Remark: Principally, with the above given formulations, the multi-criterion objective function can be formally written in the same form as the single-criterion objective function (4.1) using the following settings:

$$f(\mathbf{s}) = \sum_{i=1}^{N_k} \sum_{k=1}^{K} W_k \, w_i^k \, (\phi_i^k(\mathbf{s}) - \tilde{\phi}_i^k)^2 = \sum_{j=1}^{M} \bar{w}_j \, (\phi_j(\mathbf{s}) - \tilde{\phi}_j)^2$$

$$\text{with} \quad M = \sum_{k=1}^{K} N_k \quad \text{and} \quad \bar{w}_j = w_i^k \, W_k \,. \tag{4.18}$$

Therewith, all formulations concerning the single objective function are also valid for the multi-criterion objective function.

4.3   Stepwise identification

The constitutive equations of the model, cf. Section 2.4, contain a lot of different material parameters. Theoretically, one can try to identify all these material parameters together by use of one multi-criterion objective function combining all required material tests. As

a consequence, the objective function depends on a high dimensional parameter space containing, potentially, a lot of local minima.

For this reason, the identification of the parameters is carried out by a stepwise procedure, whereby, for each step a separate objective function is defined based on relevant material tests. Thus, the overall identification process is separated into two major steps, where the first step, concerning the non-polar part of the overall material model, is subdivided into an elastic part 1(a) and a plastic part 1(b):

1(a). Identification of the material parameters $\mathbf{p}_{el}$, cf. (2.70) and (2.73) in Section 2.4.3, concerning the non-polar elasticity,

$$\mathbf{p}_{el} = (\mu,\ \lambda,\ n_{\max}^S)^T\,, \tag{4.19}$$

Note that the initial solid volume fraction n_0^S is measured at the beginning of the test and, consequently, it has not to be taken into account in the identification process. For the determination of these parameters, unloading-loading cycles of triaxial compression tests in combination with hydrostatic triaxial tests are used, cf. Appendix A.1.

1(b). Identification of the parameters $\mathbf{p}_{pl}$ controlling the non-polar plastic behavior. These parameters can be divided into three groups: Firstly, the parameters $\mathbf{p}_{dev}$ governing the deviatoric plane of the yield condition, secondly, the parameters $\mathbf{p}_{hyd}$ controlling the hydrostatic plane of the yield condition and, finally, the additional parameters $\mathbf{p}_{yield}$ of the plastic potential, cf. (2.76) and (2.78) in Section 2.4.4:

$$\mathbf{p}_{pl} = (\mathbf{p}_{dev}^T,\ \mathbf{p}_{hyd}^T,\ \mathbf{p}_{yield}^T)^T \quad \text{with}$$

$$
\begin{aligned}
\mathbf{p}_{dev} &= (m,\ \gamma_0,\ \overset{\star}{\gamma},\ C_\gamma^V,\ C_\gamma^D)^T\,, \\
\mathbf{p}_{hyd} &= (\epsilon_0,\ \overset{\star}{\epsilon},\ C_\epsilon^V,\ C_\epsilon^D,\ \delta_0,\ \overset{\star}{\delta},\ C_\delta^V,\ C_\delta^D,\ \beta_0,\ \overset{\star}{\beta},\ C_\beta^V,\ C_\beta^D)^T\,, \\
\mathbf{p}_{yield} &= (\psi_1,\ \psi_2)^T\,.
\end{aligned}
\tag{4.20}
$$

The determination of all these parameters is realized on the basis of homogeneous triaxial compression tests with different confining pressures combined with a hydrostatic triaxial test as well as the homogeneous part of a biaxial test.

2. Identification of the additional parameters $\mathbf{s}_{\mathrm{Co}}$, cf. (2.70), (2.73) and (2.76), of the micropolar *Cosserat* theory,

$$\mathbf{s}_{\mathrm{Co}} = (l_c,\ \mu_c,\ k_\mu,\ k_\sigma)^T\,. \tag{4.21}$$

Therefore, biaxial tests with shear banding are used, cf. Appendix A.2.

The complete identification process is carried out step by step, i. e., firstly, the parameters of the first group are determined, then, secondly, the parameters of the second group are determined, whereby the parameters of the first group are assumed as given. Finally, basing on the known parameters of the first two groups, the parameters of the third

group can be determined. For an overview, the required material test and the obtained kind of experimental data are summarized in Table 4.2.

The above order also shows the range of complexity of the single steps. Thus, the determination of the three non-polar elastic parameters is easier than the determination of the parameters of the non-polar plasticity, and at last, the identification of the additional micropolar parameters is the most complex part. This part requires the simulation of the inhomogeneous biaxial test, with shear banding, by use of the FEM with an adequate mesh. Furthermore, for this step, the consideration of the thickness of the shear band is necessary, wherefore, a new method has been developed.

step	parameter group	required material tests	used kind of data
1(a)	homogeneous elasticity $\mathbf{p}_{el}$	unloading-loading cycles of triaxial compression and hydrostatic tests	- axial stress-strain data - volumetric strain versus axial strain
1(b)	homogeneous plasticity $\mathbf{p}_{pl}$	triaxial compression, extension and hydrostatic tests and homogeneous biaxial tests	- axial stress-strain data - volumetric strain versus axial strain
2	micropolar properties $\mathbf{p}_{mp}$	inhomogeneous biaxial tests with shear banding	- axial stress-strain data - stereophotogrammetric strain measures

Table 4.2: Required material tests for the complete identification of all material parameters.

4.4   Thickness and orientation of the shear band

Granular materials always include micropolar effects due to the grain rotations. The principal reason for the consideration of these effects by application of the *Cosserat* theory is the thus obtained regularization of the ill-posed localization problem. This regularization effect of the *Cosserat* theory is especially seen in the finite thickness of the shear band during the numerical simulation of the biaxial test, cf., e.g., Figure 4.1 (b) or *Mühlhaus & Vardoulakis* [104], and can also be observed during material tests, cf. *Mokni & Desrues* [101]. Thus, the measurable thickness of the shear band is an essential effect resulting from the usage of the micropolar theory. Following this, it is obvious to use the shear band thickness directly for the identification of the additional micropolar material parameters.

For this purpose, first of all, a clear definition of the shear band thickness is required. Studying the literature, one can find a high number of papers dealing with localization effects caused by shear banding, but only a very spare selection of them give a clear definition of the shear band thickness. One of them is the paper of *Gudehus & Nübel* [68], wherein the thickness of the shear band is defined based on mean values of the shear rate or

the couple stress, respectively, which in each case yields different values for the shear band thickness. In other papers, the measured shear band thickness is determined by measuring the visibly observable shear zone, cf. *Huang* et al. [78]. These methods are not suitable in the context of the parameter identification, because, therefore, a distinct method, which yields unique values is required. Additionally, the definition has to be applicable for the computed as well as for measured data in the same manner, and, furthermore, all steps must be differentiable in consequence of the usage of the semi-analytical sensitivity analysis.

Other papers dealing with parameter identification based on inhomogeneous tests, mostly use a direct comparison of the measured and computed data at discrete spatial points, cf., e. g., *Hartmann* et al. [72], *Rieger* [114] or *Scheday* [117]. The advantages of this direct approach, within the identification problem considered here, would be, firstly, that no explicit definition of a shear band thickness is required due to the fit of the whole strain field and, secondly, the differentiability of the resulting objective function would be directly given. However, the problem of using this direct method, in context of the identification of the additional parameters of the micropolar theory, is that the influence of the direction and the thickness of the shear band cannot be considered separately in the identification process. This is a very important fact, because the effects, which are causal for the direction and for the thickness of the shear band are totally different. Hence, a new method for the consideration of the shear band thickness is developed in this work. Thereby, the thickness and direction of the shear band are identified independently basing on the measured as well as the calculated data in the same manner. Consequently, the shear band thickness can be separately considered in the identification process. The requirements on the new method can be summarized as follows:

1. The resulting value of the thickness of the shear band must be an independent value indicating the effect of the regularization.

2. For a set-up of an objective function, the values must be clearly calculably defined.

3. The method must be applicable in the same manner for the computed and measured results.

4. The method must be completely differentiable in order to use the semi-analytical sensitivity analysis.

Generally, the incoming of a shear band in granular media is the result of a material instability caused by softening behavior in consequence of an increasing of pore volume due to the dilatant plastic flow, which is considered in this work by the evolution law of the yield condition, cf. Section 2.4.5. This process yields the localization of the plastic strain in a narrow band. Following this, the shear band thickness should be defined by use of the plastic strain. However, the problem using the plastic part of the total strain is the measurement of this quantity. Whereas, in the homogeneous case, the plastic part of the deformation can be detected by a complete unloading of the specimen, in the inhomogeneous case the measuring of the pure plastic part of the strain is generally impossible. For this reason, the complete strain $\bar{\varepsilon}$ is taken into account for the definition

of the shear zone, which can be directly computed from the measured displacements in various spatial points. Considering granular materials, the elastic part of the total strain is, in comparison with the plastic part, very small. As a consequence, there is, in practice, nearly no difference in the determined shear band properties based on the whole strain instead on the plastic part only.
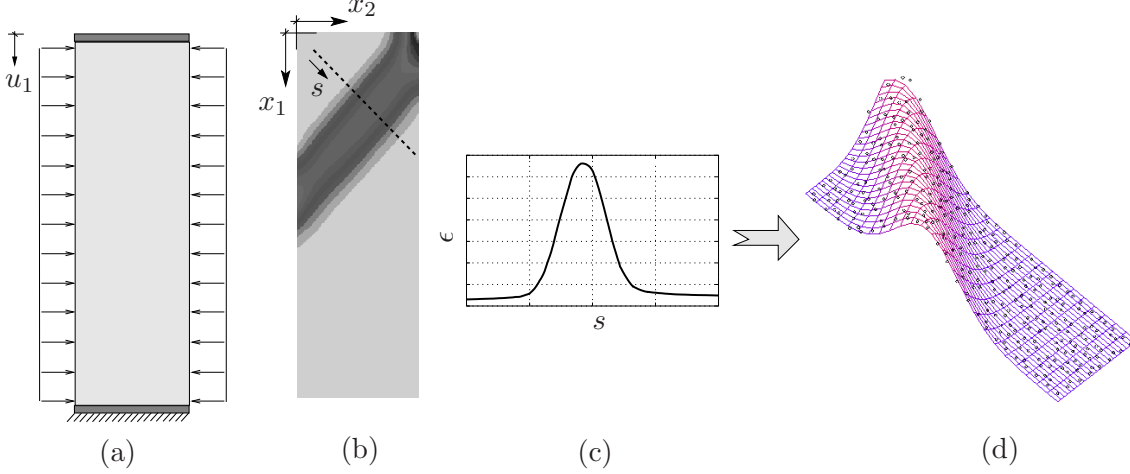

Figure 4.1: Determination of the thickness and direction of the shear band: (a) setup of the biaxial test, (b) computed norm of the total strain, (c) cut of this data, (d) approximation with a bell-shaped curve.

The procedure for the determination of the thickness and the direction of the shear band is displayed in Figure 4.1 by means of the numerical remodeling of the biaxial test. Therein, the underlying boundary-value problem of the biaxial test is shown in Figure 4.1 (a), cf. Appendix A.2. After overstepping a critical load level, a shear band occurs as the result of strain localization, cf. Figure 4.1 (b), wherein the norm of the strain $\|\bar{\varepsilon}_S\|$ is shown. Now, by a cut through this data, cf. Figure 4.1 (c), it can be realized that the obtained curve looks like a bell-shaped curve. This observation motivates the approximation, realized by the function ϵ, of the norm of strain $\|\bar{\varepsilon}\|$ with a bell-shaped curve moving along the axis of the shear band, thus yielding a bell-shaped surface, cf. Figure 4.1 (d):

$$\epsilon(x_1,\, x_2,\, \mathbf{r}) = \epsilon_0 + A \, \exp\left\{-\frac{1}{2\,H^2}\left[(x_1 - x_{10})\,\cos(\alpha_S) - x_2\,\sin(\alpha_S)\right]^2\right\},$$
$$(4.22)$$

with $\mathbf{r} = (h_0,\, A,\, H,\, x_{10},\, \alpha_S)^T$.

Therein, the approximated strain ϵ depends, on the one hand, on the spatial coordinates x_1 and x_2 and, on the other hand, on the parameter vector $\mathbf{r}$, whose components are described in Table 4.3. Thus, the parameters included in $\mathbf{r}$ can be used for the fit of the function $\epsilon(\mathbf{r})$ to the calculated or measured norm of strain $\|\bar{\varepsilon}\|$. The application of the least-squares method on this task leads to the following objective function,

$$f(\mathbf{r}) = \sum_{i=0}^{M} \left(\epsilon(x_{1\,i},\, x_{2\,i},\, \mathbf{r}) - \|\bar{\varepsilon}_i\|\right)^2,$$
$$(4.23)$$
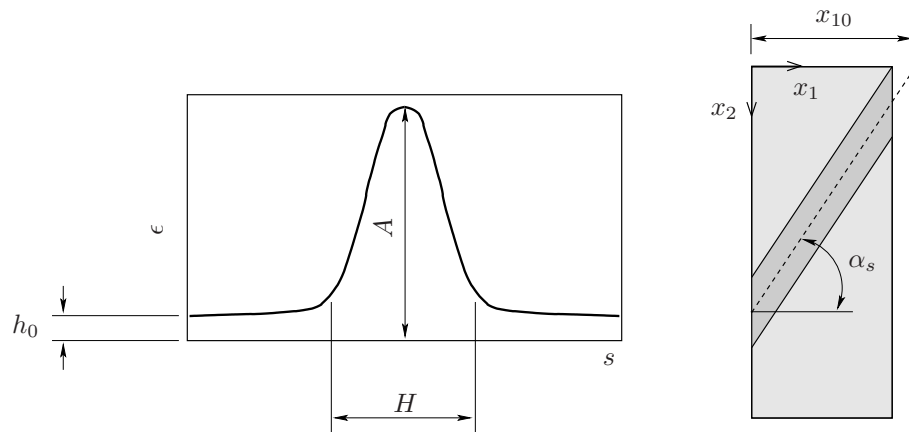
parameter	meaning
h_0	overall strain
A	peak value of the strain
H	standard deviation of the corresponding bell-shaped curve as a quantity for the shear band thickness
x_{10}	x_1 start coordinate of the bell-shaped curve
α_S	angle of the shear band

Table 4.3: Description of the parameters using for the fit of the approximated strain ϵ, cf. (4.22).

which has to be minimized. Therein, M is the number of measurement points or the number of integration points of computed data, respectively. The resulting unconstrained optimization problem, $f(\mathbf{r}) \to \min$, yields the nonlinear system of equations

$$\mathbf{h}(\mathbf{r}) = \frac{\mathrm{d}f}{\mathrm{d}\mathbf{r}} = 2 \sum_{i=1}^{N} (\epsilon_i(\mathbf{r}) - \|\bar{\boldsymbol{\varepsilon}}_i\|) \frac{\mathrm{d}\epsilon_i}{\mathrm{d}\mathbf{r}} = \mathbf{0} \,, \tag{4.24}$$

where $\epsilon_i(\mathbf{r})$ stands for $\epsilon(x_{1i}, x_{2i}, \mathbf{r})$. The solution of the above nonlinear system of equations for $\mathbf{r}$ is carried out by the *Newton*'s method, whereby the *Jacobi* matrix

$$\frac{\mathrm{d}\mathbf{h}}{\mathrm{d}\mathbf{r}} = 2 \sum_{i=1}^{N} \left[\frac{\mathrm{d}\epsilon_i}{\mathrm{d}\mathbf{r}} \left(\frac{\mathrm{d}\epsilon_i}{\mathrm{d}\mathbf{r}} \right)^T + (\epsilon_i(\mathbf{r}) - \|\bar{\boldsymbol{\varepsilon}}_i\|) \frac{\mathrm{d}^2\epsilon_i}{\mathrm{d}\mathbf{r}\,\mathrm{d}\mathbf{r}^T} \right] \,, \tag{4.25}$$

can be calculated analytically.

With this method, it is possible to determine the thickness[1] H and the direction of the shear band α_S independently for both, the computed and the measured data. Furthermore, it is possible to compute the derivatives of the fitted parameters included in $\mathbf{r}$ with respect to the material parameters $\mathbf{s}$, which are necessary for the calculation of the sensitivities, cf. Section 5.3.

---

[1]Principally, H is the standard deviation in the function (4.3), but, to simplify matters, H is denoted in the following as shear band thickness.

4.5 Error analysis

After the minimum of the objective function has been found, one has to evaluate the accuracy of the detected material parameters. This is the purpose of the error analysis, whereby the measured data are considered as a stochastic data series including statistical errors. Thus, the error analysis leads to the nonlinear regression, which is well described in the textbooks of, e.g., *Larsen & Marx* [88], *Bates & Watts* [4] or *Weisberg* [137]. Applications to the parameter identification are given in, e.g., *Beck & Arnold* [7], *Eykhoff* [61] or *Finsterle* [62].

Generally, the reliability of the identified material parameters bases on the quality of the measurements. Thus, in the first step of the error analysis, the accuracy of the measurements are evaluated, which requires a set of at least three independent material tests. Therewith, in the next step, the so-called residual analysis, the quality of the fit in relation to the quality of the measurement, denoted as *goodness-of-fit*, is checked. Finally, the uncertainty and the correlation of the determined material parameters are verified.

4.5.1 Calculation of the uncertainty of the measured data

The measured data are the basis for the parameter identification and, therewith, the quality of the measured data has a direct influence on the accuracy of the identified material parameters. The quality or uncertainty of the measured data can be expressed with the standard deviation in using M $(M \geq 3)$ independent sets of measured data. Hence, the standard deviation σ_n of the measured data can be computed for every measured point n with the mean value $\bar{\bar{\phi}}_n$ via:

$$\sigma_n = \sqrt{\frac{1}{M-1} \sum_{i=1}^{M} (\tilde{\phi}_{ni} - \bar{\bar{\phi}}_n)^2} \quad \text{with} \quad \bar{\bar{\phi}}_n = \frac{1}{M} \sum_{i=1}^{M} \tilde{\phi}_{ni} \,. \tag{4.26}$$

4.5.2 Residual analysis

Within the residual analysis, the so-called *goodness-of-fit*, i.e., the error between the measured and calculated data is tested, cf. *Larsen & Marx* [88]. The simplest way to check the quality of the fit is the visual control of the data, which will be in many cases sufficient. If a more detailed quantification of the results is necessary, particularly, with regard to further computations of the uncertainty of the identified parameters, the residual analysis is used. Therefore, the calculation of the error of the objective function in relation to the uncertainty or standard deviation σ_n of the measured data, which is also denoted as the *posteriori error variance*, is expressed via

$$s_0^2 = \frac{1}{N-P} \sum_{n=1}^{N} \frac{1}{\sigma_n^2} \left(\phi_n(\mathbf{s}) - \tilde{\phi}_n \right)^2 , \tag{4.27}$$

where N is the number of data points, and P is the number of material parameters in the parameter vector $\mathbf{s}$. Note that the value of s_0^2 corresponds, approximately, to the mean

value of the objective function (4.1), if the reciprocal $1/\sigma_n^2$ of the measurement errors are used as weighting factors and, moreover, $N \gg P$ is given. Based on the obtained value of s_0, the quality of the fit can be verified. Namely, a value of s_0 smaller than 1 denotes that the error of the fit is less than the uncertainty of the measured data. Otherwise, a large value of s_0 means that the model does not match the measured data well, and, thus, the estimated parameters are meaningless. However, a good match, i. e., a small value of s_0, does not guarantee that the inverse problem is solved in a reasonable way. Therefore, further considerations, namely, uncertainty analysis and the correlation analysis, are necessary.

Note that in case of very small measurement errors, σ_n, a large value of s_0, does not automatically denote that the obtained fit is bad and the parameters are meaningless. For such cases, larger errors of the fit than the measurement errors, i. e., $(\phi_{(\mathbf{s})} - \tilde{\phi}_n)^2 > \sigma_n^2$, are inevitable. Thus, additionally to the calculation of s_0, the visual control for the verification of the quality of the fit is indispensable. Anyhow, in case of a large value of s_0, the uncertainty of the determined parameters can be reduced by reaching a better fit, whereas, in case of a small value for s_0, a better fit does not lead to a smaller uncertainty, because, in this case, the influence of the measurement errors will dominate.

4.5.3 Uncertainty analysis

Due to the fact that the measured data $\tilde{\phi}_n$ contain a random component expressed by σ_n (4.26), the parameter vector $\hat{\mathbf{s}}$ resulting from the identification process represents only the most likely point of a probability distribution of all possible parameter sets. Following this, in addition to the mean values given by the identified parameters, the standard deviations σ_{pi} or variance of every material parameter s_i can be determined via the covariance matrix:

$$\mathbf{K} = s_0^2 \left(\sum_{n=1}^{N} \frac{1}{\sigma_n^2} \frac{\mathrm{d}\phi_n}{\mathrm{d}\mathbf{s}} (\frac{\mathrm{d}\phi_n}{\mathrm{d}\mathbf{s}})^T \right)^{-1} . \tag{4.28}$$

The computation of this matrix requires the standard deviation of the measured data σ_n (4.26), the value s_0 obtained by the residual analysis (4.27) as well as the sensitivities of the computed data ϕ_n with respect to the material parameters, cf. Chapter 5. The requested standard deviation of the estimated parameters $\hat{\mathbf{s}}$ are given by the square root of the diagonal elements of $\mathbf{K}$:

$$\sigma_{pi} = \sqrt{k_{(ii)}} . \tag{4.29}$$

With this standard deviations σ_{pi}, the certainty of the determined parameters is given. Hence, a small value of the relation σ_{pi}/s_i indicates that the parameter s_i has been determined with full meaning. Otherwise, if the relation σ_{pi}/s_i is in the range of 1, the determined parameter s_i will be meaningless. Regarding (4.28), it is obvious that the components of $\mathbf{K}$ and, therewith, σ_{pi} is reciprocally proportional to the sensitivities $\mathrm{d}\phi_n/\mathrm{d}\mathbf{s}$. This denotes that the certainty of one material parameter s_i additionally depends to the quality of the measured data and to the *goodness-of-fit*, also on the sensitivity of the measured data with respect to the material parameter s_i.

A further unique method for the evaluation of data uncertainties in the framework of the statistics is the definition of confidence regions. In application of the parameter identification, this indicates the region in which the value of the parameter can be found with the probability $1-\alpha$. Basing on the computed standard deviation σ_{pi}, (4.29), the confidence region is defined as

$$(\hat{p}_i - l_{1-\alpha}\,\sigma_{pi}) \leq p_i < (\hat{p}_i + l_{1-\alpha}\,\sigma_{pi}), \quad \text{where} \quad l_{1-\alpha} = \sqrt{P\,F_{P,N-P,1-\alpha}}\,. \tag{4.30}$$

Therein, $\hat{p}_i$ is the result of the identification process, N is the number of data points, P is the number of material parameters and $F_{P,N-P,1-\alpha}$ is the $1-\alpha$ quantile of the F-distribution with the two degrees of freedom, P and $N-P$. For further details, the interested reader is referred to the textbooks by *Larsen & Marx* [88] as well as *Weisberg* [137].

4.5.4   Correlation analysis

The off-diagonal elements of **K** (k_{ij} with $i \neq j$) contain the covariances, which are the result of conjoint effects of changes of the parameters i and j on the observed quantities $\tilde{\phi}_n$ in the material tests. The normalized covariances are given by the correlation coefficient

$$r_{ij} = \frac{k_{ij}}{\sqrt{k_{(ii)}\,k_{(jj)}}}\,. \tag{4.31}$$

Naturally, these coefficients are in the range between -1 and 1, whereby a value of zero indicates no statistical correlation between parameter i and j, whereas, a value close to -1 or 1 indicates a strong correlation. In this case, the two parameters are correlated and, following this, they cannot be determined independently basing on the actual given test data.

Remark: The calculation of uncertainties and correlations of the estimated material parameters is as important as the computation of the value of the material parameters itself. Because, if the variance of one parameter is very large, i. e., the ratio $|\,p_i/\sigma_{pi}\,|$ gives a value close to 1, then the variance of the parameters is in the same range like the value of the parameter itself, and, therewith, the value of the estimated parameter is meaningless. If, in such a case, the quality of the measurements σ_n is in a tolerable range and, furthermore, the fit is sufficient ($s_0 \approx 1$), the reason can be found in small sensitivities of the observed data ϕ_n with respect to the material parameter p_i. This denotes that the parameter cannot be identified with the chosen material tests. This is also the case if the correlation between two parameters is near -1 or 1, which implies that only one of the two parameters can be identified with the chosen set of material tests. In both cases, other tests are necessary for the identification of these parameters or, if this is not possible, the constitutive model has to be modified.

Chapter 5: Sensitivity Analysis

The aim of the sensitivity analysis is the determination of the gradient of the objective function $f(\mathbf{s})$, cf. (4.1), with respect to the material parameters summarized in the parameters vector $\mathbf{s}$:

$$\frac{\mathrm{d}f(\mathbf{s})}{\mathrm{d}\mathbf{s}} = 2 \sum_{n=1}^{N} w_n \frac{\mathrm{d}\phi_n(\mathbf{s})}{\mathrm{d}\mathbf{s}} \left(\phi_n(\mathbf{s}) - \tilde{\phi} \right). \tag{5.1}$$

For this purpose, the gradient $\mathrm{d}\phi_n(\mathbf{s})/\mathrm{d}\mathbf{s}$ of the numerically calculated values $\phi_n(\mathbf{s})$ with respect to the material parameters $\mathbf{s}$ is required. This gradient is denoted as the sensitivity vector, whereas its components $\mathrm{d}\phi_n(\mathbf{s})/\mathrm{d}s_k$ are the single sensitivities of $\phi_n(\mathbf{s})$, which contain information about the change of the numerical result with respect to the variation of the material parameters.

The primal application of the sensitivity analysis in this work, is the computation of the *Hessean* matrix of the objective function $f(\mathbf{s})$ for the *Newton* like methods, which are applied for the identification of the material parameters, cf. Section 4.2.4. Thus, the effectivity of the parameter identification process is strongly coupled with the effectivity of the sensitivity analysis. A further application is given in context with the error analysis, cf. Section 4.2.4, wherein the sensitivities are required for the evaluation of the uncertainty of the determined material parameters.

Generally, the methods used for the computation of the sensitivities of a numerically calculated result $\phi(\mathbf{s})$, e.g., by use of the FEM, can be classified in the numerical and in the semi-analytical methods. Whereby the numerical methods only consist in the computation of the discrete difference quotient, the semi-analytical methods represent the exact derivative of the numerically obtained result with respect to material parameters $\mathbf{s}$. In consequence of the high numerical effort of the numerical sensitivity analysis, an effective usage of the gradient-based parameter identification methods is only realizable in combination with the semi-analytical sensitivity analysis. Thus, in the present contribution, the numerical calculation of the sensitivities is entirely necessary for the verification of the semi-analytically calculated values.

The development of this semi-analytical methods in the framework of the FEM started in the middle of the 1980's with papers of *Adelmann & Haftka* [1] as well as *Vidal & Haber* [134]. Further applications in context with the parameter identification are demonstrated, e.g., in the works by *Finsterle* [62], *Mahnken & Stein* [96] or *Mahnken* [95]. Furthermore, a general overview about the several methods are given in the book by *Kleiber* [83] or in context with the structural optimization problems in works by *Barthold* [3] or *Schwarz* [122].

Firstly, in this chapter, the procedure of the numerical sensitivity analysis is shortly demonstrated, cf. Section 5.1. Afterwards, the several steps of the semi-analytical sensitivity analysis are particularly described, cf. Section 5.2. Due to the fact that the shear band thickness is required during the identification process, finally, the computation of the sensitivities of the shear band properties is discussed, cf. Section 5.3.

5.1 Numerical sensitivity analysis

The numerically computation of the sensitivities requires the numerical evaluation of the difference quotient $\mathrm{d}\phi/\mathrm{d}\mathbf{s}$. This is realized by the calculation of function values of $\phi(\mathbf{s})$ in a small neighborhood $\Delta\mathbf{s}$ of the observed solution $\hat{\mathbf{s}}$. The common methods, therefore, are the forward, the backward as well as the central difference methods, which all can be derived from a forward or backward *Taylor* series, respectively:

$$\phi(\hat{\mathbf{s}} + \Delta\mathbf{s}) = \phi(\hat{\mathbf{s}}) + \left.\frac{\mathrm{d}\phi}{\mathrm{d}\mathbf{s}}\right|_{\hat{s}} \Delta\mathbf{s} + \frac{1}{2}\left.\frac{\mathrm{d}^2\phi}{\mathrm{d}\mathbf{s}^2}\right|_{\hat{s}} (\Delta\mathbf{s})^2 + \dots \quad \text{or}$$

$$\phi(\hat{\mathbf{s}} - \Delta\mathbf{s}) = \phi(\hat{\mathbf{s}}) - \left.\frac{\mathrm{d}\phi}{\mathrm{d}\mathbf{s}}\right|_{\hat{s}} \Delta\mathbf{s} + \frac{1}{2}\left.\frac{\mathrm{d}^2\phi}{\mathrm{d}\mathbf{s}^2}\right|_{\hat{s}} (\Delta\mathbf{s})^2 - \dots \; . \tag{5.2}$$

Truncating the first equation $(5.2)_1$ after the linear term, one obtains the forward difference method. Thus, the i-th component of the sensitivity vector $\mathrm{d}\phi/\mathrm{d}\mathbf{s}$ is given by

$$\left.\frac{\mathrm{d}\phi(\mathbf{s})}{\mathrm{d}s_i}\right|_{\hat{s}_i} \approx \frac{\phi(\hat{s}_i + \Delta s_i) - \phi(\hat{s}_i)}{\Delta s_i} \; . \tag{5.3}$$

Similarly, truncating the second equation $(5.2)_2$ after the linear term leads to the backward difference method:

$$\left.\frac{\mathrm{d}\phi(\mathbf{s})}{\mathrm{d}s_i}\right|_{\hat{s}_i} \approx \frac{\phi(\hat{s}_i) - \phi(\hat{s}_i - \Delta s_i)}{\Delta s_i} \; . \tag{5.4}$$

The central difference method is obtained by the subtraction of $(5.2)_2$ from $(5.2)_1$ by neglecting terms of third and higher order:

$$\left.\frac{\mathrm{d}\phi(\mathbf{s})}{\mathrm{d}s_i}\right|_{\hat{s}_i} \approx \frac{\phi(\hat{s}_i + \Delta s_i) - \phi(\hat{s}_i - \Delta s_i)}{2\,\Delta s_i} \; . \tag{5.5}$$

Hence, it is obvious, that the central difference method is exactly of second order, whereas the forward as well as the backward difference method are only first order exact. But it is also obvious that for the central difference method two additional computations of the variable $\phi(\mathbf{s})$ are required, which denotes that the numerical effort is twice as by using the forward or backward difference method.

One problem in the realization of the numerical sensitivity analysis lies in the choice of the increment Δs_i. Hence, if Δs_i is too small, rounding errors in consequence of the machine accuracy occur (round-off-errors). Otherwise, if Δs_i is too large, the error due to the neglecting higher order terms in the *Taylor* series increases (truncation errors). For this reason, *Gill* et al. [65] advise a method for the computation of an optimal increment, however, therewith, the numerical cost increases. Anyhow, with a reasonable choice of increments Δs_i, the numerical sensitivity analysis yields suitable results, for the most cases. Furthermore, the equations (5.3) – (5.5) show that the numerical sensitivities can be computed only by the use of discrete function values of $\phi(\mathbf{s})$. Therewith, the implementation of such methods is very simple, because no modification of the FEM program code is needed.

The substantial disadvantage of the numerical sensitivity analysis is its high numerical cost, because even in using single order accurate methods for every material parameter, an additional computation of $\phi(\mathbf{s})$ is necessary. Thus, for an effective application of the gradient-based methods, the semi-analytical sensitivity analysis is indispensable.

5.2 Semi-analytical sensitivity analysis

The semi-analytical sensitivity analysis denotes the exact computation of the derivative of the numerical solution $\phi_n(\mathbf{s})$ with respect to the material parameters $\mathbf{s}$. This computation is accomplished by the implicit differentiation of the weak formulations of the balance of momentum $\mathcal{G}_M$, cf. (3.4), and the balance of moment of momentum $\mathcal{G}_{MoM}$, cf. (3.5), with respect to the material parameters $\mathbf{s}$. Therefore, first of all, the two balances are added to the generalized weak form,

$$\mathcal{G} = \mathcal{G}_M + \mathcal{G}_{MoM}. \tag{5.6}$$

Hence, the weak form $\mathcal{G}$ depends primarily on the stress $\boldsymbol{\sigma}$ and the couple stress $\boldsymbol{\mu}$, cf. (3.4) and (3.5), i.e., on the generalized stress $\boldsymbol{\Sigma}$, cf. $(3.33)_2$. Further on, $\boldsymbol{\Sigma}$ depends, on the one hand, directly on the material parameters $\mathbf{s}$, and, on the other hand, on the generalized strain $\boldsymbol{\mathcal{E}}$, cf. $(3.33)_1$, which itself depends on the material parameters $\mathbf{s}$. Thus, the following dependencies are given:

$$\mathcal{G} = \mathcal{G}(\boldsymbol{\Sigma}(\mathbf{s}, \boldsymbol{\mathcal{E}}(\mathbf{s}))) \equiv 0. \tag{5.7}$$

In the above equation, $\mathcal{G}$ has to be zero for all modifications of the material parameters. Therewith, the implicit derivative of $\mathcal{G}$ with respect to $\mathbf{s}$ reads

$$\frac{\mathrm{d}\mathcal{G}}{\mathrm{d}\mathbf{s}} = \frac{\partial\mathcal{G}}{\partial\boldsymbol{\Sigma}}\left(\frac{\partial\boldsymbol{\Sigma}}{\partial\mathbf{s}} + \frac{\partial\boldsymbol{\Sigma}}{\partial\boldsymbol{\mathcal{E}}}\frac{\mathrm{d}\boldsymbol{\mathcal{E}}}{\mathrm{d}\mathbf{s}}\right) \overset{!}{=} \mathbf{0}. \tag{5.8}$$

which can also be written in detail, by use of s_k as the k-th component of the set $\mathbf{s}$:

$$\frac{\mathrm{d}\mathcal{G}}{\mathrm{d}s_k} = \int\limits_\Omega \frac{\partial\boldsymbol{\sigma}}{\partial s_k}\cdot\operatorname{Grad}\delta\mathbf{u}\,\mathrm{d}v + \int\limits_\Omega\left(\frac{\partial\boldsymbol{\sigma}}{\partial\bar{\varepsilon}}\frac{\mathrm{d}\bar{\varepsilon}}{\mathrm{d}s_k} + \frac{\partial\boldsymbol{\sigma}}{\partial\bar{\boldsymbol{\kappa}}}\frac{\mathrm{d}\bar{\boldsymbol{\kappa}}}{\mathrm{d}s_k}\right)\cdot\operatorname{Grad}\delta\mathbf{u}\,\mathrm{d}v +$$

$$+ \int\limits_\Omega \frac{\partial\boldsymbol{\mu}}{\partial s_k}\cdot\operatorname{Grad}\delta\bar{\boldsymbol{\varphi}}\,\mathrm{d}v - \int\limits_\Omega(\mathbf{I}\times\frac{\partial\boldsymbol{\sigma}}{\partial s_k})\cdot\delta\bar{\boldsymbol{\varphi}}\,\mathrm{d}v +$$

$$+ \int\limits_\Omega\left(\frac{\partial\boldsymbol{\mu}}{\partial\bar{\varepsilon}}\frac{\mathrm{d}\bar{\varepsilon}}{\mathrm{d}s_k} + \frac{\partial\boldsymbol{\mu}}{\partial\bar{\boldsymbol{\kappa}}}\frac{\mathrm{d}\bar{\boldsymbol{\kappa}}}{\mathrm{d}s_k}\right)\cdot\operatorname{Grad}\delta\bar{\boldsymbol{\varphi}}\,\mathrm{d}v - \int\limits_\Omega\left[\mathbf{I}\times(\frac{\partial\boldsymbol{\sigma}}{\partial\bar{\varepsilon}}\frac{\mathrm{d}\bar{\varepsilon}}{\mathrm{d}s_k} + \frac{\partial\boldsymbol{\sigma}}{\partial\bar{\boldsymbol{\kappa}}}\frac{\mathrm{d}\bar{\boldsymbol{\kappa}}}{\mathrm{d}s_k})\right]\cdot\delta\bar{\boldsymbol{\varphi}}\,\mathrm{d}v \overset{!}{=} 0. \tag{5.9}$$

5.2.1 Sensitivity of the primary variables

The first step of the semi-analytical sensitivity analysis is the computation of the sensitivities of the primary variables. For this reason, firstly, the above derivatives (5.9) are

discretized element-wise by use of the shape functions $\boldsymbol{\phi}$ and $\boldsymbol{\psi}$, cf. Section 3.2, which yields the following formulations:

$$
\begin{aligned}
\frac{\mathrm{d}\mathcal{G}^E}{\mathrm{d}s_k} = &\int_{\Omega_E} \sum_{i=1}^N \frac{\partial\boldsymbol{\sigma}}{\partial s_k} \cdot \operatorname{Grad}\boldsymbol{\phi}^i\,\delta\mathbf{u}_i\,\mathrm{d}v + \int_{\Omega_E} \sum_{i=1}^N \left(\frac{\partial\boldsymbol{\sigma}}{\partial\bar{\boldsymbol{\varepsilon}}}\frac{\mathrm{d}\bar{\boldsymbol{\varepsilon}}}{\mathrm{d}s_k} + \frac{\partial\boldsymbol{\sigma}}{\partial\bar{\boldsymbol{\kappa}}}\frac{\mathrm{d}\bar{\boldsymbol{\kappa}}}{\mathrm{d}s_k}\right) \cdot \operatorname{Grad}\boldsymbol{\phi}^i\,\delta\mathbf{u}_i\,\mathrm{d}v + \\[1em]
&+ \int_{\Omega_E} \sum_{i=1}^M \frac{\partial\boldsymbol{\mu}}{\partial s_k} \cdot \operatorname{Grad}\boldsymbol{\psi}^i\,\delta\bar{\boldsymbol{\varphi}}_i\,\mathrm{d}v - \int_{\Omega_E} \sum_{i=1}^M (\mathbf{I}\times\frac{\partial\boldsymbol{\sigma}}{\partial s_k}) \cdot \boldsymbol{\psi}^i\,\delta\bar{\boldsymbol{\varphi}}_i\,\mathrm{d}v + \\[1em]
&+ \int_{\Omega_E} \sum_{i=1}^M \left(\frac{\partial\boldsymbol{\mu}}{\partial\bar{\boldsymbol{\varepsilon}}}\frac{\mathrm{d}\bar{\boldsymbol{\varepsilon}}}{\mathrm{d}s_k} + \frac{\partial\boldsymbol{\mu}}{\partial\bar{\boldsymbol{\kappa}}}\frac{\mathrm{d}\bar{\boldsymbol{\kappa}}}{\mathrm{d}s_k}\right) \cdot \operatorname{Grad}\boldsymbol{\psi}^i\,\delta_i\bar{\boldsymbol{\varphi}}\,\mathrm{d}v - \\[1em]
&- \int_{\Omega_E} \sum_{i=1}^M \left[\mathbf{I}\times(\frac{\partial\boldsymbol{\sigma}}{\partial\bar{\boldsymbol{\varepsilon}}}\frac{\mathrm{d}\bar{\boldsymbol{\varepsilon}}}{\mathrm{d}s_k} + \frac{\partial\boldsymbol{\sigma}}{\partial\bar{\boldsymbol{\kappa}}}\frac{\mathrm{d}\bar{\boldsymbol{\kappa}}}{\mathrm{d}s_k})\right] \cdot \boldsymbol{\psi}^i\,\delta\bar{\boldsymbol{\varphi}}_i\,\mathrm{d}v \overset{!}{=} 0\,.
\end{aligned}
\tag{5.10}
$$

Therein, N is the number of the nodes used for the approximation of the displacements $\mathbf{u}$ and M is the number of the nodes used for the approximation of the rotations $\bar{\boldsymbol{\varphi}}$, cf. (3.6). Taking into account that the element-wise defined strain $\bar{\boldsymbol{\varepsilon}}$ and the curvature $\bar{\boldsymbol{\kappa}}$ directly depend on the primary variables of the element $\mathbf{y}^E = ((\mathbf{u}^E)^T, (\bar{\boldsymbol{\varphi}}^E)^T)^T$ one obtains

$$
\frac{\mathrm{d}\mathcal{G}^E}{\mathrm{d}\mathbf{s}} = \frac{\partial\mathcal{G}^E}{\partial\mathbf{s}} + \frac{\partial\mathcal{G}^E}{\partial\mathbf{y}^E}\frac{\mathrm{d}\mathbf{y}^E}{\mathrm{d}\mathbf{s}}\,,
\tag{5.11}
$$

Therein, $\partial\mathcal{G}^E/\partial\mathbf{y}^E$ is given via

$$
\frac{\partial\mathcal{G}^E}{\partial\mathbf{y}^E} = \begin{pmatrix} \dfrac{\partial\mathcal{G}^E}{\partial\mathbf{u}^E} \\[1em] \dfrac{\partial\mathcal{G}^E}{\partial\bar{\boldsymbol{\varphi}}^E} \end{pmatrix} = \begin{pmatrix} \dfrac{\partial\mathcal{G}_M^E}{\partial\mathbf{u}^E} + \dfrac{\partial\mathcal{G}_{MoM}^E}{\partial\mathbf{u}^E} \\[1em] \dfrac{\partial\mathcal{G}_M^E}{\partial\bar{\boldsymbol{\varphi}}^E} + \dfrac{\partial\mathcal{G}_{MoM}^E}{\partial\bar{\boldsymbol{\varphi}}^E} \end{pmatrix}\,.
\tag{5.12}
$$

Comparing the above expressions with the derivatives of the weak formulations with respect to the primary variables, cf. (3.19), it can be seen that the derivatives of $\mathcal{G}_M^E$ and $\mathcal{G}_{MoM}^E$ with respect to $\mathbf{u}^E$ and $\boldsymbol{\varphi}^E$ are always used in (3.19). Thus, the spatial and temporal discretization procedure leads to the following system of equations:

$$
\frac{\partial\mathbf{R}_n^E}{\partial\mathbf{y}^E}\frac{\mathrm{d}\mathbf{y}_n^E}{\mathrm{d}\mathbf{s}} - \frac{\partial\mathbf{R}_n^E}{\partial\mathbf{s}} = \mathbf{0}\,,
\tag{5.13}
$$

where $\partial\mathbf{R}_n^E/\partial\mathbf{s}$ is the partial derivative of the residuum vector with respect to the material parameters, which represents the load term in the above system of equations. Hence, this term is defined as the element-wise sensitivity load term:

$$
\mathbf{f}_{sn}^E := \frac{\partial\mathbf{R}_n^E}{\partial\mathbf{s}}\,.
\tag{5.14}
$$

This sensitivity load term results from the partial derivatives of the element-wise discretized weak formulation (5.10) with respect to $\mathbf{s}$, i.e.:

$$
\frac{\partial \mathcal{G}^E_{nM}}{\partial s_k} = \int\limits_{\Omega_E} \sum_{i=1}^N \frac{\partial \boldsymbol{\sigma}_n}{\partial s_k} \cdot \operatorname{Grad} \boldsymbol{\phi}^i \, \delta \mathbf{u}_i \, \mathrm{d}v \,,
$$

$$
\frac{\partial \mathcal{G}^E_{nMoM}}{\partial s_k} = \int\limits_{\Omega_E} \sum_{i=1}^M (\mathbf{I} \times \frac{\partial \boldsymbol{\sigma}_n}{\partial s_k}) \cdot \boldsymbol{\psi}^i \, \delta \bar{\boldsymbol{\varphi}}_i \, \mathrm{d}v + \int\limits_{\Omega_E} \sum_{i=1}^M \frac{\partial \boldsymbol{\mu}_n}{\partial s_k} \cdot \operatorname{Grad} \boldsymbol{\psi}^i \, \delta \bar{\boldsymbol{\varphi}} \, \mathrm{d}v \,,
$$

(5.15)

Following this, the element-wise sensitivity load term $\mathbf{f}^E_{sn}$ is obtained by (5.15) while using the same procedure as for the determination of the element-wise residual $\mathbf{R}^E_n$, cf. (3.15) in Section 3.2, i.e., testing separately in every single degree of freedom and replacing the integral by the sum over the integration points. Thus, one obtains, in index notation, for the $i-$th component of the part $\mathbf{f}^E_{sM}$ in consequence of the partial derivative of the balance of momentum

$$
f^E_{snMik} = \sum_{q=1}^{N_q} \sum_{p=1}^N \frac{\partial \sigma^q_{(i)j}}{\partial s_k} \, \phi^{pq}_{(i),j} \ w_q \, J^q_E \,,
$$

(5.16)

and for the part $\mathbf{f}^E_{sMoM}$ in consequence of the balance of moment of momentum

$$
f^E_{snMoMik} = \sum_{q=1}^{N_q} \sum_{p=1}^M \left[-(e_{(i)mn} \frac{\partial \sigma_{nm}}{\partial s_k}) \psi^{pq}_{(i)} + \frac{\partial \mu^q_{(i)j}}{\partial \mathbf{s}_k} \psi^{pq}_{(i),j} \right] \ w_q \, J^q_E \,.
$$

(5.17)

Therein, the meaning of the indices is the same as described in (3.15) in Section 3.2. Hence, the total element-wise sensitivity load term results from the combination of the parts (5.16) and (5.17) to,

$$
\mathbf{f}^E_{sn} = \begin{pmatrix} \mathbf{f}^E_{snM} \\[2mm] \mathbf{f}^E_{snMoM} \end{pmatrix} \,.
$$

(5.18)

To obtain the global system of equations for the computation of the sensitivities of the primary variables, the element-wise defined equations (5.20) are assembled over all elements. For the global tangent matrix $\partial \mathbf{R}/\partial \mathbf{s}$ this is shown in (3.22)[1], whereas the global sensitivity load term results, in analogy to (3.17), in:

$$
\mathbf{f}_{sng} = \sum_{E=1}^{N_E} \sum_{i=1}^{N_y} \mathbf{A}^g_i \, \mathbf{f}^E_{sni} \,,
$$

(5.19)

where the element-wise defined degree of freedom i is replaced by the global defined degree of freedom g. Note, $\mathbf{f}^G_{sng}$ is an vector summarizing the N_s sensitivities of all material

---

[1]Due to the fact that in (3.22) no dependency of the material parameters has been considered, the total derivative $\mathrm{d}\mathbf{R}/\mathrm{d}\mathbf{s}$ corresponds to $\partial \mathbf{R}/\partial \mathbf{s}$.

parameters in the set $\mathbf{s}$ at the global degree of freedom g. Thus, the system of equations for the computation of the sensitivities $\mathrm{d}\mathbf{y}_n/\mathrm{d}\mathbf{s}$ can be written as

$$\frac{\partial \mathbf{R}_n}{\partial \mathbf{y}} \frac{\mathrm{d}\mathbf{y}_n}{\mathrm{d}\mathbf{s}} - \mathbf{f}_{s\,n} = \mathbf{0}\,, \tag{5.20}$$

where the sensitivity load term $\mathbf{f}_{s\,n}$ contains the sensitivities $\mathbf{f}_{s\,n\,g}$ of all global degrees of freedom g. Following this, the whole sensitivity load term $\mathbf{f}_{s\,n}^G$ is a $(N_E \cdot N_y) \times N_s$ matrix (N_E number of elements, N_y number of degrees of freedom per element).

5.2.2   Sensitivity load term

For the computation of the global sensitivity load term $\mathbf{f}_{s\,n}$, the element-wise sensitivity load terms $\mathbf{f}_{s\,n}^E$, must be computed for every element. Moreover, from (5.15) it is obvious that for the computation of these element-wise sensitivity load terms $\mathbf{f}_{s\,n}^E$ the partial derivative of the generalized stress $\mathbf{\Sigma}_n$ with respect to $\mathbf{s}$ is needed, i. e., the derivatives of the stress $\boldsymbol{\sigma}$ and the couple stress $\boldsymbol{\mu}$ at the frozen deformation state $\mathbf{y}_n = \mathbf{y}_{n\,\mathrm{const}}$ are required. This is carried out by using the system of equations $\mathbf{G}$, cf. (3.31) and Table 3.1 in Section 3.4, which is used for the computation of stress and couple stress at the integration points of the FE mesh. Considering this system of equations, the following dependencies can be recognized,

$$\mathbf{G}_n = \mathbf{G}_n(\mathbf{s}, \mathbf{\Sigma}_n(\mathbf{s}), \mathbf{p}_n(\mathbf{s}), \mathbf{p}_{n-1}(\mathbf{s}), \Lambda_n, \mathbf{q}_{n-1}(\mathbf{s})) \equiv \mathbf{0}\,, \tag{5.21}$$

where $\mathbf{q}_n$ is the vector of the internal variables, $\mathbf{p}_n$ is the vector of the hardening variables and Λ is the plastic multiplier. The derivative of this system of equations with respect to $\mathbf{s}$ yields for the fixed deformation state $\boldsymbol{\mathcal{E}}_n$ at the time step n the following condition:

$$\left.\frac{\mathrm{d}\mathbf{G}_n}{\mathrm{d}\mathbf{s}}\right|_{\boldsymbol{\mathcal{E}}_n} = \frac{\partial \mathbf{G}_n}{\partial \mathbf{s}} + \frac{\partial \mathbf{G}_n}{\partial \mathbf{\Sigma}_n} \left.\frac{\mathrm{d}\mathbf{\Sigma}_n}{\mathrm{d}\mathbf{s}}\right|_{\boldsymbol{\mathcal{E}}_n} + \frac{\partial \mathbf{G}_n}{\partial \mathbf{p}_n} \left.\frac{\mathrm{d}\mathbf{p}_n}{\mathrm{d}\mathbf{s}}\right|_{\boldsymbol{\mathcal{E}}_n} + \frac{\partial \mathbf{G}_n}{\partial \mathbf{p}_{n-1}} \frac{\mathrm{d}\mathbf{p}_{n-1}}{\mathrm{d}\mathbf{s}} +$$

$$+ \frac{\partial \mathbf{G}_n}{\partial \Lambda_n} \left.\frac{\mathrm{d}\Lambda_n}{\mathrm{d}\mathbf{s}}\right|_{\boldsymbol{\mathcal{E}}_n} + \frac{\partial \mathbf{G}_n}{\partial \mathbf{q}_{n-1}} \frac{\mathrm{d}\mathbf{q}_{n-1}}{\mathrm{d}\mathbf{s}} \stackrel{!}{=} \mathbf{0}\,. \tag{5.22}$$

Note that in consequence of the appearance of $\mathbf{p}_{n-1}(\mathbf{s})$ and $\mathbf{q}_{n-1}(\mathbf{s})$ from the last time step, the total derivatives $\mathrm{d}\mathbf{p}_{n-1}/\mathrm{d}\mathbf{s}$ and $\mathrm{d}\mathbf{q}_{n-1}/\mathrm{d}\mathbf{s}$ occur in (5.22). Moreover, with the definition of $\boldsymbol{\mathcal{S}}_n = (\mathbf{\Sigma}_n^T, \Lambda_n, \mathbf{p}_n^T)^T$, the above equation can be solved for $\mathrm{d}\boldsymbol{\mathcal{S}}_n/\mathrm{d}\mathbf{s}$ in the following manner:

$$\left.\frac{\mathrm{d}\boldsymbol{\mathcal{S}}_n}{\mathrm{d}\mathbf{s}}\right|_{\boldsymbol{\mathcal{E}}_n} = - \left[\frac{\partial \mathbf{G}_n}{\partial \mathbf{s}} + \frac{\partial \mathbf{G}_n}{\partial \mathbf{p}_{n-1}} \frac{\mathrm{d}\mathbf{p}_{n-1}}{\mathrm{d}\mathbf{s}} + \frac{\partial \mathbf{G}_n}{\partial \mathbf{q}_{n-1}} \frac{\mathrm{d}\mathbf{q}_{n-1}}{\mathrm{d}\mathbf{s}} \right] \left(\frac{\partial \mathbf{G}_n}{\partial \boldsymbol{\mathcal{S}}_n}\right)^{-1}\,. \tag{5.23}$$

Therein, $\partial \mathbf{G}/\partial \boldsymbol{\mathcal{S}}_n$ is known from the computation of the consistent tangent, cf. (3.36) in Section 3.4. Due to the fact that in (5.23) the total derivatives of the history and hardening variables at the time step $n-1$ appear, the solution of the above system of equations (5.23) requires an iterative procedure, i. e., for the computation of the sensitivities at the time step n, the sensitivities of the time step $n-1$ must be known. With the solution of (5.23),

the partial sensitivities of the stress $\boldsymbol{\sigma}$ and the couple stress $\boldsymbol{\mu}$ are known, because the total derivatives of $\boldsymbol{\mathcal{S}}_n$ from (5.21) on the fixed strain state $\boldsymbol{\mathcal{E}}_n$ corresponds with the overall partial derivatives, viz.:

$$\frac{\mathrm{d}\boldsymbol{\mathcal{S}}_n}{\mathrm{d}\mathbf{s}}\bigg|_{\boldsymbol{\mathcal{E}}_n} = \frac{\partial\boldsymbol{\mathcal{S}}_n}{\partial\mathbf{s}} = \left[(\frac{\partial\boldsymbol{\sigma}_n}{\partial\mathbf{s}})^T, (\frac{\partial\boldsymbol{\mu}_n}{\partial\mathbf{s}})^T, (\frac{\partial\Lambda_n}{\partial\mathbf{s}})^T, (\frac{\partial\mathbf{p}_n}{\partial\mathbf{s}})^T, \right]^T . \tag{5.24}$$

Thus, the sensitivity load term $\mathbf{f}_{sn}$ can be computed in using (5.16), (5.17) and (5.19).

5.2.3 Sensitivities of the strain and curvature

In consequence of the solution of the global system (5.20) the sensitivities $\mathrm{d}\mathbf{y}_n/\mathrm{d}\mathbf{s}$ of the primary variables are known, which contain the sensitivities $\mathrm{d}\mathbf{u}_n/\mathrm{d}\mathbf{s}$ and $\mathrm{d}\boldsymbol{\varphi}_n/\mathrm{d}\mathbf{s}$ of the displacements $\mathbf{u}_n$ and rotations $\boldsymbol{\varphi}_n$. In the next step, the sensitivities of the strain $\bar{\boldsymbol{\varepsilon}}_n$ and curvature $\bar{\boldsymbol{\kappa}}_n$ can be directly computed based on the sensitivities of the primary variables using the shape functions $\boldsymbol{\phi}$ and $\boldsymbol{\psi}$, cf. (3.6) in Section 3.2:

$$\frac{\mathrm{d}\bar{\boldsymbol{\varepsilon}}_n}{\mathrm{d}\mathbf{s}} = \sum_{i=1}^{N} \mathrm{Grad}\,\boldsymbol{\phi}^i \frac{\mathrm{d}\mathbf{u}_{in}}{\mathrm{d}\mathbf{s}} + \overset{3}{\mathbf{E}}\sum_{i=1}^{M}\boldsymbol{\psi}^i\frac{\mathrm{d}\bar{\boldsymbol{\varphi}}_{in}}{\mathrm{d}\mathbf{s}} ,$$

$$\frac{\mathrm{d}\bar{\boldsymbol{\kappa}}_n}{\mathrm{d}\mathbf{s}} = \sum_{i=1}^{M}\mathrm{Grad}\,\boldsymbol{\psi}^i\frac{\mathrm{d}\bar{\boldsymbol{\varphi}}_{in}}{\mathrm{d}\mathbf{s}} . \tag{5.25}$$

5.2.4 Sensitivities of the stress and couple stress

The stress $\boldsymbol{\sigma}_n$ and the coupled stress $\boldsymbol{\mu}_n$, summarized in $\boldsymbol{\Sigma}_n$ are computed at the integration points of the FE mesh based on the strain and the curvature, which are summarized in $\boldsymbol{\mathcal{E}}_n$. Thus, the following dependencies are given:

$$\boldsymbol{\Sigma}_n = \boldsymbol{\Sigma}_n(\mathbf{s}, \boldsymbol{\mathcal{E}}_n(\mathbf{s})) . \tag{5.26}$$

Following (5.26), the total derivative of $\boldsymbol{\Sigma}_n$ with respect to $\mathbf{s}$ is directly obtained via

$$\frac{\mathrm{d}\boldsymbol{\Sigma}_n}{\mathrm{d}\mathbf{s}} = \frac{\partial\boldsymbol{\Sigma}_n}{\partial\mathbf{s}} + \frac{\partial\boldsymbol{\Sigma}_n}{\partial\boldsymbol{\mathcal{E}}_n}\frac{\mathrm{d}\boldsymbol{\mathcal{E}}_n}{\mathrm{d}\mathbf{s}} . \tag{5.27}$$

Therein, $\mathrm{d}\boldsymbol{\mathcal{E}}_n/\mathrm{d}\mathbf{s}$ is known from (5.25) and $\partial\boldsymbol{\Sigma}_n/\partial\mathbf{s}$ is known from (5.23).

5.2.5 Sensitivities of the hardening variables and of the plastic multiplier

The procedure for the computation of the sensitivities of the hardening variables is principally identical with the computation of the sensitivities of the stress and couple stress. Hence, one finds the following dependencies:

$$\mathbf{p}_n = \mathbf{p}_n(\boldsymbol{\mathcal{E}}_n, \boldsymbol{\mathcal{E}}_n(\mathbf{s})) ,$$

$$\Lambda_n = \Lambda_n(\boldsymbol{\mathcal{E}}_n, \boldsymbol{\mathcal{E}}_n(\mathbf{s})) . \tag{5.28}$$

Following this, in analogy to (5.27), the sensitivities of the hardening variables and the plastic multiplier can be written as

$$
\begin{aligned}
\frac{\mathrm{d}\mathbf{p}_n}{\mathrm{d}\mathbf{s}} &= \frac{\partial\mathbf{p}_n}{\partial\mathbf{s}} + \frac{\partial\mathbf{p}_n}{\partial\boldsymbol{\mathcal{E}}_n}\frac{\mathrm{d}\boldsymbol{\mathcal{E}}_n}{\mathrm{d}\mathbf{s}}, \\
\frac{\mathrm{d}\Lambda_n}{\mathrm{d}\mathbf{s}} &= \frac{\partial\Lambda_n}{\partial\mathbf{s}} + \frac{\partial\mathbf{p}_n}{\partial\boldsymbol{\mathcal{E}}_n}\frac{\mathrm{d}\boldsymbol{\mathcal{E}}_n}{\mathrm{d}\mathbf{s}},
\end{aligned}
\tag{5.29}
$$

where $\mathrm{d}\boldsymbol{\mathcal{E}}_n/\mathrm{d}\mathbf{s}$ is known from (5.25), and $\partial\mathbf{p}_n/\partial\mathbf{s}$ as well as $\partial\Lambda_n/\partial\mathbf{s}$ is known from (5.23).

5.2.6 Sensitivities of the internal variables

The plastic strain $\bar{\varepsilon}_{pn}$ and curvature $\bar{\boldsymbol{\kappa}}_{pn}$ at the time step n, which are combined in the vector of the internal variables $\mathbf{q}_n$, are computed basing on the plastic evolution, cf. (2.79) in Section 2.4. Therein, actually, the time derivatives $\dot{\mathbf{q}}_n$ of the internal variables $\mathbf{q}_n$ are computed. Thus, an equation for the increment $\Delta\mathbf{q}_n$ is obtained by the time discretization $\dot{\mathbf{q}}_n = \Delta\mathbf{q}_n/\Delta t$. Therewith, based on the evolution equations (2.79), the following dependencies for the increment $\Delta\mathbf{q}_n$ exist:

$$
\Delta\mathbf{q}_n = \Delta\mathbf{q}_n(\boldsymbol{\Sigma}_n,\, \mathbf{p}_n,\, \Lambda_n) = \Delta\mathbf{q}_n(\boldsymbol{\mathcal{S}}_n)\,.
\tag{5.30}
$$

Thus, one easily finds

$$
\frac{\mathrm{d}\Delta\mathbf{q}_n}{\mathrm{d}\mathbf{s}} = \frac{\partial\Delta\mathbf{q}_n}{\partial\mathbf{s}} + \frac{\partial\Delta\mathbf{q}_n}{\partial\boldsymbol{\mathcal{S}}_n}\frac{\mathrm{d}\boldsymbol{\mathcal{S}}_n}{\mathrm{d}\mathbf{s}}\,.
\tag{5.31}
$$

Therein, the total derivative $\mathrm{d}\boldsymbol{\mathcal{S}}_n/\mathrm{d}\mathbf{s}$ is known from (5.27) in combination with (5.29). Regarding that $\Delta\mathbf{q}_n = \mathbf{q}_n - \mathbf{q}_{n-1}$, one obtains the following iterative procedure for the computation of the sensitivities of the internal variables:

$$
\frac{\mathrm{d}\mathbf{q}_n}{\mathrm{d}\mathbf{s}} = \frac{\mathrm{d}\mathbf{q}_{n-1}}{\mathrm{d}\mathbf{s}} + \frac{\mathrm{d}\Delta\mathbf{q}_n}{\mathrm{d}\mathbf{s}}\,.
\tag{5.32}
$$

Therein, $\mathrm{d}\mathbf{q}_{n-1}/\mathrm{d}\mathbf{s}$ is known from the time step before. Note that in consequence of the occurrence of the internal and hardening variables at the time step $n - 1$ in the above equations, these variables have to be saved as history variables during the solution in addition to the internal variables $\mathbf{q}_n$.

5.2.7 Procedure of the semi-analytical sensitivity analysis

The whole procedure of the sensitivity analysis is illustrated in Figure 5.1. Thus, the following steps are required based on the solution of the primary variables $\mathbf{y}_n$ at the time step n:

1. Computation of the sensitivity load term $\mathbf{f}_{s\,n}$ based on the derivatives of the stress and hardening variables, which are included in $\boldsymbol{\mathcal{S}}_n$, cf. (5.23).
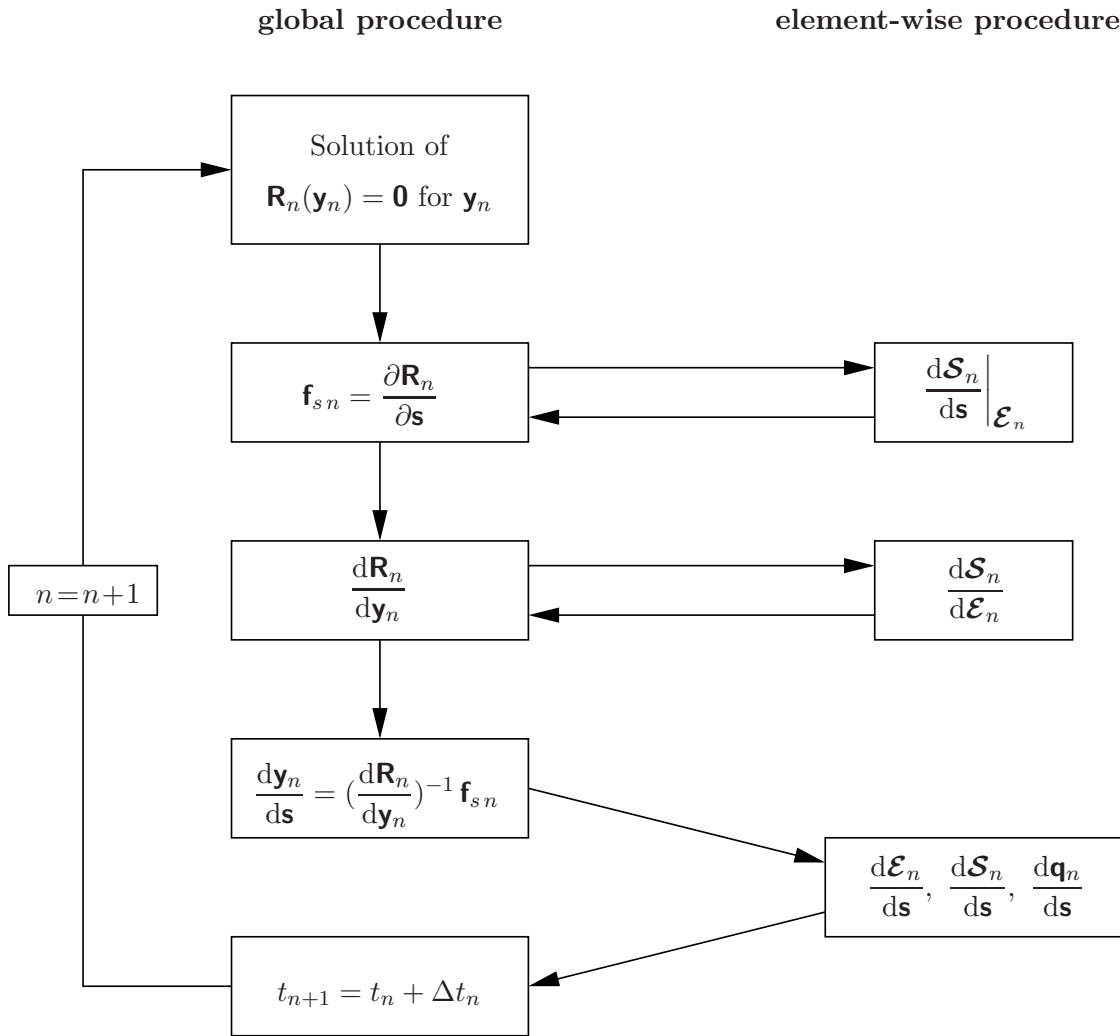
replacemen

$$\mathbf{R}_n(\mathbf{y}_n) = \mathbf{0}$$ for $\mathbf{y}_n$

$$\mathbf{f}_{sn} = \frac{\partial \mathbf{R}_n}{\partial \mathbf{s}}$$

$$\left.\frac{\mathrm{d}\boldsymbol{\mathcal{S}}_n}{\mathrm{d}\mathbf{s}}\right|_{\boldsymbol{\mathcal{E}}_n}$$

$$\frac{\mathrm{d}\mathbf{R}_n}{\mathrm{d}\mathbf{y}_n}$$

$$\frac{\mathrm{d}\boldsymbol{\mathcal{S}}_n}{\mathrm{d}\boldsymbol{\mathcal{E}}_n}$$

$$n = n+1$$

$$\frac{\mathrm{d}\mathbf{y}_n}{\mathrm{d}\mathbf{s}} = \left(\frac{\mathrm{d}\mathbf{R}_n}{\mathrm{d}\mathbf{y}_n}\right)^{-1}\mathbf{f}_{sn}$$

$$\frac{\mathrm{d}\boldsymbol{\mathcal{E}}_n}{\mathrm{d}\mathbf{s}}, \ \frac{\mathrm{d}\boldsymbol{\mathcal{S}}_n}{\mathrm{d}\mathbf{s}}, \ \frac{\mathrm{d}\mathbf{q}_n}{\mathrm{d}\mathbf{s}}$$

$$t_{n+1} = t_n + \Delta t_n$$

Figure 5.1: Procedure of the sensitivity analysis.

2. Computation of the consistent tangent based on the local algorithmic tangents at the integration points under consideration of the updated solution $\mathbf{y}_n$, cf. (3.22) and (3.36) in Section 3.4.

3. Computation of the sensitivities of the primary variables by use of (5.20).

4. Computation of the sensitivities of the generalized strain $\boldsymbol{\mathcal{E}}_n$ directly from the primary variables, cf. (5.25). Following this, the total derivatives of the generalized stress $\boldsymbol{\Sigma}_n$, cf. (5.27), the hardening variables $\mathbf{p}_n$ and the plastic multiplier Λ_n, cf. (5.29), which are summarized in $\boldsymbol{\mathcal{S}}$, can be computed. Furthermore, the sensitivities of the internal variables $\mathbf{q}_n$, cf. (5.31) and (5.32), are determined, too.

Therewith, the sensitivity analysis is finished and the next time step can be computed.

5.3   Sensitivity of the shear band data

In Chapter 4, it was demonstrated that the thickness of the shear band is necessary for the identification of the additional parameters of the *Cosserat* theory, and a new method for the determination of this shear band thickness has been presented in Section 4.4. Within this method, the strain is approximated by a bell-shape function, cf. (4.23), depending on the parameter vector $\mathbf{r}$, which includes the shear band thickness. Following this, the shear band thickness has been found by the fit of the approximated strain to the computed strain, cf. (4.24). As a consequence of the usage of the shear band thickness during the overall identification process, the sensitivities of these data are also required during the identification process. These sensitivities are computed basing on the implicit derivative of the system of equations $\mathbf{h}(\mathbf{r}(\mathbf{s}), \mathbf{s}) \equiv \mathbf{0}$, cf. (4.24), with respect to the material parameters $\mathbf{s}$. Thus, one obtains the following system of equations:

$$\frac{\mathrm{d}\mathbf{h}}{\mathrm{d}\mathbf{s}} = \frac{\partial\mathbf{h}}{\partial\mathbf{s}} + \frac{\partial\mathbf{h}}{\partial\mathbf{r}} \frac{\mathrm{d}\mathbf{r}}{\mathrm{d}\mathbf{s}} = \mathbf{0}\,. \tag{5.33}$$

In this equation, $\partial\mathbf{h}/\partial\mathbf{r}$ is already known from the previous computation of $\mathbf{r}$, cf. (4.25). Furthermore, the partial derivative of $\mathbf{h}$ with respect to $\mathbf{s}$ is given by

$$\frac{\partial\mathbf{h}}{\partial\mathbf{s}} = -2 \sum_{i=1}^{N} \frac{\mathrm{d}\|\bar{\varepsilon}_i\|}{\mathrm{d}\mathbf{s}} \left(\frac{\partial\epsilon_i}{\partial\mathbf{r}}\right)^T, \tag{5.34}$$

where $\bar{\varepsilon}_i$ represents the strain at the integration point i and $\mathrm{d}\|\bar{\varepsilon}_i\|/\mathrm{d}\mathbf{s}$ is the total derivative of the norm of strain, which is given via

$$\frac{\mathrm{d}\|\bar{\varepsilon}_i\|}{\mathrm{d}\mathbf{s}} = \frac{\bar{\varepsilon}_i}{2\,\|\bar{\varepsilon}_i\|} \frac{\mathrm{d}\bar{\varepsilon}_i}{\mathrm{d}\mathbf{s}}\,. \tag{5.35}$$

Therein, the sensitivities of the strain are given in $(5.25)_1$. Moreover, $\partial\epsilon_i/\partial\mathbf{r}$ in (5.34) can be easily calculated using (4.22), whereas $\partial\mathbf{h}/\partial\mathbf{r}$ in (5.33) is known from (4.25). Thus, all terms in (5.33) are known and the system of equations (5.33) can be solved for the sensitivities $\mathrm{d}\mathbf{r}/\mathrm{d}\mathbf{s}$, which includes the requested sensitivities $\mathrm{d}H/\mathrm{d}\mathbf{s}$ of the shear band thickness.

Chapter 6: Numerical Examples

In this chapter, the stepwise identification process, which was explained in detail in Chapter 4 is exemplarily illustrated based on experimental data of *Hostun* sand. *Hostun* sand is chemically nearly a pure silica sand with a grain density of $2.643\,\mathrm{g/cm^3}$, whereas the material density ranges from $1.34\,\mathrm{g/cm^3}$ in the loosest package ($n_s = 0.508$) and $1.71\,\mathrm{g/cm^3}$ in the densest package ($n_s = 0.647$). A special characteristic of this sand is the narrow grain size distribution, cf. Figure 6, wherein, in addition to the grain size distribution, a magnified photography of the grains is shown.
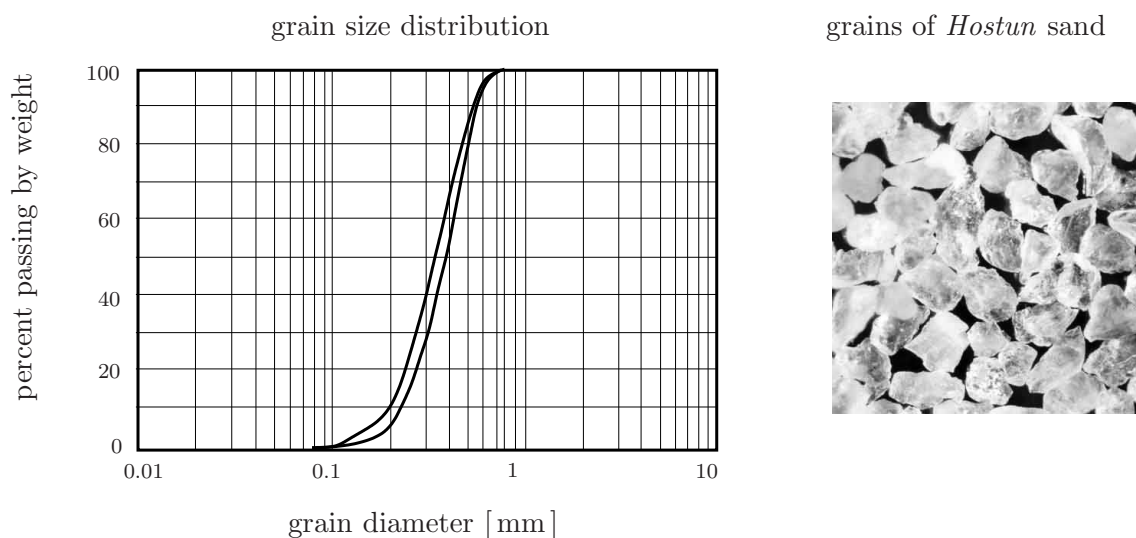
Figure 6.1: Grain size distribution and magnified photography of the grains of *Hostun* sand.

Following the stepwise identification procedure described in Section 4.3, this chapter starts with the first step, the determination of the material parameters of the homogeneous, non-polar case. For this purpose, homogeneous triaxial compression and hydrostatic loading in combination with the homogeneous part of a biaxial test is used. Moreover, this step is subdivided into the identification of the parameters of the non-polar elastic part of the material model taken from unloading-loading cycles during the overall homogeneous loading procedure, and the determination of the parameters of the non-polar plasticity. Afterwards, in the second step, the *Cosserat* parameters have to be determined. Due to the fact that the influence of these material parameters is only measurable on non-homogeneous tests including a shear-band geometry a biaxial test with shear banding is used for this task. Such tests were performed by the university of Grenoble, whereby the strain localization along the shear band was measured by use of the stereophotogrammetry, cf. *Mokni & Desrues* [101] and *Desrues & Viggiani* [80].

For the identification procedure, the material tests must be numerically simulated by use of the material model introduced in Chapter 2. For the homogeneous tests, this is nu-

merically very cheap, because in every material point the same state of stress exists and, thus, all calculations can be carried out at one integration point. However, the computations for the inhomogeneous tests are much more expensive. In this case, a full FEM computation of the boundary-value problem of the biaxial test with an adequate mesh for the simulation of the localization is required, which is connected with high numerical costs. Following this, an effective optimizing algorithm is essential, which is given by the gradient based SQP method, cf. Chapter 4, in combination with the semi-analytical computation of the gradient, cf. Chapter 5. Due to the complexity of the usage of inhomogeneous tests, the complete identification of the material parameters related to the *Cosserat* theory is demonstrated step by step. Hence, firstly, the semi-analytical computed sensitivities are verified by use of the numerically computed sensitivities. Secondly, the whole identification procedure is tested using the parameter re-identification and, finally, the identification basing real measured data is carried out.

6.1   Parameter identification of the non-polar behavior

The first part of the identification process contains the determination of the non-polar elasticity as well as the non-polar plasticity by use of homogeneous triaxial compression and hydrostatic tests, cf. Appendix A.1, in combination with the homogeneous part of a biaxial test, cf. Appendix A.2. Whereas the parameters of the homogeneous elasticity result directly from the unloading-loading cycles, the identification of the parameters of the plasticity requires the solution of an inverse problem basing on a multi-criterion objective function. Thus, for this case, additionally to the values of the parameters, the uncertainty of the parameters are also computed by use of the error analysis.

6.1.1   Parameter identification of non-polar elasticity

In the homogeneous case without microrotations, no *Cosserat* effects appear, i.e., the stress tensor $\boldsymbol{\sigma}$ is symmetric and the couple stress $\boldsymbol{\mu}$ is zero. Thus, the elasticity law (2.73) can be reduced to

$$\boldsymbol{\sigma} = 2\,\mu\,\bar{\boldsymbol{\varepsilon}}_e + \lambda\,\frac{\varepsilon^V_{e\,\mathrm{crit}}}{\varepsilon^V_{e\,\mathrm{crit}} - \varepsilon^V_e}\,\varepsilon^V_e\,\mathbf{I} \quad \mathrm{with} \quad \varepsilon^V_{e\,\mathrm{crit}} = 1 - \frac{n^S_{\mathrm{max}}}{n^S_0\,(1 - \varepsilon^V_p)}\,. \tag{6.1}$$

Therein, four material parameters appear, the *Lamé* constants μ and λ, the maximal possible solid volume fraction n^S_{max} and the initial solid volume fraction n^S_0. Due to the fact that n^S_0 is directly measured at the initialization of the tests, three elastic parameters, λ, μ and n^S_{max}, remain for the identification process.

The identification of these parameters is carried out basing on unloading-loading cycles of homogeneous triaxial compression and hydrostatic tests. In Figure 6.2 (a), the fit of the computed data on the axial stress-strain (σ_{11}-ε_{11}) curve as well as on the volumetric strain ε^V versus the axial strain ε_{11} from triaxial compression tests is shown. Furthermore,

Figure 6.2 (b) exhibits the additional fit of the hydrostatic stress ($\sigma_V = 1/3\,\boldsymbol{\sigma}\cdot\mathbf{I}$) versus the volumetric strain ε^V resulting from a hydrostatic compression test. In both cases, the computations proceed from plastic pre-deformations.
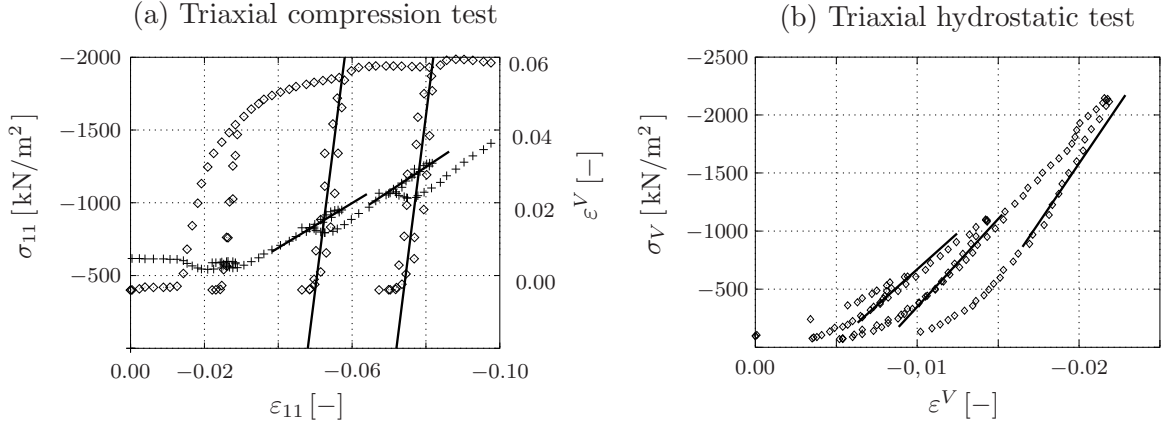

Figure 6.2: Identification of the parameters of the elastic case, (a): Stress and volumetric strain versus vertical strain from a triaxial compression test. (b): Hydrostatic stress versus volumetric strain from a hydrostatic triaxial test.

The identified values of the material parameters of the non-polar elasticity as well as the measured value of the initial density n_0^S of the specimen are listed in Table 6.1.

parameter	value	unit
μ	91.0	$[\,\mathrm{MN/m^2}\,]$
λ	49.4	$[\,\mathrm{MN/m^2}\,]$
$n_{\max}^S$	0.635	$[-]$
n_0^S	0.604	$[-]$

Table 6.1: Values of the material parameters of the non-polar elasticity.

6.1.2 Parameter identification of the non-polar plasticity

After the identification of the parameters of the elasticity law, secondly, all parameters of the non-polar plasticity have to be determined. This step includes the parameters of the evolution of the yield condition, cf. (2.76) and (2.82), i.e., the initial values $p_{i\,0}$, the limit values $\overset{\star}{p}_i$ as well as the volumetric and deviatoric evolution constants C_{pi}^V and C_{pi}^D with $p_i = \{\beta,\,\delta,\,\epsilon,\,\gamma\}$, and, moreover, the additional parameters ψ_1 and ψ_2 of the plastic potential (2.78). Due to the fact that non-preloaded sand exhibits plastic yielding with the onset of the loading process, the determination of an initial yield surface is useless. Hence, the initial values of the yield condition are assumed in such a way that plastic deformations occur at the first load step in each test.

Thus, altogether the 14 material parameters

$$\mathbf{s}_{\mathrm{pl\,hom}} = (C_\beta^D,\ C_\beta^V,\ \overset{\star}{\beta},\ C_\delta^D,\ C_\delta^V,\ \overset{\star}{\delta},\ C_\epsilon^D,\ C_\epsilon^V,\ \overset{\star}{\epsilon},\ C_\gamma^D,\ C_\gamma^V,\ \overset{\star}{\gamma},\ \psi_1,\ \psi_2)^T \qquad (6.2)$$

remain for the identification. Due to this high number of material parameters, one has to use experimental data of different material tests for the identification, namely:

- Vertical stress and volumetric strain versus axial strain of triaxial compression with three different confining pressures, $100\,\mathrm{kN/m^2}$, $300\,\mathrm{kN/m^2}$ and $600\,\mathrm{kN/m^2}$,

- volumetric stress versus volumetric strain at hydrostatic loading,

- vertical stress versus vertical strain of the homogeneous part of a biaxial test with a lateral pressure of $100\,\mathrm{kN/m^2}$.

Thus, altogether five different material tests are considered with the following multi-criterion objective function:

$$f(\mathbf{s}_{\mathrm{pl\,hom}}) = \sum_{\mathrm{t}=1}^{3} \frac{1}{N_{\mathrm{t}}} \left\{ \frac{1}{\sigma_0^{\mathrm{t}}} \sum_{i=1}^{N_{\mathrm{t}}} [\,\sigma_{11}^{\mathrm{t}} - \tilde{\sigma}_{11}^{\mathrm{t}}\,]^2 + \frac{1}{\varepsilon_0^{V\mathrm{t}}} \sum_{i=1}^{N_{\mathrm{t}}} [\,\varepsilon^{V\mathrm{t}} - \tilde{\varepsilon}^{V\mathrm{t}}\,]^2 \right\} +$$

$$+ \quad \frac{1}{N_{\mathrm{hyd}}\,\varepsilon_0^{V\mathrm{hyd}}} \sum_{i=1}^{N_{\mathrm{hyd}}} [\,\varepsilon^{V\mathrm{hyd}} - \tilde{\varepsilon}^{V\mathrm{hyd}}\,]^2 + \qquad (6.3)$$

$$+ \quad \frac{1}{N_{\mathrm{biax}}\,\sigma_0^{\mathrm{biax}}} \sum_{i=1}^{N_{\mathrm{biax}}} [\,\sigma_{11}^{\mathrm{biax}} - \tilde{\sigma}_{11}^{\mathrm{biax}}\,]^2$$

$$\text{with} \quad \mathrm{t} = \{\mathrm{triax}_{100},\ \mathrm{triax}_{300},\ \mathrm{triax}_{600}\}.$$

Therein, the indices "triax$_{100}$", "triax$_{300}$" and "triax$_{600}$" stand for the triaxial compression tests with confining pressures of 100, 300 and 600 kN/m^2, "hyd" indexes the hydrostatic

factor	value	unit
$\sigma_0^{\mathrm{triax}_{100}}$	500	$[\,\mathrm{kN/m^2}\,]$
$\varepsilon_0^{V\,\mathrm{triax}_{100}}$	0.1	$[-]$
$\sigma_0^{\mathrm{triax}_{300}}$	1500	$[\,\mathrm{kN/m^2}\,]$
$\varepsilon_0^{V\,\mathrm{triax}_{300}}$	0.07	$[-]$
$\sigma_0^{\mathrm{triax}_{600}}$	2500	$[\,\mathrm{kN/m^2}\,]$
$\varepsilon_0^{V\,\mathrm{triax}_{600}}$	0.03	$[-]$
$\varepsilon_0^{V\,\mathrm{hyd}}$	0.017	$[-]$
σ_0^{biax}	650	$[\,\mathrm{kN/m^2}\,]$

Table 6.2: Values of the normalization factors in (6.3).
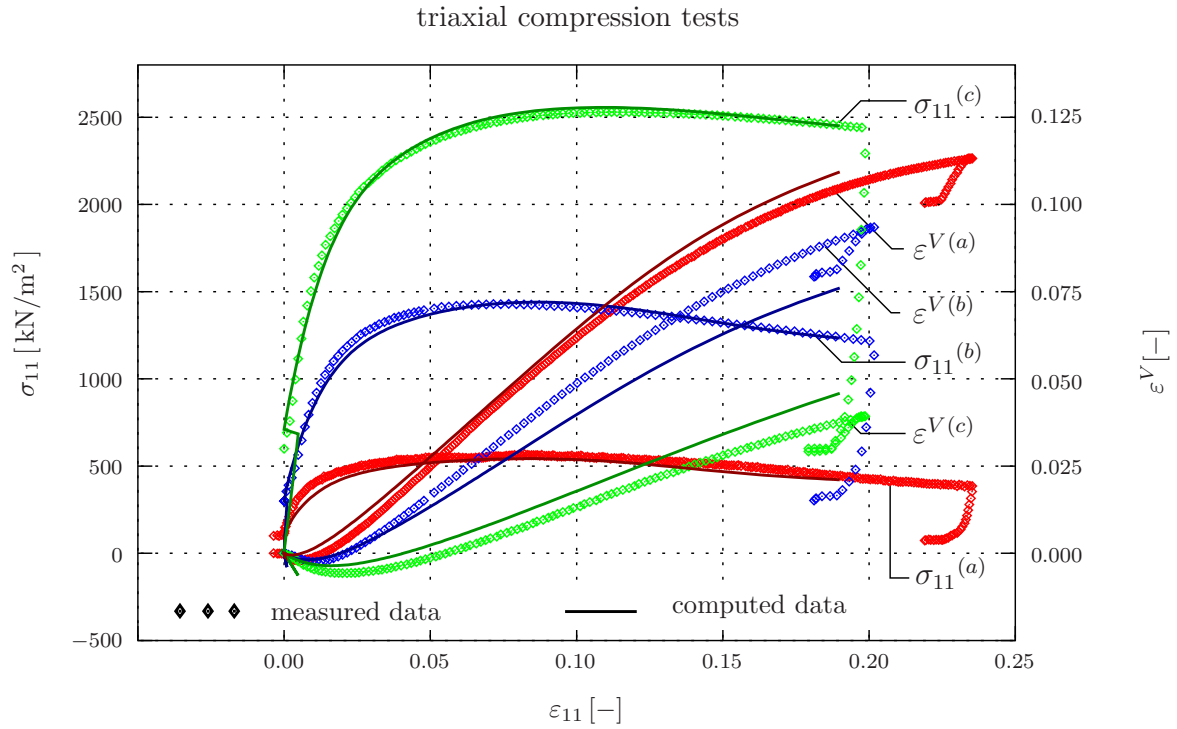
triaxial compression tests

Figure 6.3: Fit of triaxial compression tests by use of the material parameters of the non-polar plasticity, for various confining pressures: (a) $p = 100$ kN/m^2, (b) $p = 300$ kN/m^2 and (c) $p = 600$ kN/m^2.

triaxial test and "biax" the homogeneous biaxial test. Furthermore, N_{t}, N_{hyd} and N_{biax} are the number of considered data points in each test, whereas σ_0^{t} and $\varepsilon_0^{V\text{t}}$ as well as $\varepsilon_0^{V\text{hyd}}$ and σ_0^{biax}, cf. Table 6.2, are the reference values for the different kinds of data, which are used for the normalization of the various quantities in (6.3).

The results of the identification process basing on the multi-criterion objective function (6.3) are shown in Figure 6.3, wherein, the fit of the vertical stress and volumetric strain of the three triaxial compression tests are displayed. Furthermore, in Figure 6.4, the fit of the hydrostatic triaxial tests as well as of the homogeneous part of the biaxial tests are shown. Thereby, in Figure 6.3, it is obvious that the fit of the volumetric strain for the test with a confining pressure of 100 kN/m^2 as well as a confining pressure of 300 kN/m^2 is not so good as for the other data. One possible reason therefore can be found in the assumption of a purely isotropic evolution of the yield function in the material model, whereas in nature, the evolution is given by a combination of an isotropic as well as a kinematic part. Thus, one possibility to reach a better fit is a more detailed approximation of the evolution of the yield function regarding the kinematic part of the hardening, additionally to the isotropic hardening. However, under consideration of the obtained good results for all the other tests including the hydrostatic triaxial test and the homogeneous part of the biaxial test, cf. Figure 6.4, the used constitutive model seems to be sufficient for the modeling of the non-polar plasticity.

Particularly, with the split of the evolution function in a deviatoric and volumetric part,
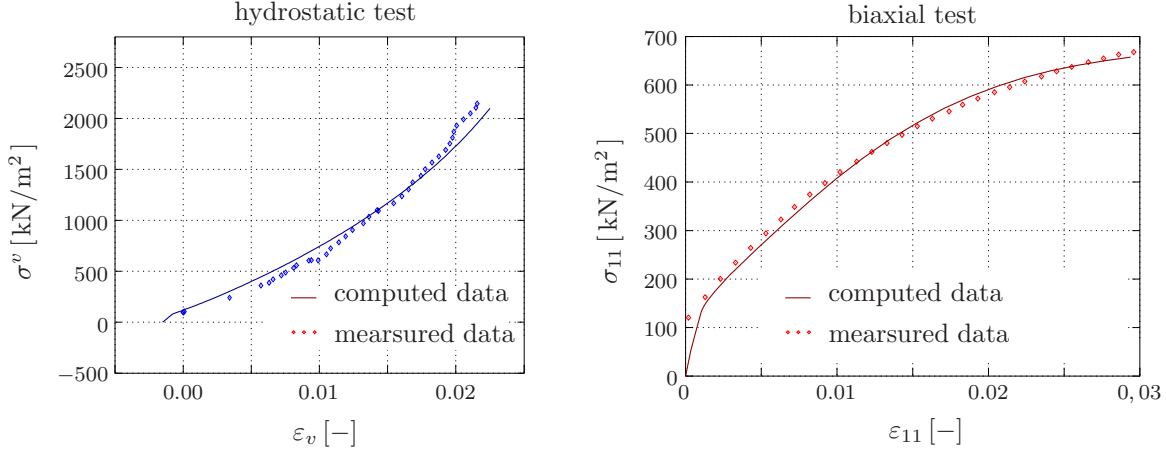
Figure 6.4: Fit of the hydrostatic triaxial test and homogeneous biaxial test with the material parameters of the homogeneous plasticity .

in addition to the material hardening, softening behavior can be modeled. Considering the measured data as well as the computed fit in Figure 6.3, one can observe a slight decrease of the vertical stress after overstepping the maximum value. This effect can be interpreted as material softening, which occurs in consequence of the increasing of the pores in the material due to the positive volumetric yielding (dilatant yielding). This material softening is the principal reason for the instability of the material, i. e., for the formation of shear bands, which will be shown later since it is an important part of the overall material behavior. The obtained values of the material parameters as well as the initial values of the hardening parameters, which was assumed in a reasonable way, are listed in Table 6.4 together with the results of the following error analysis.

Furthermore, the evolution of the yield condition in the hydrostatic plane is exemplarily shown in Figure 6.5 for compressive loading with a confining pressure of $300 \, \text{kN/m}^2$. Therein the single yield conditions during the evolution are shown, from light gray to black, whereby the current stress states are marked by points. Hence in Figure 6.5, three different parts of the evolution can be recognized:

1. The upset of the stabilizing hydrostatic stress states up to a confining pressure of $300 \, \text{kN/m}^2$ (equal with $\text{I} = 900 \, \text{kN/m}^2$). Thereby the yield surface increases in consequence of the contractant plastic yielding ($\dot{\varepsilon}_p^V < 0$), cf. (2.82) in Section 2.4.5 whereby the stress state remains on the hydrostatic axis.

2. Afterwards, the confining pressure is kept constant and the specimen is vertically displacement-driven loaded. Thus, the vertical stress increases due to the deviatoric yielding ($\|\dot{\varepsilon}_p^D\|$) and the yield surface grows up.

3. In consequence of the dilatant yielding ($\dot{\varepsilon}_p^V > 0$) material softening occurs. When this effect becomes dominant the yield surface decreases. This can be also observed by the decrease of the vertical stress in the stress-strain relations shown in Figure 6.3.
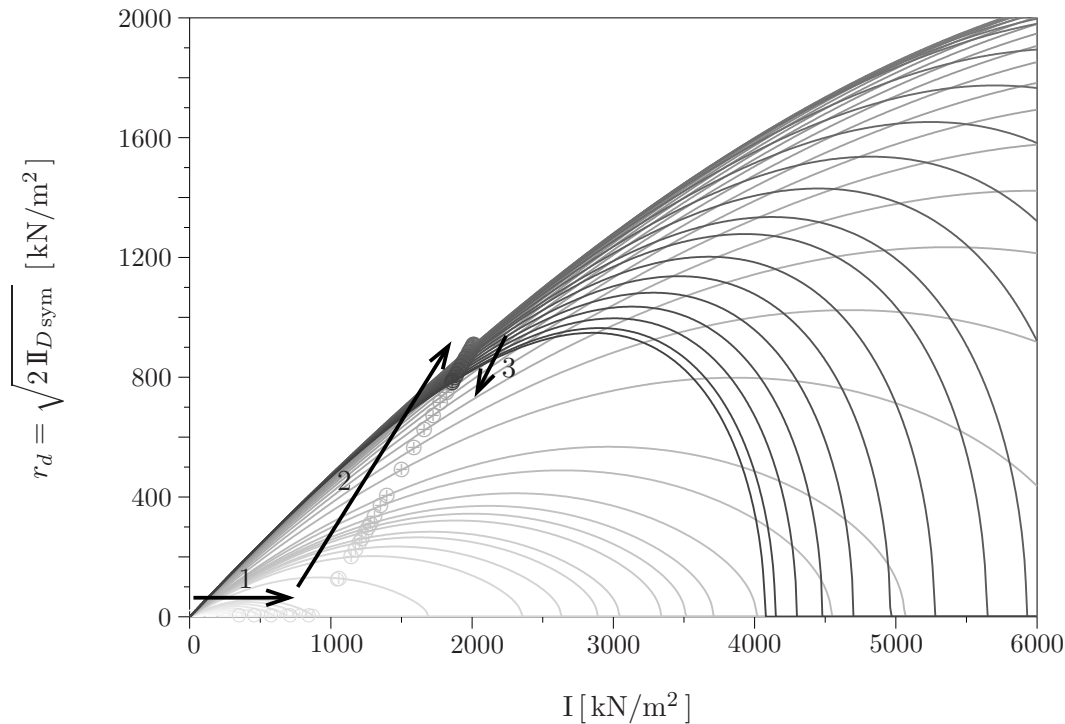
Figure 6.5: Evolution of the yield condition (from light gray to black) for the triaxial test with a confining pressure of 300 kN/m²: (1) Hydrostatic hardening, (2) deviatoric hardening and (3) softening in consequence of dilatant yielding.

6.1.3   Error analysis

With the determination of the values for the material parameters, the identification process is not completed, because no information about the accuracy of the identified parameters exists. Therefore, the error analysis, cf. Section 4.5, is required. This error analysis bases on the reliability or, vice versa, uncertainty of the measured data, which is expressed by the standard deviation σ_i, cf. (4.26), of every single data point i of the measurement. Thus, for the calculation of σ_i, at least three independent measurements are required. Generally, in case of geomaterials, like sand, the measurements show a wide distribution caused in the complexity of the realization of the material tests. Thus, small differences in the density of the specimen or a variation in the lubrication of the load plates lead to differences in the measured results. This is exemplarily shown for the triaxial test with a confining pressure of $300 \, \text{kN/m}^2$ in Figure 6.6. Therein, the stress-strain relations as well as the volumetric strain versus the axial strain of six independent tests are shown and, additionally, the mean values of the data and the standard deviation are plotted.

Due to the fact that the parameters of the elasticity have been directly determined by use of unloading cycles of one triaxial and one hydrostatic tests, these parameters are not considered for the error analysis. Hence, the error analysis is only carried out for

the parameters of the non-polar plasticity. In the following, the procedure of the error analysis is demonstrated in the same order as it has been described in Section 4.5 beginning with the residual analysis, followed by the uncertainty analysis and concluded with the correlation analysis.
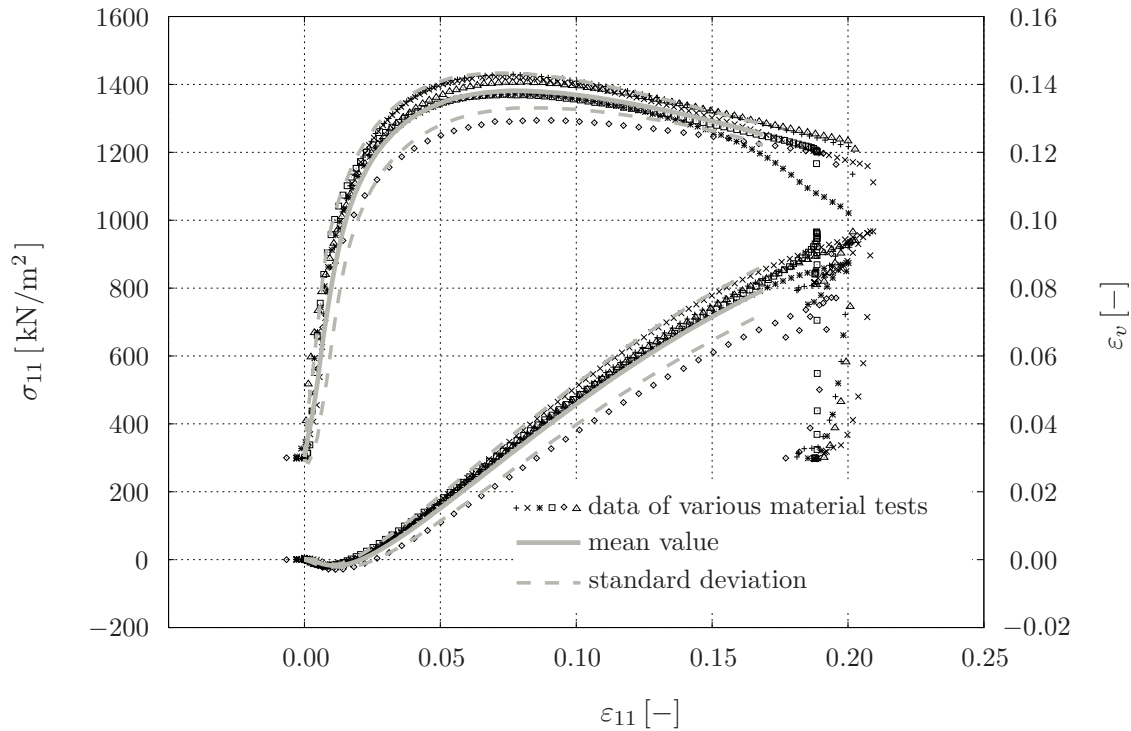

Figure 6.6: Mean value and standard deviation of six independent triaxial tests.

Residual analysis

On the basis of the uncertainty of the measured data expressed by the standard deviation σ_i, the so-called *goodness-of-fit* s_0, cf. (4.27), can be computed. The obtained value for s_0 is the relation between the quality of the fit and the quality of the measurements summarized over all data points of the measurement. Due to the fact that for the optimization process a multi-criterion objective function is used, which is based on different numbers of data points, s_0 is firstly determined separately for every single material test. Thus,

using (4.27), one obtains:

$$
s_{0\text{t}}^2 = \frac{1}{N_\text{t} - P} \left\{ \sum_{i=1}^{N_\text{t}} \frac{1}{(\sigma_{\sigma\,i})^2} [\,\sigma_{11\,i}^\text{t} - \tilde{\sigma}_{11\,i}^\text{t}\,]^2 + \sum_{i=1}^{N_\text{t}} \frac{1}{(\sigma_{\varepsilon\,i})^2} [\,\varepsilon_i^{V\text{t}} - \tilde{\varepsilon}_i^{V\text{t}}\,]^2 \right\} ,
$$

where $\quad$ t $= \{\text{triax}_{100}, \text{triax}_{300}, \text{triax}_{600}\}$

$$
s_{0\text{hyd}}^2 = \frac{1}{N_\text{hyd} - P} \sum_{i=1}^{N_\text{hyd}} \frac{1}{(\sigma_{\varepsilon\,i})^2} [\,\varepsilon_i^{V\text{hyd}} - \tilde{\varepsilon}_i^{V\text{hyd}}\,]^2 \quad \text{and}
$$

(6.4)

$$
s_{0\text{biax}}^2 = \frac{1}{N_\text{biax} - P} \sum_{i=1}^{N_\text{biax}} \frac{1}{(\sigma_{\sigma\,i})^2} [\,\sigma_{11\,i}^\text{biax} - \tilde{\sigma}_{11\,i}^\text{biax}\,]^2 .
$$

Therein, P is the number of material parameters, i.e., in this case 14, and $\sigma_{\sigma\,i}$ is the standard deviation of the stress for the data point i, cf. Section 4.5.1, whereas $\sigma_{\varepsilon\,i}$ is the standard deviation of the volumetric strain for one single data point. With these five different values, the square of the overall *goodness-of-fit* s_0^2 can be estimated as the mean value of the single tests. Thus, one obtains:

$$
s_0 = \tfrac{1}{5} \sqrt{s_{0\text{triax}100}^2 + s_{0\text{triax}300}^2 + s_{0\text{triax}600}^2 + s_{0\text{hyd}}^2 + s_{0\text{biax}}^2} .
$$

(6.5)

Therewith, the obtained overall value for s_0 as well as the values for the single tests and the number of considered data points in each test are summarized in Table 6.3. Moreover, in Table 6.3, the averaged measurement errors

$$
\bar{\sigma}_\sigma = \frac{1}{N} \sum_{i=1}^{N} \sigma_{\sigma\,i} \quad \text{and} \quad \bar{\sigma}_\varepsilon = \frac{1}{N} \sum_{i=1}^{N} \sigma_{\varepsilon\,i}
$$

(6.6)

of the single tests are specified, where N is the number of data points of each test. Considering Table 6.3, it is obvious that s_0 for the triaxial test with a confining pressure of 100 kN/m² is much higher than for the other tests. The reason therefore can be basically found in the high accuracy of the measured data, i.e., in the low value of the averaged measurement error $\bar{\sigma}_\sigma$, in comparison to the other tests. Therewith, the same quality of the fit leads to a higher value of s_0. Anyhow, the obtained value of about $s_0 = 2$ for the overall *goodness-of-fit* is on an acceptable level.

Uncertainty analysis

After the evaluation of the global fit, one is mainly interested in the information about the accuracy of the computed values for the material parameters. For this purpose, the covariance matrix **K** (4.28) has to be computed by the use of the multi-criterion objective function (6.3). To obtain **K**, the parts of the single tests are summarized, whereby for each test the value for s_0 computed in the above residual analysis is considered. Thus,

type of material test	$s_0\,[-]$	N	$\bar{\sigma}_\sigma\,[\mathrm{kN/m^2}]$	$\bar{\sigma}_\varepsilon\,[-]$
triaxial test conf. press. $100\,\mathrm{kN/m^2}$	3.81	261	13.5	0.00199
triaxial test conf. press. $300\,\mathrm{kN/m^2}$	1.67	84	48.3	0.00343
triaxial test conf. press. $600\,\mathrm{kN/m^2}$	1.68	109	47.0	0.00207
hydrostatic triaxial test	1.58	34	–	0.000912
homogeneous biaxial test	0.68	28	18.2	–
all tests together	2.01	519		

Table 6.3: Results of the residual analysis for the single tests, cf. (6.6).

one obtains the covariance matrix **K** basing on the sensitivities of the computed data with respect to the parameters of the non-polar plasticity $\mathbf{s}_{\mathrm{pl\,hom}}$ (6.2):

$$\mathbf{K} = \left\{ \sum_{\mathrm{t}=1}^{3} \frac{1}{s_{0\mathrm{t}}^2} \left[\sum_{i=1}^{N_\mathrm{t}} \frac{1}{(\sigma_{\sigma\,i})^2} \Big(\frac{\mathrm{d}\sigma_{11\,i}^\mathrm{t}}{\mathrm{d}\mathbf{s}_{\mathrm{pl\,hom}}}\Big)^T \frac{\mathrm{d}\sigma_{11\,i}^\mathrm{t}}{\mathrm{d}\mathbf{s}_{\mathrm{pl\,hom}}} + \sum_{i=1}^{N_\mathrm{t}} \frac{1}{(\sigma_{\varepsilon\,i})^2} \Big(\frac{\mathrm{d}\varepsilon_i^{V\mathrm{t}}}{\mathrm{d}\mathbf{s}_{\mathrm{pl\,hom}}}\Big)^T \frac{\mathrm{d}\varepsilon_i^{V\mathrm{t}}}{\mathrm{d}\mathbf{s}_{\mathrm{pl\,hom}}} \right] + \right.$$

$$+ \frac{1}{s_{0\mathrm{hyd}}^2} \sum_{i=1}^{N_\mathrm{hyd}} \frac{1}{(\sigma_{\varepsilon\,i})^2} \Big(\frac{\mathrm{d}\varepsilon_i^{V\,\mathrm{hyd}}}{\mathrm{d}\mathbf{s}_{\mathrm{pl\,hom}}}\Big)^T \frac{\mathrm{d}\varepsilon_i^{V\,\mathrm{hyd}}}{\mathrm{d}\mathbf{s}_{\mathrm{pl\,hom}}} + \tag{6.7}$$

$$\left. + \frac{1}{s_{0\mathrm{biax}}^2} \sum_{i=1}^{N_\mathrm{biax}} \frac{1}{(\sigma_{\sigma\,i})^2} \Big(\frac{\mathrm{d}\sigma_{11\,i}^\mathrm{biax}}{\mathrm{d}\mathbf{s}_{\mathrm{pl\,hom}}}\Big)^T \frac{\mathrm{d}\sigma_{11\,i}^\mathrm{biax}}{\mathrm{d}\mathbf{s}_{\mathrm{pl\,hom}}} \right\}^{-1}.$$

Therewith, the standard deviation of the investigated material parameters are given by the diagonal elements of the covariance matrix **K**, cf. Section 4.5.3. The values of the standard deviation of the single parameters and the values of the parameters themselves are shown in Table 6.4. Therein, it can be seen that the parameter C_γ^V has a very high uncertainty and, therewith, the determined value for this parameter is not relevant, because the uncertainty of the parameter is in the same range as the value of the parameter. Furthermore, the parameters C_β^V and C_δ^D imply high uncertainties and, thus, their determined values are not very relevant either. The values of the standard deviations for all the other parameters are in a more or less reasonable range and, consequently, the identified values for these parameters are relevant.

Correlation analysis

The last part of the error analysis is the calculation of the correlations between the single material parameters, which is carried out by the computation of the correlation coefficients r_{ij} between the parameters i and j, cf. (4.31) in Section 4.5.4. The obtained values are shown in Table 6.5. Therein, it can be seen that the parameters C_δ^V and C_δ^D as well as ψ_1 and ψ_2 are strongly correlated. For all the other parameters, the correlation coefficient is less than 0.8 and thus the correlation is in principal on an acceptable level.

parameter	value	σ_{pi}	unit	$\sigma_{pi}/|p_i|\,[\%]$
$\overset{\star}{\beta}$	0.273	0.00735	$[-]$	2.7
β_0	0.120	$-$	$[-]$	
C_β^D	127	6.19	$[-]$	4.9
C_β^V	-66.6	29.17	$[-]$	44.0
$\overset{\star}{\delta}$	1.59	0.0766	$[\mathrm{m}^2/\mathrm{MN}]$	12.0
δ_0	0.01	$-$	$[\mathrm{m}^2/\mathrm{MN}]$	
C_δ^D	-6.94	3.01	$[-]$	43.0
C_δ^V	46.1	9.94	$[-]$	21.6
$\overset{\star}{\epsilon}$	0.0115	0.000873	$[\mathrm{m}^2/\mathrm{MN}]$	7.6
ϵ_0	0.486	$-$	$[\mathrm{m}^2/\mathrm{MN}]$	
C_ϵ^D	34.2	3.78	$[-]$	11.0
C_ϵ^V	-25.3	2.20	$[-]$	8.7
$\overset{\star}{\gamma}$	1.55	0.0188	$[-]$	1.2
γ_0	1.00	$-$	$[-]$	
C_γ^D	33.4	9.43	$[-]$	28.0
C_γ^V	-4.52	3.65	$[-]$	81.0
ψ_1	1.85	0.151	$[-]$	8.2
ψ_2	0.669	0.0277	$[-]$	4.1

Table 6.4: Values of the material parameters of the non-polar plasticity and their standard deviations.

Summary of the error analysis

Firstly, by use of the residual analysis, it has been shown that the overall fit is on an acceptable level. For the triaxial test with a confining pressure of $100\,\mathrm{kN/m^2}$, the obtained value of s_0 is higher than for the other tests in consequence of the hight accuracy of the measured data.

The result of the uncertainty analysis is that the parameter C_γ^V is definitely not identifiable with the set of chosen material tests, and the values for the parameters C_β^V and C_δ^D can only be roughly estimated. Further on, the result of the correlation analysis is that the parameters ψ_1 and ψ_2, as well as the parameters C_δ^D and C_δ^V are coupled, which denotes that they cannot be identified independently from each other. Following this, only 10 material parameters from the set $\mathbf{s}_{\mathrm{pl\,hom}}$, cf. (6.2), can succesfully be identified with the used material tests. Generally, one can try to consider additional test data from other kind of material tests to identify all material parameters. However, due to the fact that here already five different material tests have been taken into account, as a consequence of the error analysis, the number of material parameters in the model should be reduced.

Thus, the high number of 14 parameters in $\mathbf{s}_{\mathrm{pl\,hom}}$ can be reduced by disregarding the

parameters C_γ^V, C_β^V and C_δ^D as a result of the uncertainty analysis. Furthermore, as a result of the correlation analysis, only one of the parameters ψ_1 and ψ_2 has to be taken into account, e. g., by setting $\psi_1 = 1$. Following this, the 14 material parameters can be reduced to a set of 10 material parameters, without a decline of the quality of the fit. Anyhow, the identification with consideration of all 14 material parameters was necessary, since only with the error analysis, one knows which parameters can be neglected and which are essential for the description of the behavior observed in the measurements.

Thus, in the next step, the identification procedure could be repeated with only 10 parameters selected in way described above. This is not demonstrated in the context of this work, because the procedure is similar to the identification process demonstrated in the sections above. Moreover, for the following computations of the micropolar behavior the complete set of 14 parameters is used. Note that although four material parameters have not been determined successfully, the behavior observed in the material tests can be well described with the complete set of identified material parameters.

r_{ij}	$\overset{\star}{\beta}$	C_β^D	C_β^V	$\overset{\star}{\delta}$	C_δ^D	C_δ^V	$\overset{\star}{\epsilon}$	C_ϵ^D	C_ϵ^V	$\overset{\star}{\gamma}$	C_γ^D	C_γ^V	ψ_1	ψ_2
$\overset{\star}{\beta}$	1.00	0.36	−0.42	−0.45	−0.65	0.66	0.79	0.19	−0.16	0.07	0.45	−0.46	0.79	0.79
C_β^D		1.00	−0.49	−0.26	−0.24	0.29	0.30	−0.44	0.23	0.31	0.21	−0.38	0.54	0.56
C_β^V			1.00	0.13	0.19	−0.20	−0.27	−0.06	−0.72	−0.03	0.04	0.12	−0.39	−0.35
$\overset{\star}{\delta}$				1.00	0.63	−0.78	−0.45	−0.09	0.16	−0.21	−0.22	0.24	−0.39	−0.44
C_δ^D					1.00	−0.96	−0.79	−0.44	0.35	−0.11	−0.46	0.35	−0.61	−0.64
C_δ^V						1.00	0.77	0.35	−0.32	0.22	0.41	−0.37	0.62	0.66
$\overset{\star}{\epsilon}$							1.00	0.58	−0.45	0.38	0.57	−0.62	0.88	0.89
C_ϵ^D								1.00	−0.36	0.12	0.24	−0.15	0.26	0.24
C_ϵ^V									1.00	−0.25	−0.44	0.34	−0.25	−0.30
$\overset{\star}{\gamma}$										1.00	0.02	−0.56	0.46	0.50
C_γ^D											1.00	−0.71	0.58	0.58
C_γ^V												1.00	−0.75	−0.75
ψ_1													1.00	0.97
ψ_2														1.00

Table 6.5: Complete correlation matrix for the parameters of the non-polar plasticity.

6.2   Parameter identification of the micropolarity

The second step of the overall identification process concerns the remaining parameters of the *Cosserat* theory

$$\mathbf{s}_{\mathrm{Co}} = (\mu_c,\ l_c,\ k_\sigma,\ k_\mu)^T\,, \tag{6.8}$$

which are relevant when micropolar effects occur, e. g., in the case of shear banding. For the identification of these parameters, a full computation of the boundary-value problem of the biaxial test with an adequate spatial and temporal discretization is required. Thus, the numerical effort is very high and, as a result, the effectivity of the identification method is an important factor.

First of all, the principial effects of the strain localization are briefly introduced by use of numerical results of the simulation of the biaxial test. Following this, the semi-analytical computed sensitivities are verified by use of the numerically computed sensitivities. Before the identification is carried out, the whole identification process is tested while using the parameter re-identification method and, finally, the real identification process is shown on the basis of experimental data from biaxial tests.

6.2.1   Hardening and softening effects at the biaxial test

The principal reason for the consideration of the softening effect, in addition to the material hardening, cf. Section 2.4.5, is that this effect is the reason for material instabilities and, therewith, for the incoming of the shear band. This is demonstrated by the simulation of the biaxial test, cf. Figure 6.7. Therein, the boundary-value problem of the biaxial test is shown, which is described in Appendix A.2, whereas an exemplary stress-strain relation is shown in Figure 6.8 (a). In Figure 6.7, the evolution of the yield criterion on two specific points is illustrated, whereby the actual stress state is marked by points. Firstly, for a point (point 1) inside the shear band, and, secondly, for a point (point 2) outside the shear zone. Regarding these two diagrams, one can observe that during the begining of the loading process the yield condition increases in both points in the same manner, as far as the maximum yield stress is reached. Afterwards, at a specific position, which is weakened for the simulation, the yield surface decreases. This is the consequence of the dilatant plastic flow, which is considered in the pasticity model for the simulation of the material softening, cf. Section 2.4.5. Therewith, the material stiffness in this point continuously decreases connected with an increase of the plastic flow and so on. This behavior yields the incoming of a shear and, therewith, the failure of the material, and can be seen in the diagram of the point inside the shear band (point 1), wherein the decrease of the yield condition can be observed. In contrast, the digram of the point outside the shear band (point 2) shows no decrease of the yield criterion. Taking a more precise view on the diagram for point 2, one can see that the stress, marked by the points, goes inside the yield condition, i. e., inside the elastic domain, which denotes that the material, in this point, is unloaded.
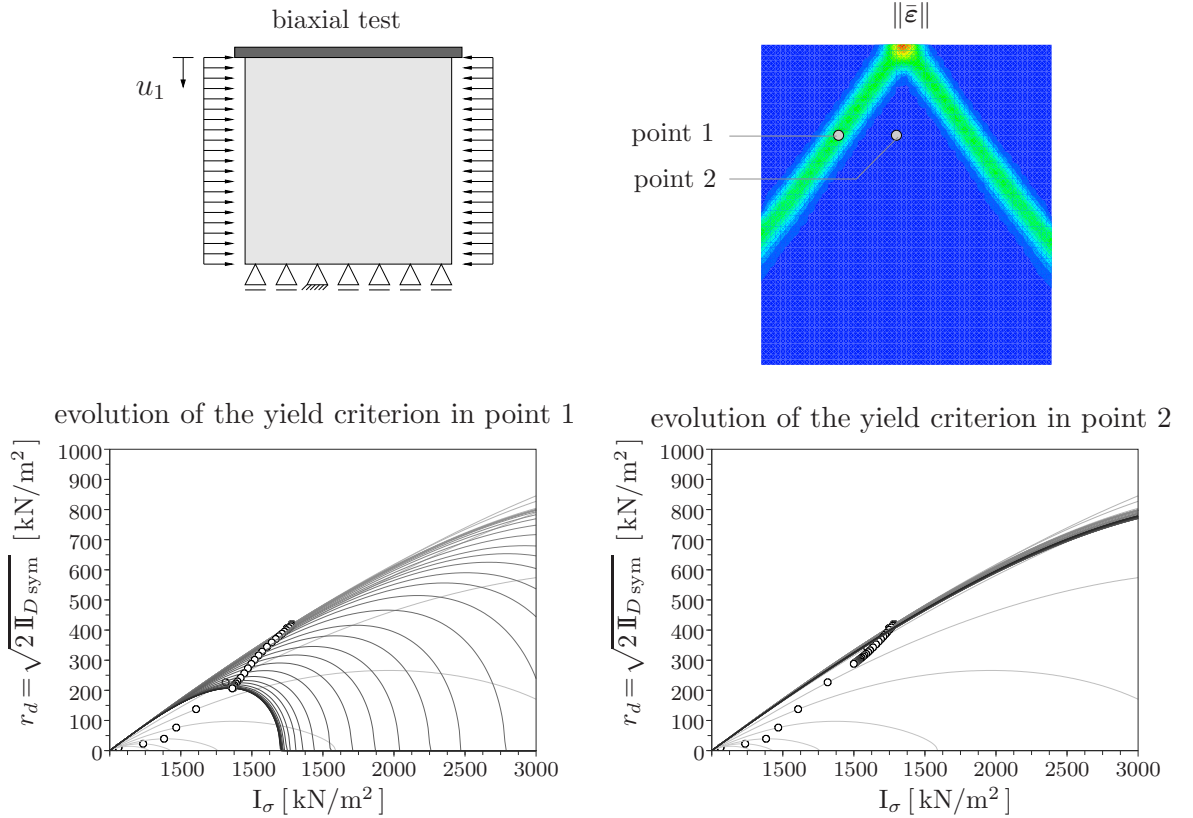
Figure 6.7: Hardening and softening behavior of the material inside and outside the localization zone.

6.2.2 Computation of the sensitivities

The verification of the semi-analytically computed sensitivities using the methods described in Section 5.2 is carried out for of the vertical stress σ_{11} as well as for the thickness H of the incoming shear band by use of biaxial tests. For both cases, this is performed for all parameters $\mathbf{s}_{\mathrm{Co}}$ of the *Cosserat* theory, cf. Figure 6.8 and Figure 6.9. Therein, the normalized values for the sensitivities of the stress σ_{11} and of the shear band thickness H are used in sake of a better comparability of the different sensitivities, i.e.,

$$(\frac{\mathrm{d}\sigma_{11}}{\mathrm{d}s_i})_{\mathrm{norm}} = \frac{\mathrm{d}\sigma_{11}}{\mathrm{d}s_i}\frac{s_i}{\sigma_{11}} \quad \text{and} \quad (\frac{\mathrm{d}H}{\mathrm{d}s_i})_{\mathrm{norm}} = \frac{\mathrm{d}H}{\mathrm{d}s_i}\frac{s_i}{H}, \tag{6.9}$$

where s_i is the $i-$th component of $\mathbf{s}_{\mathrm{Co}}$.

In Figure 6.8 (a), the vertical stress versus the vertical strain is shown. Therein, it can be recognized that the decrease of the stress coincides with the development of the shear band. The comparison of the normalized semi-analytical and the numerical sensitivities is visualized in Figure 6.8 (b), where a very good correlation can be seen, i.e., the lines for l_c, μ_c and k_σ are almost congruent. However, for the sensitivities with respect of k_μ, a small difference between the semi-analytical and the numerical sensitivities occurs. The reason therefore can be found in rounding errors due to reaching the machine accuracy during the computation of the numerical sensitivities. Furthermore, in Figure 6.8 (b), it

can be recognized that the influence of the parameters in consequence of the *Cosserat* theory only appears after the decrease of the stress, which is coincident with the incoming of the shear band.
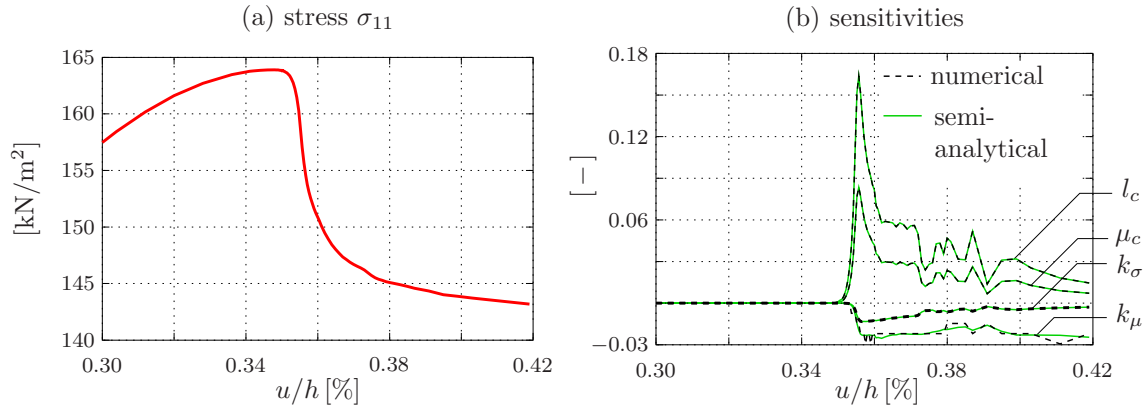
Figure 6.8: Comparison between numerically and semi-analytically calculated sensitivities of the vertical stress σ_{11}.

In Figure 6.9 (a), the computed thickness of the shear band is illustrated, while in Figure 6.9 (b), the corresponding normalized sensitivities (6.9) are shown. Again, a good correlation between the numerically and the semi-analytically computed values can be observed. The congruence of the numerical and semi-analytical values indicates the correctness of the implemented semi-analytical sensitivities analysis but also the correctness of the implemented material tangent, because the semi-analytical computation of the sensitivities is based on the material tangent, cf. (5.20). It is furthermore observed from Figure 6.8 (b) and Figure 6.9 (b) that the sensitivities of l_c and μ_c are scaled by a constant factor. This fact gives a first hint to a full correlation of these parameters.
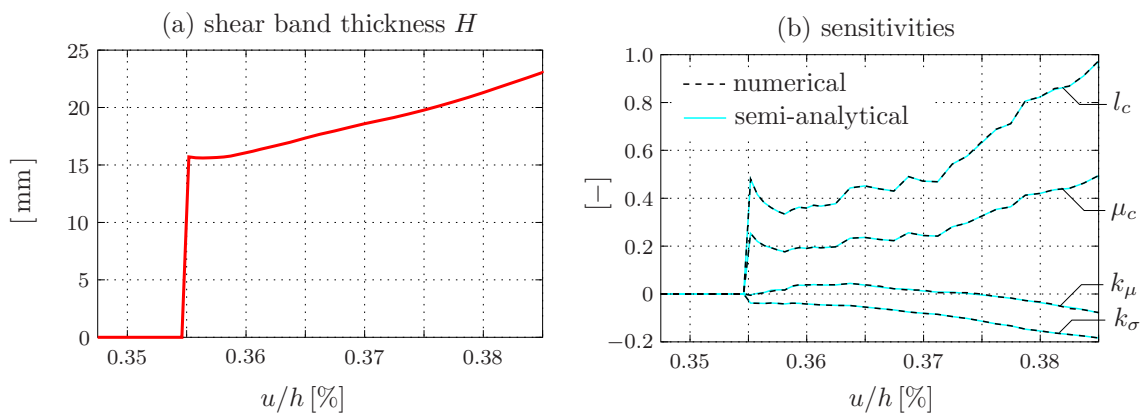
Figure 6.9: Comparison between numerically and semi-analytically calculated sensitivities of the shear band thickness.

6.2.3   Parameter re-identification

For the realization of the parameter re-identification, a numerical solution with a set $\bar{\mathbf{s}}$ of reference parameters is computed. The results of this computation are used as virtual test data. Afterwards, the reference parameters $\bar{\mathbf{s}}$ are disturbed, and the task is to re-identify the original values $\bar{\mathbf{s}}$ by use of the parameter identification process. Hereby, the identification is carried out based on the overall vertical stress σ_{11} under the load platen in N_σ load steps in combination with the thickness H of the shear band in N_H load steps. This procedure yields the following multi-criterion objective function, which has to be minimized:

$$f(\mathbf{s}) = \frac{1}{N_\sigma\,\sigma_0^2} \sum_{i=1}^{N_\sigma} [\,\sigma_{11}(\mathbf{s}) - \tilde{\sigma}_{11}\,]^2 + \frac{1}{N_H\,H_0^2} \sum_{i=1}^{N_H} [\,H(\mathbf{s}) - \tilde{H}\,]^2\,. \tag{6.10}$$

Therein, the stress is normalized with σ_0 and the shear band thickness with H_0.

Basically, all additional parameters of the *Cosserat* theory (μ_c, l_c, k_σ, k_μ) have to be identified in this way. But for a first test of the method, the identification is only carried out for the parameters l_c and k_σ. The stress σ_{11}, which is used in (6.10), is plotted in Figure 6.10 for the reference values $\bar{\mathbf{s}}$ as well as for the modified values. The corresponding material parameters are listed in Table 6.6. As a result of the big modification of l_c from $3\,\mathrm{mm}$ to $10\,\mathrm{mm}$, there is no shear band in the first steps of the identification process, i. e., the initial shear band thickness is larger than the size of the specimen. The algorithm starts with the disturbed parameters, cf. Table 6.6, and after 22 iterations, the reference parameters are recovered.

Further on, the correlation matrix of the parameters of the *Cosserat* theory on the basis of the objective function (6.10),

$$\mathbf{K} = \left[\frac{1}{\sigma_0^2} \sum_{i=1}^{N_\sigma} (\frac{\mathrm{d}\sigma_{11}}{\mathrm{d}\mathbf{s}_{\mathrm{Co}}})^T \frac{\mathrm{d}\sigma_{11}}{\mathrm{d}\mathbf{s}_{\mathrm{Co}}} + \frac{1}{H_0^2} \sum_{i=1}^{N_H} (\frac{\mathrm{d}H}{\mathrm{d}\mathbf{s}_{\mathrm{Co}}})^T \frac{\mathrm{d}H}{\mathrm{d}\mathbf{s}_{\mathrm{Co}}} \right]^{-1}, \tag{6.11}$$
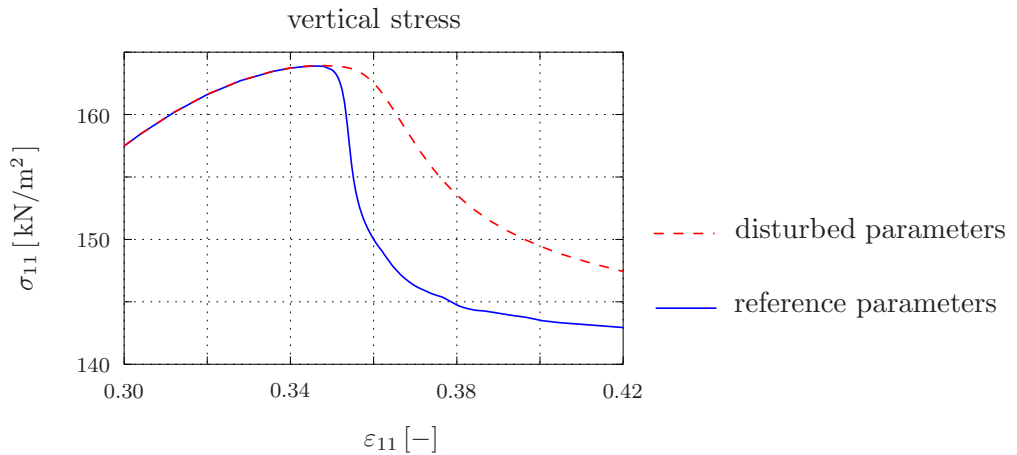
Figure 6.10: Vertical stresses with reference and disturbed parameters.

	l_c^S	k_σ
reference parameter	3.0 [mm]	10.0 [−]
disturbed parameter	10.0 [mm]	0.0 [−]

Table 6.6: Values of the reference and the modified parameters.

is analyzed for all parameters governing the polar behavior $\mathbf{s}_{\mathrm{Co}}$, cf. Table 6.7. Therein, a total correlation between the parameters of the elastic domain of the *Cosserat* theory, l_c and μ_c is observed, while the correlations between the other parameters are in an uncritical range. This behavior can also be observed on the sensitivities of the stress, cf. Figure 6.8, as well as of the shear band thickness, cf. Figure 6.9, with respect to l_c and μ_c. Therein, it is obvious that both curves only differ by a constant factor. As a consequence of this correlation at subsequent identifications, only one parameter, either l_c or μ_c, can be fitted independently.

	μ_c	l_c	k_σ	k_μ
μ_c	1	−0.998	0.506	0.439
l_c		1	−0.534	−0.423
k_σ			1	0.138
k_μ				1

Table 6.7: Correlation matrix for the parameters of the *Cosserat* theory.

6.2.4   Parameter identification of the micropolar behavior

After the principal applicability of the identification method has been demonstrated by the parameter re-identification, the identification of the *Cosserat* parameters is finally demonstrated on the basis of measured data. Therefore, in the same manner as above for the parameter re-identification, the vertical stress σ_{11} as well as the thickness H of the shear band is considered. Thus, the same objective function, which is used for the parameters re-identification (6.10), is applied, where the shear band thickness is taken into account only at the final state, i. e., $N_H = 1$.

Computation of the shear band thickness using meassured data

The first step of the identification process is the computation of the shear band thickness based on stereophotogrammetric measurements from the university of Grenoble. The measured strain data (norm of strain) are exhibited in Figure 6.11. Basing on these measured data, the shear band thickness has to be dertermined by use of the method described in Section 4.4. The results obtained thereby are shown in the diagram in Figure 6.11. Regarding this diagram, it seems, in contrast to the computed results, that
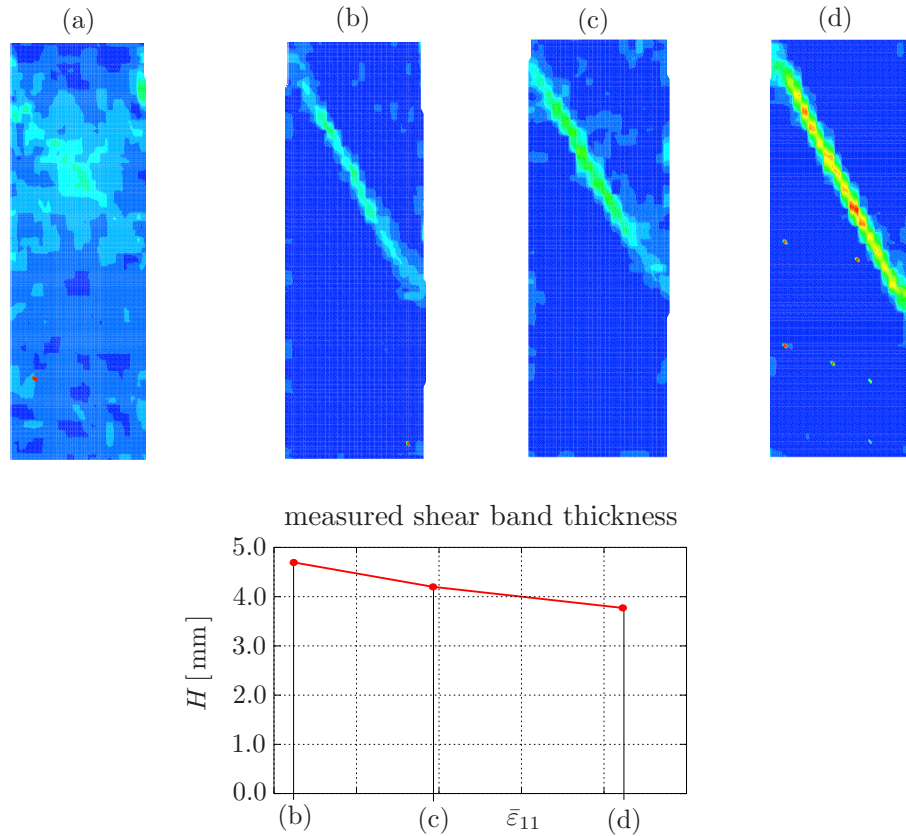
Figure 6.11: Determination of the measured shear band thickness.

the shear band thickness decreases after the incoming of the shear band. But, regarding the evolution strain in Figure 6.11, it is obvious that a continuous shear band is only visible in the last state. Thus, the apparent decreasing of the shear band thickness is rather the effect of the development of the shear band.

Finding of the decrease in the stress-strain line

Due to the fact that the particular time, when the shear band occurs, varies during the identification procedure, only the decrease of the stress is used in the identification process. Consequently, a criterion for the definition of the beginning of the decrease of the stress-strain curve is necessary. In Figure 6.13, it can be seen that the start of the decrease coincides with the minimum of the curvature. Following this, the minimum curvature of the stress-strain relationship is used as the criterion for the begin of the decrease. Due to the fact that every small discontinuity in the stress-strain curve yields a peak of the curvature, a direct computation of the curvature using the numerical differentiation method cannot be applied. Instead a method has been developed, which enables a smoothing of the curvature κ_i at the data point i. Therefore, two straight lines, $g_{i\,\text{left}}$ and $g_{i\,\text{right}}$, are defined, which are found as regression lines, i.e., $g_{i\,\text{left}}$ is the regression line for the points in the region $(\varepsilon_i - \varepsilon_{\text{left}})$ and $g_{i\,\text{right}}$ is the regression line including the points in $(\varepsilon_i + \varepsilon_{\text{right}})$,
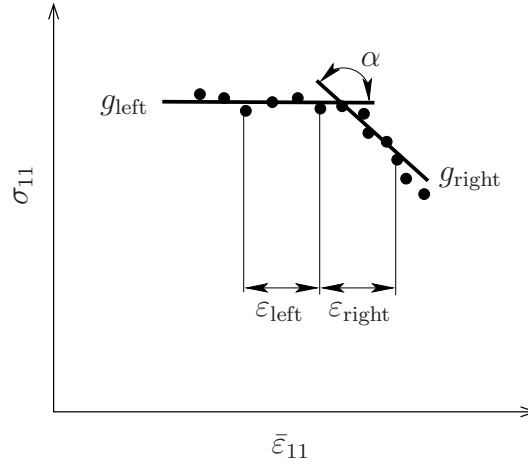
Figure 6.12: Determination of the smooth curvature of the stress strain curve.

cf. Figure 6.12. Thus, one obtains

$$g_{i\,\text{left}} = \sigma_{0\,i}^{\text{left}} + m_{i\,\text{left}}\,\bar{\varepsilon}_{11} \quad \text{and} \quad g_{i\,\text{right}} = \sigma_{0\,i}^{\text{right}} + m_{i\,\text{right}}\,\bar{\varepsilon}_{11}\,, \tag{6.12}$$

where $\sigma_{0\,i}^{\text{left}}$ and $\sigma_{0\,i}^{\text{right}}$ are non-relevant constants, whereas $m_{i\,\text{left}}$ and $m_{i\,\text{right}}$ represent the slope of the straight lines. Following the methods of the linear regression, $m_{i\,\text{left}}$ is given by

$$m_{i\,\text{left}} = \frac{\displaystyle\sum_{j=1}^{N_{\text{left}}} (\sigma_j - \sigma_i)\,(\varepsilon_j - \varepsilon_i)}{\displaystyle\sum_{j=1}^{N_{\text{left}}} (\varepsilon_j - \varepsilon_i)^2} \quad \text{with} \quad \varepsilon_i > \varepsilon_j \geq (\varepsilon_i - \varepsilon_{\text{left}})\,, \tag{6.13}$$

and $m_{i\,\text{right}}$ is calculated similarly, using the region $(\varepsilon_i - \varepsilon_{\text{right}}) \geq \varepsilon_j > \varepsilon_i$. Therewith, the smoothed curvature of the data point i can be computed via the difference of $m_{i\,\text{left}}$ and $m_{i\,\text{right}}$:

$$\kappa_i = \frac{m_{i\,\text{left}} - m_{i\,\text{right}}}{\frac{1}{2}\left(\varepsilon_{\text{left}} + \varepsilon_{\text{right}}\right)}\,. \tag{6.14}$$

Therein, $\varepsilon_{\text{left}} = \varepsilon_{\text{right}} = 0.003$ is chosen. Hence, with this method, the minimum value of the curvature can be determined and used as the initial point for the fit..

Results of the identification process

The identification of the remaining parameters of the *Cossert* theory principially means the determination of the values for $\mathbf{p}_{\text{inhom}} = (l_c,\, \mu_c,\, k_\sigma,\, k_\mu)^T$. In the section above, namely, the parameter re-identification, it has been shown that on the basis of the biaxial test data an independent identification of l_c and μ_c is impossible, because they are are totally correlated, cf. Table 6.7. As a consequence of these results, only the parameter l_c of the micropolar elasticity is taken into account, whereas μ_c is set to μ. The results of the identification are shown in Figure 6.13, where the measured stress versus the computed values

with the identified parameters as well as the measured and the computed distribution of the strain are shown. By comparing the strain distribution, it can be seen that the angle of the shear band fits also well, although the shear band angle has not been considered in the identification.
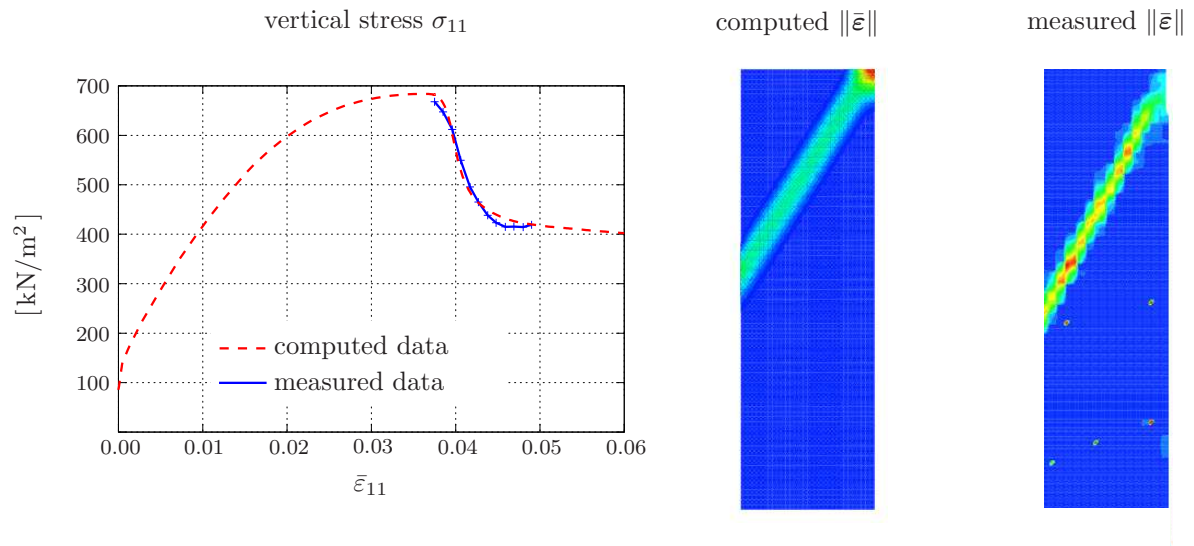

Figure 6.13: Identification of the parameters of the micropolar theory by use of stress strain data in combination with the shear band thickness.

Chapter 7: Simulation of the Granular Media Via a Particle Model

Whereas in the above chapters, a continuum model for the simulation of the localization phenomena of granular media was presented, in this chapter, the discrete description using a particle model is presented. This a completely different approach, whereby the material grains are directly modeled as a package of rigid bodies containing translational and rotational degrees of freedom. The aim of this chapter is to demonstrate that both methods yield the same results qualitatively, i. e., one has to show that rotations and couple stress appear by use of the particle model in the same manner, as it has been observed during simulations with the *Cosserat* theory along the localization zone. Therewith, one can show that granular materials can generally be classified as micropolar *Cosserat* materials. This is not automatically given in consequence of the granular structure of the materials. In fact, the grain structure of the material directly leads to rotations of the single grains, but one has to show, based on a homogenization method, that these rotations are not statistically distributed, i. e., that after the homogenization procedure a significant mean value remains. Furthermore, one has to show that the homogenized rotations and the curvatures associated therewith, are connected with couple stresses in the sense of the *Cosserat* theory.

The modeling of granular media on the micro-level by use of the *Discrete Element Method* (DEM) was firstly introduced in 1979 with the work by *Cundall & Strack* [23]. Furthermore, some current developments in the context of the modeling of micropolar materials are given by the works of *Chang & Ma* [21], *Lätzel* [89], or *Luding* [92, 93]. The critical point in the comparison of the results from discrete particle model with the continuum approach is the formulation of an appropriate homogenization strategy based on a *Representative Elementary Volume* (REV). For this purpose, a lot of methods have been developed in the last years, cf., e. g., *Bear & Bachmat* [6], *Hashin* [73], *Hill* [77] or *Schröder* [120]. Moreover, especially for granular media, methods have been developed by *Diebels & Ehlers* [30], *Ehlers* et al. [50] or *Kruyt & Rothenburg* [84].

This chapter begins with the introduction of the applied two-dimensional particle model, cf. Section 7.1. Afterwards, the used homogenization strategy following the paper of *Ehlers* et al. [50] is discussed, cf. Section 7.2. The main issue of this chapter, the comparison between the continuum and the particle model, is carried out by use of the boundary value problem of the biaxial test, which has been used within this work for the parameter identification. Hence, the boundary conditions of the biaxial test must be simulated within the particle model, cf. Section 7.3, before the results of the two approaches can finally be compared in Section 7.4.

7.1 Particle model

The microscopic modeling, in the framework of the *Molecular Dynamics* (MD), gener-
ally, bases on the dynamics of rigid bodies, whereby, the contacts among two or more
particles (particle-particle contact) are modeled by a system of springs, viscous dampers
and friction elements, cf. Figure 7.3. Furthermore, the *Dirichlet* boundary conditions are
taken into account by use of rigid walls and the formulation of the contact forces between
the particles and the rigid wall (particle-wall contact), whereas the *Neumann* boundary
conditions are realized by direct forces on the boundary particles. In the presented work,
a two-dimensional model with circular particles is used, whereby translations and rota-
tions of the particles are considered. In consequence, every particle has three degrees of
freedom, two translations and one rotation. The mechanical properties of the particle
ensemble are controlled primarily by the contact laws of the particle-particle contacts,
apart from the density of the package and the particle-size distribution.

In the present section, the particle model itself is described, whereas, the boundary con-
ditions, for the special case of the biaxial test, are formulated in Section 7.3. The particle
model is described in three steps, firstly, the *Newton*ian equations of motion for a single
particle are discussed, secondly the particle-particle contact law is described, and, finally,
the time integration method is briefly illustrated.

7.1.1 Equations of motion

Following the *Newton*ian mechanical description of the motion of a rigid body, the axiom
of conservation of momentum for one particle $\mathcal{P}^{(i)}$ reads:

$$m_p^{(i)}\, \ddot{\mathbf{x}}_M^{(i)} = \sum_{c=1}^{N}(\mathbf{f}_c^{(i)} + \mathbf{f}_B^{(i)} + m_p^{(i)}\,\mathbf{g})\,. \tag{7.1}$$

Therein, $m_p^{(i)}$ is the mass and $\mathbf{x}_M^{(i)}$ is the actual position vector to the center of the particle
$\mathcal{P}^{(i)}$. Moreover, $\mathbf{f}_c^{(i)}$ are the contact forces acting on the particle in consequence of N
particle-particle contacts, $\mathbf{g}$ represents the overall gravitation, and $\mathbf{f}_B^{(i)}$ is the force in
consequence of boundary effects, e.g., in the case of *Dirichlet* boundaries, $\mathbf{f}_B^{(i)}$ is given by
the particle-wall contact force $\mathbf{f}_w^{(i)}$, cf. Figure 7.1. Due to the fact that within the particle
model also the rotations $\boldsymbol{\varphi}_p^{(i)}$ of particles are considered, the axiom of the conservation of
moment of momentum is also required. Thus, for the particle $\mathcal{P}^{(i)}$, one obtains

$$\Theta_p^{(i)}\, \dot{\boldsymbol{\omega}}_p^{(i)} = \sum_{c=1}^{N}(\mathbf{r}_c^{(i)} \times \mathbf{f}_c^{(i)} + \mathbf{m}_B^{(i)})\,, \tag{7.2}$$

where $\Theta_p^{(i)}$ is the moment of inertia of the circular particle, and $\boldsymbol{\omega}_p^{(i)} = \dot{\boldsymbol{\varphi}}_p^{(i)}$ is the rotational
velocity of $\mathcal{P}^{(i)}$. Furthermore, $\mathbf{r}_c^{(i)}$ is the vector from the center of the particle $\mathcal{P}^{(i)}$ to the
contact point of a particle-particle contact, whereas $\mathbf{m}_B^{(i)}$ represents the moments resulting
from boundary effects, e.g., in case of *Dirichlet* boundaries $\mathbf{m}_B^{(i)} = \mathbf{r}_w^{(i)} \times \mathbf{f}_w^{(i)}$, where $\mathbf{r}_w^{(i)}$
points from the particle center to the contact point of the boundary wall, cf. Figure 7.1.
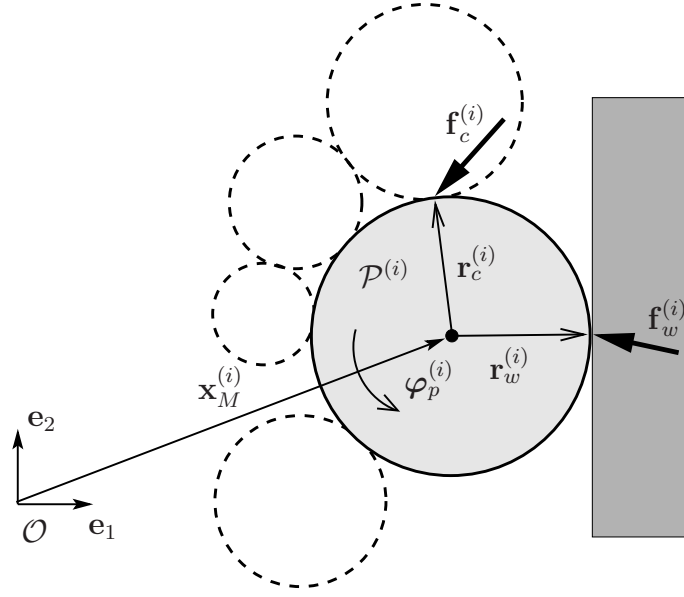
Figure 7.1: Exemplary contact situation of the particle $\mathcal{P}^{(i)}$.

7.1.2 Constitutive settings for the particle-particle contact

Whereas in the continuum model the macroscopic stress-strain relation is defined with the constitutive equations, cf. Section 2.4, in the particle model the constitutive modeling consists in the formulation of the particle-particle contact laws on the micro-level. These particle-particle contact laws are formulated independently in the normal and tangential directions. Thus, firstly, the contact force $\mathbf{f}_c^{(i)}$, acting on the particle $\mathcal{P}^{(i)}$ due to the contact with $\mathcal{P}^{(j)}$, is split into a normal part $\mathbf{f}_{cn}^{(i)}$ and a tangential part $\mathbf{f}_{ct}^{(i)}$:

$$\mathbf{f}_c^{(i)} = \mathbf{f}_{cn}^{(i)} + \mathbf{f}_{ct}^{(i)} = -f_{cn}^{(i)}\,\mathbf{n}^{(ij)} + f_{ct}^{(i)}\,\mathbf{t}^{(ij)}\,. \tag{7.3}$$

Therein, the positive normal contact force $\mathbf{f}_{cn}^{(i)} = -f_{cn}^{(i)}\,\mathbf{n}^{(ij)}$ is defined in negative direction of the normal vector $\mathbf{n}^{(ij)}$ pointing from the particle $\mathcal{P}^{(i)}$ to particle $\mathcal{P}^{(j)}$, whereas the positive tangential contact force $\mathbf{f}_{ct}^{(i)} = f_{ct}\,\mathbf{t}^{(ij)}$ is defined in direction of the tangential vector $\mathbf{t}^{(ij)}$, perpendicular to the $\mathbf{n}^{(ij)}$ by use of a right-hand coordinate system, cf. Figure 7.2.

Considering a real particle-particle contact between, e.g., two grains of sand, it is obvious that the deformation of the grains will be very small and mostly elastic. In contrast to that, in the tangential direction, the sliding of the particles has to be considered as an inelastic displacement. Following this, for the formulation of the contact forces $\mathbf{f}_{cn}^{(i)}$ in the normal direction, an elastic constant $E_n^{(ij)}$ is taken into account, which is represented by a spring between the particle $\mathcal{P}^{(i)}$ and $\mathcal{P}^{(j)}$. Furthermore, a numerically motivated viscous *Newto*nian damper with the damping constant $D_n^{(ij)}$ is considered, cf. Figure 7.3. Hence, the contact law in normal direction reads:

$$f_{cn}^{(i)} = E_n^{(ij)}\,\Delta^{(ij)} + D_n^{(ij)}\,\dot{\Delta}^{(ij)}\,. \tag{7.4}$$
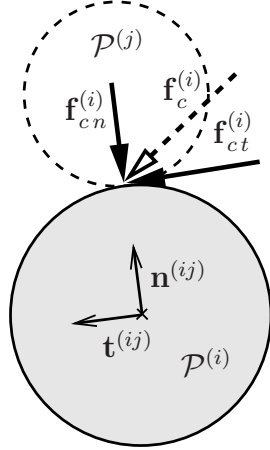
Figure 7.2: Split of the acting force in a normal and a tangential part.

where $\Delta^{(ij)}$ is the overlap of the particles $\mathcal{P}^{(i)}$ and $\mathcal{P}^{(j)}$, which is given by:

$$\Delta^{(ij)} = \left\langle \|\mathbf{x}_M^{(j)} - \mathbf{x}_M^{(i)}\| - (r^{(i)} + r^{(j)}) \right\rangle , \qquad (7.5)$$

wherein $r^{(i)}$ and $r^{(j)}$ are the radii of $\mathcal{P}^{(i)}$ and $\mathcal{P}^{(j)}$ and $\langle \cdot \rangle$ is defined via $\langle \cdot \rangle := \frac{1}{2} \left[(\cdot) + |(\cdot)| \right]$. Due to the fact that with the tangential contact law the sliding of the particles has to be modeled in addition to the spring and the viscose damper, a frictional element has been included, cf. Figure 7.3. Thus, for the formulation of the tangential contact law, firstly, the relative velocity $v_t^{(ij)}$ between the contacting particles $\mathcal{P}^{(i)}$ and $\mathcal{P}^{(j)}$ is required, which takes the form:

$$v_t^{(ij)} := \dot{u}_t^{(ij)} = \mathbf{t}^{(ij)} \cdot (\mathbf{x}_M^{(j)} - \mathbf{x}_M^{(i)}) + r^{(i)} \, \boldsymbol{\omega}_p^{(i)} + r^{(j)} \, \boldsymbol{\omega}_p^{(j)} . \qquad (7.6)$$

Moreover, in order to consider a tangential spring and a frictional element, the relative tangential displacement $u_t^{(ij)}$ has to be computed by the integration of $\dot{u}_t^{(ij)}$ during the contact time T_e:

$$u_t^{(ij)} := \int_{(T_e)} \dot{u}_t^{(ij)} \, \mathrm{d}t . \qquad (7.7)$$

Note that $\mathbf{v}_t^{(ij)} = v_t^{(ij)} \, \mathbf{t}^{(ij)}$ is a vector in the tangential direction, whereas $u_t^{(ij)}$ has no unique direction, because the direction of the tangential vector $\mathbf{t}^{(ij)}$ varies during the contact time. With the definitions (7.6) and (7.7), the tangential contact forces can be formulated by use of a viscoelasto-plasticity approach:

$$f_{ct}^i = E_t^{(ij)} (u_t^{(ij)} - u_{tp}^{(ij)}) + D_t^{(ij)} (\dot{u}_t^{(ij)} - \dot{u}_{tp}^{(ij)}) . \qquad (7.8)$$

Therein, $E_t^{(ij)}$ is the elastic constant and $D_t^{(ij)}$ is the damping constant between the particles $\mathcal{P}^{(i)}$ and $\mathcal{P}^{(i)}$. Moreover, in (7.8) only the elastic parts of the relative displacement

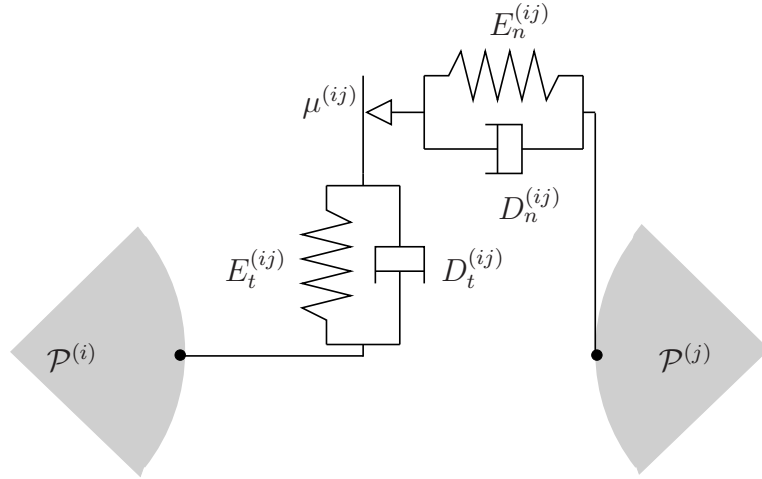$$u_{te}^{(ij)} = u_t^{(ij)} - u_{tp}^{(ij)} \qquad (7.9)$$

Figure 7.3: Schematic sketch of the particle-particle contact.

and the relative velocity

$$\dot{u}_{te}^{(ij)} = \dot{u}_{t}^{(ij)} - \dot{u}_{tp}^{(ij)} \tag{7.10}$$

are taken into account. Hence, an evolution law for the computation of the plastic relative displacement $u_{tp}^{(ij)}$, which represents an internal variable, is required. In comparison to the elasto-plasticity used in the continuum model, cf. Section 2.4.4, the *Coulomb*'s frictional law is formulated in the form the following yield condition:

$$F := \sqrt{\mathbf{f}_{ct}^{(i)} \cdot \mathbf{f}_{ct}^{(i)}} - \mu^{(ij)} \, f_{cn}^{(i)}, \tag{7.11}$$

where $\mu^{(ij)}$ is the frictional constant between the particle $\mathcal{P}^{(i)}$ and $\mathcal{P}^{(j)}$. Due to the fact that with $u_{tp}^{(ij)}$ only one internal variable exists, the plastic evolution is directly given via the *Kuhn-Tucker* conditions,

$$F \leq 0, \quad \Lambda \geq 0, \quad \Lambda \, F = 0, \tag{7.12}$$

which results in

$$\dot{u}_{tp}^{(ij)} = \Lambda. \tag{7.13}$$

This result will also obtained, if the evolution is written in the same manner as for the continuum model, cf. (2.79) in Section 2.4, using F as plastic potential:

$$\dot{\mathbf{u}}_{tp}^{(ij)} = \dot{u}_{tp}^{(ij)} \, \mathbf{t}^{(ij)} = \Lambda \frac{\partial F}{\partial \mathbf{f}_{ct}^{(i)}} = \Lambda \, \mathbf{t}^{(ij)}. \tag{7.14}$$

7.1.3 Time integration method

For the numerical simulation, the equations of motion (7.1) and (7.2) must be solved numerically. This is carried out by using the explicit *Verlet* integration scheme, also

known as explicit *Newmark* scheme. Thereby, the unknown particle positions $\mathbf{x}_M^{(i)}$ and rotations $\boldsymbol{\varphi}_p^{(i)}$ at the time $t + \Delta t$ are computed based on the known values at the time t and $t - \Delta t$ by use of the following formulations:

$$
\mathbf{x}_M^{(i)}(t + \Delta t) = \mathbf{f}_p^{(i)}(t)\frac{\Delta t^2}{m_p^{(i)}} + 2\,\mathbf{x}_M^{(i)}(t) - \mathbf{x}_M^{(i)}(t - \Delta t) \quad \text{and}
$$

$$
\boldsymbol{\varphi}_p^{(i)}(t + \Delta t) = \mathbf{m}_p^{(i)}(t)\frac{\Delta t^2}{\Theta_p^{(i)}} + 2\,\boldsymbol{\varphi}_p^{(i)}(t) - \boldsymbol{\varphi}_p^{(i)}(t - \Delta t)\,.
$$

(7.15)

Therein, $\mathbf{f}_p^{(i)}(t)$ and $\mathbf{m}_p^{(i)}(t)$ are the resulting total force and moment in the center of the particle $\mathcal{P}^{(i)}$ due to N contacting particles, i. e.,

$$
\mathbf{f}_p^{(i)}(t) = \sum_{i=1}^{N}[\mathbf{f}_c^{(i)}(t) + \mathbf{f}_B^{(i)}(t) + m_p^{(i)}\,\mathbf{g}] \quad \text{and}
$$

$$
\mathbf{m}_p^{(i)}(t) = \sum_{i=1}^{N}[\mathbf{r}_c^{(i)}(t) \times \mathbf{f}_c^{(i)}(t) + \mathbf{m}_B^{(i)}(t)]\,.
$$

(7.16)

Furthermore, due to the viscous damping elements in the particle model, the velocity $\dot{\mathbf{x}}_M^{(i)}$ and the rotational velocity $\boldsymbol{\omega}_p^{(i)} = \dot{\boldsymbol{\varphi}}_p^{(i)}$ are required, which are computed via

$$
\dot{\mathbf{x}}_M^{(i)}(t + \Delta t) = \dot{\mathbf{x}}_M^{(i)}(t) + \mathbf{f}_p^{(i)}(t)\frac{\Delta t}{m_p^{(i)}} \quad \text{and}
$$

$$
\dot{\boldsymbol{\varphi}}_p^{(i)}(t + \Delta t) = \dot{\boldsymbol{\varphi}}_p^{(i)}(t) + \mathbf{m}_p^{(i)}(t)\frac{\Delta t}{\Theta_p^{(i)}}\,.
$$

(7.17)

7.2 Homogenization approach

The results of the simulations using the particle model consist, on the one hand, in the motions and rotations of the single particles and, on the other hand, in the contact forces between the particles. In contrast, the computations using the *Cosserat* continuum approach results in strain and curvature tensors as well as stress and couple stress tensors. Hence, for the comparison of both kinds of view, it is necessary to find strain and curvature tensors on the basis of the motion of the particles as well as stress and couple stress tensors based on the contact forces. This task is carried out via a homogenization strategy over a defined particle ensemble denoted as REV. The size of this REV has to be small enough to represent a macroscopic material point, but, otherwise, it has to be large enough to smooth local perturbations, cf. *Diebels & Ehlers* [30], *Drescher* et al. [34] or *Kruyt & Rothenburg* [84]. The homogenization strategy is illustrated very briefly in this work, the in more details interested reader is referred to the works by, *Ehlers* et al. [50], *Hashin* [73], *Nemat-Nasser & Hori* [108] or *Schröder* [120].

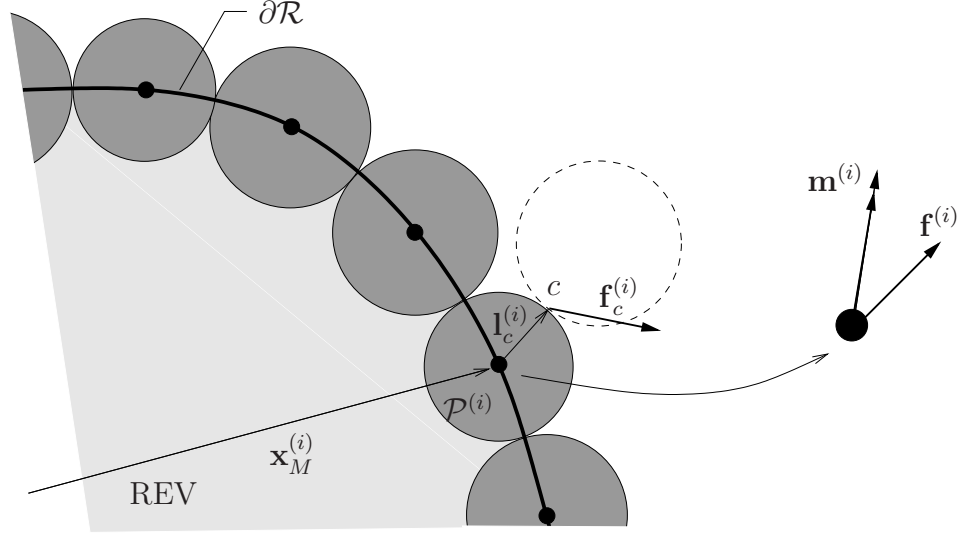### 7.2.1 From contact forces to stress and couple stresses

Figure 7.4: Boundary particles of the REV with contact forces as well as force and moment resultants, taken from [50].

Following the homogenization strategy of *Ehlers* et al. [50] for granular media, the boundary $\partial \mathcal{R}$ of the REV is represented by the mass centers of the bounding particles, cf. Figure 7.4. Hence, the resulting force $\mathbf{f}^{(i)}$ and the resulting moment $\mathbf{m}^{(i)}$ of one boundary particle $\mathcal{P}^{(i)}$ are obtained by the sum of all outside contact forces and the sum of the moments in consequence of these forces, respectively:

$$\mathbf{f}^{(i)} = \sum_{c=1}^{N^o} \mathbf{f}_c^{(i)} \quad \text{and} \quad \mathbf{m}^{(i)} = \sum_{c=1}^{N^o} \mathbf{l}_c^{(i)} \times \mathbf{f}_c^{(i)}. \tag{7.18}$$

Therein, $\mathbf{f}_c^{(i)}$ are the contact forces between the particle $\mathcal{P}^{(i)}$ and N^o particles outside, whereas $\mathbf{l}_c^{(i)}$ is the vector from the center of $\mathcal{P}^{(i)}$ to the contact point c, cf. Figure 7.4.

Regarding the REV as a material point of the polar continuum, one can interpret the forces $\mathbf{f}^{(i)}$ acting on the REV as stress vectors $\mathbf{t}$ and the moments $\mathbf{m}^{(i)}$ acting on the REV as couple stress vectors $\mathbf{m}$, cf. Figure 7.5. Thus, the following equilibrium conditions can be formulated:

$$\int_{\partial \mathcal{R}} \mathbf{t} \, \mathrm{d}a = \sum_{i=1}^{B} \mathbf{f}^{(i)} = \mathbf{0} \,,$$

$$\int_{\partial \mathcal{R}} (\mathbf{x}_M \times \mathbf{t} + \mathbf{m}) \, \mathrm{d}a = \sum_{i=1}^{B} (\mathbf{x}_M^{(i)} \times \mathbf{f}^{(i)} + \mathbf{m}^{(i)}) = \mathbf{0} \,. \tag{7.19}$$

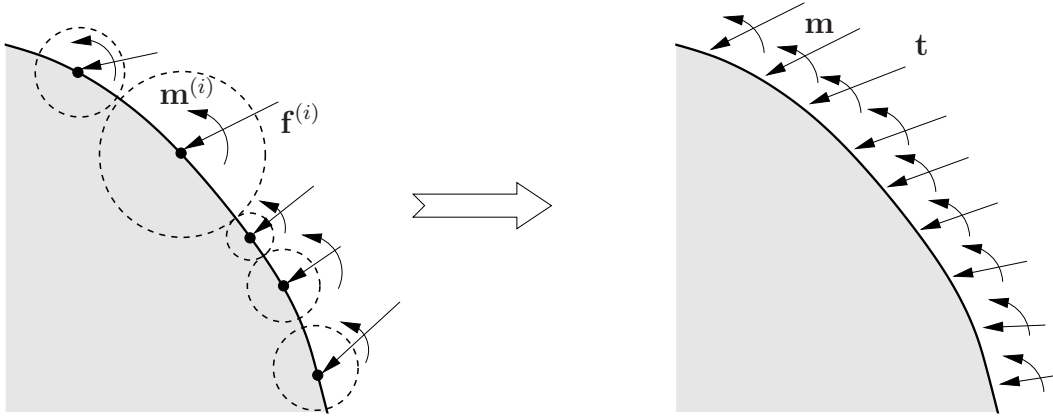Therein, B is number of particles on the boundary of the REV. Furthermore, using the

Figure 7.5: Idealization of the forces and moments acting on the REV as stress and couple stress vectors.

Cauchy theorem, the stress vector $\mathbf{t}$ is coupled with the stress tensor $\mathbf{T}$ and the couple stress vector $\mathbf{m}$ is associated with the couple stress tensor $\mathbf{M}$, i. e.,

$$\mathbf{t} = \mathbf{T}\,\mathbf{n} \quad \text{and} \quad \mathbf{m} = \mathbf{M}\,\mathbf{n}\,, \tag{7.20}$$

where $\mathbf{n}$ is the outward oriented normal vector. Following this, (7.19) can also written as:

$$\int_{\partial\mathcal{R}} \mathbf{T}\,\mathbf{n}\,\mathrm{d}a = \int_{\mathcal{R}} \mathrm{div}_M\,\mathbf{T}\,\mathrm{d}v = \mathbf{0}\,,$$

$$\int_{\partial\mathcal{R}} (\mathbf{x}_M \times \mathbf{T}\,\mathbf{n} + \mathbf{M}\,\mathbf{n})\,da = \int_{\mathcal{R}} \mathrm{div}_M(\mathbf{M}^\star + \mathbf{M})\,\mathrm{d}v = \mathbf{0}\,, \tag{7.21}$$

where $\mathrm{div}_M(\cdot)$ is the divergence operator with respect to the field $\mathbf{x}_M$, and

$$\mathbf{M}^\star := \mathbf{x}_M \times \mathbf{T} \tag{7.22}$$

contains the moments in consequence of the stress vectors acting on the REV. With (7.21) the following local statements can be formulated:

$$\mathrm{div}_M\,\mathbf{T} = \mathbf{0} \quad \text{and} \quad \mathrm{div}_M(\mathbf{M}^\star + \mathbf{M}) = \mathbf{0}\,. \tag{7.23}$$

Using (7.22), one obtains by applying the rules of tensor calculus, cf. [42],

$$\mathrm{div}_M\,\mathbf{M}^\star = \mathrm{grad}_M(\mathbf{x}_M) \times \mathbf{T} + \mathbf{x}_M \times \mathrm{div}_M\,\mathbf{T} = \mathbf{I} \times \mathbf{T} + \mathbf{x}_M \times \mathrm{div}_M\,\mathbf{T}\,. \tag{7.24}$$

Therewith, in combination with $(7.23)_2$ and under consideration of $\mathrm{div}_M\,\mathbf{T} = \mathbf{0}$ the following expression finally results in:

$$\mathrm{div}_M\,\mathbf{M} + \mathbf{I} \times \mathbf{T} = \mathbf{0}\,. \tag{7.25}$$

This result is similar to the balance of moment of momentum for the *Cosserat* continuum, cf. (2.39) in Section 2.2.

7.2.2 Homogenization of the stress and couple stress

Proceeding from an arbitrary tensor $\mathbf{A}$ defined on the micro-level, the volume average of $\mathbf{A}$ of the body $\mathcal{R}$ representing the REV is defined as

$$\langle \mathbf{A} \rangle := \frac{1}{V_R} \int\limits_{\mathcal{R}} \mathbf{A} \, \mathrm{d}v \,, \tag{7.26}$$

where V_R is the volume of $\mathcal{R}$. With the assumption that $\mathbf{A}$ represents an equilibrium quantity, i.e.,

$$\mathrm{div}_M \, \mathbf{A} = \mathbf{0} \,, \tag{7.27}$$

one can substitute the above volumetric integral by the following surface integral

$$\langle \mathbf{A} \rangle^T := \frac{1}{V_R} \int\limits_{\partial\mathcal{R}} (\mathbf{x}_M \otimes \mathbf{A}) \, \mathbf{n} \, \mathrm{d}a \,, \tag{7.28}$$

cf. *Ehlers* et al. [50] or *Schröder* [120]. Thus, replacing the abstract equilibrium quantity $\mathbf{A}$ by the stress tensor $\mathbf{T}$ one obtains

$$\langle \mathbf{T} \rangle^T = \frac{1}{V_R} \int\limits_{\partial\mathcal{R}} (\mathbf{x}_M \otimes \mathbf{T}) \, \mathbf{n} \, \mathrm{d}a = \frac{1}{V_R} \int\limits_{\partial\mathcal{R}} \mathbf{x}_M \otimes \mathbf{t} \, \mathrm{d}a \,, \tag{7.29}$$

which yields the homogenized stress tensor

$$\langle \mathbf{T} \rangle = \frac{1}{V_R} \int\limits_{\partial\mathcal{R}} \mathbf{t} \otimes \mathbf{x}_M \, \mathrm{d}a \,. \tag{7.30}$$

In order to receive a formulation for the homogenized stress of the particle model, one can replace the stress vector $\mathbf{t}$ by the outer contact forces $\mathbf{f}^{(i)}$ and the field $\mathbf{x}_M$ by the position vectors $\mathbf{x}_M^{(i)}$ of the particle centers, which yields, finally, cf. *Ehlers* at al. [50]:

$$\langle \mathbf{T} \rangle = \frac{1}{V_R} \sum\limits_{i=1}^{B} \mathbf{f}^{(i)} \otimes \mathbf{x}_M^{(i)} \,. \tag{7.31}$$

Similar to the homogenization of the stress and with intend to obtain a homogenized couple stress tensor for the particle model, $\mathbf{A}$ in (7.28) can be substituted by the equilibrium quantity $(\mathbf{M}^\star + \mathbf{M})$, viz.:

$$\langle \mathbf{M}^\star + \mathbf{M} \rangle^T = \frac{1}{V_R} \int\limits_{\partial\mathcal{R}} [\mathbf{x}_M \otimes (\mathbf{M}^\star + \mathbf{M})] \, \mathbf{n} \, \mathrm{d}a \,. \tag{7.32}$$

Moreover, using (7.22), this can also be written as

$$\langle \mathbf{M}^\star + \mathbf{M} \rangle^T = \frac{1}{V_R} \int\limits_{\partial\mathcal{R}} \mathbf{x}_M \otimes (\mathbf{x}_M \times \mathbf{t}) \, \mathrm{d}a + \frac{1}{V_R} \int\limits_{\partial\mathcal{R}} \mathbf{x}_M \otimes \mathbf{m} \, \mathrm{d}a \,. \tag{7.33}$$

Thus, $\langle \mathbf{M}^\star + \mathbf{M} \rangle$ is given via:

$$\langle \mathbf{M}^\star + \mathbf{M} \rangle = \frac{1}{V_R} \int\limits_{\partial\mathcal{R}} (\mathbf{x}_M \times \mathbf{t}) \otimes \mathbf{x}_M \, \mathrm{d}a + \frac{1}{V_R} \int\limits_{\partial\mathcal{R}} \mathbf{m} \otimes \mathbf{x}_M \, \mathrm{d}a \,. \qquad (7.34)$$

Furthermore, the cross product in the above equation can be replaced by using the *Ricci* tensor, i. e.,

$$\mathbf{x}_M \times \mathbf{t} = \overset{3}{\mathbf{E}}(\mathbf{x}_M \otimes \mathbf{t}) \,. \qquad (7.35)$$

With a view to the particle model, one can substitute $\mathbf{t}$ by $\mathbf{f}^{(i)}$, $\mathbf{x}_M$ by $\mathbf{x}_M^{(i)}$ and the couple stress vector $\mathbf{m}$ by single moments $\mathbf{m}^{(i)}$ acting on the bounding particles. Thus, from (7.34), one obtains

$$\langle \mathbf{M}^\star + \mathbf{M} \rangle = \frac{1}{V_R} \sum_{i=1}^{B} \left[\overset{3}{\mathbf{E}} \left(\mathbf{x}_M^{(i)} \otimes \mathbf{f}^{(i)} \right) \otimes \mathbf{x}_M^{(i)} + \mathbf{m}^{(i)} \otimes \mathbf{x}_M^{(i)} \right] \,. \qquad (7.36)$$

In comparison with (7.31), it is obvious that the first part represents the moment on the REV in consequence of the skew-symmetric part of the stress, whereas the second part contains the moment in consequence of the moments $\mathbf{m}^{(i)}$ acting on the REV. Moreover, regarding that

$$\langle \mathbf{M}^\star + \mathbf{M} \rangle = \langle \mathbf{M}^\star \rangle + \langle \mathbf{M} \rangle \,, \qquad (7.37)$$

which follows directly from (7.28), the homogenized couple stress tensor can be found via, cf. *Ehlers* at al. [50]:

$$\langle \mathbf{M} \rangle = \frac{1}{V_R} \sum_{i=1}^{B} \mathbf{m}^{(i)} \otimes \mathbf{x}_M^{(i)} \,. \qquad (7.38)$$

7.2.3   Homogenization of the strain and curvature

For the comparison with the results of computations using the continuum model, in addition to the homogenized stress and couple stress tensors, homogenized strain and curvature measured are required. These quantities are obtained in the same manner as it has been shown in the above section for the stress and couple stress by averaging the quantity of interest over the volume of the REV. Hence, following, e. g., *Hill* [77] or *Schröder* [120], one obtains the following general formulations for the homogenized displacement and rotational gradients,

$$\langle \mathrm{grad}_M \, \mathbf{u} \rangle := \frac{1}{V_R} \int\limits_{\mathcal{R}} \mathrm{grad}_M \, \mathbf{u} \, \mathrm{d}v = \frac{1}{V_R} \int\limits_{\partial\mathcal{R}} (\mathbf{u} \otimes \mathbf{n}) \, \mathrm{d}a \,,$$

$$\langle \mathrm{grad}_M \, \boldsymbol{\varphi} \rangle := \frac{1}{V_R} \int\limits_{\mathcal{R}} \mathrm{grad}_M \, \boldsymbol{\varphi} \, \mathrm{d}v = \frac{1}{V_R} \int\limits_{\partial\mathcal{R}} (\boldsymbol{\varphi} \otimes \mathbf{n}) \, \mathrm{d}a \,, \qquad (7.39)$$

where the *Gauß*ian integral theorem has been used. For the application to the particle model, the homogenized gradients are obtained by the sum over the bounding particles,

i. e.:

$$\langle \operatorname{grad}_M \mathbf{u} \rangle = \frac{1}{V_R} \sum_{i=1}^{B} (\mathbf{u}^{(i)} \otimes \mathbf{n}^{(i)}) \,,$$

$$\langle \operatorname{grad}_M \boldsymbol{\varphi} \rangle = \frac{1}{V_R} \sum_{i=1}^{B} (\boldsymbol{\varphi}^{(i)} \otimes \mathbf{n}^{(i)}) \,. \tag{7.40}$$

Therein, $\mathbf{u}^{(i)}$ is the absolute displacement of the boundary particle $\mathcal{P}^{(i)}$, $\boldsymbol{\varphi}^{(i)}$ is the total rotation[1], whereas $\mathbf{n}^{(i)}$ is the outward oriented normal vector on the REV at the center of bounding particle $\mathcal{P}^{(i)}$. Furthermore, the homogenized value of the rotations $\boldsymbol{\varphi}$ is needed for the formulation of the *Cosserat* strain tensor. For this purpose, the average value of the REV is directly used, which is given by

$$\langle \boldsymbol{\varphi} \rangle := \frac{1}{V_R} \int_{\mathcal{R}} \boldsymbol{\varphi} \, \mathrm{d}v = \frac{1}{V_R} \sum_{i=1}^{R} \boldsymbol{\varphi}^{(i)} \, v_R^{(i)} \,, \tag{7.41}$$

where R is the total number of particles in the REV, and $v_R^{(i)}$ is the volume of the particle $\mathcal{P}^{(i)}$ inside the REV. With the above formulations, the homogenized strain and curvature measurements of the *Cosserat* theory, cf. (2.49) and (2.52) from Section 2.3, are obtained:

$$\langle \bar{\boldsymbol{\varepsilon}} \rangle = \langle \operatorname{grad}_M \mathbf{u} \rangle + \overset{3}{\mathbf{E}} \langle \boldsymbol{\varphi} \rangle \quad \text{and} \quad \langle \bar{\boldsymbol{\kappa}} \rangle = \langle \operatorname{grad}_M \boldsymbol{\varphi} \rangle \,. \tag{7.42}$$

Remark: Whereas in (7.39) gradients with respect to the actual configuration are considered, in (7.42) the strain and curvature of the geometrically linear theory are used, which are the result of a formal linearization, cf. Section 2.3. Moreover, this approach is only available in case of small deformations and rotations.

7.3 Modeling of the biaxial test

The biaxial test, cf. Appendix A.2, is one of the standard tests for analyzing the localization phenomena of granular materials. Due to the fact that in the present work this test is used for the identification of the material parameters of the *Cosserat* theory, cf. Section 6.2, it is evident to also use this test also for the comparison of the effects of the continuum and the discrete model.

The main challenge in the modeling of the biaxial test with the particle model lies in the transfer of the macroscopic boundary conditions to the corresponding boundary conditions of the particle model. These boundary conditions consist of three different parts. Firstly, the plane-strain condition, which is given by the two glass plates on the front and the back

---

[1]Due to the fact that $\boldsymbol{\varphi}^{(i)}$ represents the total rotation, $\boldsymbol{\varphi}^{(i)}$ from the particle model corresponds to $\bar{\boldsymbol{\varphi}}$ from the *Cosserat* model

of the specimen. Secondly, the load plates on the top and the bottom of the specimen, whereby the top platen is displacement-driven pressed down and, finally, the constant pressure conditions on the left and right sides of the specimen, which are realized by an ambient fluid. For this reason the specimen is enclosed by a latex membrane separating the granular material and the fluid. These three boundary conditions must be simulated in a physically reasonable way to obtain comparable results with the biaxial test. Whereas the plane-strain condition is naturally given by the use of a two-dimensional model, the conditions on the top and the bottom as well as on the left and the right sides are discussed in the following. In comparison with the continuum model, the displacement-driven conditions on the top and the bottom correspond with *Dirichlet* conditions of the FEM model, whereas the constant pressure condition on the left and right sides corresponds with the *Neumann* boundaries.

7.3.1   Simulation of the top and bottom load plates

The boundary conditions on the top and bottom platen are simulated by use of rigid walls, which are slowly driven together, i. e., the top platen is driven down, whereas the bottom platen is driven up. The contact forces $\mathbf{f}_w^{(i)}$ between a wall and a contacting particle $\mathcal{P}^{(i)}$ are modeled, similarly to the particle-particle normal contact, cf. (7.4), by a elastic spring
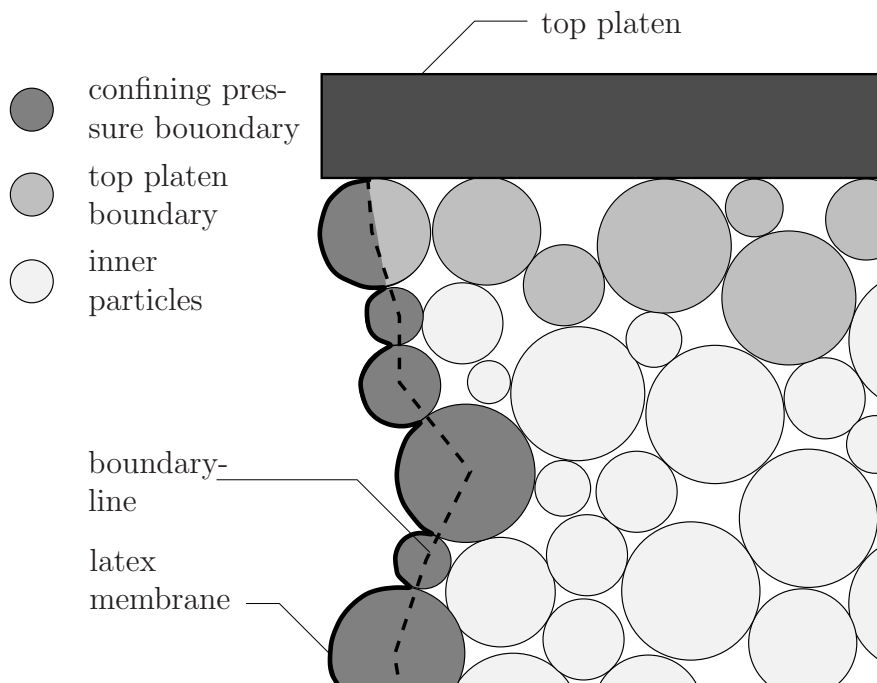

Figure 7.6: Boundary conditions of the biaxial test.

and a viscous damper. Thus, one obtains

$$\mathbf{f}_w^{(i)} = (E_n^{iw} \, \Delta^{(iw)} + D_n^{iw} \, \dot{\Delta}^{(iw)}) \, \mathbf{n}^{(iw)} \, , \tag{7.43}$$

where E_n^{iw} is the elasticity and D_n^{iw} the viscosity constant between the wall and the particle, whereby the same values are used as for the constants $E_n^{(ij)}$ and $D_n^{(ij)}$ of the particle-particle contact in normal direction, cf. (7.4). Furthermore, in contrast to the particle-particle contact, no tangential contact forces between particles and walls are taken into account.

7.3.2   Simulation of the confining pressure

The simulation of the constant pressure on the left and right sides of the specimen is a very complex task, in comparison with the top and bottom boundary conditions, because therefore, firstly, the pressure on the boundary particles must be simulated and, secondly, the stiffness of the latex membrane has to be taken into account, which is required for the coherence of the particle ensemble. Moreover, due to the fact that no limiting wall on the left and right sides of the ensemble exists, the geometry of the surfaces on the left and right sides varies during the simulation. This is an essential fact, because the variable geometry enables the nose-like deformation figure, which is known from the biaxial test as a result of the shear banding. The effects of the variable boundary geometry versus a realization by use of soft walls are described in detail in *Ehlers* et al. [53], wherein, moreover, the algorithm for the detection of the free boundary-line, which is applied here, is explained.

The first part of the modeling of the left and right sides boundary conditions consists in the simulation of forces in consequence of the confining pressure. These forces only act on the boundary particles, which are not associated with the top or bottom platen contact area excluding the edge particles, cf. Figure 7.6. Whereas, in the real biaxial experiment, the latex membrane covers the package of the granular material is more or less stretched between the single boundary grains, in the simulation, these breaks of the membrane contact are neglected so that the membrane is covering the outside of the boundary
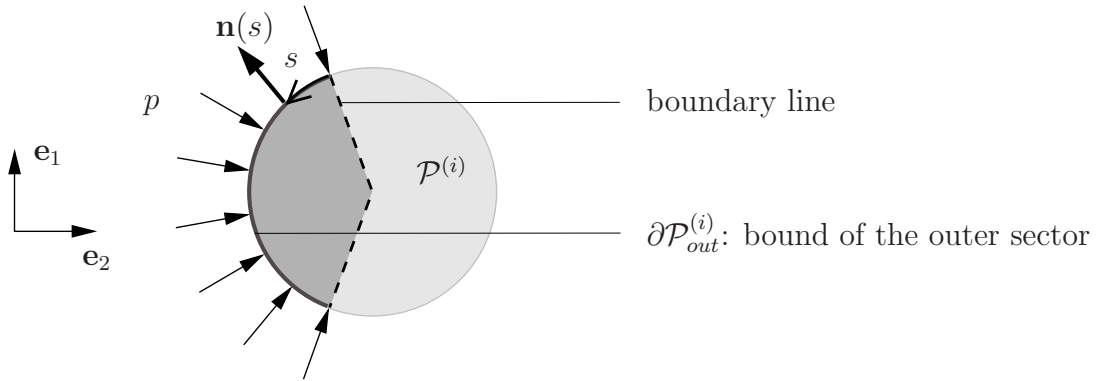

Figure 7.7: Force induced by the confining pressure.

particles perfectly, cf. Figure 7.6. Following this, the force $\mathbf{f}_{press}^{(i)}$ in consequence of the confining pressure p on the boundary particle $\mathcal{P}^{(i)}$ results directly from the integration of the pressure p along the whole outside sector $\partial\mathcal{P}_{out}^{(i)}$ of the boundary particle $\mathcal{P}^{(i)}$, cf. Figure 7.7:

$$\mathbf{f}_{press}^{(i)} = f_{press\,1}^{(i)}\,\mathbf{e}_1 + f_{press\,2}^{(i)}\,\mathbf{e}_2 = -p\left[\int\limits_{\partial\mathcal{P}_{out}^{(i)}}\mathbf{n}(s)\cdot\mathbf{e}_1\,\mathrm{d}s\,\mathbf{e}_1 + \int\limits_{\partial\mathcal{P}_{out}^{(i)}}\mathbf{n}(s)\cdot\mathbf{e}_2\,\mathrm{d}s\,\mathbf{e}_2\right]. \quad (7.44)$$

Therein, $\mathbf{e}_1$ and $\mathbf{e}_2$ are unit vectors defining the global basis and $\mathbf{n}(s)$ is the normal vector on the current arc length s, cf. Figure 7.7. Moreover, the outside part $\partial\mathcal{P}_{out}$ of the whole boundary of $\mathcal{P}^{(i)}$ is limited by the boundary-line, cf. Figure 7.6 and Figure 7.7.

The second part of the left and right sides boundary conditions are the forces in consequence of the extensional stiffness of the latex membrane. This membrane stiffness is considered by an attractive force between two adjacent boundary particles $\mathcal{P}^{(i)}$ and $\mathcal{P}^{i+1}$, which is given via:

$$\mathbf{f}_m^{(i,i+1)} = E_m\left\langle\left|\mathbf{x}_M^{(i)} - \mathbf{x}_M^{(i+1)}\right| - r_i - r_{i+1}\right\rangle\mathbf{n}^{(i,i+1)}, \quad (7.45)$$

where E_m represents the stiffness of the membrane and $\mathbf{n}^{(i,i+1)}$ is the normal vector, pointing from the center of $\mathcal{P}^{(i)}$ to the center of $\mathcal{P}^{(i+1)}$. Hence, the total force on the boundary particle $\mathcal{P}^{(i)}$ on the left or right side boundary is obtained by the sum of (7.44) and (7.45), i.e.,

$$\mathbf{f}_{mp}^{(i)} = \mathbf{f}_{press}^{(i)} + \mathbf{f}_m^{(i,i+1)} + \mathbf{f}_m^{(i,i-1)}. \quad (7.46)$$

7.4   Numerical simulations using the particle model

The simulations are performed by use of an ensemble of 30,000 monodisperse particles, which are generated on a regular triangular grid, cf. Figure 7.8. As a consequence of this arrangement with the initial formation the densest package is already given and, thus, no further consolidation during the motion of the particles is possible. Furthermore, gravitational effects are not relevant for the simulations, due to the fact that the forces in consequence of the loading process are much higher than the gravitational forces. Following this, $\mathbf{g}$ is set to zero. The mechanical properties of the particle ensemble are governed by the parameters of the particle-particle contact, for which one has to find reasonable values. Firstly, for the particle radii and density the reference values $1\,\mathrm{m}$ and $1\,\mathrm{kg}^3/\mathrm{m}^3$, respectively, have been chosen. Note, since no quantitative calculations are carried out, this values are only standard values, which are completely scalable, i.e., instead of a radius of $1\,\mathrm{m}$ one can also use $1\,\mathrm{cm}$ or $1\,\mathrm{mm}$. Moreover, considering a real contact of two material grains, e.g., of sand, it is obvious that the contact stiffness in the normal direction is much higher than in the tangential direction. Finally, in normal direction, a moderate damping constant is chosen to avoid dynamic effects. In the tangential direction, no additional damping is necessary due to the fact that in tangential direction damping occurs as a result of the included friction element. Theoretically, it is possible to use different

parameters for every particle, e. g., to simulate the diffusion of the material properties, which are naturally existent in real materials. However, for the following simulations, identical parameters for all particles are used, which are listed in Table 7.1.

parameter	symbol	value	unit
particle radius	r_p	1.0	[m]
particle density	ρ_p	1.0	[kg^3/m^3]
normal stiffness	E_n	10000.0	[N/m]
tangential stiffness	E_t	100.0	[N/m]
normal viscosity	D_n	100.0	[Ns/m]
tangential viscosity	D_t	0	[Ns/m]
coefficient of friction	μ	0.8	[$-$]

Table 7.1: Used parameters for the simulations with the particle model.

In the first instance, in this section, the principal formation of the localization zone is illustrated by the result of the motion of the particles. Afterwards, the above described homogenization method is applied to compute strain and curvatures based on the particle motions as well as stress and couple stress based on the forces between the particles. As a next step, the homogenized results are compared with the corresponding results of the continuum model. Finally, a parameter study is performed, wherein the effects of the tangential stiffness E_t and the frictional coefficient μ on the thickness of the localization zone are analyzed.
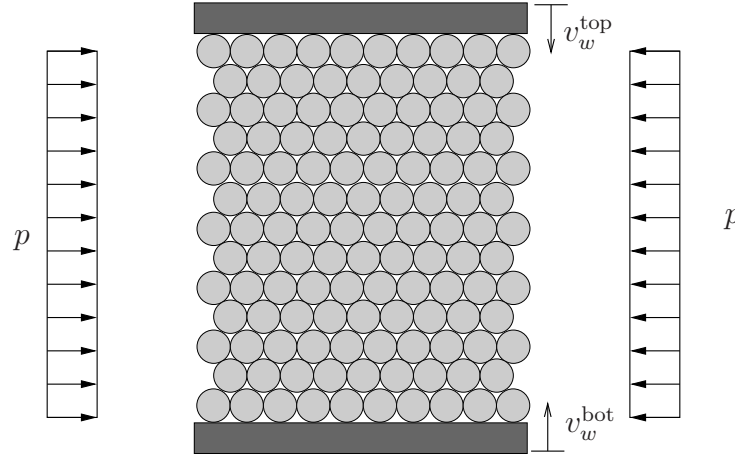

Figure 7.8: Schematic view of the boundary value problem.

7.4.1   Formation of the localization zone

The set up of the biaxial test is shown in Figure 7.8. The computation of the biaxial test starts with the stabilizing of the specimen by a confining pressure of $50 \, \text{N/m}^2$, whereby

the depth of the biaxial box is set to $1\,\mathrm{m}$. Subsequently, the upper load platen is driven down with the velocity $v_w^{\mathrm{top}} = 0.03\,\mathrm{m/s}$ and bottom platen is driven up with the same velocity $v_w^{\mathrm{bot}} = 0.03\,\mathrm{m/s}$. In Figure 7.9, the initial situation and the situations after 90, 120 and 340 seconds are shown. At the time $t = 90\,s$, cf. Figure 7.9 (b), the formation of two shear bands, one from the upper right edge and one from the lower left edge can be observed. With the proceeding of the simulation, the upper band vanishes and the deformation is concentrated in the lower shear band, cf. Figure 7.9 (c). This shear band expands until the final state is reached, cf. Figure 7.9 (d). The effect of the free boundary conditions on the left and right sides of the specimen can be well observed in the nose-like deformation figure, in consequence of the sliding of two wedges along the shear band.
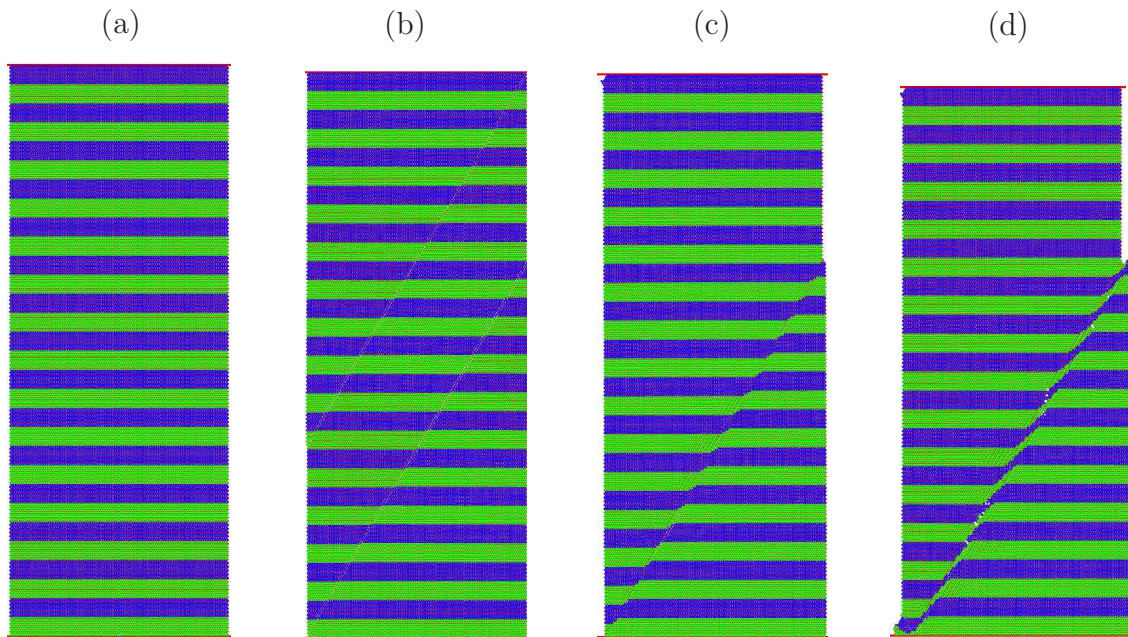
Figure 7.9: Simulation with the particle model, (a) initial situation, (b) after $90\,s$, (c) after $120\,s$, (d) after $340\,s$.

Generally, the reason for the appearance of a shear band can be found in the material softening. In the continuum model, material softening is modeled by the decrease of the yield surface in consequence of positive volumetric strain, cf. Section 2.4.5, whereas in the particle model the parameters are always constant. However, softening occurs in the particle model as the result of the decreasing density in the ensemble. Due to the fact that with the initial situation the densest package is given, the density of the ensemble decreases during the deformation and, therewith, the number of particle-particle contacts is reduced, which is connected with the reduction of the overall stiffness of the ensemble.

7.4.2 Stress and couple stress in the location zone

After it has been shown that the simulation based on the boundary conditions described in Section 7.3 yields a shear band in the same manner as it can be observed during real

biaxial experiments, one is mainly interested in the calculation of the homogenized stress $\langle \mathbf{T} \rangle$, cf. (7.31), and couple stress $\langle \mathbf{M} \rangle$, cf. (7.38), by use of the forces between the particles. Therefore, firstly, an appropriate REV must be defined. The size of this REV should be, on the one hand, large enough so that the strain and stress tensors can be computed in a reasonable way, and, on the other hand, it has to be small enough to represent the stress and strain state of a material point. Regarding the results presented in Section 7.4.1 for the particle motions, cf. Figure 7.9, the REV is chosen in the following manner:

1. One particle is selected,

2. all particles, which are in contact with the selected particle, are marked,

3. the REV is bordered by the line through the centers of the marked surrounding particles,

cf. Figure 7.10, wherein an exemplary REV at the undeformed initial state is shown. This procedure is performed separately in every time step, in which the stress is computed and independently for every single particle. Thus, the single REVs overlap each other. In this way, one obtains the smallest possible REV under regarding of the homogenization aspects. A detailed study of the influence of the REV size on the homogenized results is performed in *Bear & Bachmat* [6] or *Ehlers* et al. [50].

particle outside of the REV
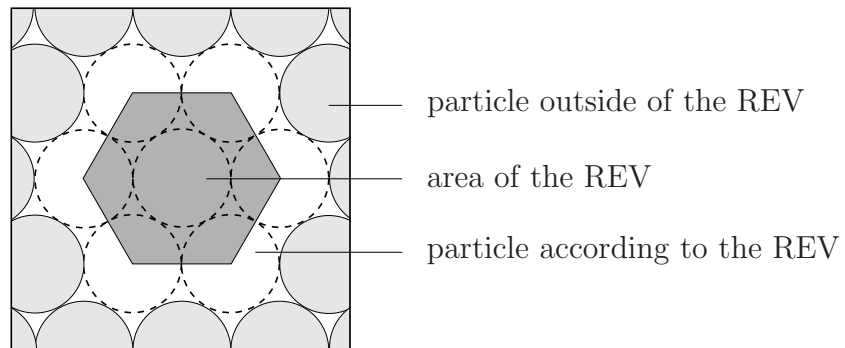
area of the REV

particle according to the REV

Figure 7.10: Generation of a REV for the homogenization procedure, exemplarily illustrated at the undeformed state.

The results of the homogenization based on the result of the simulation at the time $t = 120\,\mathrm{s}$ are shown in Figure 7.11. Therein, the homogenized values of the norm of strain $\|\langle \bar{\boldsymbol{\varepsilon}} \rangle\|$, curvature $\|\langle \bar{\boldsymbol{\kappa}} \rangle\|$, and couple stress tensor $\|\langle \mathbf{M} \rangle\|$ are shown as well as the 3-rd component of the vector $\mathbf{I} \times \langle \mathbf{T} \rangle$, which is given for the two-dimensional case by $T_{21} - T_{12}$. Hence, one can notice that all exhibited quantities are concentrated along the shear band. With regard to the particle motions, cf. Figure 7.9, this result has been expected for the strain and the curvature, because therein the concentration of the deformations along the shear band has already been observed. However, the concentration of the couple stress and

the skew-symmetric stress along the shear band is a recent outcome of the homogenization procedure. These results indicate that the description of a granular material on the micro-level with the particle model corresponds to the macroscopic description using the *Cosserat* theory.
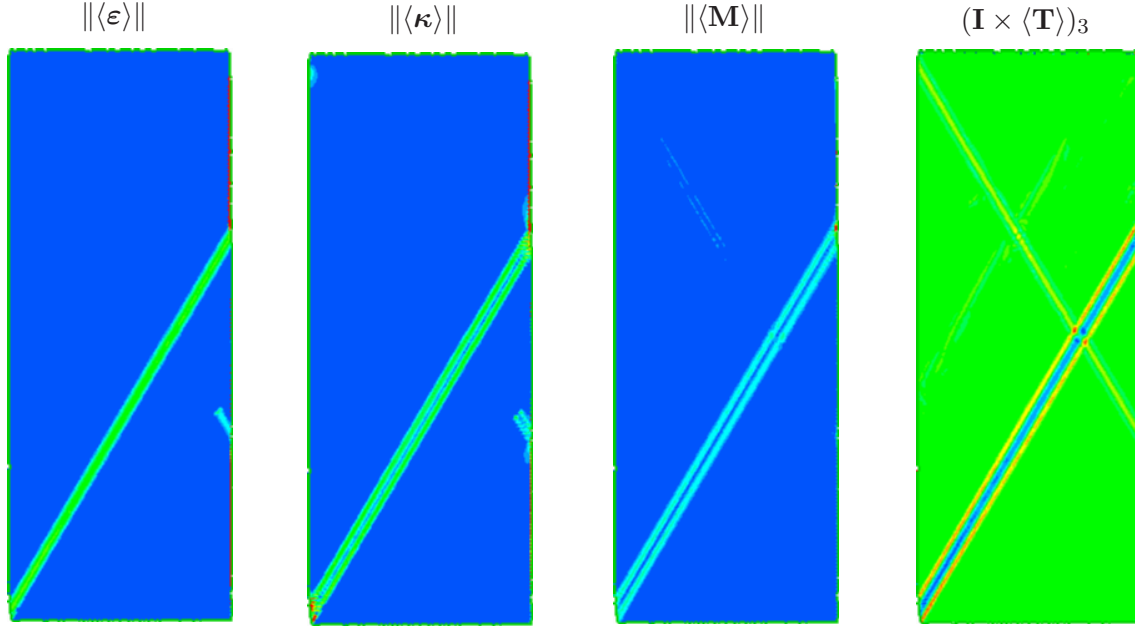

Figure 7.11: Homogenized results of the particle simulation.

Furthermore, with the above results for the stress and couple stress fields, the balance of moment of momentum, cf. (7.25), can be verified. Using the homogenized quantities, this balance reads:

$$\mathbf{0} = \mathbf{I} \times \langle \mathbf{T} \rangle + \mathrm{div}_M \langle \mathbf{M} \rangle . \tag{7.47}$$

Hence, the divergence of the couple stress $\mathrm{div}_M \langle \mathbf{M} \rangle$ and $-\mathbf{I} \times \langle \mathbf{T} \rangle$ should be equivalent. For the determination of $\mathrm{div}_M \langle \mathbf{M} \rangle$, the couple stress field is approximated by a polynomial $p(x_1, x_2)$ basing on a patch of seven particles, whereby each particle represents the center of a REV. In this manner, one is able to compute the gradient $\mathrm{grad}_M \langle \mathbf{M} \rangle$ and, finally, $\mathrm{div}_M \langle \mathbf{M} \rangle$. The results of this procedure are shown in Figure 7.12. Therein, firstly, on the left side, the contour plot of the 3-rd component of $\mathrm{div}_M \langle \mathbf{M} \rangle$ is exhibited. Comparing this result with the plot of the 3-rd component of $\mathbf{I} \times \mathbf{T}$ in Figure 7.11, no difference can be recognized. Moreover, on the right side in Figure 7.12, $\mathrm{div}_M \langle \mathbf{M} \rangle$ and $\mathbf{I} \times \mathbf{T}$ are compared by using a horizontal cut through the shear band. Therein, the qualitative agreement of both data can also be seen, whereby, the curve of $(\mathrm{div}_M \langle \mathbf{M} \rangle)_3$ is smoother. This can be interpreted as a result of the averaging over more REVs, which can also be the reason for the divergence in the extreme values. However, these results show that the coherence between the skew-symmetric stress and the couple stress fields is principally given by the homogenized results of the particle model.

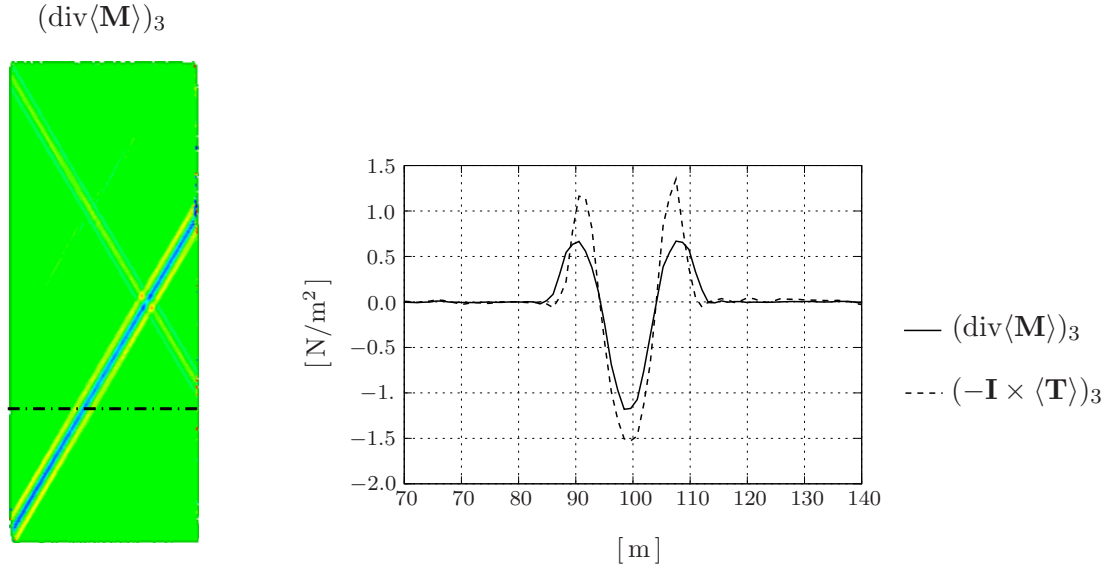$(\mathrm{div}\langle\mathbf{M}\rangle)_3$

Figure 7.12: Comparison between homogenized skew-symmetric stress and divergence of the couple stress.

7.4.3 Comparison between the particle and the continuum model

The main reason for the usage of the particle model is to show that granular material can be modeled within a macroscopic micropolar approach. With the above computations, the effects, which characterize a micropolar material, have been shown by means of the occurrence of curvatures and couple stress along the shear band. In the next step, the results of the *Cosserat* continuum model are compared directly with the results of the particle model. This is carried out for the M_{31} component of the couple stress tensor and the $\bar{\kappa}_{31}$ component of curvature tensor by use of contour plots, cf. Figure 7.13, as well as by horizontal cuts through the shear band, cf. Figure 7.14. Firstly, in Figure 7.13, nearly identical results for the particle and the continuum model can be recognized, i. e., the concentration of the curvature and the couple stress on the left and right sides of the shear band. Furthermore, on the horizontal cuts in Figure 7.14, one finds that for both models, the curves of the curvature and the couple stress look proportional to each other, i. e., scaled by a constant factor. In case of the continuum model, the coupling between the curvature and the couple stress is directly given by the constitutive assumption, cf. (2.74) in Section 2.4. However, for the particle model, no constitutive assumption between the homogenized curvature $\langle\bar{\kappa}\rangle$ and the couple stress $\langle\mathbf{M}\rangle$ has been made. Thus, the coherence between the curvature and the couple stress is a real result of the simulation, which shows that the micropolar effects of the continuum model are naturally given by use of the particle model.

7.4.4 Variation of the parameters

Finally, in this chapter, a parameter study is performed in order to detect which parameters of the particle model are comparable to the additional parameters of the *Cosserat*
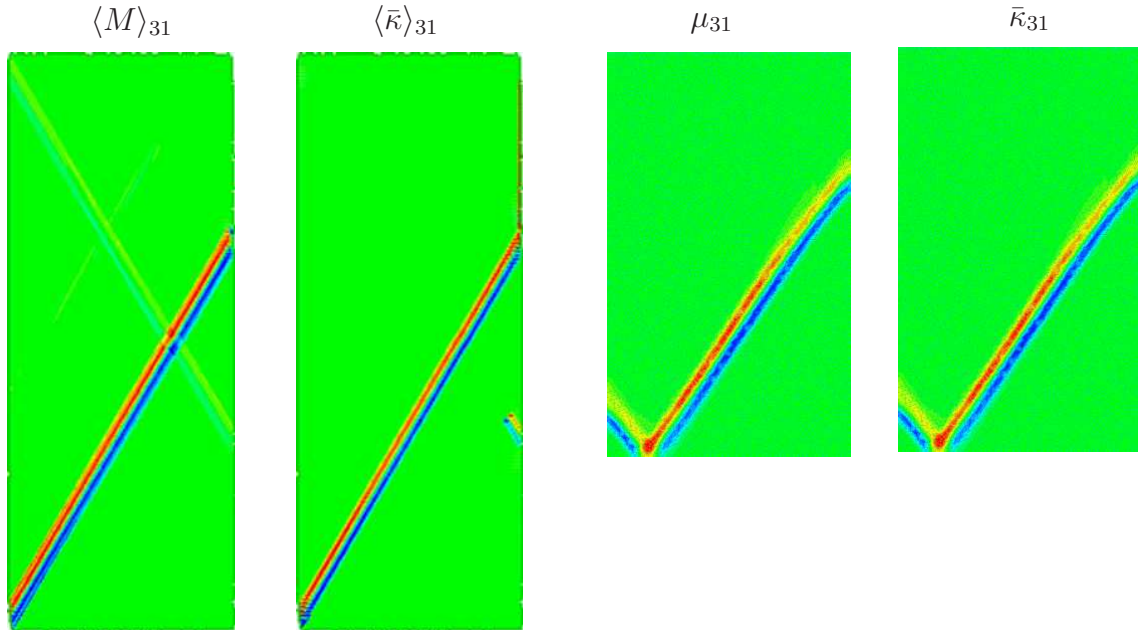
Figure 7.13: Comparison between the homogenized results of the particle simulation ($\langle M \rangle_{31}$ and $\langle \kappa \rangle_{31}$) and the results macroscopic FEM model (μ_{31}, κ_{31}).
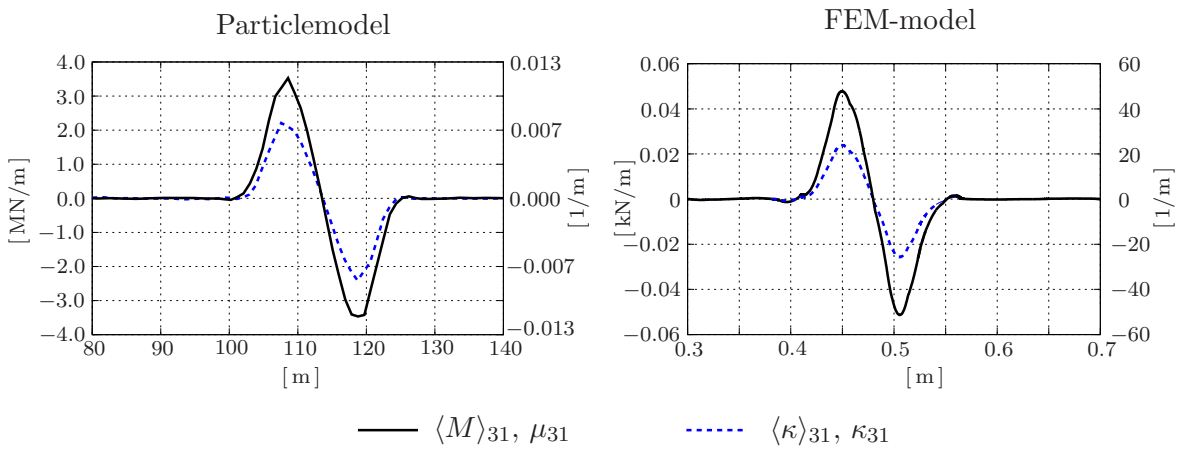

Figure 7.14: Comparison between the couple stress M_{31} and the curvature κ_{31} along horizontal cuts through the shear band.

theory. An indicator therefore is that these parameters must have an influence on the thickness of the shear band, like the *Cosserat* parameters, whose influence on the shear band thickness is demonstrated in Section 6.2.2. Considering the particle model, one supposes that the parameters of the tangential stiffness E_t and the frictional constant μ could have an influence on the shear band geometry. Furthermore, it is self-evident that with a change of the particle radii the shear band thickness will be linearly scaled.

Thus, firstly, the influence of the parameter E_t on the shear band geometry is analyzed by the variation of E_t, whereby for the other parameters the values given in Table 7.1
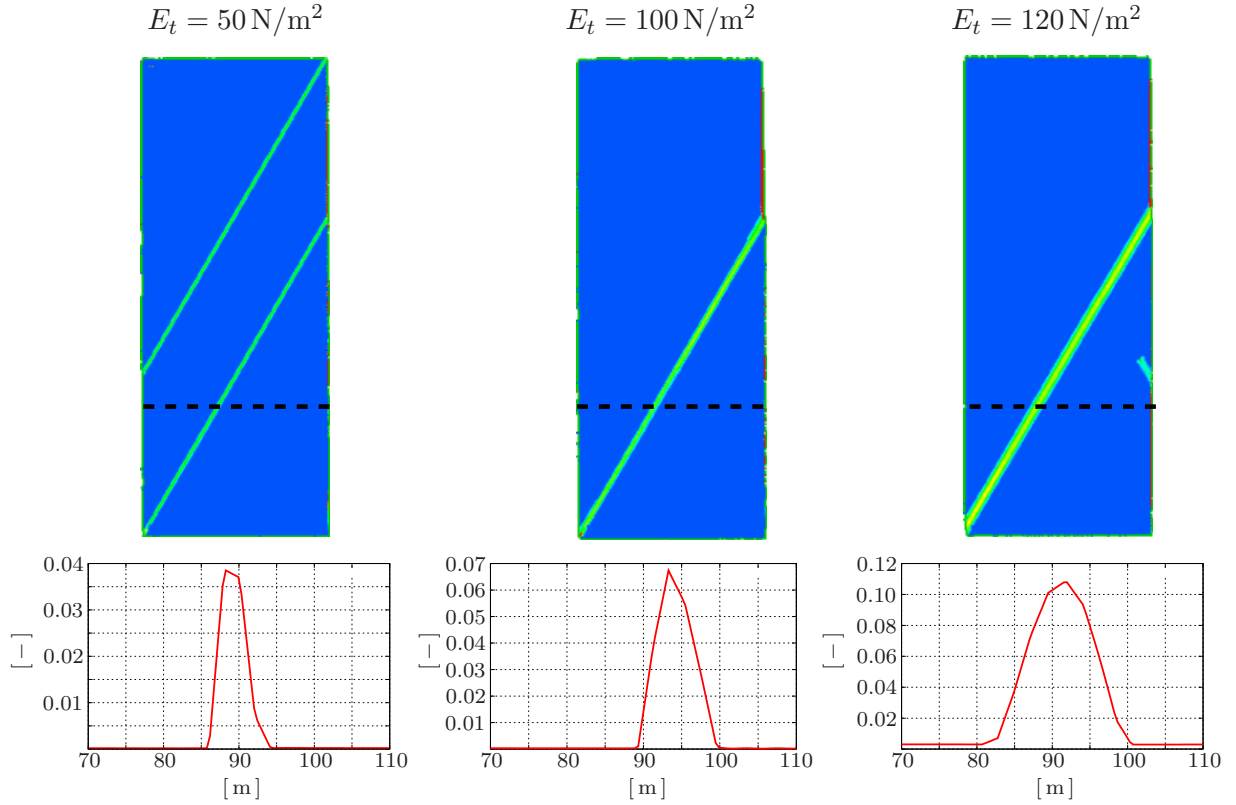
Figure 7.15: Results of the norm of strain $\|\langle\bar{\varepsilon}\rangle\|$ for three different values of E_t.

are retained. Therefore, three simulations with $E_t = 50\,\text{N/m}^2$, $E_t = 100\,\text{N/m}^2$ and $E_t = 125\,\text{N/m}^2$ are carried out. The results of the homogenized norm of strain $\|\langle\varepsilon\rangle\|$ are shown in Figure 7.15 by use of contour plots. Moreover, horizontal cuts through the data are given in the diagrams under the plots. In the contour plots as well as in the cuts, a distinct influence of the tangential stiffness E_t on the thickness of the shear band can be observed.

Secondly, the influence of the frictional constant μ on the shear band thickness is analyzed, by once again using three different simulations with $\mu = 0.4$, $\mu = 0.8$ and $\mu = 1.0$, whereby E_t is reset to $E_t = 100\,\text{N/m}^2$. The results are shown in Figure 7.16, wherein the norm of the homogenized strain $\|\langle\varepsilon\rangle\|$ along a horizontal cut through the shear band is exhibited. Although there is such a wide variation of the frictional angle, no influence on the shear band thickness can be realized in the diagram. Hence, it is obvious that the variation of the frictional constant has no influence on the shear band thickness. This observation demonstrates that the frictional constant μ of the particle model is not comparable with the additional material parameters of the *Cosserat* theory.

Summary of the numerical examples

With the above numerical simulations, it has been shown that the simulation of the biaxial test using the particle model yields the appearance of a shear band in the same manner as
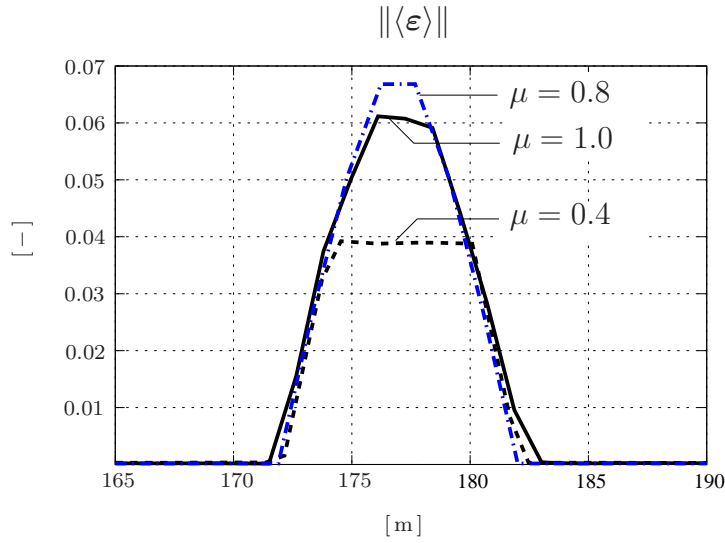
Figure 7.16: Norm of strain $\|\langle\bar{\varepsilon}\rangle\|$ during the variation of the frictional constant μ.

it is known from computations using a continuum model and also can be observed during material tests. Furthermore, the concentration of the couple stress along the shear band has been shown, which is qualitatively similar to the results using the *Cosserat* theory. This indicates that the *Cosserat* approach is a physically correct method for the modeling of granular material. Additionally, with the comparison of the homogenized curvature and couple stress, cf. Figure 7.14, it has been demonstrated that the assumption of a direct coherence between the curvature and the couple stress, which is constitutively made within the *Cosserat* model, also results from the particle model. This result gives a hint that the constitutive assumption in the *Cosserat* model is reasonable. Finally, a parameter variation has been performed with the result that the tangential stiffness E_t has an influence on the shear band thickness, whereas the frictional constant has no influence. Therewith, it is clear that only the parameter E_t as well as the particle radii govern the polar properties of the particle ensemble.

Chapter 8: Summary and outlook

8.1 Summary

In the present work, the localization phenomena of granular material has been analyzed in order to provide a method for the computation of realistic boundary-value problems. The reason for this localization effects are material instabilities caused by the softening behavior of the material, which can be observed at homogeneous material tests. For this purpose, in the first step, the non-polar behavior of granular material is considered. Based on observations from material tests, a non-linear elastic law as well as hardening and softening laws in the context of the elasto-plasticity have been developed. In the next step, based on the described non-polar behavior, inhomogeneous biaxial tests are taken into account for the investigation of the micropolar behavior. As a consequence of the material softening, localization zones, so-called shear bands, appear. For the numerical computation of such localization phenomena, regularization techniques are required, since the standard continuum theory results in an ill-posed problem. Due to the fact that in the biaxial tests a finite thickness of the shear band can be observed, a regularization of the problem is naturally given by the effects due to the microstructure of the material. In case of granular material, the microstructure can be taken into account by application of the *Cosserat* or micropolar theory, which is applied in this thesis for the computation of localization problems.

One of the main problems by use of the *Cosserat* theory is, beside the numerically implementation, the identification of the associated material parameters. Considering inhomogeneous biaxial tests with shear banding, the effect of regularization can be observed by two facts. Firstly, by the gradual decrease of the stress after the appearance of the shear band and, secondly, by the finite thickness of the incoming shear band. Hence, both effects are used for the determination of the additional parameters of the *Cosserat* theory. Whereas the usage of stress-strain relations, in the context of the literature concerning the parameter identification procedure is a usual method, the consideration of the shear band thickness is a new challenge. Hence, a new method has therefore been developed. In addition to the *Cosserat* parameters, all the other material parameters, namely, the parameters of the elastic behavior as well as the parameters of the plastic hardening and softening must be identified. In consequence of the high number of material parameters given therewith, the overall identification process was performed by two major steps. Thus, in the first step, homogeneous material tests are applied for the determination of the parameters governing the non-polar behavior. In the second step, the material parameters of the micropolar behavior are determined basing on inhomogeneous biaxial tests, which enable the observation of the incoming shear band by use of the stereophotogrammetry.

Generally, the identification procedure yields an inverse problem. For the solution of such problems, a lot of methods in the framework of the non-linear optimization exist. With a view to the high numerical costs for the computation of the boundary-value

problem of the biaxial test, the gradient-based SQP method has been applied in this work. The computational cost can be further reduced by the application of the semi-analytical sensitivity analysis, which is also discussed in this work. The stepwise realization of the overall identification process as well as the semi-analytical computation of the sensitivities is demonstrated exemplarily by use of experimental data basing on *Hostun* sand.

Finally, in the present work, with the particle model a completely different approach for the modeling of granular material is discussed which traces back to the *Molecular Dynamics*. Using this particle model, one is able to simulate the granular microstructure of the material, i.e., the single material grains, directly. Basing on a two-dimensional particle model, the biaxial test has been modeled, with a set of $30,000$ monodisperse, circular particles. With these simulations, the appearance of shear bands were shown and, furthermore, the occurrence of couple stress along the shear band was demonstrated in the same manner as done before with the continuum model. With these results, it has been illustrated that the *Cosserat* theory is a correct approach for the simulation of localization effects of granular media.

8.2   Outlook

In the present work, a two-dimensional model for the computation was presented. Therewith, one is able to compute plain problems like the biaxial test. For the realization of realistic simulations of geomechanical localization problems, e.g., landslides or base-failure problems, the two-dimensional model must be extended to three dimensions. This yields an extreme increase of the numerical effort, which requires the parallelization of the FEM code. For non-polar materials, three-dimensional computations have been shown in *Ammann* [2] and *Wieners* et al. [140].

Moreover, the influence of the pore fluid is an essential fact considering real geomechanical problems, whereas, in this thesis, the influence of a pore fluid has been neglected, in order to find a description of the solid skeleton. Thus, for the computation of naturally existing problems, the presented formulations have to be enhanced by considering a multi-phase material on the basis of the TPM.

Appendix A: Material tests

A.1   Triaxial test

For the triaxial test, a cylindrical specimen, enclosed by a latex membrane, is put into a so-called triaxial cell, cf. *Müllerschön* [105]. Therein, the specimen is horizontally loaded by a confining fluid pressure and vertically by a load platen. Firstly, a hydrostatic stress state is driven for the stabilizing of the specimen. After reaching the predefined confining pressure, three different tests can be carried out, cf. Figure A.1:

1. Compression test: The load platen at the top can be driven down, whereby the vertical stress σ_{11} does not increase anymore. Thereby the vertical stress σ_{11}, the vertical strain ε_{11} as well as the volumetric strain $\varepsilon^V = (\varepsilon^{11} + \varepsilon^{22} + \varepsilon^{33})$ are measured.

2. Extension test: The load platen can be driven up, which yields a decreasing of σ_{11}, whereby the same kind of data as in the compression test are measured.

2. Hydrostatic test: The hydrostatic load is continually increased, whereby the pressure $p = \frac{1}{3}(\sigma_{11} + \sigma_{22} + \sigma_{33})$ and the volumetric strain ε^V are measured.
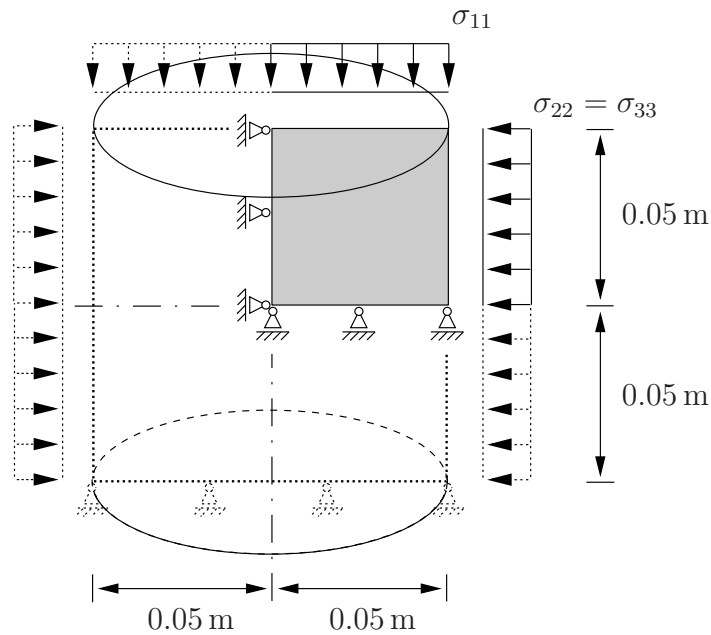

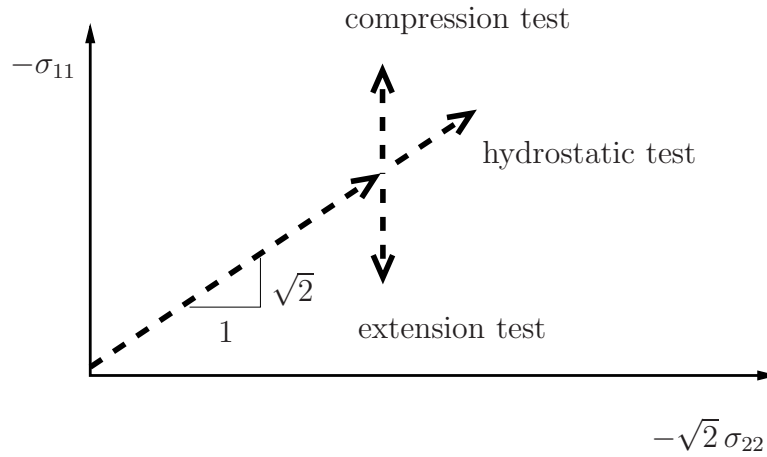Figure A.1: Boundary conditions of the triaxial test.

Figure A.2: Stress path for the triaxial compression, extension and hydrostatic tests.

In consequence of the axially symmetric geometry of the specimen and upset of the load, the following principal stress state is obtained,

$$\boldsymbol{\sigma} = \begin{pmatrix} \sigma_{11} & 0 & 0 \\ 0 & \sigma_{33} & 0 \\ 0 & 0 & \sigma_{33} \end{pmatrix} \mathbf{e}_i \otimes \mathbf{e}_j \,, \tag{A.1}$$

which is connected with the corresponding principal strain state

$$\boldsymbol{\varepsilon} = \begin{pmatrix} \varepsilon_{11} & 0 & 0 \\ 0 & \varepsilon_{33} & 0 \\ 0 & 0 & \varepsilon_{33} \end{pmatrix} \mathbf{e}_i \otimes \mathbf{e}_j \,. \tag{A.2}$$

A.2 Biaxial test

In the biaxial test, a prismatic specimen, enclosed by a latex membrane, is stabilized by an ambient fluid pressure on the left and right sides, while a load platen is slowly driven down. To generate a plane strain, the deformation in the third direction is inhibited by two glass plates in the front and the back of the specimen, cf. Figure A.3. For a detailed description, cf. *Mokni & Desrues* [101].
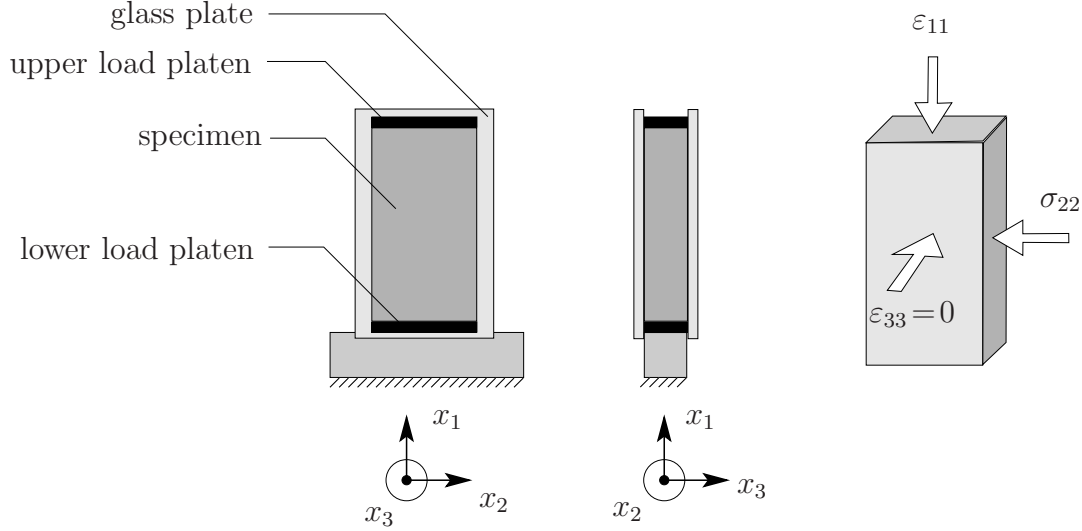

Figure A.3: Set up of the biaxial test.

At the beginning of the test, a complete homogeneous strain and stress state exist as long as the increasing of the deformation is incorporated with plastic hardening. After a critical load level, softening occurs, therewith the measured vertical load declines and the incoming of a shear band can be observed, cf. Figure 2.5. Thus, the following stress and couple stress tensors of the *Cosserat* theory are valid,

$$\boldsymbol{\sigma} = \begin{pmatrix} \sigma_{11} & \sigma_{12} & 0 \\ \sigma_{21} & \sigma_{22} & 0 \\ 0 & 0 & \sigma_{33} \end{pmatrix} \mathbf{e}_i \otimes \mathbf{e}_j \quad \boldsymbol{\mu} = \begin{pmatrix} 0 & 0 & 0 \\ 0 & 0 & 0 \\ \mu_{31} & \mu_{32} & 0 \end{pmatrix} \mathbf{e}_i \otimes \mathbf{e}_j \qquad \text{(A.3)}$$

as well as the corresponding strain and curvature tensors

$$\bar{\boldsymbol{\varepsilon}} = \begin{pmatrix} \bar{\varepsilon}_{11} & \bar{\varepsilon}_{12} & 0 \\ \bar{\varepsilon}_{21} & \bar{\varepsilon}_{22} & 0 \\ 0 & 0 & 0 \end{pmatrix} \mathbf{e}_i \otimes \mathbf{e}_j \quad \bar{\boldsymbol{\kappa}} = \begin{pmatrix} 0 & 0 & 0 \\ 0 & 0 & 0 \\ \bar{\kappa}_{31} & \bar{\kappa}_{32} & 0 \end{pmatrix} \mathbf{e}_i \otimes \mathbf{e}_j \, . \qquad \text{(A.4)}$$

Appendix B: Tensor calculus

The main definitions for the tensorial expressions, which were presented within this thesis, are briefly summarized here. Therein, the chosen notation follows the rules and definitions of the absolute tensor notation given in the book by *de Boer* [11] and in the lecture notes on vector and tensor calculus by *Ehlers* [42]. For simplicity, the underlying basis system for the following definitions is a normalized *Cartes*ian basis, in which no differentiation between covariant or contravariant basis vectors has to be carried out. Furthermore, the well-known summation convention of *Einstein* holds for indices appearing twice within a term.

B.1   Tensor algebra

B.1.1   Basic tensor products

Among the variety of different tensor products, here, only the rules for the products, which were used within the discussions of this thesis, are presented, namely the dyadic and scalar products as well as the linear mapping ("contracting product") and the tensor product. For a better understanding of the absolute tensor notation, additionally, an orthonormal basis notation of the respective products is given.

Dyadic product

Within a dyadic tensor product, all the basis vectors $\mathbf{e}_i$ of the involved tensors are combined in a dyadic sense. The order (or rank) of the resulting tensor equals the sum of the ranks of the involved tensors:

$$
\begin{aligned}
\mathbf{C} &= \mathbf{a} \otimes \mathbf{b} = a_i\, b_j\ \ \mathbf{e}_i \otimes \mathbf{e}_j, \\
\overset{4}{\mathbf{C}} &= \mathbf{A} \otimes \mathbf{B} = A_{ij}\, B_{kl} \mathbf{e}_i \otimes \mathbf{e}_j \otimes \mathbf{e}_k \otimes \mathbf{e}_l\,.
\end{aligned}
\tag{B.1}
$$

Note that within the used notation, vectors (or 1-st order tensors) are symbolized by bold, small Latin characters, whereas tensors of n-th order ($n > 1$) are defined by bold, capital Latin characters. Furthermore, the rank of a n-th order tensor is clarified by the superscripted rank for $n > 2$.

Scalar product

The scalar product can only be carried out between tensors of the same order, whereby the single basis vectors are combined scalarly and the result of this product always yields

a scalar value:

$$\alpha = \mathbf{a} \cdot \mathbf{b} = a_i \, b_i \,,$$
$$\alpha = \mathbf{A} \cdot \mathbf{B} = A_{ij} \, B_{ij} \,. \tag{B.2}$$

Linear mapping and tensor product

The linear mapping as well as the tensor product are operations, in which the rank of the resulting tensor is reduced (contracted) with respect to the sum of the ranks of all involved tensors. In both operations, the resulting tensor is formed by a combination of both scalar and dyadic products of the basis vectors of the involved tensors:

$$\mathbf{c} = \mathbf{A}\,\mathbf{b} = A_{ij}\,b_j \quad \mathbf{e}_i \,,$$
$$\mathbf{C} = \mathbf{A}\mathbf{B} = A_{ij}\,B_{jk}\ \mathbf{e}_i \otimes \mathbf{e}_k \,, \tag{B.3}$$
$$\mathbf{C} = \overset{4}{\mathbf{A}}\mathbf{B} = A_{ijkl}\,B_{kl}\mathbf{e}_i \otimes \mathbf{e}_j \,.$$

Incomplete mapping

If higher order tensors are applied to other tensors in the sense of incomplete mappings, one has to know how many of the basis vectors have to be linked by scalar products. Therefore, an underlined superscript $(\,\cdot\,)^{\underline{n}}$ indicates the order of the desired result after the tensor operation has been carried out. In this context, an incomplete mapping of two 3-rd order tensors results in the following way in a 2-nd order tensor:

$$\mathbf{C} = (\overset{3}{\mathbf{A}}\ \overset{3}{\mathbf{B}})^{\underline{2}} = A_{ijk}\,B_{jkn}\,(\mathbf{e}_i \otimes \mathbf{e}_n)\,. \tag{B.4}$$

B.1.2 Symmetric and skew-symmetric parts of a tensor

Each arbitrary 2-nd order tensor $\mathbf{A}$ can be uniquely decomposed into symmetric and skew-symmetric parts:

$$\mathbf{A} \quad = A_{ij}\,\mathbf{e}_i \otimes \mathbf{e}_j \ = \ \mathbf{A}_{\text{sym}} + \mathbf{A}_{\text{skw}} \,,$$
$$\mathbf{A}_{\text{sym}} := \tfrac{1}{2}\left(\mathbf{A} + \mathbf{A}^T\right) \quad \rightsquigarrow \quad \mathbf{A}_{\text{sym}} = \mathbf{A}_{\text{sym}}^T \,, \tag{B.5}$$
$$\mathbf{A}_{\text{skw}} := \tfrac{1}{2}\left(\mathbf{A} - \mathbf{A}^T\right) \quad \rightsquigarrow \quad \mathbf{A}_{\text{skw}} = -\mathbf{A}_{\text{skw}}^T \,.$$

Therein, the transpose of a tensor is given by $\mathbf{A}^T = A_{ji}\,\mathbf{e}_i \otimes \mathbf{e}_j$.

B.1.3 Fundamental tensors

A fundamental tensor is a tensor, whose coefficient matrix is exclusively built by combinations of basis vectors and which is independent of any variable quantity.

2-nd order fundamental tensor

The 2-nd order fundamental tensor (or identity tensor) $\mathbf{I}$ leads to an identical map, if it is applied to an arbitrary vector $\mathbf{a}$ or an arbitrary 2nd order tensor $\mathbf{A}$, respectively:

$$\mathbf{a} = \mathbf{I}\,\mathbf{a}\,, \qquad \mathbf{A} = \mathbf{I}\,\mathbf{A}\,, \qquad \mathbf{I} := \delta_{ij}\,\mathbf{e}_i \otimes \mathbf{e}_j\,, \tag{B.6}$$

where δ_{ij} is the so-called *Kronecker* symbol, which takes for $i = j$ the value 1 and otherwise the value 0.

3-rd order fundamental tensor

The 3-rd order fundamental tensor (or *Ricci* permutation tensor) $\overset{3}{\mathbf{E}}$ is defined via the following relation:

$$\overset{3}{\mathbf{E}} := e_{ijk}\,(\mathbf{e}_i \otimes \mathbf{e}_j \otimes \mathbf{e}_k)\,, \tag{B.7}$$

whereby the so-called permutation symbol e_{ijk} is given by

$$e_{ijk} = \begin{cases} 1 & : \text{ even permutation} \\ -1 & : \text{ odd permutation} \\ 0 & : \text{ double indexing} \end{cases} \longrightarrow \begin{cases} e_{123} = e_{231} = e_{312} = 1 \\ e_{321} = e_{213} = e_{132} = -1 \\ \text{all remaining } e_{ijk} \text{ vanish} \end{cases} \tag{B.8}$$

4-th order fundamental tensors

4-th order fundamental tensors are built by dyadic combinations of the 2-nd order identity tensor $\mathbf{I}$. By additional transpositions of the respective basis vectors, altogether three different 4-th order fundamental tensors can be defined, which have the following properties:

$$(\mathbf{I} \otimes \mathbf{I})^{\overset{23}{T}}\mathbf{A} = \mathbf{A} \qquad\qquad (\text{identical map})\,,$$

$$(\mathbf{I} \otimes \mathbf{I})^{\overset{24}{T}}\mathbf{A} = \mathbf{A}^T \qquad\qquad (\text{"transposing" map})\,, \tag{B.9}$$

$$(\mathbf{I} \otimes \mathbf{I})\,\mathbf{A} = (\mathbf{A} \cdot \mathbf{I})\,\mathbf{I} = (\operatorname{tr}\mathbf{A})\,\mathbf{I} \qquad (\text{"tracing" map})\,.$$

Therein, the transpositions $(\,\cdot\,)^{\overset{ik}{T}}$ indicate an exchange of the i-th and k-th basis systems.

B.1.4 Spherical and deviatoric parts of a tensor

Each arbitrary 2-nd order tensor $\mathbf{A}$ can be decomposed into spherical and deviatoric parts:

$$\mathbf{A} = \mathbf{A}^K + \mathbf{A}^D\,,$$

$$\mathbf{A}^K := \tfrac{1}{3}\,(\mathbf{A} \cdot \mathbf{I})\,\mathbf{I}\,, \tag{B.10}$$

$$\mathbf{A}^D := \mathbf{A} - \tfrac{1}{3}\,(\mathbf{A} \cdot \mathbf{I})\,\mathbf{I} = \mathbf{A} - \mathbf{A}^K\,.$$

By the above definition, the deviatoric part $\mathbf{A}^D$ always results in a traceless tensor, i. e., $\mathbf{A}^D \cdot \mathbf{I} = 0$.

B.1.5   Invariants of a 2-nd order tensor

From the solution of the eigenvalue problem, the principal invariants of an arbitrary 2-nd order tensor $\mathbf{A}$ yield:

$$
\begin{aligned}
\mathrm{I}_A &= \mathbf{A} \cdot \mathbf{I} = \mathrm{tr}\,\mathbf{A}\,, \\
\mathbb{II}_A &= \tfrac{1}{2}\left(\mathrm{I}_A^2 - \mathbf{A}^T \cdot \mathbf{A}\right), \\
\mathbb{III}_A &= \tfrac{1}{6}\,\mathrm{I}_A^3 - \tfrac{1}{2}\,\mathrm{I}_A^2\left(\mathbf{A}\,\mathbf{A} \cdot \mathbf{I}\right) + \tfrac{1}{3}\,\mathbf{A}^T\,\mathbf{A}^T \cdot \mathbf{A} = \det \mathbf{A}\,.
\end{aligned}
\tag{B.11}
$$

Bibliography

[1] *Adelmann, H.; Haftka, R.*: Sensitivity analysis of discrete structural systems. *AIAA Journal* **24** (1986), 823–832.

[2] *Ammann, M.*: *Parallel Finite Element Simulations of Localization Phenomena in Porous Media.* Dissertation, Bericht Nr. II-11 aus dem Institut für Mechanik (Bauwesen), Universität Stuttgart 2005.

[3] *Barthold, F.-J.*: *Theorie und Numerik zur Berechnung und Optimierung von Strukturen aus isotropen, hyperelastischen Materialien.* Dissertation, Forschungs- und Seminarberichte aus dem Bereich der Mechanik der Universität Hannover, Bericht-Nr. F 93/2, Universität Hannover 1993.

[4] *Bates, D. M.; Watts, D. G.*: *Nonlinear regression analysis and its applications.* Wiley, New York 1988.

[5] *Bathe, K.-J.*: *Finite-Elemente-Methoden.* Springer-Verlag, Berlin 1990.

[6] *Bear, J.; Bachmat, Y.*: *Introduction to Modeling of Transport Phenomena in Porous Media.* Kluwer Academic Publishers, Dordrecht 1991.

[7] *Beck, J. V.; Arnold, K. J.*: *Parameter Estimation in engineering and science.* Wiley, New York 1977.

[8] *Benedix, U.*: *Parameterschätzung für elastisch-plastische Deformationsgesetze bei Berücksichtigung lokaler und globaler Vergleichsgrößen.* Dissertation an der Fakultät für Maschinenbau und Verfahrenstechnik der Technischen Universität Chemnitz, Institut für Mechanik 2000.

[9] *Besdo, D.*: Ein Beitrag zur nichtlinearen Theorie des Cosserat-Kontinuums. *Acta Mechanica* **20** (1974), 105–131.

[10] *Blome, P.*: *Ein Mehrphasen-Stoffmodell für Böden mit Übergang auf Interface-Gesetze.* Dissertation, Bericht Nr. II-10 aus dem Institut für Mechanik (Bauwesen), Universität Stuttgart 2003.

[11] *de Boer, R.*: *Vektor- und Tensorrechnung für Ingenieure.* Springer-Verlag, Berlin 1982.

[12] *de Boer, R.*: Highlights in the historical development of porous media theory: toward a consistent macroscopic theory. *Applied Mechanics Review* **49** (1996), 201–262.

[13] *de Boer, R.*: *Theory of Porous Media.* Springer-Verlag, Berlin 2000.

[14] *de Boer, R.; Ehlers, W.*: *Theorie der Mehrkomponentenkontinua mit Anwendung auf bodenmechanische Probleme.* Forschungsberichte aus dem Fachbereich Bauwesen, Heft 40, Universität-GH-Essen 1986.

[15] *Bolzon, G.; Schrefler, B. A.; Zienkiewicz, O. C.*: Elastoplastic soil constitutive laws generalized to partially saturated states. *Géotechnique* **46** (1996), 279–289.

[16] *de Borst, R.*: Simulation of strain localization: A reappraisal of the Cosserat continuum. *Engineering Computations* **8** (1991), 317–332.

[17] *de Borst, R.; Mühlhaus, H.-B.*: Gradient-dependent plasticity: Formulation and algorithmic aspects. *International Journal for Numerical Methods in Engineering* **35** (1992), 521–539.

[18] *Bowen, R. M.*: Theory of mixtures. In *Eringen, A. C.*, editor, *Continuum Physics*, Vol. III. Academic Press, New York 1976, pp. 1–127.

[19] *Bowen, R. M.*: Incompressible porous media models by use of the theory of mixtures. *International Journal of Engineering Sciences* **18** (1980), 1129–1148.

[20] *Braess, D.*: *Finite Elemente.* Springer-Verlag, Berlin 1997.

[21] *Chang, C. S.; Ma, L.*: A micromechanical-based micropolar theory for deformation of granular solids. *International Journal of Solids and Structures* **28** (1991), 67–86.

[22] *Cosserat, E.; Cosserat, F.*: *Théorie des corps déformables.* A. Hermann et fils, Paris 1909. (Theory of Deformable Bodies, NASA TT F-11 561, 1968).

[23] *Cundall, P.; Strack, O. D. L.*: A discrete numerical model for granular assemblies. *Géotechnique* **29** (1979), 47–65.

[24] *D'Addetta, G. A.*: *Discrete models for cohesive frictional materials.* Dissertation, Bericht Nr. 42 aus dem Institut für Baustatik, Universität Stuttgart 2004.

[25] *Desai, C. S.*: A general basis for yield and potential functions in plasticity. *International Journal for Numerical and Analytical Methods in Geomechanics* **4** (1980), 361–375.

[26] *Diebels, S.*: A micropolar theory of porous media: Constitutive modelling. *Transport in Porous Media* **34** (1999), 193–208.

[27] *Diebels, S.*: *Mikropolare Zweiphasenmodelle: Formulierung auf der Basis der Theorie Poröser Medien.* Habilitation, Bericht Nr. II-4 aus dem Institut für Mechanik (Bauwesen), Universität Stuttgart 2000.

[28] *Diebels, S.; Ehlers, W.*: Dynamic analysis of a fully saturated porous medium accounting for geometrical and material non-linearities. *International Journal for Numerical Methods in Engineering* **39** (1996), 81–97.

[29] *Diebels, S.; Ehlers, W.*: On fundamental concepts of multiphase micropolar materials. *Technische Mechanik* **16** (1996), 77–88.

[30] *Diebels, S.; Ehlers, W.*: Homogenization method for granular assemblies. In *Wall, W. A.; Bletzinger, W. A.; Schweizerhof, K. U.*, editors, *Trends in Computational Mechanics*. CIMNE, Barcelona 2001, pp. 79–88.

[31] *Diebels, S.; Ellsiepen, P.; Ehlers, W.*: Error-controlled *Runge-Kutta* time integration of a viscoplastic hybrid two-phase model. *Technische Mechanik* **19** (1999), 19–27.

[32] *Diepolder, W.*: *Das Cosserat-Kontinuum als Strukturmodell für plastische Korndrehungen.* Dissertation, Fakultät für Maschinenwesen, Technische Universität München 1992.

[33] *Dietsche, A.; Steinmann, P.; Willam, K.*: Micropolar elastoplasticity and its role in localisation. *International Journal of Plasticity* **9** (1993), 813–831.

[34] *Drescher, A.; de Josselin de Jong, G.*: Photoelastic verification of a mechanical model for the flow of a granular material. *Journal of the Mechanics and Physics of Solids* **20** (1972), 337–351.

[35] *Drucker, D. C.; Prager, W.*: Soil mechanics and plastic analysis of limit design. *Quart. Appl. Math.* **10** (1952), 157–165.

[36] *Dubujet, P.; Doanh, T.*: Undrained instability of very loose Hostun sand in triaxial compression an extension. part2: theoretical analysis using an elastoplastic model. *Mechanics of Cohesive-Frictional Materials* **2** (1997), 71–92.

[37] *Ehlers, W.*: *Poröse Medien – ein kontinuumsmechanisches Modell auf der Basis der Mischungstheorie.* Habilitation, Forschungsberichte aus dem Fachbereich Bauwesen, Heft 47, Universität-GH-Essen 1989.

[38] *Ehlers, W.*: Toward finite theories of liquid-saturated elasto-plastic porous media. *International Journal of Plasticity* **7** (1991), 443–475.

[39] *Ehlers, W.*: Constitutive equations for granular materials in geomechanical context. In *Hutter, K.*, editor, *Continuum Mechanics in Environmental Sciences and Geophysics*, CISM Courses and Lectures No. 337. Springer-Verlag, Wien 1993, pp. 313–402.

[40] *Ehlers, W.*: A single-surface yield function for geomaterials. *Archive of Applied Mechanics* **65** (1995), 246–259.

[41] *Ehlers, W.*: Foundations of multiphasic and porous materials. In *Ehlers, W.; Bluhm, J.*, editors, *Porous Media: Theory, Experiments and Numerical Applications*. Springer-Verlag, Berlin 2002, pp. 3–86.

[42] *Ehlers, W.*: *Vector and tensor calculus: an introduction.* Lecture notes, Institute of Applied Mechanics (CE), University of Stuttgart 2007. `http://www.mechbau.uni-stuttgart.de/ls2/lehre/uebungen/index.php`.

[43] *Ehlers, W.; Ammann, M.; Diebels, S.*: *h*-Adaptive FE methods applied to single- and multiphase problems. *International Journal for Numerical Methods in Engineering* **54** (2002), 219–239.

[44] *Ehlers, W.; Blome, P.*: A triphasic model for unsaturated soils based on the Theory of Porous Media. *Mathematical and Computer Modelling* **37** (2003), 507–513.

[45] *Ehlers, W.; Diebels, S.; Volk, W.*: Deformation and compatibility for elasto-plastic micropolar materials with application to geomechanical problems. *Journal de Physique IV France* **8** (1998), 127–134.

[46] *Ehlers, W.; Ellsiepen, P.*: Theoretical and numerical methods in environmental continuum mechanics based on the Theory of Porous Media. In *Schrefler, B. A.*, editor, *Environmental Geomechanics*, CISM Courses and Lectures No. 417. Springer-Verlag, Wien 2001, pp. 1–81.

[47] *Ehlers, W.; Ellsiepen, P.; Ammann, M.*: Time- and space-adaptive methods applied to localization phenomena in empty and saturated micropolar and standard porous materials. *International Journal for Numerical Methods in Engineering* **52** (2001), 503–526.

[48] *Ehlers, W.; Graf, T.; Ammann, M.*: Deformation and localization analysis in partially saturated soil. *Computer Methods in Applied Mechanics and Engineering* **193** (2004), 2885–2910.

[49] *Ehlers, W.; Markert, B.; Klar, O.*: Biphasic description of viscoelastic foams using an extended Ogden-type formulation. In *Ehlers, W.; Bluhm, J.*, editors, *Porous Media: Theory, Experiments and Numerical Applications*. Springer-Verlag, Berlin 2002, pp. 275–294.

[50] *Ehlers, W.; Ramm, E.; Diebels, S.; D'Addetta, G. A.*: From particle ensembles to *Cosserat* continua: Homogenization of contact forces towards stresses and couple stresses. *International Journal of Solids and Structures* **40** (2003), 6681–6702.

[51] *Ehlers, W.; Scholz, B.*: Localization analysis of porous granular materials. In *Helmig, R.; Mielke, A.; Wohlmuth, B.*, editors, *Multifield Problems in Solid and Fluid Mechanics*. Springer-Verlag, Berlin 2006, pp. 83–112.

[52] *Ehlers, W.; Scholz, B.*: An inverse algorithm for the identification and the sensitivity analysis of the parameters governing elasto-plastic micropolar granular material. *Archive of Applied Mechanics* (2007), in print.

[53] *Ehlers, W.; Scholz, B.; Wenz, S.*: Biaxial shear band localisation computed by particle dynamics and homogenisation techniques. *Granular Matter* (2007), submitted.

[54] *Ehlers, W.; Volk, W.*: On shear band localization phenomena of liquid-saturated granular elasto-plastic porous solid materials accounting for fluid viscosity and micropolar solid rotations. *Mechanics of Cohesive-frictional Materials* **2** (1997), 301–320.

[55] *Ehlers, W.; Volk, W.*: On theoretical and numerical methods in the theory of porous media based on polar and non-polar elasto-plastic solid materials. *International Journal of Solids and Structures* **35** (1998), 4597–4617.

[56] *Ehlers, W.; Volk, W.*: Localization phenomena in liquid-saturated and empty porous solids. *Transport in Porous Media* **34** (1999), 159–177.

[57] *Ehlers, W.; Wenz, S.*: From particle ensembles to cosserat continua: Definition of the macroscopic variables. In *Vermeer, P. A.; Ehlers, W.; Herrmann, H. J.; Ramm, E.*, editors, *Modelling of Cohesive-Frictional Materials*. Balkema at Taylor & Francis, Leiden 2004, pp. 149–159.

[58] *Eipper, G.*: *Theorie und Numerik finiter elastischer Deformationen in fluidgesättigten porösen Medien*. Dissertation, Bericht Nr. II-1 aus dem Institut für Mechanik (Bauwesen), Universität Stuttgart 1998.

[59] *Ellsiepen, P.*: *Zeit- und ortsadaptive Verfahren angewandt auf Mehrphasenprobleme poröser Medien*. Dissertation, Bericht Nr. II-3 aus dem Institut für Mechanik (Bauwesen), Universität Stuttgart 1999.

[60] *Eringen, A. C.; Kafadar, C. B.*: Polar field theories. In *Eringen, A. C.*, editor, *Continuum Physics*, Vol. VI. Academic Press, New York 1976, pp. 1–73.

[61] *Eykhoff., P.*: *System identification: parameter and state estimation*. Wiley, London 1974.

[62] *Finsterle, S.*: *Inverse Modellierung zur Bestimmung hydrogeologischer Parameter eines Zweiphasensystems*. Dissertation, Technischer Bericht der Versuchsanstalt für Wasserbau, Hydrologie und Glaziologie der Eidgenössischen Technischen Hochschule Zürich 1993.

[63] *Gajo, A.; Wood, D. M.*: A kinematic hardening consitutive model for sands: the multiaxial formulation. *International Journal for Numerical and Analytical Methods in Geomechanics* **23** (1999), 925–965.

[64] *Ghadiani, S.*: *A multiphasic continuum mechanical model for design investigations of an effusion-cooled rocket thrust chamber*. Dissertation, Bericht Nr. II-13 aus dem Institut für Mechanik (Bauwesen), Universität Stuttgart 2004.

[65] *Gill, P. E.; Murray, W.; Saunders, M. A.; Wright, H. M.*: Computing forward-difference intervals for numerical optimization. *SIAM Journal on Scientific and Statistical Computing* **4** (1983), 310–321.

[66] *Grammenoudis, P.*: *Mikropolare Plastizität*. Dissertation, aus dem Fachbereich Mechanik, Technische Universität Darmstadt 2003.

[67] *Gudehus, G.*: Elastoplastische Stoffgleichungen für trockenen Sand. *Ingenieur-Archiv* **42** (1973), 151–169.

[68] *Gudehus, G.; Nübel, K.*: Evolution of shear bands in sand. *Géotechnique* **54** (2004), 187–201.

[69] *Günther, W.*: Zur Statik und Kinematik des Cosseratschen Kontinuums. *Abhandlungen der Braunschweigischen Wissenschaftlichen Gesellschaft* **10** (1958), 195–213.

[70] *Hairer, E.; Lubich, C.; Roche, M.*: *The Numerical Solution of Differential-Algebraic Equations by Runge-Kutta Methods.* Springer-Verlag 1989.

[71] *Hairer, E.; Wanner, G.*: *Solving Ordinary Differential Equations, Vol. 2: Stiff and Differential-Algebraic Problems.* Springer-Verlag, Berlin 1991.

[72] *Hartmann, S.; Tschöpe, T.; Schreiber, L.; Haupt, P.*: Finite deformations of a carbon black-filled rubber. Experiment, optical measurement and material parameter identification using finite elements. *European Journal of Mechanics - A/Solids* **22** (2003), 309–324.

[73] *Hashin, Z.*: Analysis of composite materials – a survey. *ASME Journal of Applied Mechanics* **50** (1983), 481–505.

[74] *Haupt, P.*: On the concept of an intermediate configuration and its application to a representation of viscoelastic-plastic material behavior. *International Journal of Plasticity* **1** (1985), 303–316.

[75] *Haupt, P.*: *Continuum Mechanics and Theory of Materials.* Springer-Verlag, Berlin 2000.

[76] *Heinz, J.; Spellucci, P.*: A succesful implementation of the Pantoja-Mayne SQP-method. *Optimization Methods and Software* **4** (1994), 1–28.

[77] *Hill, R.*: On constitutive macro-variables for heterogeneous solids at finite strain. *Proceedings of the Royal Society of London, Series A* **326** (1972), 131–147.

[78] *Huang, W.; Nübel, K.; Bauer, E.*: Polar extension of a hypoplastic model for granular materials with shear localization. *Mechanics of Materials* **34** (2002), 563–576.

[79] *Hughes, T. J. R.*: *The Finite Element Method.* Prentice-Hall, London 1987.

[80] *J. Desrues, G. V.*: Strain localization in sand: an overview of the experimental results obtained in grenoble using stereophotogrammetry. *International Journal for Numerical and Analytical Methods in Geomechanics* **28** (2004), 279–321.

[81] *Jirásek, M.*: Objective modeling of strain localization. *Revue française de génie civil* **6** (2002), 1119–1132.

[82] *Kim, M. K.; Lade, P. V.*: Single hardening constitutive model for frictional materials, I. Plastic potential function. *Computers and Geotechnics* **5** (1988), 307–324.

[83] *Kleiber, M.*: *Parameter Sensitivity in Nonlinear Mechanics.* John Wiley & Sons, Chichester 1997.

[84] *Kruyt, N. P.; Rothenburg, L.*: Statistical theories for the elastic moduli of two-dimensional assemblies of granular materials. *International Journal of Engineering Science* **36** (1998), 1127–1142.

[85] *Lade, P. V.; Duncan, J. M.*: Elastoplastic stress-strain theory for cohesionless soil. *Journal of the Geotechnical Engineering Division* **101** (1975), 1037–1053.

[86] *Lade, P. V.; Kim, M. K.*: Single hardening constitutive model for frictional material, II. Yield criterion and plastic work contours. *Computers and Geotechnics* **6** (1988), 13–29.

[87] *Lade, P. V.; Kim, M. K.*: Single hardening constitutive model for frictional material, III: Comparison with experimental data. *Computers and Geotechnics* **6** (1988), 31–47.

[88] *Larsen, R. J.; Marx, M. L.*: *An Introduction to Mathematical Statistics and Its Applications.* Prentice-Hall, New Jersey 1986.

[89] *Lätzel, M.*: *From microscopic simulations towards a macroscopic description of granular media.* Dissertation, Universität Stuttgart 2003.

[90] *Lippmann, H.*: Eine Cosserat-Theorie des plastischen Fließens. *Acta Mechanica* **8** (1969), 285–303.

[91] *Liu, X.; Cheng, X. H.; Scarpas, A.; Blaauwendraad, J.*: Numerical modelling of nonlinear response of soil. part 1: Constitutive model. *International Journal of Solids and Structures* **42** (2004), 1849–1881.

[92] *Luding, S.*: Micro- macro transition for anisotropic, frictional granular packings. *International Journal of Solids and Structures* **41** (2004), 5821–5836.

[93] *Luding, S.*: Shear flow modeling of cohesive and frictional fine powder. *Powder Technology* **158** (2005), 45–50.

[94] *Luenberger, D. V.*: *Introduction to Linear and Nonlinear Programming.* Addison-Wesley, Massachusetts 1973.

[95] *Mahnken, R.*: *Theoretische und numerische Aspekte zur Parameteridentifikation und Modellierung bei metallischen Werkstoffen.* Habilitation, Forschungs- und Seminarberichte aus dem Bereich der Mechanik der Universität Hannover, Bericht-Nr. F. 98/2, Universität Hannover 1998.

[96] *Mahnken, R.; Stein, E.*: Parameter identification for viscoplastic models based on analytical derivatives of a least-squares functional and stability investigations. *International Journal of Plasticity* **12** (1996), 451–479.

[97] *Mahnken, R.; Steinmann, P.*: A finite element algorithm for parameter identification of material models for fluid-saturated porous media. *International Journal for Numerical and Analytical Methods in Geomechanics* **25** (2001), 415–434.

[98] *Mahnkopf, D.*: *Lokalisierung fluidgesättigter poröser Festkörper bei finiten elastoplastischen Deformationen.* Dissertation, Bericht Nr. II-5 aus dem Institut für Mechanik (Bauwesen), Universität Stuttgart 2000.

[99] *Markert, B.*: *Finite viscoelasticity.* Dissertation, Bericht Nr. II-12 aus dem Institut für Mechanik (Bauwesen), Universität Stuttgart 2004.

[100] *McDowell, G. R.; Nakata, Y.; Hyodo, M.*: On the plastic harding of sand. *Géotechnique* **52** (2002), 349–358.

[101] *Mokni, M.; Desrues, J.*: Strain localization measurements in undrained plane-strain biaxial tests on Hostun RF sand. *Mechanics of Cohesive-Frictional Materials* **4** (1998), 419–441.

[102] *Mühlhaus, H.-B.*: Scherfugenanalyse bei granularem Material im Rahmen der Cosserat-Theorie. *Ingenieur-Archiv* **56** (1986), 389–399.

[103] *Mühlhaus, H.-B.; Aifantis, E. C.*: A variational principle for gradient plasticity. *International Journal of Solids and Structures* **28** (1991), 845–857.

[104] *Mühlhaus, H.-B.; Vardoulakis, I.*: The thickness of shear bands in granular materials. *Géotechnique* **37** (1987), 271–283.

[105] *Müllerschön, H.*: *Spannungs-Verzerrungsverhalten granularer Materialien am Beispiel von Berliner Sand.* Dissertation, Bericht Nr. II-6 aus dem Institut für Mechanik (Bauwesen), Universität Stuttgart 2000.

[106] *Myers, R. H.; Montgomery, D. C.*: *Response Surface Methodology. Process and Product Optimization using Designed Experiments.* Wiley 1995.

[107] *Nelder, J. A.; Mead, R.*: A simplex method for function minimization. *Computer Journal* **7** (1965), 308–313.

[108] *Nemat-Nasser, S.; Hori, M.*: *Micromechanics: Overall Properties of Heterogeneous Materials.* 1999.

[109] *Nowacki, W.*: *Theory of Asymmetric Elasticity.* Pergamon Press, Oxford 1986.

[110] *Perzyna, P.*: Fundamental problems in viscoplasticity. *Advances in Applied Mechanics* **9** (1966), 243–377.

[111] *Pijaudier-Cabot, G.; Bažant, Z. P.*: Nonlocal damage theory. *ASCE: Journal of Engineering Mechanics* **113** (1987), 1512–1533.

[112] *Powell, M.*: A direct search optimization method that models the objective and constraint functions by linear interpolation. In *Advances in Optimization and Numerical Analysis, Proceedings of the Sixth Workshop on Optimization and Numerical Analysis, Oaxaca, Mexico.* Kluwer Academic Publishers, Dordrecht 1994, pp. 51–67.

[113] *Rao, S. S.*: *Engineering Optimization: Theory and Practice.* Wiley, New York 1996.

[114] *Rieger, A.*: *Zur Parameteridentifikation komplexer Materialmodelle auf der Basis realer und virtueller Testdaten.* Dissertation, aus dem Institut für Mechanik (Bauwesen), Universität Stuttgart 2005.

[115] *Schaefer, H.*: Das Cosserat-Kontinuum. *Zeitschrift für Angewandte Mathematik und Mechanik (ZAMM)* **47** (1967), 485–498.

[116] *Schanz, T.*: *Zur Modellierung des mechanischen Verhaltens von Reibungsmaterialien.* Habilitation, Mitteilung 45 des Instituts für Geotechnik, Universität Stuttgart 1998.

[117] *Scheday, G.*: *Theorie und Numerik der Parameteridentifikation von Materialmodellen der finiten Elastizität und Inelastizität auf der Grundlage optischer Feldmeßmethoden.* Dissertation, aus dem Institut für Mechanik (Bauwesen), Universität Stuttgart 2003.

[118] *Schittkowski, K.*: Solving constrained nonlinear least squares problems by a general purpose SQP-method. *International Series of Numerical Mathematics* **84** (1988), 295–309.

[119] *Schrefler, B. A.*: Computer modelling in environmental geomechanics. *Computers and Structures* **79** (2001), 2209–2223.

[120] *Schröder, J.*: *Homogenisierungsmethoden der nichtlinearen Kontinuumsmechanik unter Beachtung von Stabilitätsproblemen.* Habilitation, Bericht Nr. I-7 aus dem Institut für Mechanik (Bauwesen), Universität Stuttgart 2000.

[121] *Schwarz, H. R.*: *Methode der finiten Elemente.* Teubner, Stuttgart 1991.

[122] *Schwarz, S.*: *Sensitivitätsanalyse und Optimierung bei nichtlinearem Strukturverhalten.* Dissertation, Institut für Baustatik, Universität Stuttgart 2001.

[123] *Schwefel, H. P.*: *Evolution and optimum seeking.* Wiley, New York 1995.

[124] *Spellucci, P.*: *Numerische Verfahren der Nichtlinearen Optimierung*, Vol. 2. Birkhäuser, Basel-Boston-Berlin 1993.

[125] *Spellucci, P.*: A SQP method for general linear programs using only equality constrained subproblems. *Mathematical Programming* **82** (1998), 413–448.

[126] *Spendley, W.*: Sequential applications of simplex designs in optimization and evolutionary operation. *Technometrics* **4** (1962), 441–461.

[127] *Steinmann, P.*: A micropolar theory of finite deformation and finite rotation multiplicative elasto-plasticity. *International Journal of Solids and Structures* **31** (1994), 1063–1084.

[128] *Steinmann, P.*: Theory and numerics of ductile micropolar elastoplastic damage. *International Journal for Numerical Methods in Engineering* **38** (1995), 583–606.

[129] *Steinmann, P.; Stein, E.*: A unifying treatise of variational principles for two types of micropolar continua. *Acta Mechanica* **121** (1997), 215–232.

[130] *Steinmann, P.; Willam, K.*: Localization within the framework of micropolar elasto-plasticity. In *Brüller, O.; Mannl, V.; Najar, J.*, editors, *Advances in Continuum Mechanics.* Springer-Verlag, Berlin 1991, pp. 296–313.

[131] *Thielecke, F.*: *Parameteridentifizierung von Simulationsmodellen für das visko-plastische Verhalten von Metallen – Theorie, Numerik, Anwendung.* Dissertation, Braunschweiger Schriften zur Mechanik No. 34-1998, Mechanik-Zentrum, TU Braunschweig 1998.

[132] *Truesdell, C.; Toupin, R. A.*: The classical field theories. In *Flügge, S.*, editor, *Handbuch der Physik*, Vol. III/1. Springer-Verlag, Berlin 1960, pp. 226–902.

[133] *Vermeer, P. A.*: A Double Hardening Model for Sand. *Géotechnique* **28** (1978), 413–433.

[134] *Vidal, C. A.; Haber, R. B.*: Design sensitivity for rate-independent elastoplasticity. *Computer Methods in Applied Mechanics and Engineering* **107** (1993), 393–431.

[135] *Volk, W.*: *Untersuchung des Lokalisierungsverhaltens mikropolarer poröser Medien mit Hilfe der Cosserat-Theorie.* Dissertation, Bericht Nr. II-2 aus dem Institut für Mechanik (Bauwesen), Universität Stuttgart 1999.

[136] *Wang, Q.; Lade, P. V.*: Shear banding in true tests and its effect on failure in sand. *Journal of Engineering Mechanics* **127** (2001), 754–761.

[137] *Weisberg, S.*: *Applied Linear Regression.* Wiley 1980.

[138] *Wieners, C.; Ammann, M.; Diebels, S.; Ehlers, W.*: Parallel 3-d simulations for porous media models in soil mechanics. *Computational Mechanics* **29** (2002), 73–87.

[139] *Wieners, C.; Ammann, M.; Ehlers, W.*: Distributed Point Objects: A new concept for parallel finite elements applied to a geomechanical problem. *Future Generation Computer Systems* **22** (2006), 532–545.

[140] *Wieners, C.; Ammann, M.; Ehlers, W.; Graf, T.*: Parallel Krylov methods and the application to 3-d simulations of a triphasic porous media model in soil mechanics. *Computational Mechanics* **36** (2005), 409–420.

[141] *Wood, W. L.*: *Practical time-stepping schemes.* Clarendon Press, Oxford 1990.

[142] *Yamada, Y.; Ishihara, K.*: Anisotropic deformation characteristic of sand under three dimensional stress conditions. *Soils and Foundation* **19** (1979), 79–94.

[143] *Zienkiewicz, O. C.; Taylor, R. L.*: *The Finite Element Method: The Basis*, Vol. 1. Butterworth-Heinemann, London 2000.

Curriculum Vitae

Bernd Scholz

28. September 1970	geboren in Stuttgart
1977 – 1981	Grundschule in Bietigheim-Bissingen
1981 – 1987	Realschule in Konstanz
1987 – 1990	Technisches Gymnasium in Konstanz
1990 – 1991	Grundwehrdienst in Sigmaringen
10/1991 – 04/1996	Studium des Bauingenieurwesens an der Universität Stuttgart
06/1996 – 11/2000	Projektingenieur im Büro für Baudynamik in Stuttgart
12/1999 – 12/2006	Wissenschaftlicher Angestellter am Institut für Mechanik (Bauwesen) der Universität Stuttgart
seit 1/2007	Berechnungsingenieur bei der TWT in Neuhausen

Bisher in dieser Reihe erschienen:

II-1   G. EIPPER: Theorie und Numerik finiter elastischer Deformationen in fluidgesättigten porösen Festkörpern, Juni 1998.

II-2   W. VOLK: Untersuchung des Lokalisierungsverhaltens mikropolarer poröser Medien mit Hilfe der *Cosserat*-Theorie, Mai 1999.

II-3   P. ELLSIEPEN: Zeit- und ortsadaptive Verfahren angewandt auf Mehrphasenprobleme poröser Medien, Juli 1999.

II-4   S. DIEBELS: Mikropolare Zweiphasenmodelle: Formulierung auf der Basis der Theorie Poröser Medien, März 2000.

II-5   D. MAHNKOPF: Lokalisierung fluidgesättigter poröser Festkörper bei finiten elastoplastischen Deformationen, März 2000.

II-6   H. MÜLLERSCHÖN: Spannungs-Verformungsverhalten granularer Materialien am Beispiel von Berliner Sand, August 2000.

II-7   S. DIEBELS (Hrsg.): Zur Beschreibung komplexen Materialverhaltens: Beiträge anläßlich des 50. Geburtstages von Herrn Prof. Dr.-Ing. Wolfgang Ehlers, August 2001.

II-8   J. WIDJAJAKUSUMA: Quantitative Prediction of Effective Material Parameters of Heterogeneous Materials, Juni 2002.

II-9   A. DROSTE: Beschreibung und Anwendung eines elastisch-plastischen Materialmodells mit Schädigung für hochporöse Metallschäume, Oktober 2002.

II-10   P. BLOME: Ein Mehrphasen-Stoffmodell für Böden mit Übergang auf Interface-Gesetze, Oktober 2003.

II-11   M. AMMANN: Parallel Finite Element Simulations of Localization Phenomena in Porous Media, April 2005.

II-12   B. MARKERT: Porous Media Viscoelasticity with Application to Polymeric Foams, July 2005.

II-13   S. R. GHADIANI: A multiphasic continuum mechanical model for design investigations of an effusion-cooled rocket thrust chamber, Oktober 2005.

II-14   W. EHLERS & B. MARKERT (Eds.): Proceedings of the 1st GAMM Seminar on Continuum Biomechanics, September 2005.

II-15   B. SCHOLZ: Application of a Micropolar Model to the Localization Phenomena in Granular Materials: General Model, Sensitivity Analysis and Parameter Optimization, August 2007.